Advances in Experimental Medicine and Biology 1380

Rosalind Sadleir
Atul Singh Minhas *Editors*

Electrical Properties of Tissues

Quantitative Magnetic Resonance Mapping

Springer

Advances in Experimental Medicine and Biology

Volume 1380

Advances in Experimental Medicine and Biology provides a platform for scientific contributions in the main disciplines of the biomedicine and the life sciences. This series publishes thematic volumes on contemporary research in the areas of microbiology, immunology, neurosciences, biochemistry, biomedical engineering, genetics, physiology, and cancer research. Covering emerging topics and techniques in basic and clinical science, it brings together clinicians and researchers from various fields.

Advances in Experimental Medicine and Biology has been publishing exceptional works in the field for over 40 years, and is indexed in SCOPUS, Medline (PubMed), EMBASE, BIOSIS, Reaxys, EMBiology, the Chemical Abstracts Service (CAS), and Pathway Studio.

2021 Impact Factor: 3.650 (no longer indexed in SCIE as of 2022)

Rosalind Sadleir • Atul Singh Minhas
Editors

Electrical Properties of Tissues

Quantitative Magnetic Resonance Mapping

Springer

Editors
Rosalind Sadleir
School of Biological and Health
Systems Engineering
Arizona State University
Tempe, AZ, USA

Atul Singh Minhas
School of Engineering
Macquarie University
Wallumattagal Campus,
Macquarie Park, NSW, Australia

ISSN 0065-2598 ISSN 2214-8019 (electronic)
Advances in Experimental Medicine and Biology
ISBN 978-3-031-03872-3 ISBN 978-3-031-03873-0 (eBook)
https://doi.org/10.1007/978-3-031-03873-0

Preface

The electrical properties of tissues are a fundamental characteristic providing a unique and extremely sensitive insight into their composition and function. While values for intrinsic tissue conductivity and permittivity may be determined using excised samples or in situ using conductivity cells or probes, there is increasing interest in imaging the distribution of these properties within the body. The area of electrical impedance tomography (EIT) has now existed for over 40 years and has important applications in areas such as non-invasive lung monitoring and functional imaging. Though EIT is a very sensitive monitoring technique, limitations arise because of the general ill-posedness of the inverse problem. Current density imaging using magnetic resonance imaging was first demonstrated by Scott and Joy, working at the University of Toronto in the early 1990s. The suggestion to use this approach to image conductivity distributions was also made by this group. The earliest approaches to imaging both current density and conductivity proceeded assuming three different measurements, representing the three components of the magnetic flux density distribution caused by an external current. In the early 2000s, Seo and Woo contributed to an approach that involved measuring and using only a single component of the magnetic flux density. At around the same time, Katscher and colleagues were developing practical strategies for imaging conductivity and permittivity distributions at the Larmor frequencies of MRI systems. Over the years, numerous methods for reconstructing electromagnetic fields and conductivity distributions have been suggested and tested. The currents required to image conductivities at the lowest frequencies have reduced from over 20 mA to around 1.5 mA, and measurements of human head conductivities have been obtained in vivo. High-frequency conductivity measurements are being tested in clinical trials, and the newest conductivity reconstruction methods involve no current administration at all, involving only diffusion tensor imaging and high-frequency conductivity distributions. The area is also benefiting from interest in studying mechanisms and individualized treatments in neuromodulation therapies such as transcranial AC and DC stimulation, which require measurement of current density and electric field distributions.

The volume is organized assuming the reader is an undergraduate or graduate student focusing on advanced topics in MRI, or a researcher unfamiliar with the general area of tissue electrical properties and MRI. Chapter 1 begins

with a basic treatment of the factors underlying the electrical properties of tissues. A practical introduction to the finite element analysis and electromagnetic modeling, typically required during reconstructions, is given in Chap. 2. Chapter 3 covers a basic introduction to MRI focusing on hardware, physics, mathematical expressions for k-space, pulse sequences, image reconstruction, and SNR methods, forming the basis of phase imaging in MRI. Chapters 4 and 5 are concerned with constructing phantoms for conductivity imaging, and the next two chapters present a comprehensive overview of MRI methods for reconstructing current density (Chap. 6) and conductivity (Chap. 7). The volume concludes with an examination of important factors in measuring high-frequency conductivity (Chap. 8).

This book arose out of a successful workshop that was held at the 39th Annual International Conference of the IEEE Engineering in Medicine and Biology conference which took place at Jeju Island, Republic of Korea, in 2018. We would like to thank and acknowledge our friends and mentors Eung Je Woo, Jin Keun Seo, and Oh In Kwon; our co-authors Camelia Gabriel, Munish Chauhan, Saurav Z. K. Sajib, Ulrich Katscher, Ruth Oliver, and Nitish Katoch; and our families and colleagues for their contributions to this project. We would also like to convey our gratitude to Merry Stuber and Deepak Ravi at Springer for their assistance in compiling this volume.

Tempe, AZ, USA — Rosalind Sadleir
Sydney, NSW, Australia — Atul Singh Minhas
February 2022

Contents

Electromagnetic Properties and the Basis for CDI, MREIT, and EPT

1

Rosalind Sadleir, Camelia Gabriel, and Atul Singh Minhas

Abstract

The electromagnetic properties of body tissues depend on numerous factors, the most important of which are ionic concentrations and, particularly in the low-frequency regime, membrane density and geometry. In this chapter, the characteristics of these properties and their spectra are introduced. The properties measured by different types of MR-based methods are described.

1.1 Electrical Properties of Tissue

1.1.1 What Underlies Tissue Electromagnetic Properties

The electromagnetic properties of body tissues are characteristic of their cellular structure and composition, that is, of biological molecules and electrolytes arranged in an aqueous solution. Tissue electrical properties can be summarized using electrical conductivity and permittivity values and their spectra. For most biological materials, the magnetic permeability is close to that of free space, which implies very weak interaction with the magnetic component of electromagnetic fields at low field strength. The most significant magnetic contrasts in body tissues are related to the presence of paramagnetic iron (in ferritin and deoxygenated hemoglobin) and calcium [34].

Tissue response to an incident electromagnetic field can therefore be considered as mostly depending on electrical conductivity or capacity (permittivity) properties and can be modeled from either perspective. Depending on the tissue composition involved, one approach may be more natural than another. For example, more solid tissues tend to have larger charge storage capability or polarizability and may be described more appropriately using permittivity rather than conductivity. In either case, the property characterizing tissue electrical properties is a complex quantity, and conductive or capacitive properties may be measured using in-phase (real) or quadrature (imaginary) measurements, respectively.

Tissue properties result from multiple influences including tissue heterogeneity, interfacial effects, and directionality or *anisotropy*. At frequencies below around 100 kHz, phase shifts

R. Sadleir (✉)
School of Biological and Health Systems Engineering, Arizona State University, Tempe, AZ, USA
e-mail: Rosalind.Sadleir@asu.edu

C. Gabriel
C. Gabriel Consultants, San Diego, CA, USA

A. S. Minhas
School of Engineering, Macquarie University, Wallumattagal Campus, Macquarie Park, NSW, Australia
e-mail: atul.minhas@mq.edu.au

R. Sadleir, A. S. Minhas (eds.), *Electrical Properties of Tissues*, Advances in Experimental Medicine and Biology 1380, https://doi.org/10.1007/978-3-031-03873-0_1

resulting from capacitive tissue characteristics are very small, and measurements almost all relate to conductive properties. The conductive properties of tissues in this range are mostly due to the presence of electrolytes in body fluids as well as the concentration and membrane geometry. At higher frequencies, conductivity mostly depends on ionic concentrations. Because tissues contain a lot of water, all tissues also show effects of the large absorption energy by of water molecules around 2 GHz (the same frequency used by microwave ovens).

The dependencies of real and imaginary tissue electrical properties on frequency are related via the Kramers-Kronig relations; therefore, characteristics of conductivity spectra may be intuited from permittivity spectra, and vice versa. The compound nature of these properties means that special electrical components must be introduced to best model tissue spectra.

In the sections below, we consider ionic contributions to tissue conductivities, followed by reactive and frequency-dependent characteristics. Commonly observed features of conductivity and permittivity spectra will be described and properties of tissues important to imaging electromagnetic properties will be outlined. Last, methods and important considerations for making "benchtop" measurements of tissue properties for verification of these imaging methods will be summarized, as they are important for reconstruction validation. Validation, including constructing phantoms to test methods, is also discussed further in Chap. 4.

1.1.1.1 Ionic Conductivities

Because the water content of tissues is significant, their properties are closely related to those of electrolytes in aqueous solution. The most common ions in the body are sodium and chloride, with ions of potassium, bicarbonate, calcium, and magnesium also contributing to the ionic environment of intra- or extracellular environments. Properties of electrolytic solutions were investigated extensively in the nineteenth century. The Kohlrausch law describes the dependence of the molar conductivity on concentration. At low concentrations, this experimental data agrees very well with the resistivity values that may be calculated using the expression

$$\Lambda_m = \Lambda_m^o - Kc^{1/2} \tag{1.1}$$

where Λ_m is the molar conductivity in S $m^{-1}mol^{-1}$ L and where c is the molar conductivity of the electrolyte. K is the Kohlrausch coefficient, a value that depends on the solvent and the charge on ionic species as well as the molar concentration itself. The molar conductivity of the salt at infinite dilution is Λ_m^o. The conductivity of a solution and its conductivity σ are related via

$$\sigma = \Lambda_m c \tag{1.2}$$

Following (1.2), the conductivity of a solution broadly increases linearly with molar concentration of electrolyte, but this dependence progressively decreases as concentration increases. Figure 1.1 shows the conductivity of NaCl in solution (saline) as a function of molar concentration at 25 C. Data from this plot were obtained from published experimental data [13]. In the case of NaCl dissolved in water, the value for K is $89.14 \times 10^{-4}\ \Omega^{-1}\ m^2mol^{-1}/(mol.L^{-1})^{-1/2}$. The molar conductivity at infinite dilution at 25 C is approximately $126.4 \times 10^{-4}\ \Omega^{-1}m^2mol^{-1}$. The curves start to diverge at a molar concentration of around 0.3 mol/L (17 g/L) which is also about twice the NaCl concentration of normal (0.9% or 9 g/L) saline solution. Note that the graph indicates that at very high molarities, the conductivity predicted by Eqs. (1.1) and (1.2) actually begins to decrease, which is because this approximation breaks down as concentrations become high. Note also that at very high concentrations (> 6 mol/L) of NaCl the solution becomes saturated.

The conductivity of an aqueous salt solution will also tend to increase with increasing temperature because of the decrease in the viscosity of water with temperature. This leads to an increase in the mobility of ions in solution and hence in the molar conductivity. This trend underlies the observed temperature dependence of tissue conductivity. Measurements of tissue properties,

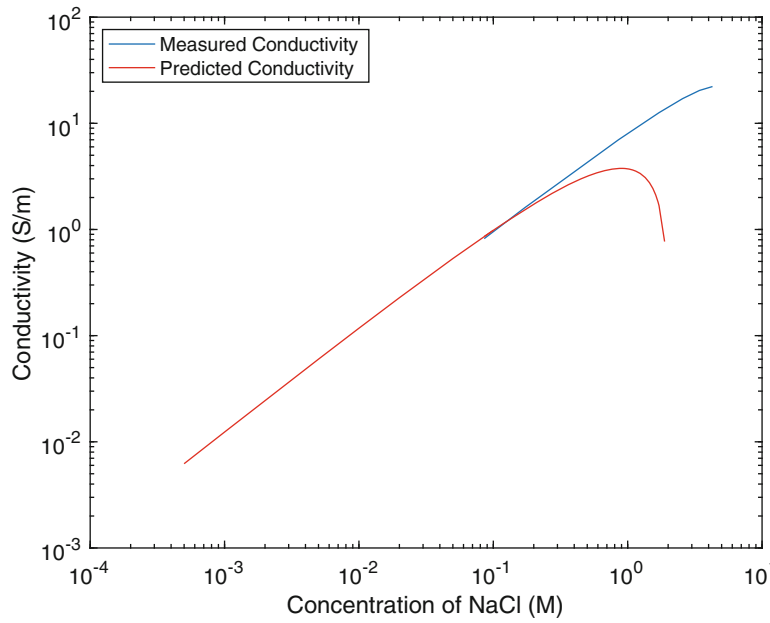

Fig. 1.1 Dependence of conductivity of sodium chloride in aqueous medium on molar concentration at 25 °C. The red line shows the predicted dependence of conductivity following Eqs. (1.1) and (1.2). The blue line plots experimental measurements of saline conductivity

if not made in vivo, should therefore also specify the ambient temperature. Tissue properties change rapidly after death [23], and measured conductivities in excised tissues, even if measured at body temperature, may not be representative of those found in vivo. Conductivity measurements made using a dielectric probe or conductivity cell may be calibrated using simple, fully dissociated ionic salt solutions whose conductivities can be characterized described using (1.2), such as NaCl or KCl. For example, Gabriel et al. [8] present measurements of tissue conductivities and permittivities calibrated over the range 10 Hz–20 GHz based on dielectric probe calibrations performed using 5 mM saline solutions. Measurements of saline properties over a range of concentrations, frequencies, and temperatures, as reported in Peyman et al. [24], may also assist calibrations. Conductivity standards (usually KCl solutions) having known and calibrated conductivities can also be purchased.

1.1.1.2 Membranes and Solid Tissues

Solid tissues demonstrate dielectric-like properties. In the treatment below, we follow the convention established by Grimnes and Martinsen [12]. The complex conductivity, $\boldsymbol{\sigma}$, consists of real and imaginary parts σ' and σ''

$$\boldsymbol{\sigma} = \sigma' + i\sigma'' \tag{1.3}$$

Similarly, the complex permittivity $\boldsymbol{\varepsilon}$ can be expressed as

$$\boldsymbol{\varepsilon} = \varepsilon' - i\varepsilon'' \tag{1.4}$$

where $\varepsilon' = \varepsilon_r'\varepsilon_0$, $\varepsilon'' = \varepsilon_r''\varepsilon_0$, ε_0 is the permittivity of free space (8.8542×10^{-12} F/m, and ε_r' and ϵ_r'' are dimensionless relative parameters characteristic of the material.

If a measured electrical property is assumed to be capacitive in nature and is expressed as a complex admittance $\mathbf{Y} = i\omega\mathbf{C}$, this quantity can be expressed as

$$\mathbf{Y} = G + i\omega C = \frac{A}{d}\left(\sigma' + i\omega\varepsilon'\right) \tag{1.5}$$

where the capacitor or electrodes have face area A and thickness d. The relationship between the complex conductivity and permittivity

parameters can be found by substitution of (1.4) into (1.5):

$$\mathbf{Y} = i\omega\mathbf{C} = i\omega\frac{A\boldsymbol{\varepsilon}}{d} = \omega\frac{A}{d}\varepsilon'' + i\frac{A}{d}\omega\varepsilon'. \quad (1.6)$$

Comparing (1.5) and (1.6) leads to the identification

$$\varepsilon'' = \frac{\sigma'}{\omega}. \quad (1.7)$$

This tells us that the quadrature component of measured permittivity can be obtained from the in-phase conductivity by dividing by the angular frequency $\omega = 2\pi f$, where f is the measurement frequency in Hz.

Note that a quantity of interest to in EPT is denoted $\boldsymbol{\kappa}$, where

$$\boldsymbol{\kappa} = \omega\boldsymbol{\varepsilon} = \omega\varepsilon' - i\sigma'. \quad (1.8)$$

1.1.1.3 Relaxation Models of Tissue Properties

An equivalent circuit that can be used to describe both capacitive and conductive tissue properties over a small frequency range consists of a capacitor in parallel with a series capacitor and resistor (Fig. 1.2).

It can be shown that if ω is the angular frequency and τ is a time constant ($\tau = R\Delta C$), the complex capacitance of the circuit is given by

$$\mathbf{C} = C_\infty + \frac{\Delta C}{1 + i\omega\tau} \quad (1.9)$$

You can see that the capacitance tends to an asymptotic value C_∞ at high (∞) angular frequencies and as $\omega\tau >> 1$.

At low frequencies, when $\omega\tau << 1 : C \approx \Delta C + C_\infty$, which makes $\Delta C = C_0 - C_\infty$ where we denote the low-frequency "static" capacitance with the subscript (0).

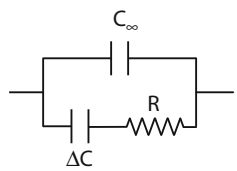

Fig. 1.2 Example Debye dispersion circuit consisting of two capacitors and one resistor

A parallel equation that can be written of terms of ε' and ε'' (taking out the geometrical factor $\frac{A}{d}$) is

$$\boldsymbol{\varepsilon} = \frac{\varepsilon_0 - \varepsilon_\infty}{1 + i\omega\tau} = \varepsilon'(\omega) - i\varepsilon''(\omega). \quad (1.10)$$

This relationship is known as the Debye equation; it applies whenever the decay of polarization is exponential and associated with a single relaxation time.

The frequency dependencies of the Debye parameters ε' and ε'' and measured impedances have the form illustrated in Fig. 1.3 for R=500 Ω, $\varepsilon'_{\infty,r} = 1000$, $\Delta\varepsilon' = 10000 = \Delta C d / A\varepsilon_0$, and a geometric factor $\frac{A}{d}$ of 20 m.

The effective permittivity and conductivity of the material vary as a function of frequency. The permittivity reduces as frequency increases, and the conductivity increases, with the frequency of the transition occurring at the critical frequency ω_c, that is the frequency at which $\omega\tau = 1$.

Debye or parallel or series simple resistor-capacitor models involve ideal components, as well as describe only a single transition (dispersion). Naturally, properties of biological materials do not show the characteristics of pure resistors and capacitors; complex tissue properties are characteristic of multiple, overlapping polarizations better described in terms of a relaxation time *distribution*. Such properties are better described using circuits containing components whose properties vary as a function of frequency.

For most materials (at $\omega\tau >> 1$), a power law dependence of the type $\frac{\omega^{m-1}}{\tau}$ applies for both $\varepsilon'(\omega)$ and $\varepsilon''(\omega)$, with $m \neq 0$, making the ratio $\varepsilon''(\omega)/\varepsilon'(\omega)$ frequency independent (constant phase). These dependencies are modeled with constant phase elements (CPEs), such that the overall phase of $\mathbf{Y}$ does not vary.

Instead of using a lumped resistor or capacitor, consider a parallel-component circuit where the admittance $\mathbf{Y}$ is described by

$$\begin{aligned}\mathbf{Y}_{cpe} &= G_{cpe} + iB_{cpe} = (\omega\tau)^m \left(G_{\boxed{1}} + iB_{\boxed{1}}\right) \\ &= (\omega\tau)^m G_{\boxed{1}} + i\omega^m\tau^{m-1}C_{\boxed{1}}, \end{aligned} \quad (1.11)$$

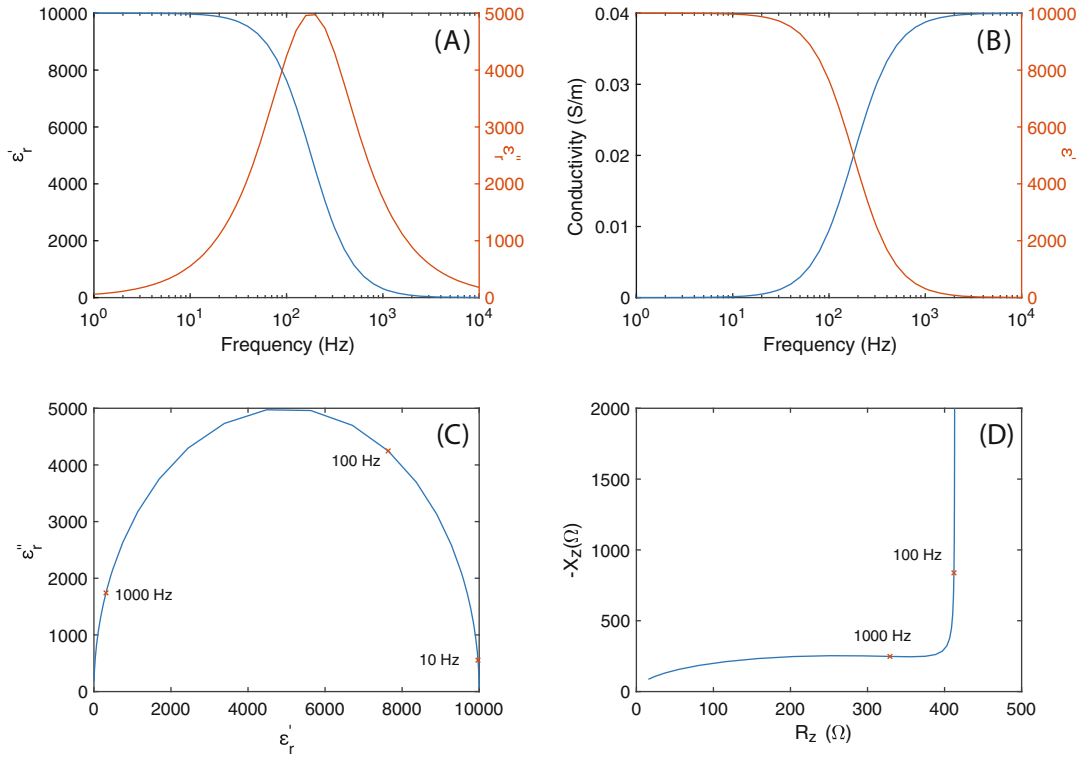

Fig. 1.3 Characteristics of Debye circuit calculated with $R = 500\Omega$, $\varepsilon'_{\infty,r} = 1000$, $\Delta\varepsilon' = 10000$, and (A/d) of 20 m. Part (**a**) shows characteristics of real (blue curve, left axis) and imaginary (red, right) components of relative permittivity as a function of frequency, (**b**) shows conductivity (blue, left) and real component of relative permittivity (red, right), (**c**) plots real and imaginary components of frequency, and (**d**) plots real and imaginary components of effective impedance (R_z and $-X_z$)

where the susceptance $B = \omega C$, m is a real number between 0 and 1, and τ is a frequency scaling factor. The notation $(\cdot)_{\boxed{1}}$ refers to value of G, B, or C when $\omega\tau = 1$. Since both G and B scale with frequency in the same way, the constant phase value is

$$\varphi_{cpe} = \tan^{-1}\frac{B}{G}. \tag{1.12}$$

Using the constant phase element approach, both $G = (\omega\tau)^m G_{\boxed{1}}$ and $B = (\omega\tau)^m B_{\boxed{1}}$ increase with frequency. At 0 Hz, both Y and B are zero; therefore, a DC admittance is not included in the model. Since $B_{\boxed{1}} = 1/\tau C_{\boxed{1}}$ (recall $B = \omega C$ and $\omega_c = \omega = 1/\tau$ at $\omega\tau = 1$), it also follows that $C = (\omega\tau)^{m-1} C_{\boxed{1}}$ and that C decreases with frequency (since $m - 1 < 1$). As frequency increases, G tends toward infinity.

A special case of the CPE model was observed, in experimental data, by Fricke [5]; the frequency dependence of capacitance depends on a parameter, α, such that $C \propto f^{-\alpha}$ and that the constant phase angle is $\varphi_{cpe} = \alpha\pi/2$. In this case, the model properties are described using the Fricke CPE as

$$\mathbf{Y}_{cpe} = (i\omega\tau)^\alpha G_{\boxed{1}} = (\omega\tau)^\alpha G_{\boxed{1}} \left(\cos\tfrac{\alpha\pi}{2} + i\sin\tfrac{\alpha\pi}{2}\right) \tag{1.13}$$

As noted above, the general CPE of (1.11) has an infinite admittance at DC if $m \neq 0$. This is also true of the Fricke CPE in (1.13) if $\alpha \neq 0$. The parallel Fricke CPE can be modified to add

a parallel frequency-independent conductance to modify this behavior. Another behavior can be derived if the two CPEs are combined in series. In this case, the impedance of the CPE is

$$\mathbf{Z}_{cpe} = (i\omega\tau)^{-\alpha} R\boxed{1}\left(\cos\frac{\alpha\pi}{2} - i\sin\frac{\alpha\pi}{2}\right) \tag{1.14}$$

A special case of the Fricke CPE, the Cole-Cole model, involves a series Fricke CPE combination with a fixed series capacitance and one parallel capacitance, as shown in Fig. 1.4. In this model, resistive and capacitive CPEs are shown in series in the lower arm of the parallel combination and are indicated with modified symbols. It is most appropriate for characterization of tissues with little DC conductance or to describe higher-frequency properties.

The admittance of this model is described by

$$\begin{aligned}\mathbf{Y} &= i\omega\mathbf{C} = i\omega\frac{A}{d}\boldsymbol{\varepsilon} \\ &= i\omega\frac{A}{d}\left(\varepsilon_\infty + \frac{\Delta\varepsilon}{1+(i\omega\tau)^{1-\alpha}}\right)\end{aligned} \tag{1.15}$$

where we define

$$\Delta\varepsilon = \frac{d}{A}\Delta C \text{ and } \varepsilon_\infty = \frac{d}{A}C_\infty \tag{1.16}$$

and α is a distribution parameter in the range $1 > \alpha \geq 0$. The factor ΔC describes the difference between capacitances of the CPE static element at low and high frequencies, that is, $\Delta C = C_L - C_\infty$.

From (1.4) and (1.5), the Cole-Cole dependence may alternatively be written as

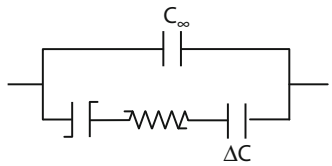

Fig. 1.4 Cole-cole permittivity model. The tagged resistor and capacitor symbols indicate constant phase element types arranged in series. The capacitors C_∞ and ΔC describe capacitance values at high frequencies or changes in capacitance from low to high frequencies, respectively

$$\boldsymbol{\varepsilon} = \varepsilon_\infty + \frac{\Delta\varepsilon}{1+(i\omega\tau)^{1-\alpha}} \text{ or} \tag{1.17}$$

$$\mathbf{C} = C\infty + \frac{\Delta C}{1+(i\omega\tau)^{1-\alpha}} \tag{1.18}$$

which is known as the Cole-Cole model; for $\alpha = 0$, it reverts to a Debye dispersion model.

The Cole-Cole models can be used to fit observed tissue measurements to the parameters α, $(\cdot)_\infty$, $\Delta(\cdot)$, and τ in (1.15), (1.17), or (1.18). This may be used to characterize tissue properties over a wide frequency range. A plot of the dependence of parameters on frequency for a tissue having a single dispersion characterized by a Cole-Cole model with $\Delta\varepsilon = 10000$, $\tau = 1$ ms, and $\alpha = 0.3$ is shown in Fig. 1.5. It may be compared with matching parameters for the Debye dispersion in Fig. 1.3. Note that the low-frequency properties shown in Fig. 1.5d are markedly different from those in Fig. 1.3d.

In real tissue, several characteristic relaxations are observed, with individual dispersions typically in the Hz, kHz, and MHz ranges. The processes involved in each transition are presumed to be related to interfacial processes at the different scales involved and are of course also each due to a mixture of possible relaxation times and processes. The transitions are labeled alpha, beta, and gamma dispersions at lower-, intermediate-, and higher-frequency ranges, respectively. In addition, all tissues show a strong water-related dispersion in the GHz range (Fig. 1.6).

To characterize individual dispersions, parameters in (1.15), (1.17), or (1.18) may be fitted by considering frequencies around each dispersion, as in [8]. In this case, the parameters $\alpha(\cdot)_\infty$, $\Delta(\cdot)$, and τ_c are defined only over the frequency range of each dispersion where $(\cdot)_\infty$ would be more correctly defined as $(\cdot)_H$; the parameter at the higher frequency, $\Delta(\cdot)$, denotes the change in ε or C that occurs over the frequency range of the dispersion; and τ indicates the center frequency of the dispersion $f_c = 1/(2\pi\tau_c)$. Each dispersion, characterized by its parameters, provides an indication of the distribution of relaxation times and the scales of physical processes involved in each frequency range.

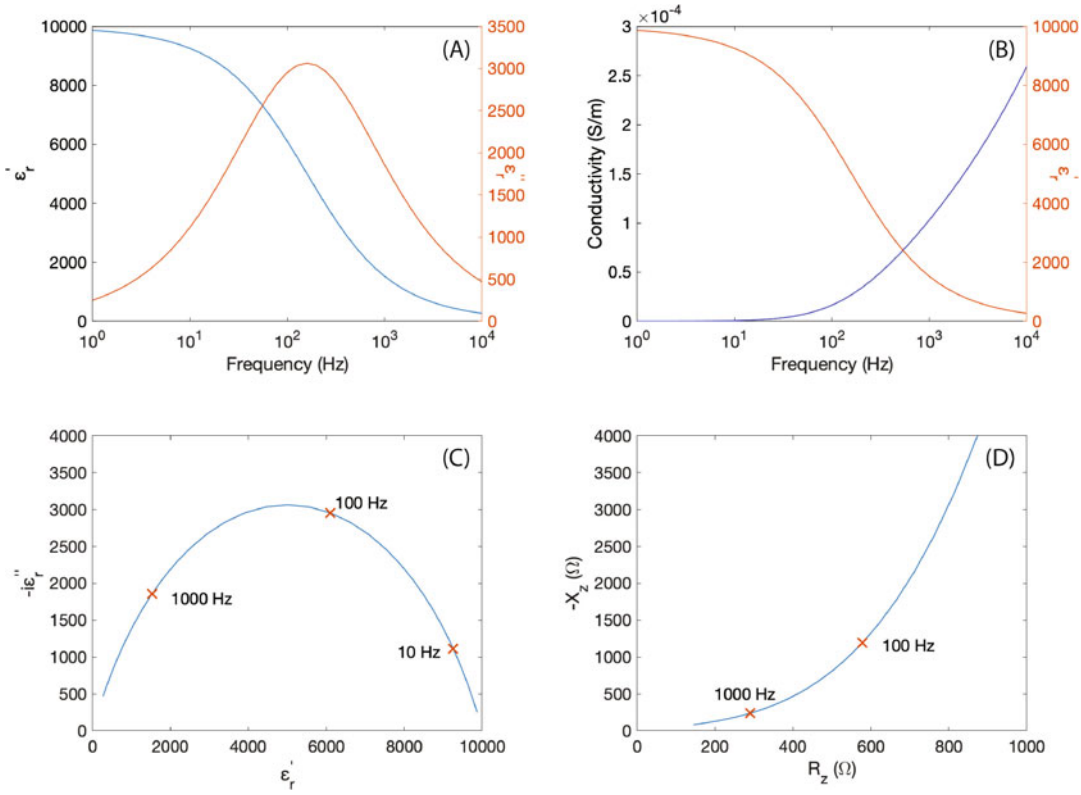

Fig. 1.5 Cole-cole dependency for tissue with $\Delta\varepsilon = 10000$, $\tau = 1$ ms, and $\alpha = 0.3$. As in Fig. 1.3, part (**a**) shows characteristics of real (blue curve, left axis) and imaginary (red, right) components of relative permittivity as a function of frequency, (**b**) shows conductivity (blue, left) and real component of relative permittivity (red, right), (**c**) plots real and imaginary components of frequency, and (**d**) plots real and imaginary components of effective impedance (R_z and $-X_z$)

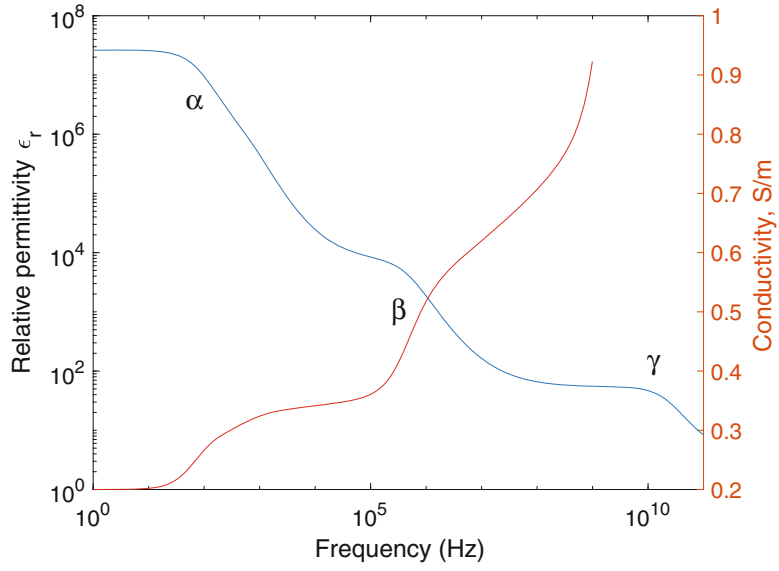

Fig. 1.6 Alpha, beta, and gamma dispersions illustrated in conductivity and permittivity spectra for muscle. Plots generated using parameters determined by Gabriel et al. [9]

1.1.1.4 Relationship Between Diffusion and Conductivity

We noted in Sect. 1.1.1.1 that tissue conductivity is closely related to ionic mobility. As a consequence, tissue conductivity is also intimately connected to the diffusivity properties of tissue. Tuch et al. [32] showed that conductivity and water diffusion eigenvectors σ_v and d_v are linked by the approximation

$$\sigma_v = \frac{\sigma_e}{d_e}\left[d_v\left(\frac{d_i}{3d_e}+1\right)+\frac{d_v^2 d_i}{3d_e^2}-\frac{2}{3}d_i\right]+O(d_i^2) \tag{1.19}$$

where d_i and d_e and σ_e are the diffusion coefficients and conductivities in intra- (i) or extracellular (e) spaces. This leads to the inference that low-frequency conductivity tensors should be recoverable only from measurements of diffusion tensor distribution obtained via MRI and assumptions or measurements of intra- and extracellular diffusion coefficients. In practice, accurate employment of the relationship requires additional measurements. Practical measurements of conductivity have been approached by using diffusion tensor information combined with current administration (DT-MREIT; see Chapter 7.6) [3, 18] or combined with high-frequency conductivity measurements [17] to reconstruct an isotropic scaling factor η that relates conductivity ($\mathbb{C}$) and diffusion ($\mathbb{D}$) tensors as

$$\mathbb{D} = \eta\mathbb{C}. \tag{1.20}$$

You can find more information about diffusion tensor imaging (DTI) and methods for reconstructing conductivity tensors using DTI data in Chap. 7.

1.1.2 Anisotropic Tissue Properties

Anisotropy relates to the directionality of a property. Electrical anisotropy is manifested when the tissue conductivity is different when measured along different geometric directions, and as a consequence, anisotropy is a sensitive metric of local tissue microstructure defined by membrane architecture. Because membranes are thin and their capacitance is effectively "shorted out" at very high frequencies, anisotropy is mostly manifested at low-frequency ranges (<100 kHz). The best examples of tissue electrical anisotropy are observed in skeletal and cardiac muscle and in white matter. The directionality properties arise from the cellular structure of these tissues. In both white matter and skeletal muscle, the tissue is composed of long cell bundles aligned such that ion transport along these cells and consequently conductivity is lower along bundles than across them. Shorter cardiac cells are connected in long chains to achieve similar properties. It is important to emphasize that anisotropy is not the same as tissue inhomogeneity. Consider the case of measuring impedances across a cubic sample of tissue in the chamber shown in Fig. 1.10. While different impedances may be measured if the tissue rotated into different orientations relative to the electrodes, this may be because the sample consists of mixed tissue types. In a simple case, the tissue might consist of layers of two different substances as illustrated in Fig. 1.7. The apparent anisotropy σ_l/σ_t is the ratio of the conductivity measured on the object along the layers in the longitudinal (l) direction to that measured across them (t). The ratio is plotted as a function of the relative layer thickness.

The apparent anisotropy depends on the relative thickness of the layers ($\alpha = t_1/t_2$) and relative conductivities, with this quantity being much smaller than the actual conductivity contrast of the layers. As shown in Fig. 1.7, the maximum apparent anisotropy for a conductivity ratio of 10 occurs when both layers have the same thickness and is only around 3 [25]. The characterization of tissue as anisotropic relates to the geometric scale of the directionality or inhomogeneity with respect to the geometric scale of the measurement. In Fig. 1.8 , the apparent (measured) resistivity recovered by a specific four-terminal measurement configuration as layer number increases is plotted as a function of the relative conductivity of the layered structure that would be measured by a uniform field. The measurements are compared with apparent resistivities characteristic of a truly anisotropic and inhomogeneous structure.

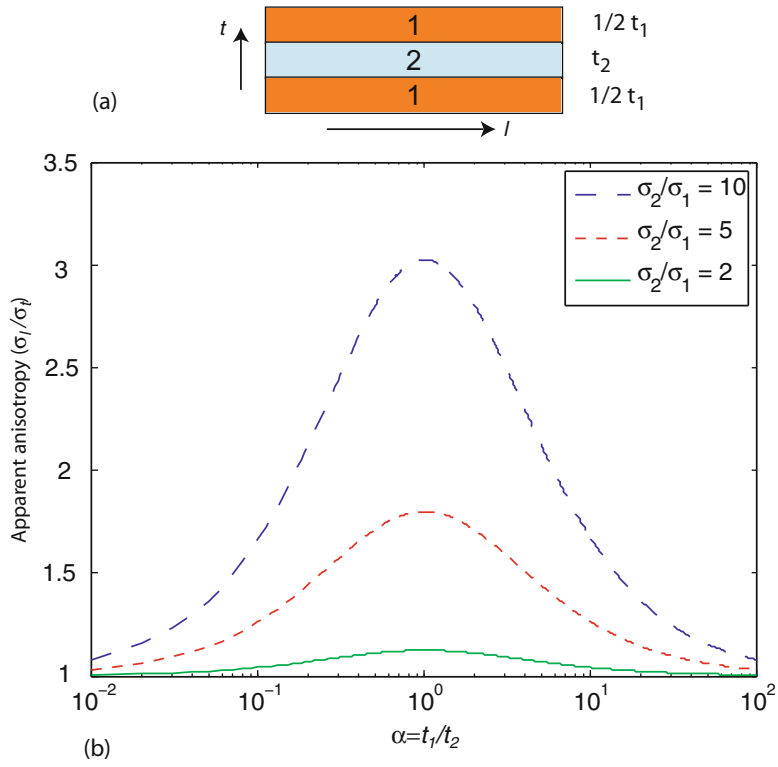

Fig. 1.7 Measurement of anisotropy using simple layered structure. (**a**) Object composed of three layers of two different conductivities, σ_1 and σ_2 (with respective total thicknesses t_1 and t_2, such that $t_1 = t_2$ or $\alpha = 1$), having overall tangential length l, radial thickness T, and width w. (**b**) Plot of apparent anisotropy σ_l/σ_t against α for conductivity ratios σ_2/σ_1 of 2, 3, and 10 for the brick-shaped object shown in (**a**)

It is clear from Fig. 1.8 that as the relative thickness of the layers decreases in the measurement configuration, the apparent resistivity becomes closer to the anisotropic curve.

1.1.3 Active Membrane Properties

Conductivity changes are observed in active tissue membranes as a consequence of ionic flows during action potentials. This mechanism can be used for non-invasive neural source monitoring using EIT [2, 26, 33]. While large conductivity increases are found in the membrane itself, effects on impedance measurements are only of the order of around 0.1% [11] because of the small effects on bulk current distributions. Models of EIT or MREIT measurements have been developed to verify changes observed during active processes [20,27,29,30]. The Hodgkin-Huxley equations [14,22] describe the evolution of membrane conductance and voltage in neurons during activity. Membrane voltage is conventionally defined as the difference between intra- and extracellular potentials

$$V_m = V_i - V_e \tag{1.21}$$

Membrane conductance is governed by activity level of ion-specific channels within it. The simplest active membrane descriptions include probability states for sodium activation (m), inactivation (h), and potassium channels (n). The current flowing through the membrane is

$$I_m = C_m \frac{dV_m}{dt} + (V_m - V_{Na})G_{Na} + (V_m - V_K)G_K + (V_m - V_L)G_L \tag{1.22}$$

where I_m is the membrane current per unit area and C_m is the membrane capacitance. V_{Na},V_K, and V_L are resting (Nernst) voltages for sodium, potassium, and leakage ions, respectively, determined by the equilibrium concentrations of these species within or without the cell. The total membrane conductance per unit area is the sum of sodium, potassium, and leakage conductances where

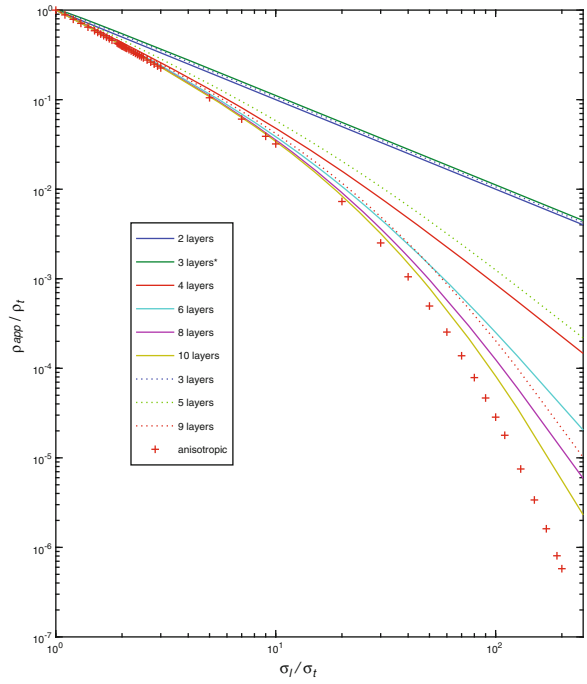

Fig. 1.8 Transition to anisotropy. Comparison of (two-dimensional) calculations using a single four-terminal observation configuration for homogeneous anisotropic and layered structures. Graph plots apparent resistivities normalized with respect to the structure transverse resistivity as a function of relative conductivity as layer number n is increased. Layer thicknesses are equal in each case except where indicated by an asterisk (*) where the central layer had twice the thicknesses of the outer two layers

$$G_{Na} = m^3 h G_{Na,max} \tag{1.23}$$

$$G_K = n^4 G_{K,max} \tag{1.24}$$

The leakage conductance G_L is assumed constant. The differential equations describing m, h, and n channel states are

$$\frac{dm}{dt} = \frac{1}{\tau_m}(m_\infty - m) \tag{1.25}$$

$$\frac{dn}{dt} = \frac{1}{\tau_n}(n_\infty - n) \tag{1.26}$$

$$\frac{dh}{dt} = \frac{1}{\tau_h}(h_\infty - h) \tag{1.27}$$

and the variables m_∞, n_∞, h_∞, τ_m, τ_n, and τ_h depend on channel-specific constants and resting membrane potential.

The total membrane conductance $G = G_{Na} + G_K + G_L$ in this model depends on whether the membrane is active or inactive, and there is a large variation in total membrane conductance between these two states. In fact, the total membrane conductance in the active state is about 1/40 of its inactive value. This may sound large, but it has only a small effect on the measured bulk conductivity of tissue containing active cells. However, because MREIT methods allow measurement over local regions containing active cells, it may be possible to use MREIT as a functional method (fMREIT).

1.1.4 Tissue Properties

As noted in Sect. 1.1.1.3, the overall observed frequency dependence of tissue electrical properties is a consequence of their specific mix of cell types, sizes, and relaxation processes. A meta-analysis by Faes [4] found that properties could be primarily classified with reference to the bulk tissue water content. Properties of tissues have been measured in many different contexts, ranging from excised tissues or removed fluids; using multiple or single frequencies; using different measurement techniques; and in animal or human tissues in vivo.

Spectra and characteristic properties of many different tissues may be found in the database

Table 1.1 Electrical properties of tissues at 50 kHz

Tissue	ε_r	σ (S/m)	Tissue	ε_r	σ (S/m)
Air (vacuum)	1.	0.	Lens	2626.5	0.33849
Aorta	1633.3	0.31686	Liver	690.	0.072042
Bladder	1912.4	0.21688	Lung (deflated)	8531.4	0.26197
Blood	5197.7	0.7008	Lung (inflated)	4272.5	0.10265
Bone (cancellous)	613.18	0.083422	Muscle	10094.	0.35182
Bone (cortical)	264.19	0.020642	Nerve	9587.5	0.069315
Breast fat	117.75	0.024929	Ovary	3010.	0.33615
Cartilage	2762.1	0.17706	Skin (dry)	1126.8	0.00027309
Cerebrospinal fluid	109.	2.	Skin (wet)	21876.	0.029369
Cervix	3150.7	0.54431	Small intestine	17405.	0.58028
Colon	4160.6	0.24438	Spleen	5492.8	0.11789
Cornea	16970.	0.48145	Stomach	3551.2	0.53369
Dura	393.83	0.50168	Tendon	814.98	0.38779
Eye sclera	5494.6	0.51475	Testis	6486.3	0.4344
Fat	172.42	0.024246	Thyroid	4023.1	0.53395
Gall bladder	113.99	0.90012	Tongue	5496.	0.28422
Gall bladder bile	120.	1.4	Trachea	6912.4	0.32987
Gray matter	5461.4	0.12752	Uterus	5669.9	0.52584
Heart	16982.	0.19543	Vitreous humor	98.558	1.5
Kidney	11429.	0.15943	White matter	3548.2	0.077584

maintained by the Nello Carrara Institute of Applied Physics.[1] Another database has been established by the Foundation for Research on Information Technologies in Society.[2]

Table 1.1 shows the conductivity of several key tissues at 50 kHz generated using the Italian database, which in turn was established using data collected by Gabriel et al. [7–9].

1.1.5 Measurement of Impedance Properties

The reconstruction methods used in MR-based conductivity measurement must be carefully validated with respect to reference measurements. This normally involves direct measurement on sample tissues using an impedance probe or measurement cell. All measured impedance or apparent conductivity values are influenced by the measurement method. For low-frequency measurements (below <50 MHz), electrodes may be attached to the sample boundary, and the properties of the electrode-tissue interface must be modeled, measured minimized, or compensated prior to producing corrected data. Measurement of high-frequency properties (> 50 MHz) may be made using a dielectric probe. In this case, the properties of the probe must also be considered. A schematic diagram of a low-frequency impedance measurement is shown in the figure below. The process of measuring low-frequency electrical properties via electrodes is complex, because measured voltages also depend on electrode properties. Electrode properties are themselves complex and are influenced by the materials composing the electrode-electrolyte interface, the electrode area, the frequency of measurement, and the amount of current flowing through the interface, among other factors. Four-terminal measurements greatly reduce the influence of electrode properties, but they must still be taken into

[1] http://niremf.ifac.cnr.it/tissprop/.

[2] https://itis.swiss/virtual-population/tissue-properties/database/.

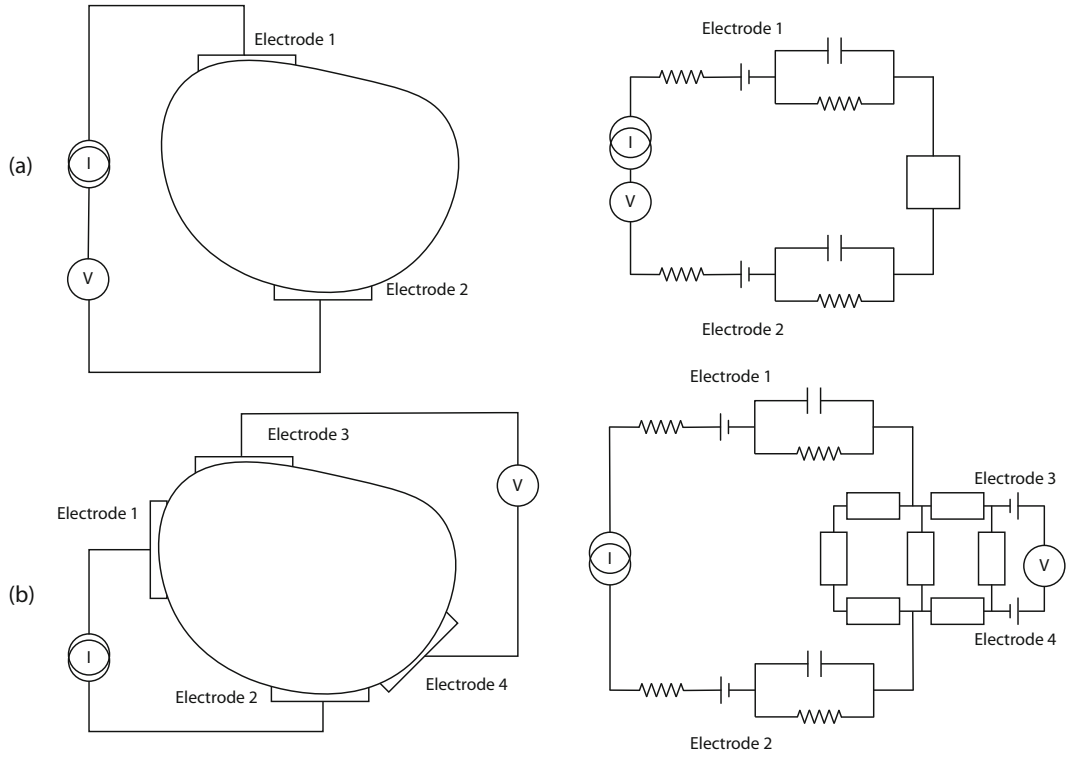

Fig. 1.9 (**a**) Two-terminal measurement electrodes and (**b**) four-terminal measurement circuit

account and included in models when performing EIT reconstructions [15].

1.1.5.1 Electrode Properties

The connections linking wires, electrodes, and tissue involve transitions in current flow from electronic to ionic. The interfaces between these entities and their resulting effects on measurements may be represented, with electrical elements. If a two-terminal measurement is made, as shown in Fig. 1.9a, the resulting voltage measurement includes the interface properties. In its simplest form, an electrode electrolyte interface comprises a half-cell potential, a resistance part, and a capacitive contribution. Values for the effective resistance and capacitance of the interface are characteristic of the interface and concentrations of electrolytes in the ionic conduction compartment. An excellent basic summary of electrode properties can be found in the book by Geddes [10].

1.1.5.2 Conductivity Cell and Dependence on Geometry

The relationship between a voltage difference measured on the periphery of an object and a current flowing through the object (a transfer impedance) is determined by both the geometry of the object and its electrical properties. For example, in the simple case of longitudinal current flow in a cylindrical object with length l, cross-sectional area A, and conductivity σ, the measured resistance is

$$R = \frac{l}{\sigma A} \tag{1.28}$$

Here, the geometrical factor is l/A , measured in m^{-1}. Knowledge of the geometric factor combined with the measured resistance enables computation of the conductivity σ. If a conductivity cell has a complicated shape, this geometrical factor can be retrieved using a substance of known conductivity: a conductivity standard.

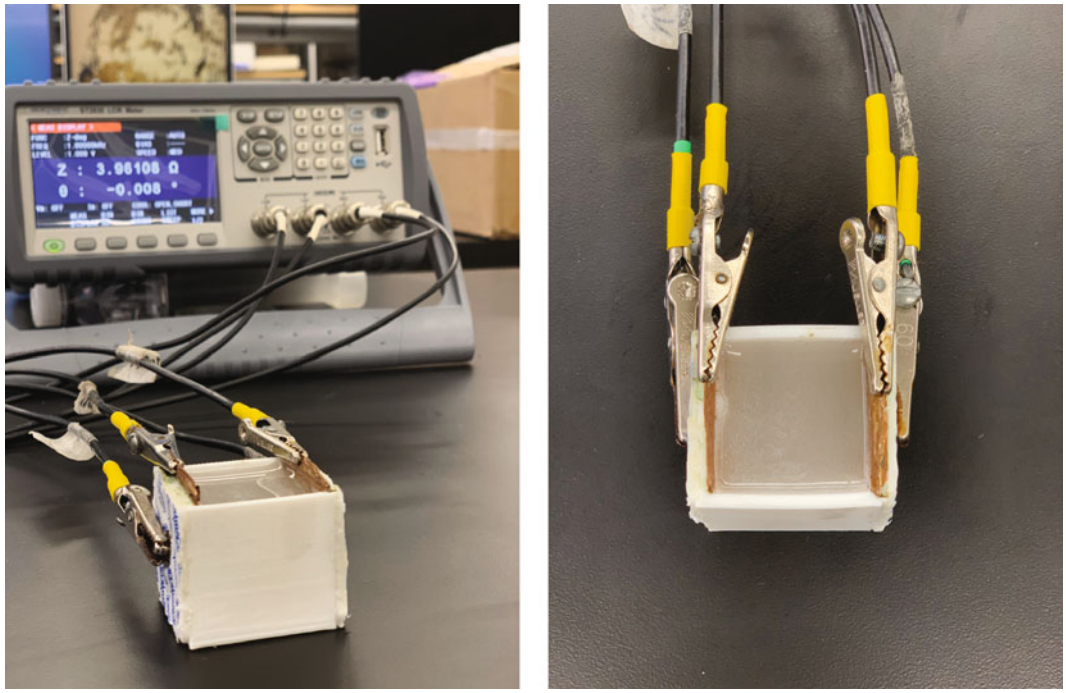

Fig. 1.10 Conductivity cell example. The cell used here is a cube, but any shape of cell can be used. A standard conductivity sample can be used to compute the geometric factor α. This cell has two inner electrodes on opposing faces (snap connector, left) used to deliver current. The resulting voltage difference is measured between the inner electrodes that cover the remainder of each opposing face (right). An LCR meter is useful for simple, low-frequency impedance characterization

Such conductivity standards are conventionally used for low-frequency measurements and are usually potassium chloride solutions of different concentrations, chosen to have conductivity in a similar range as the materials to be tested. An approximately cubic conductivity cell is shown in Fig. 1.10. A reading may be taken using a particular geometry using the standard, and the geometric or shape factor α can be derived using the relation

$$\alpha = R_{std}\sigma_{std} \tag{1.29}$$

where the shape factor is in units of m^{-1}. Subsequently, resistances measured with an unknown substance may be converted to conductivity using

$$\sigma_{meas} = \frac{\alpha}{R_{meas}} \tag{1.30}$$

Commercial conductivity cells also measure temperature so that compensation can be performed.

If a measurement of properties of a solid tissue is required, it may be easier to cut the sample to a simple geometric shape with a known shape factor instead of computing a shape factor separately.

1.1.5.3 High-Frequency (>50 MHz) Properties

The dielectric properties of biological materials are often measured open-ended coaxial probes. The measurements are made by placing by placing the probe in contact with the sample and measuring its admittance or reflection coefficient. The technique was described in numerous papers in the 1980s–1990s, for example, [6]. The probe in Fig. 1.11 has a ground plate, but this is not necessary at low frequencies. Probes of different sizes are used for measurement across the frequency of interest; in general, the higher the frequency, the smaller the probe.

In the low-frequency range of interest to MREIT (e.g., below 100 Hz), the admittance

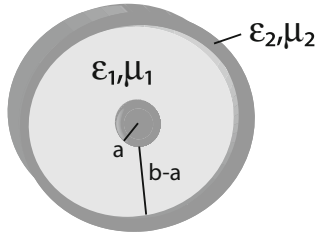

Fig. 1.11 Dielectric probe, showing inner and outer radii of a and b, respectively. Permittivities and permeabilities of inner and outer dielectric are indicated

of the probe in contact with the sample is

$$\mathbf{Y} = G + i\omega C \text{ where} \tag{1.31}$$

$$G = \frac{\mathcal{K}\sigma}{\varepsilon_0} \text{and} \tag{1.32}$$

$$C = \mathcal{K}\varepsilon' \tag{1.33}$$

This admittance model is adequate when the dimensions of the probe are significantly smaller than the wavelength. In practice, standard liquids (e.g., water, dilute salt solutions) are used to obtain the cell constant and to eliminate any stray capacitance within the measurement system. It is acceptable to use large probes at low frequencies; however, large probes require large samples and are therefore not suitable for measuring most tissues. A 10-mm-diameter probe offers a good compromise between size and sensitivity and may be used at frequencies from Hz to MHz.

1.1.6 Methods for Reconstructing Electrical Property Images Using MR-Based Methods

1.1.6.1 History

MRI methods such as MREIT, DT-MREIT, MREPT, and CTI have been widely used to measure the electrical properties of animals, humans, and phantoms in vivo. However, there are various other methods developed by researchers to measure the electrical properties. Some of them include electrical impedance tomography (EIT) [1], magnetic induction tomography (MIT) [21], and magnetoacoustic tomography with magnetic induction (MAT-MI) [19]. We suggest readers explore these key references for further details.

1.1.6.2 CDI and MREIT

Current density imaging (CDI) is a method to image the current densities induced in an imaging object by externally administered electric current. Notably, CDI has recently been finding applications in imaging neurostimulation-induced electric current distributions in the human brain in vivo [16]. The experimental setup of both CDI and MREIT is similar in the sense that both deliver externally administered current to an object using surface electrodes and measure a component of the magnetic flux density (B_z) induced due to this external current. However, they differ in terms of image reconstruction. CDI takes the measured B_z images and calculates the corresponding current density, whereas MREIT takes the measured B_z in at least two orthogonal directions and calculates the underlying electrical conductivity. DT-MREIT is an extension of MREIT where anisotropic conductivity images are obtained by scanning the imaging object with an additional MRI protocol of diffusion tensor imaging (DTI). Further details of CDI are provided in Chap. 6, and the details of MREIT and DT-MREIT are provided in Chap. 7.

1.1.6.3 MREPT

Magnetic resonance electrical properties tomography (MREPT), sometimes just referred to as EPT, is a method to image the high-frequency electrical properties of an object. This method has been rigorously researched over the past decade, and its feasibility has recently been demonstrated in brain tumor clinical studies [31]. Unlike MREIT, it does not require any external current delivery and instead relies on the measured B_1 magnitude or phase maps of the radiofrequency (RF) field of an MRI scanner. Since the B_1 magnetic field of an MRI scanner has an operating frequency at the Larmor frequency of spins (see details in Chap. 3), it provides the

electrical properties at the Larmor frequency of an MRI scanner. Unlike MREIT which provides only electrical conductivity images, the MREPT can provide both conductivity and permittivity images depending on the method used to acquire the B_1 maps. Further details of MREPT are described in Chap. 8.

1.1.7 Other Electromagnetic Properties Measureable Using MRI

The magnetic permeability relates the magnetic flux and magnetic field strengths as

$$\mathbf{B} = \mu_0 (\mathbf{H} + \mathbf{M}) = \mu_0 \mu_r \mathbf{H} = \mu_0 (1 + \chi) \mathbf{H} \tag{1.34}$$

where μ_r is the relative permeability and χ is the magnetic susceptibility. Note that like μ_r, χ is a dimensionless quantity. As we noted in the introduction, for most purposes, we may assume that the magnetic susceptibility of the body is uniform. However, the MR images used for reconstructing conductivity images may be affected by variations in susceptibility at air-tissue boundaries (e.g., in the sinuses of the head) or by small amounts of more magnetizable material in the body. Significant natural occurrences of magnetic susceptibility are in tissues containing the protein ferritin, a macromolecule that stores iron in the body, as well as in calcified tissue or in myelin. The area of quantitative susceptibility mapping (QSM) has developed to aid imaging susceptibility variations. We do not discuss the details of QSM in subsequent chapters in this book, but readers are encouraged to refer to [28] for more details.

References

1. D. Holder (ed.) *Electrical Impedance Tomography* (CRC Press, Boca Raton, 2005), pp. 195–249. ISBN: 9780750309523
2. K.Y. Aristovich, B.C. Packham, H. Koo, G.S. dos Santos, A. McEvoy, D. Holder, Imaging fast elecrical activity in the brain with electrical impedance tomography. NeuroImage **124**, 204–213 (2016)
3. M. Chauhan, A. Indahlastari, A.K. Kasinadhuni, M. Schär, T.H. Mareci, R.J. Sadleir, Low-frequency conductivity tensor imaging of the human head in vivo using DT-MREIT: first study. IEEE Trans. Med. Imag. **37**(4), 966–976 (2018)
4. T.J.C. Faes, H.A. van der Meij, J.C. de Munck, R.M. Heethaar, The electric resistivity of human tissues (100 Hz–10 MHz): a meta-analysis of review studies. Physiol. Measur. **20**, R1–R10 (1999)
5. H. Fricke, Theory of electrical polarization. Philos. Mag. **14**(90), 310–318 (1932)
6. C. Gabriel, T.Y.A. Chan, E.H. Grant, Admittance models for open ended coaxial probes and their place in dielectric spectroscopy. Phys. Med. Biol. **39**, 2183–2200 (1994)
7. C. Gabriel, S. Gabriel, E. Corthout, The dielectric properties of biological tissues: I. Literature survey. Phys. Med. Biol. **41**, 2231–2249 (1996)
8. S. Gabriel, R.W. Lau, C. Gabriel, The dielectric properties of biological tissues: II. Measurements in the frequency range 10 Hz to 20 GHz. Phys. Med. Biol. **41**, 2251–2269 (1996)
9. S. Gabriel, R.W. Lau, C. Gabriel, The dielectric properties of biological tissues: III Parametric models for the dielectric spectrum of tissues. Phys. Med. Biol. **41**, 2271–2293 (1996)
10. L.A. Geddes, *Electrodes and the Measurement of Bioelectric Events* (Wiley, New York, 1972)
11. O. Gilad, D. Holder, Impedance changes recorded with scalp electrodes during visual evoked responses: implications for electrical impedance tomography of fast neural activity. NeuroImage **47**, 514–522 (2009)
12. S. Grimnes, O.G. Martinsen, *Bioimpedance & Bioelectricity Basics*, 1st edn. (Academic Press, London, 2000)
13. W.M. Haynes, D.R. Lide, T.J. Bruno, *CRC Handbook of Chemistry and Physics*, 95th edn. (CRC Press, Boca Raton, 2014)
14. A.L. Hodgkin, A.F. Huxley, A quantitative description of ion currents and its applications to conductance and excitation in nerve membranes. J. Physiol. **117**, 500–544 (1952)
15. P. Hua, E.J. Woo, J.G. Webster, W.J. Tompkins, Finite element modeling of electrode-skin contact impedance in electrical impedance tomography. IEEE Trans. Biomed. Eng. **40**, 335–343 (1993)
16. A.K. Kasinadhuni, A. Indahlastari, M. Chauhan, M. Schär, T.H. Mareci, R.J. Sadleir, Imaging of current flow in the human head during transcranial electrical therapy. Brain Stimul. **10**(4), 764–772 (2017)
17. N. Katoch, B.K. Choi, S.Z.K. Sajib, E. Lee, H.J. Kim, O.I. Kwon, E.J. Woo, Conductivity tensor imaging of in vivo human brain and experimental validation using giant vesicle suspension. IEEE Trans. Med. Imag. **38**, 1569–1577 (2019)
18. O. Kwon, W.C. Jeong, S.Z. K. Sajib, H.J. Kim, E.J. Woo, Anisotropic conductivity tensor imaging in MREIT using directional diffusion rate of water molecules. Phys. Med. Biol. **59**, 2955–2974 (2014)

19. X. Li, K. Yu, B. He, Magnetoacoustic tomography with magnetic induction (MAT-MI) for imaging electrical conductivity of biological tissue: a tutorial review. Phys. Med. Biol. **61**(18), R249–R270 (2016)
20. A. Liston, R. Bayford, D. Holder, A cable theory based biophysical model of resistance change in crab peripheral nerve and human cerebral cortex during neuronal depolarisation: implications for electrical impedance tomography of fast neural activity in the brain. Med. Biol. Eng. Comput. **50**, 425–437 (2012)
21. L. Ma, M. Soleimani, Magnetic induction tomography methods and applications: a review. Measurement Science and Technology **28**(7), 072001 (2017)
22. J. Malmivuo, R. Plonsey, *Bioelectromagnetism - Principles and Applications of Bioelectric and Biomagnetic Fields*, 1st edn. (Oxford University Press, New York, 1995)
23. O.G. Martinsen, S. Grimnes, P. Mirtaheri, Noninvasive measurements of post-mortem changes in dielectric properties of haddock muscle - a pilot study. J. Food Eng. **43**, 189–192 (2000)
24. A. Peyman, C. Gabriel, E.H. Grant, Complex permittivity of sodium chloride solutions at microwave frequencies. Bioelectromagnetics **28**, 264–274 (2007)
25. R.J. Sadleir, A. Argibay, Modeling skull electrical properties. Ann. Biomed. Eng. **35**(10), 1699–1712 (2007)
26. R.J. Sadleir, F. Fu, C. Falgas, S.K. Holland, M. Boggess, S.C. Grant, E.J. Woo, Direct detection of neural activity in vitro using magnetic resonance electrical impedance tomography (MREIT). NeuroImage **161**, 104–119 (2017)
27. R.J. Sadleir, F. Fu, M. Chauhan, Functional magnetic resonance electrical impedance tomography (fMREIT) sensitivity analysis using an active bidomain finite element model of neural tissue. Magnetic Resonance in Medicine **81**, 602–614 (2019)
28. J.K. Seo, E.J. Woo, U. Katscher, Y. Wang, *Electro-Magnetic Tissue Properties MRI* (Imperial College Press, London, 2014)
29. I. Tarotin, K.Y. Aristovich, D. Holder, Effect of dispersion in nerve on compound action potential and impedance change: a modelling study. Physiol. Measur. **40**, 034001 (2019)
30. I. Tarotin, K.Y. Aristovich, D. Holder, Model of impedance changes in unmyelinated nerve fibers. IEEE Trans. Biomed. Eng. **66**(2), 471–484 (2019)
31. K. Tha, U. Katscher, S. Yamaguchi, C. Stehning, S. Terasaka, N. Fujima, K. Kudo, K. Kazumata, T. Yamamoto, M. Van Cauteren, H. Shirato, Noninvasive electrical conductivity measurement by mri: a test of its validity and the electrical conductivity characteristics of glioma. Eur. Radiol. **28**, 348–355 (2017)
32. D.S. Tuch, V.J. Wedeen, A.M. Dale, J.S. George, J.W. Belliveau, Conductivity tensor mapping of the human brain using diffusion tensor MRI. Proc. Natl. Acad. Sci. **98**, 111697–701 (2001)
33. A.N. Vongerichten, G.S. dos Santos, K.Y. Aristovich, J. Avery, A. McEvoy, M. Walker, D. Holder, Characterisation and imaging of cortical impedance changes during interictal and ictal activity in the anaesthetised rat. NeuroImage **124**, 813–823 (2016)
34. Y. Wang, P. Spincemaille, Z. Liu, A. Dimov, K. Deh, J. Li, Y. Zhang, Y. Yao, K.M. Gillen, A.H. Wilman, A. Gupta, A.J. Tsiouris, I. Kovanlikaya, G.C.-Y. Chiang, J.W. Weinsaft, L. Tanenbaum, W. Chen, W. Zhu, S.-Y. Chang, M. Lou, B.H. Kopell, M.G. Kaplitt, D. Devos, T. Hirai, X. Huang, Y. Korogi, A. Shtiilbans, G.-H. Jahng, D. Pelletier, S.A. Gauthier, D. Pitt, A.I. Bush, G.M. Brittenham, M.R. Prince, Clinical quantitative susceptibility mapping (QSM): biometal imaging and its emerging roles in patient care. Journal of Magnetic Resonance Imaging **46**, 951–971 (2017)

2 Modeling for Electromagnetic Characterization, Prediction, and Reconstruction

Rosalind Sadleir

Abstract

Electromagnetic modeling is an essential and crucial element in MRI-based methods of characterizing electromagnetic properties or current flow. In its simplest form, modeling can be used to predict measurements of magnetic flux density (B_z in the case of MREIT or B_1 fields in the case of EPT) based on realistic representations of the imaged object. Further, projected current density methods must refer to a uniform model of an imaged object in order to calculate the projected current density distribution. Modeling in this area is most commonly performed using finite element methods and often using commercial finite element software. While it is not necessary to know every feature of this type of software, understanding the basics of finite element methods will help in interpreting and examining the results and learning how to perform simulations efficiently. We describe aspects of the finite element approach and demonstrate models relevant to simulations performed in this area.

R. Sadleir (✉)
School of Biological and Health Systems Engineering, Arizona State University, Tempe, AZ, USA
e-mail: Rosalind.Sadleir@asu.edu

2.1 Introduction

Electromagnetic modeling is an essential and crucial element in MRI-based methods of characterizing electromagnetic properties or current flow. In its simplest form, modeling can be used to predict measurements of magnetic flux density (B_z in the case of MREIT or B_1 fields in the case of EPT) based on realistic representations of the imaged object. Further, projected current density methods must refer to a uniform model of an imaged object in order to calculate the projected current density distribution. Modeling in this area is most commonly performed using finite element methods and most often using commercial finite element software. While it is not necessary to know every feature of this type of software, understanding the basics of finite element methods will help in interpreting and critically examining the results and learning how to perform simulations efficiently. In this chapter, we describe aspects of the finite element approach and demonstrate models relevant to simulations performed in this area. There are many different approaches to modeling described in the literature. The examples we show in the latter parts of the chapter are just one way of going about this task.

R. Sadleir, A. S. Minhas (eds.), *Electrical Properties of Tissues*, Advances in Experimental Medicine and Biology 1380, https://doi.org/10.1007/978-3-031-03873-0_2

2.2 Overview of the Finite Element Approach

The finite element method is generally used to solve partial differential equations where an analytic solution is not possible. Finite element or finite difference techniques are very commonly used to solve partial differential equations that involve complicated boundary conditions or irregular geometries. The finite element method was first used to solve problems of aircraft structural design and other engineering of elasticity problems. Most of the formal development of this technique was done in the early 1960s, and more recent work has been concerned with formulating new and more specific elements for particular purposes. Finite element techniques are widely used in engineering applications, usually using packages designed for a particular area.

The principal approach in the finite element method is to consider a continuous region as an assembly of several discrete parts (elements) and to find a piecewise polynomial (or other basis function) approximation to the solution. Although the idea of using many small elements to approximate the behavior of a complex whole is not new, the comparatively recent development of this technique is mostly due to increases in computer power and availability. Progress in finite element techniques is also dependent on advances in numerical algorithms for the efficient assembly and solution of matrix equations.

An example of a two-dimensional finite element discretization mesh is shown in Fig. 2.1, with a region R divided into a number of triangular elements. The boundary of R is the contour C, which may be subdivided into smaller regions $C_1, C_2, \ldots, C_m$ depending on how many different boundary conditions are specified.

2.3 Partial Differential Equations

The partial differential equations (PDEs) commonly encountered in physical problems are second order and include the Laplace and Poisson equations, Schrödinger's and wave equations, and diffusion equations.

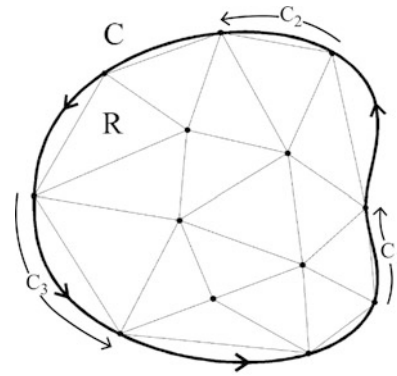

Fig. 2.1 Example two-dimensional finite element discretization, showing the domain R and the boundary C with subsections C_1, C_2, and C_3

A second-order, two-dimensional partial differential equation may be expressed as

$$L\phi = f \tag{2.1}$$

such that (in two dimensions)

$$L\phi = A\frac{\partial^2\phi}{\partial x^2} + 2B\frac{\partial^2\phi}{\partial x\partial y} + C\frac{\partial^2\phi}{\partial y^2} + F\left(x, y, \phi, \frac{\partial\phi}{\partial x}, \frac{\partial\phi}{\partial y}\right) \tag{2.2}$$

Here, L is an operator applied to the solution and f is the result. The coefficients A, B, and C are functions of x and y. The coefficients may also depend on ϕ or its derivatives. If that is the case, the PDE is non-linear.

The Poisson equation is a PDE where (now in three dimensions)

$$L = \frac{\partial^2}{\partial x^2} + \frac{\partial^2}{\partial y^2} + \frac{\partial^2}{\partial z^2} \text{ and} \tag{2.3}$$

$$L\phi = \frac{\partial^2\phi}{\partial x^2} + \frac{\partial^2\phi}{\partial y^2} + \frac{\partial^2\phi}{\partial z^2} = \rho \tag{2.4}$$

This operator is called the Laplacian operator, and it is often written using ∇, where

$$\nabla = \left[\frac{\partial}{\partial x}\ \frac{\partial}{\partial y}\ \frac{\partial}{\partial z}\right] \tag{2.5}$$

and in the case above,

$$L = \nabla \cdot \nabla = \nabla^2 \tag{2.6}$$

One form of the Poisson equation describes the relationship between voltages and activity sources within the brain. In this case, ρ represents charge density of internal sources, ϕ is replaced with V, and the overall equation can be stated

$$\nabla \cdot (-\sigma \nabla V) = \nabla \cdot (\sigma \mathbf{E}) = \nabla \cdot \mathbf{J} = \rho \quad (2.7)$$

where $\mathbf{J}$ is electrical current density, σ is the electrical current density, and $\mathbf{E} = -\nabla V$ is the electric field.

The PDE describing current flow through the head without any internal sources (e.g., in transcranial electrical stimulation) is the Laplace equation

$$\nabla \cdot \mathbf{J} = 0. \quad (2.8)$$

In the low-frequency electrical context, this equation is also called Ohm's law. When working with PDEs and their boundary conditions, it can be very useful to confirm dimensions. For example, in the case of the Poisson equation above, you can see that the dimensions of ρ are the same as the space derivative of $\mathbf{J}$. Since $\mathbf{J}$ is measured in A/m^2, the dimensions of ρ are A/m^3.

Boundary equations must be specified to solve PDES. There are three types of boundary conditions, involving specifying the actual solution on some portion of the domain surface, or the flow through a surface, or a mixture of the two.

Dirichlet boundary conditions involve specification of the solution on part of the domain. For example, in Fig. 2.1, we could specify that

$$\phi = u_1 \text{ on } C_1 \quad (2.9)$$

and a Neumann boundary condition may be defined with

$$\frac{\partial \phi}{\partial \mathbf{n}} = g_2(s) \text{ on } C_2 \quad (2.10)$$

where $\mathbf{n}$ is a vector normal to C_2 and distance along the boundary is parameterized using s.

Boundary conditions can also be specified as a weighted combination of Neumann and Dirichlet boundary conditions. This type is called a Robin boundary condition. An example of a Robin boundary condition is to require on C_3 that

$$\frac{\partial \phi}{\partial \mathbf{n}} + \lambda_3(s)\phi = h_3(s). \quad (2.11)$$

A Cauchy boundary condition involves specifying both Dirichlet and Neumann boundary conditions simultaneously on a part of a boundary.

The PDEs describing low-frequency electrical current flow and current density, as noted above, is Ohm's law (2.8). The relationship between low-frequency conductivity and measured magnetic flux densities can be developed by combining Ohm's and Ampere's laws. Methods for reconstructing low-frequency conductivity distributions from measurements of current density are described in Chap. 7. For high-frequency conductivity or permittivity properties, we must consider the full Maxwell description used as the basis for electric properties tomography (EPT) reconstructions (Chap. 8).

2.4 The Finite Element Method

A key concept involved in the finite element method is the concept of the *functional*. The functional is a function, specific to a particular PDE, that expresses, conceptually, the total potential energy contained within a solution. For a mechanical problem, the functional expression will literally be the potential energy of the solution. Minimization of the functional, denoted $I[\phi]$, is therefore equivalent to minimizing the energy of the solution. A functional expression can be defined for many PDEs, such that a unique solution of $L\phi = f$ occurs at the minimum value of $I[\phi]$.

As we noted above, the basis of the finite element method is to specify the solution using a few basis functions within each of a large number of small regions that together completely cover the domain. Thus, the solution within the entire region may be expressed as

$$\Phi(x, y) = \sum_{e=1}^{E} \phi^e(x, y) \quad (2.12)$$

In each case, outside the element e, the function for the solution ϕ^e is identically zero.

The basis functions chosen for the solution within each element are usually polynomials because of their simple form. When the expressions for minimizing the energy over each element are solved simultaneously, the result will be a distinct set of coefficients for each element, and the full solution is a piecewise continuous set of polynomial functions. One key feature of the FEM is that if enough elements are used, the finite element solution should converge to the actual solution. Since the solution of the partial differential equation is only approximated using only a few basis functions, accuracy within a particular element depends on how much the solution changes over it. If the solution is particularly active in parts of the region, the elements may be graded more finely about these points to ensure a uniform accuracy is maintained throughout.

2.5 The Shape Function

Within each element, it holds that

$$\phi^e(x, y) = \mathbf{N}^e \delta^e. \tag{2.13}$$

The matrix $\mathbf{N}^e$ is called the shape function matrix for the element. The shape function has the same form for similar elements. The vector δ^e contains the solution for the PDE at each *node* within the element. It is also often called the displacement vector. In the most simple elements, nodes are placed at vertices.

The shape function provides a means of interpolating solutions at the nodes of the element to find the solution anywhere within the element. A very simple example is the linear line segment element, shown in Fig. 2.2. In this case, the solution matrix for the element is

$$\delta^e = \begin{bmatrix} \phi_A \\ \phi_B \end{bmatrix} \tag{2.14}$$

For the linear line segment, the shape function matrix can be written as

$$\mathbf{N}^e = \left[N_A^e(\zeta)\ N_B^e(\zeta) \right] = \left[\tfrac{1}{2}(1-\zeta)\ \tfrac{1}{2}(1+\zeta) \right] \tag{2.15}$$

where ζ is a generic parameter denoting location within the element. Consider the case where we would like to interpolate the solution to the element at its midpoint x_m. At this point, $\zeta = 0$ and $N_A^e = N_B^e = \frac{1}{2}$. The value of the solution at the midpoint is therefore $\frac{1}{2}\phi_A + \frac{1}{2}\phi_B$.

What does the solution look like as a polynomial expression? Assume that the endpoints of the element are placed at $x_A = 0.25$ and $x_B = 0.75$. Then, $x_m = 0.5$, $L = 0.5$, and $\zeta = 4x - 2$, and the function within the element is

$$\begin{aligned} \phi^e(x) = \mathbf{N}^e \delta^e &= \left[\tfrac{1}{2}(1-\zeta)\ \tfrac{1}{2}(1+\zeta) \right] \begin{bmatrix} \phi_A \\ \phi_B \end{bmatrix} \\ &= \left[\tfrac{3}{2} - 2x\ \ 2x - \tfrac{1}{2} \right] \begin{bmatrix} \phi_A \\ \phi_B \end{bmatrix} \\ &= 2x(\phi_B - \phi_A) + \frac{1}{2}(3\phi_A - \phi_B) \end{aligned} \tag{2.16}$$

which is a linear function in x.

Note that the shape functions in (2.15) and illustrated in Fig. 2.2 are generic and could be used to summarize any linear line segment element. Whatever the location or size of the element, the left vertex will be at $\zeta = -1$ and the right vertex at $\zeta = 1$. This is key to formulating the expression for minimizing the functional I.

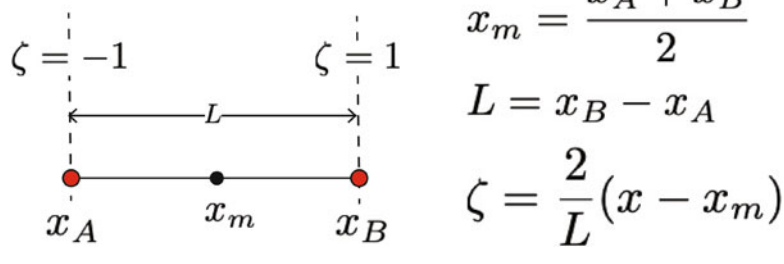

Fig. 2.2 Linear line segment element, showing nodes at segment ends (red), element midpoint (x_m), and reduced parameter ζ definition

2.6 Formulating the Global Solution Matrix

Because the overall solution is a patchwork of individual functions, the functional for the overall solution will also be a patchwork function. From (2.16), we see that each ϕ^e depends on the value of the displacement vector in individual elements. Therefore, we can say that

$$I[\Phi] = \sum_{e=1}^{E} I^e = I\left(\phi^1, \phi^2, \ldots, \phi^E\right) = I\left(\phi_1, \phi_2, \ldots, \phi_N\right). \tag{2.17}$$

where N is the total number of nodes within the mesh.

Within each element, the derivative of the functional will end up depending only on the derivative of the shape functions (since the displacement vectors just contain numbers). Because the shape functions are the same in each element, once the derivative has been computed for one element, it has been done for all elements. The remainder of the problem involves applying boundary conditions and assembling the overall solution matrix to obtain the solution vector for all the nodes within the elements.

The next step is to compute the derivative of the functional with respect to each nodal solution. Appendix 1 contains a derivation of the functional for the Laplace or Poisson equation. It is found that if the derivative of the functional is set to zero, the equation that must be solved for each element is

$$\left[\mathbf{k}^e + \bar{\mathbf{k}}^e\right]\delta^e = \mathbf{f}^e + \bar{\mathbf{f}}^e. \tag{2.18}$$

where

$$\begin{aligned} k_{ij}^e &= \iint_{R^e} \left(\frac{\partial N_i^e}{\partial x}\frac{\partial N_j^e}{\partial x} + \frac{\partial N_i^e}{\partial y}\frac{\partial N_j^e}{\partial y}\right) dxdy \\ \bar{k}_{ij}^e &= \int_{C^e} \lambda(s) N_i^e N_j^e ds \\ f_i^e &= \iint_{R^e} f N_i^e dxdy \\ \bar{f}_i^e &= \int_{C^e} h(s) N_i^e ds. \end{aligned} \tag{2.19}$$

The contributions for $\bar{k}_{ij}^e$ and $\bar{f}_i^e$ are only calculated if the element e is coincident with the boundary and if the functions $\lambda(s)$ or $h(s)$ are non-zero on that portion of the boundary. The indices i and j vary over all the nodes of the element.

The last step of solving the problem is to assemble the global solution matrix. This involves taking each individual element matrix and placing its entries in the correct locations to form a system

$$\mathbf{K}\boldsymbol{\Delta} = \mathbf{F}. \tag{2.20}$$

The matrix $\mathbf{K}$ is then inverted to solve for the overall displacement matrix, Δ, which consists of the solution values at all nodes within the mesh:

$$\Delta = \begin{bmatrix} \phi_1 \\ \phi_2 \\ \vdots \\ \phi_N \end{bmatrix}. \tag{2.21}$$

These concepts are explored in the example in Sect. 2.8.

Some additional examples of shape functions are shown in Sect. 2.7.

2.7 Shape Functions for Linear Elements

It was noted before that the shape function matrices $\mathbf{N}^e$ have the same form for each element of the same type. In this section, shape functions for rectangular, triangular, and cubic linear (first-order polynomial in x and y) elements are developed. In simple cases where elements are square or triangular shaped, the nodes are chosen to be the vertices of the element.

2.7.1 Rectangular Linear Elements

In the simplest rectangular element, each node is placed at a vertex of the rectangle as illustrated in Fig. 2.3.

Thus, the expression or the matrix of nodal variables, δ, is a 4×1 column matrix made up

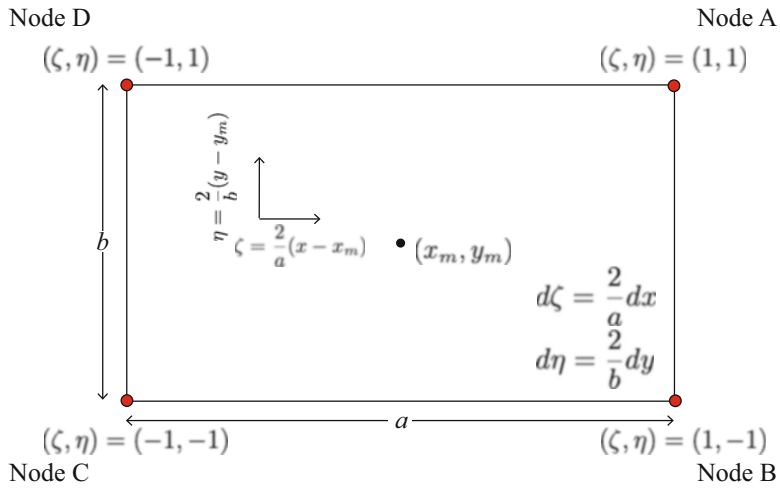

Fig. 2.3 Rectangular element showing reduced variable notation

of the solution values at each vertex

$$\delta = \begin{bmatrix} \phi_A \\ \phi_B \\ \phi_C \\ \phi_D \end{bmatrix} \tag{2.22}$$

and the interpolation polynomial used to find the solution within a rectangular element has the form

$$\phi^e(x, y) = a_0 + a_1 x + a_2 y + a_3 xy. \tag{2.23}$$

Locations within the rectangle can be expressed in terms of a reduced variable set (ζ, η) similar to the linear line segment above, and the general shape function matrix $\mathbf{N}^e$ can be expressed as

$$\mathbf{N}^e(x, y) = \left[\mathbf{N}^e_A(x, y)\ \ \mathbf{N}^e_B(x, y)\ \ \mathbf{N}^e_C(x, y)\ \ \mathbf{N}^e_D(x, y)\right]. \tag{2.24}$$

We apply the requirements that the shape function matrix entry specific to each node is identical to 1 on the node, that is,

$$\begin{aligned} \mathbf{N}^e_A(1, 1) &= \mathbf{N}^e_B(1, -1) \\ &= \mathbf{N}^e_C(-1, -1) = \mathbf{N}^e_D(-1, 1) = 1, \end{aligned} \tag{2.25}$$

and that the value of each shape function entry at all the other nodes is 0, that is,

$$\mathbf{N}^e_A(1, -1) = \mathbf{N}^e_A(-1, -1) = \mathbf{N}^e_A(-1, -1) = 0 \tag{2.26}$$

with similar rules for the other shape functions in the shape function matrix. The expression for the solution in the element e can then be stated

$$\phi^e(x, y) = \mathbf{N}^e\delta^e = \frac{1}{4}\begin{bmatrix} (1+\zeta)(1+\eta) \\ (1+\zeta)(1-\eta) \\ (1-\zeta)(1-\eta) \\ (1-\zeta)(1+\eta) \end{bmatrix} \begin{bmatrix} \phi_A \\ \phi_B \\ \phi_C \\ \phi_D \end{bmatrix} \tag{2.27}$$

The quantities that must be computed for each element are $\mathbf{k}^e$ and $\mathbf{f}^e$. You can see from (2.19) that the expression for $\mathbf{k}^e$ is the most complex. The integral is first transformed to be over ζ and η, becoming

$$\begin{aligned} k^e_{ij} &= \iint_{R^e} \left(\frac{\partial N^e_i}{\partial x}\frac{\partial N^e_j}{\partial x} + \frac{\partial N^e_i}{\partial y}\frac{\partial N^e_j}{\partial y} \right) dxdy \\ &= \int_{-1}^{1}\int_{-1}^{1} \left(\frac{\partial N^e_i}{\partial \zeta}\frac{\partial \zeta}{\partial x}\frac{\partial N^e_j}{\partial \zeta}\frac{\partial \zeta}{\partial x} \right. \\ &\quad \left. + \frac{\partial N^e_i}{\partial \eta}\frac{\partial \eta}{\partial y}\frac{\partial N^e_j}{\partial \eta}\frac{\partial \eta}{\partial y} \right) \tfrac{a}{2}\tfrac{b}{2} d\zeta d\eta \end{aligned} \tag{2.28}$$

Consider $i, j = A$. In this case,

$$
\begin{aligned}
&k^e_{AA} \\
&= \int_{-1}^{1}\int_{-1}^{1}\left(\frac{\partial N^e_A}{\partial\zeta}\frac{\partial\zeta}{\partial x}\frac{\partial N^e_A}{\partial\zeta}\frac{\partial\zeta}{\partial x}+\frac{\partial N^e_A}{\partial\eta}\frac{\partial\eta}{\partial y}\frac{\partial N^e_A}{\partial\eta}\frac{\partial\eta}{\partial y}\right)\frac{a}{2}\frac{b}{2}d\zeta d\eta \\
&= \int_{-1}^{1}\int_{-1}^{1}\left(\frac{1}{16}(1+\eta)\frac{2}{a}(1+\eta)\frac{2}{a}+\frac{1}{16}(1+\zeta)\right. \\
&\qquad \left.\frac{2}{b}(1+\zeta)\frac{2}{b}\right)\frac{a}{2}\frac{b}{2}d\zeta d\eta \\
&= \frac{1}{16}\frac{b}{a}\int_{-1}^{1}\int_{-1}^{1}\left(1+2\eta+\eta^2\right)d\zeta d\eta+\frac{1}{16}\frac{a}{b}\int_{-1}^{1}\int_{-1}^{1} \\
&\qquad \left(1+2\zeta+\zeta^2\right)d\zeta d\eta \\
&= \frac{1}{8}\frac{b}{a}\int_{-1}^{1}\left(1+2\eta+\eta^2\right)d\eta+\frac{1}{8}\frac{a}{b}\int_{-1}^{1}\frac{4}{3}d\eta \\
&= \frac{b}{a}\frac{1}{3}+\frac{a}{b}\frac{1}{3}=\frac{1}{3}\left(\frac{b}{a}+\frac{a}{b}\right)
\end{aligned}
\tag{2.29}
$$

If the element is square ($a = b$), then $k^e_{AA} = \frac{2}{3}$. Repeating the process for all indices i and j, we obtain the full $\mathbf{k}^e$ matrix for a square as

$$
\mathbf{k}^e = \frac{1}{6}\begin{bmatrix} 4 & -1 & -2 & -1 \\ -1 & 4 & -1 & -2 \\ -2 & -1 & 4 & -1 \\ -1 & -2 & -1 & 4 \end{bmatrix} \tag{2.30}
$$

You can see that the integrations are quite tedious. Luckily, since the expressions are in terms of the reduced variables, the quantities only depend on a and b and, once done for one rectangle, are done for all. Expressions for the matrices $\bar{\mathbf{k}}$, $\mathbf{f}$, and $\bar{\mathbf{f}}$ are needed to complete the formulation of the solution. These are dependent upon the particular boundary conditions, are a bit more straightforward, and they will be demonstrated in more detail in the example of triangular elements.

Rectangular elements have a number of characteristics that may make them unsuitable. First, the blocky shape results in a poor approximation of general boundary shapes. If a good approximation to any boundary shape is desired, a large number of small rectangular elements will be required. The more elements required, the more nodes are in the model, and thus the larger the system of equations describing the system. Hence, the use of a square element basis may result in inefficient solutions at any given level of accuracy. Second, as the simple rectangular element has four vertices, it does not contain a complete polynomial expression, i.e., not all second-order terms are included, and thus there is some anisotropy in the element. The interpolated solution along a side common to two rectangular elements may not be the same if, for instance, its side is not oriented parallel to the coordinate (x, y) axes.

2.7.2 Hexahedral Elements

The rectangular element of Fig. 2.3 may be simply extended to provide solutions to equations in three dimensions (Fig. 2.4). In the case where the element is cubic ($a = b = c$), in this case with $a = b = c$, the expression for $\mathbf{k}^e$ becomes

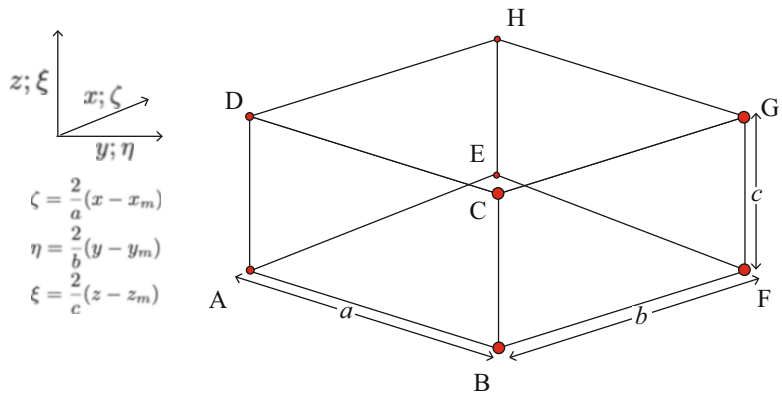

Fig. 2.4 Hexahedral element showing reduced variable notation

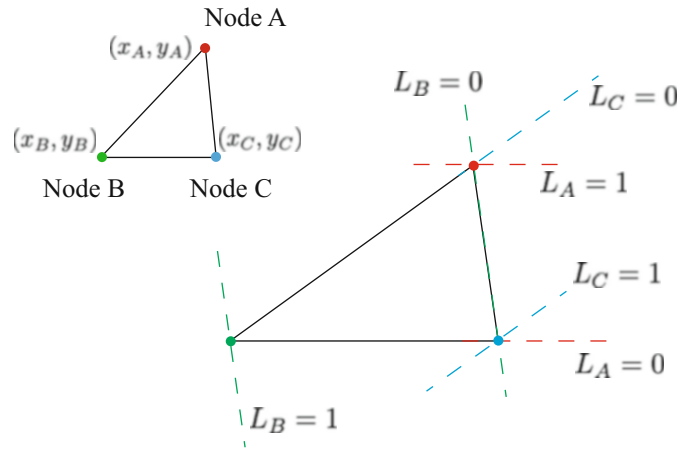

Fig. 2.5 Linear triangular element. Interpolation within the element is described using the variables L_A, L_B, and L_C. The value of each variable along the edge opposite its corresponding nodes is 0. For example, the value of L_C along the edge joining nodes A and B is 0. The value of each variable exactly on the corresponding node is 1

$$\mathbf{k}^e = \frac{1}{6}\begin{bmatrix} 48 & 0 & 0 & -12 & 0 & -12 & -12 & -12 \\ 0 & 48 & -12 & 0 & -12 & 0 & -12 & -12 \\ 0 & -12 & 48 & 0 & -12 & -12 & 0 & -12 \\ -12 & 0 & 0 & 48 & -12 & -12 & -12 & 0 \\ 0 & -12 & -12 & -12 & 48 & 0 & 0 & -12 \\ -12 & 0 & -12 & -12 & 0 & 48 & -12 & 0 \\ -12 & -12 & -12 & 0 & -12 & 0 & 0 & 48 \end{bmatrix} \tag{2.31}$$

2.7.3 Triangular Elements

Triangular and tetrahedral elements are the workhorses of all finite element frameworks. Their shape enables better approximation to general boundary shapes to be made, and, as the simplest triangle element has three vertices, the approximating polynomial solution inside a triangular element has the form

$$\phi^e(x, y) = a_0 + a_1 x + a_2 y \tag{2.32}$$

which is a complete first-order polynomial.

Expressions for the shape functions for the linear triangular element are found in a similar way to those of the rectangular element. In a similar way to the formulation of reduced coordinates $(x, y) \rightarrow (\zeta, \eta)$ for rectangular elements, locations within this linear triangular element are expressed in terms of a new coordinate system $(x, y) \rightarrow (L_A, L_B, L_C)$, such that

$$\begin{aligned} x &= L_A x_A + L_B x_B + L_C x_C \\ y &= L_A y_A + L_B y_B + L_C y_C. \end{aligned} \tag{2.33}$$

As before, we require that the shape function matrix entry referred to a particular node has the value 1 on that node and 0 at all other nodes. Figure 2.5 shows the triangle nodes A, B, and C and the properties of the functions L_A, L_B, and L_C.

The coordinates L_i have the properties that

$$L_i = \frac{a_i + b_i x + c_i y}{2\mathbb{A}} \tag{2.34}$$

where $\mathbb{A}$ is the area of the triangle. Also, with this shape function definition, $(L_A + L_B + L_C = 1)$.

The constants a_i, b_i, and c_i $(i = A, B, C)$ are defined using

$$\begin{array}{lll} a_A = x_B y_C - x_C y_B & a_B = x_C y_A - x_A y_C & a_C = x_A y_B - x_B y_A \\ b_A = y_B - y_C & b_B = y_C - y_A & b_C = y_A - y_B \\ c_A = x_C - x_B & c_B = x_A - x_C & c_C = x_B - x_A \end{array} \tag{2.35}$$

Along the edge of a triangle opposite a particular node, the node's shape function will be 0. For example, as we move along the edge joining node B and node C in Fig. 2.5, we see that L_C will start at 0 at node B and increase to be 1 at node C. Along the same edge, L_A will always be 0, and since the sum $L_A + L_B + L_C$ is always 1, L_B will decrease from 1 to 0 along the same edge and $1 - L_C$. This definition makes it very straightforward to formulate integrals along boundary edges.

As we saw for the previous shape functions, is true that

$$\phi^e(x, y) = \mathbf{N}^e \delta^e = [L_A \;\; L_B \;\; L_C] \begin{bmatrix} \phi_A \\ \phi_B \\ \phi_C \end{bmatrix}. \tag{2.36}$$

Substituting this in (2.19) gives

$$k_{ij}^e = \int_{\mathbb{A}} \left(\frac{\partial L_i}{\partial x}\frac{\partial L_j}{\partial x} + \frac{\partial L_i}{\partial y}\frac{\partial L_j}{\partial y} \right) dxdy \tag{2.37}$$

and since by (2.34)

$$\frac{\partial L_i}{\partial x} = \frac{b_i}{2\mathbb{A}} \text{ and } \frac{\partial L_i}{\partial y} = \frac{c_i}{2\mathbb{A}} \tag{2.38}$$

and the quantities b_i, b_j, and c_i, c_j are just found from locations of triangle vertices, we have that

$$\begin{aligned} k_{ij} &= \int_A \left(\frac{b_i b_j}{4\mathbb{A}^2} + \frac{c_i c_j}{4\mathbb{A}^2} \right) dxdy \\ &= \frac{b_i b_j}{4\mathbb{A}} + \frac{c_i c_j}{4\mathbb{A}} \end{aligned} \tag{2.39}$$

2.7.4 Tetrahedral Elements

Since tetrahedral elements are very similar to triangles, it makes sense that tetrahedral shape functions are closely related to those for triangles. For *linear* tetrahedral elements, we have that

$$\mathbf{N}^e = \left[N_A^e \;\; N_B^e N_C^e \;\; N_D^e \right] \tag{2.40}$$

where now

$$L_i = \frac{a_i + b_i x + c_i y + d_i z}{6\mathbb{V}} \tag{2.41}$$

and

$$\begin{aligned} a_i &= \begin{vmatrix} x_j & y_j & z_j \\ x_k & y_k & z_k \\ x_l & y_l & z_l \end{vmatrix}, \quad b_i = -\begin{vmatrix} 1 & y_j & z_j \\ 1 & y_k & z_k \\ 1 & y_l & z_l \end{vmatrix}, \\ c_i &= -\begin{vmatrix} x_j & 1 & z_j \\ x_k & 1 & z_k \\ x_l & 1 & z_l \end{vmatrix}, \quad d_i = -\begin{vmatrix} x_j & y_j & 1 \\ x_k & y_k & 1 \\ x_l & y_l & 1 \end{vmatrix}. \end{aligned} \tag{2.42}$$

where $i, j, k, l = A, B, C, D$ and $\mathbb{V}$ is the tetrahedral volume.

For an isotropic material, the elements in the $\mathbf{k}^e$ matrix for a linear tetrahedron become

$$\begin{aligned} k_{ij}^e &= \int_{\mathbb{V}} \left(\frac{\partial L_i}{\partial x}\frac{\partial L_j}{\partial x} + \frac{\partial L_i}{\partial y}\frac{\partial L_j}{\partial y} \right. \\ &\quad \left. + \frac{\partial L_i}{\partial z}\frac{\partial L_j}{\partial z} \right) dxdydz \\ &= \frac{1}{36\mathbb{V}} \left(b_i b_j + c_i c_j + d_i d_j \right) \end{aligned} \tag{2.43}$$

2.8 An Example Problem

Suppose we are asked to solve the problem

$$\nabla \cdot (\sigma(x, y) \nabla \phi) = 0 \tag{2.44}$$

in two dimensions using the linear triangular element mesh shown in Fig. 2.6. We will assume that the conductivity $\sigma(x, y)$ is constant on each element and scalar. In this case, in formulating equations for each element, we can bring $\sigma(x, y)$ out of the integral, and expressions will be identical to those shown in (2.19) except that k_{ij}^e will be multiplied by σ^e in each case. For now, we will assume that $\sigma(x, y) = 1$ throughout the disk. Cases where σ is anisotropic are considered in Sect. 2.12.

There are four boundary segments shown in Fig. 2.6. Assume the following boundary conditions apply:

$$\begin{aligned} \phi &= 0 \quad \text{on } C_1 \\ \frac{\partial \phi}{\partial n} &= h(s) \quad \text{on } C_2 \\ \frac{\partial \phi}{\partial n} &= 0 \quad \text{on } C_3 \\ \frac{\partial \phi}{\partial n} &= 0 \quad \text{on } C_4 \end{aligned} \tag{2.45}$$

The procedure used to solve the problem is to compute the matrices k_{ij}^e, $\bar{k}_{ij}^e$, f_i^e, and $\bar{k}_i^e$ for each element, assemble the overall matrix equation,

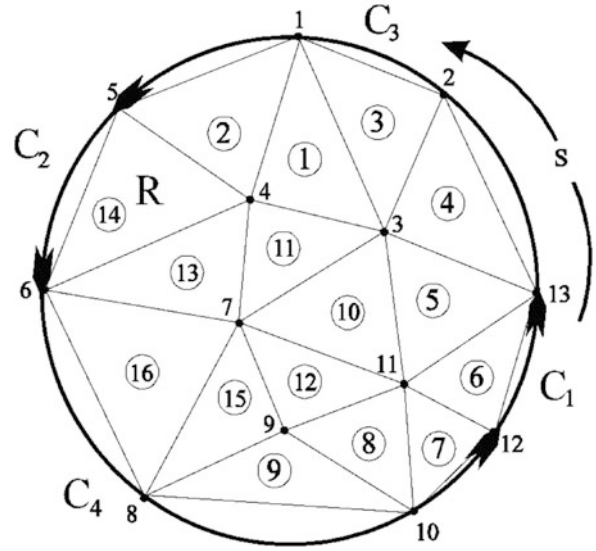

Fig. 2.6 Division of the unit disk into 16 elements and 13 nodes, with different boundary conditions applying on boundary segments C_1, C_2, C_3, and C_4. Element numbers are contained within circles

and solve. Further details of the formulation are shown in Appendix 1, but will be outlined here.

First, note the mesh definition. The triangular mesh does not completely cover the unit disk, but if more elements are used, they should approximate the boundary shape better. In Fig. 2.6, the element numbers are contained in circles. For example, element ① involves nodes 1, 4, and 3. We may choose to create a list that has dimension $E \times 3$ where each row contains the indices of nodes in each of the E elements. The ordering of nodes is important, because this may affect the sign of integrations performed along element edges. If integrals are calculated in the same sense as elements are defined, it doesn't matter which sense is chosen (clockwise or counterclockwise in this two-dimensional case) as long as the choice is consistent. Another list with dimension $N \times 2$ could contain the locations of each node.

The entries in the k_{ij}^e matrices are straightforwardly calculated from (2.39) multiplied by σⓔ (the conductivity of element ⓔ). Because (2.44) has a zero right-hand side, all entries in $\mathbf{f}^e$ are zero for each element within the mesh. Since $\lambda(s) = 0$ for the entire boundary, entries in any $\bar{\mathbf{k}}^e$ matrices are similarly all zero. As $h(s)$ is non-zero on C_2, we must calculate entries for $\bar{\mathbf{f}}^e$ on element (14), which is coincident with C_2.

Let's assume that the nodes in element (14) are (in order) 5, 6, and 4. We have that:

$$\begin{aligned} &\vdots \\ node[4] &= -0.16\ ,\ 0.39 \\ node[5] &= -0.74\ ,\ 0.78. \\ node[6] &= \ -1\ ,\ \ 0 \\ &\vdots \end{aligned}$$

The area of the triangle is 0.56. From (2.35), we find that

$$\begin{aligned} b_A = y_6 - y_4 = -0.39 \quad b_B = y_4 - y_5 = -0.39 \\ b_C = y_5 - y_6 = 0.78 \\ c_A = x_4 - x_6 = 0.84 \quad c_B = x_5 - x_4 = -0.58 \\ c_C = x_6 - x_5 = -0.26 \end{aligned} \tag{2.46}$$

and the entries in $\mathbf{k}^{(14)}$ are

$$= \begin{bmatrix} 0.39 & -0.15 & -0.23 \\ -0.15 & 0.22 & -0.07 \\ -0.23 & -0.07 & 0.304 \end{bmatrix} \tag{2.47}$$

$$\mathbf{k}^{(14)} = \begin{array}{c} \\ 5 \\ 6 \\ 4 \end{array} \begin{array}{c} \begin{array}{ccc} 5 & 6 & 4 \end{array} \\ \begin{bmatrix} 0.39 & -0.15 & -0.23 \\ -0.15 & 0.22 & -0.07 \\ -0.23 & -0.07 & 0.304 \end{bmatrix} \end{array} \tag{2.48}$$

As noted above, the entries in $\mathbf{f}^{(14)}$ and $\bar{\mathbf{k}}^{(14)}$ are all zeroes, but we must figure out $\bar{\mathbf{f}}^{(14)}$.

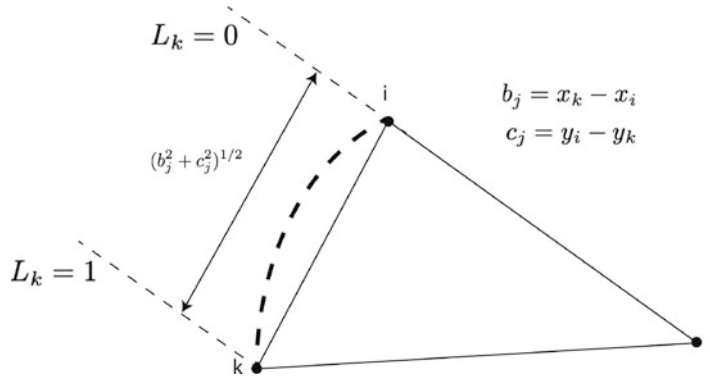

Fig. 2.7 Triangular element intersecting with boundary. The length of the boundary segment is given by $(b_j^2 + c_j^2)^{1/2}$, and over the same traverse, the parameter L_k changes from 0 to 1, and L_j is always 0. Changing variables from x, y to $L_{i,j,k}$ will involve changing the integration variable from ds to dL and scaling by the edge length $(b_j^2 + c_j^2)^{1/2}$ as in (2.50)

We need to compute

$$\bar{\mathbf{f}}^{(14)} = \begin{bmatrix} \int_{C^e} h(s) L_A^{(14)} ds \\ \int_{C^e} h(s) L_B^{(14)} ds \\ \int_{C^e} h(s) L_C^{(14)} ds \end{bmatrix}. \tag{2.49}$$

The only part of the element that is coincident with the boundary is between nodes A and B of the element (nodes 5 and 6). Traversing the boundary counterclockwise from A to B, L_B starts at 0 and ends at 1. On this edge, L_C is always 0. The integrals for the element become

$$\bar{\mathbf{f}}^{(14)} = \begin{bmatrix} \int_{node5}^{node6} h(s)(1 - L_B^{(14)}) ds \\ \int_{node5}^{node6} h(s) L_B^{(14)} ds \\ 0 \end{bmatrix}$$

$$= \begin{bmatrix} \int_0^1 h(1 - L_B^{(14)}) \sqrt{b_3^2 + c_3^2} dL_B \\ \int_0^1 h L_B^{(14)} \sqrt{b_3^2 + c_3^2} dL_B \\ 0 \end{bmatrix}. \tag{2.50}$$

Where does the factor $\sqrt{b_3^2 + c_3^2}$ come from?This quantity is the length of the triangle edge, since $ds = \sqrt{dx^2 + dy^2}$ and you can show, via (2.34), that this is the case since $b_C = y_A - y_B$ and $c_C = x_B - x_A$. Figure 2.7 shows the idea.

Finally, we obtain

$$\bar{\mathbf{f}}^{(14)} == \begin{bmatrix} \int_0^1 h(1 - L_B^{(14)}) \sqrt{b_3^2 + c_3^2} dL_B \\ \int_0^1 h L_B^{(14)} \sqrt{b_3^2 + c_3^2} dL_B \\ 0 \end{bmatrix}$$

$$= \begin{bmatrix} \frac{1}{2} h \sqrt{b_3^2 + c_3^2} \\ \frac{1}{2} h \sqrt{b_3^2 + c_3^2} \\ 0 \end{bmatrix} = \begin{bmatrix} 0.412\, h \\ 0.412\, h \\ 0 \end{bmatrix}. \tag{2.51}$$

2.9 Assembly of the Overall Matrix Equation

From the previous example, we have only filled entries for one set of element matrices. Once entries for each individual element matrix are assembled, they can be added into the global $N \times N$ matrix. For the example in Sect. 2.8, the global $\mathbf{K}$ matrix is assembled from only individual $\mathbf{k}^e$s. The entries we found from $\mathbf{k}^{(14)}$ would appear in the global matrix in rows and columns 5, 6, and 4 as shown in (2.52)

$$\begin{bmatrix}
0\,0\,0 & 0 & 0 & 0 & 0\,0\,0\,0\,0\,0\,0 \\
0\,0\,0 & 0 & 0 & 0 & 0\,0\,0\,0\,0\,0\,0 \\
0\,0\,0 & 0 & 0 & 0 & 0\,0\,0\,0\,0\,0\,0 \\
0\,0\,0 & 0.30 & -0.23 & -0.07 & 0\,0\,0\,0\,0\,0\,0 \\
0\,0\,0 & -0.23 & 0.38 & -0.15 & 0\,0\,0\,0\,0\,0\,0 \\
0\,0\,0 & -0.07 & -0.15 & 0.22 & 0\,0\,0\,0\,0\,0\,0 \\
0\,0\,0 & 0 & 0 & 0 & 0\,0\,0\,0\,0\,0\,0 \\
0\,0\,0 & 0 & 0 & 0 & 0\,0\,0\,0\,0\,0\,0 \\
0\,0\,0 & 0 & 0 & 0 & 0\,0\,0\,0\,0\,0\,0 \\
0\,0\,0 & 0 & 0 & 0 & 0\,0\,0\,0\,0\,0\,0 \\
0\,0\,0 & 0 & 0 & 0 & 0\,0\,0\,0\,0\,0\,0 \\
0\,0\,0 & 0 & 0 & 0 & 0\,0\,0\,0\,0\,0\,0 \\
0\,0\,0 & 0 & 0 & 0 & 0\,0\,0\,0\,0\,0\,0
\end{bmatrix}. \tag{2.52}$$

The entries in the matrix are the same, but the rows and columns are rearranged so that they refer to global node numbering, not the node order in the element.

The full **K** matrix can also be computed. See Appendix 1 for more details. Similarly, the $\bar{\mathbf{f}}$ contributions from element (14) are

$$\mathbf{F} = \begin{bmatrix} \vdots \\ 0 \\ 0.412h \\ 0.412h \\ \vdots \end{bmatrix}. \tag{2.53}$$

You can see that the $\mathbf{k}^e$ matrix is always symmetric. In fact, all the $\mathbf{k}^e$ matrices we have shown so far are symmetric (this is a property of the Laplacian operator), and all rows and columns sum to zero. This means these matrices are all singular. As a consequence, the global **K** matrix is also singular, and it cannot be inverted to find the solution Φ. At this point, we haven't mentioned the Dirichlet boundary conditions applied on C_1. This boundary condition will be applied by requiring that the solution on nodes 12 and 13 is 0. This can be done by eliminating all rows and columns involving nodes 12 and 13. As a consequence, the initially singular **K** matrix becomes non-singular, and Φ can be found.

2.10 Solution of the System of Equations

After working through all elements within the mesh, we obtain an overall system of equations describing the solution in the form

$$\mathbf{K}\Phi = \mathbf{F} \tag{2.54}$$

where **K** is an $N \times N$ matrix, Φ is an $N \times 1$ vector containing the nodal solutions, and **F** is an $N \times 1$ matrix. For the 13×13 system above, inverting **K** is trivial, but many meshes contain hundreds of thousands of elements and nodes, or more. One important property of all **K** matrices, regardless of the PDE, is that they are typically *sparse*. This is because of the mesh definition. Non-zero entries only occur in **K** if nodes are on the same or neighboring elements. For example, in Fig. 2.6, there will not be an entry at index 3,6 (or 6,3) in **K** because there are no mesh edges shared by nodes 3 and 6. One useful consequence of sparsity is that even if the nominal size of the **K** matrix is very large, special storage and operation methods can be used to represent and combine them compactly and efficiently.

The method used to solve the system is dependent upon the properties of **K**, which in turn relates to the PDE's properties. Inversion of **K** matrices from Poisson-type PDEs are relatively straightforward. Because of the large size of **K** matrices (even after accounting from sparseness), it is inefficient to explicitly invert **K** using Gaussian elimination because the number of operations required is of $O(N^3)$. It is more common to use iterative techniques that minimize the N-dimensional function $m(\Phi)$, where

$$m(\phi) = \Phi^T \mathbf{K}\Phi - \mathbf{F}\Phi. \tag{2.55}$$

The derivative (gradient) of $m(\Phi)$ is

$$\nabla m(\Phi) = \mathbf{K}\Phi - \mathbf{F}. \tag{2.56}$$

At the minimum of $m(\Phi)$, $\nabla m(\Phi) = 0$ and $\mathbf{K}\Phi = \mathbf{F}$, effectively inverting $\mathbf{K}$.

An example of a minimization algorithm that can be used to achieve this inversion is the conjugate gradient method [9]. Packages like COMSOL use many different types of solution methods including algebraic multiscale methods and segregated methods, and the exact solution may be chosen by the software automatically depending on the equation characteristics. The solution becomes more complicated the more partial differential equations are being solved simultaneously. If equations are time dependent, entire matrices must be inverted at each time step. Methods used for solution of finite element matrices for time-dependent PDEs is out of the scope of this book, but more details can be found in [2] or [6].

2.11 Sampling Solutions

Recall that the shape function provides a means to convert the solved vector of nodal values into the value of the solution at any point within any element (2.13). It is possible to sample your solution at *any* point within the domains making up the model. This is particularly relevant in our application, where the models and experimental data must be matched as well as possible. Details of a convenient scheme for sampling a model to match MRI data are shown in Appendix 2.

2.12 Accounting for Anisotropy

In the equations shown in the example, we did not worry about the conductivity $\sigma(x, y)$ term included in (2.44). If $\sigma(x, y)$ is isotropic, all that will be required is to premultiply expressions in k_{ij}^e by σ^e. However, important body tissues including muscle and white matter exhibit anisotropy, and, depending on the application, you may need to include it in your model. If $\sigma(x, y)$ is anisotropic, the conductivity distribution in each element is specified by a tensor $\mathbb{C}^e$. In two dimensions, we can write $\mathbb{C}^e$ as

$$\mathbb{C}^e = \begin{bmatrix} C_{xx} & C_{yx} \\ C_{xy} & C_{yy} \end{bmatrix} \tag{2.57}$$

Tensors describing diffusion or conductivity properties are usually symmetric, i.e., $C_{xy} = C_{yx}$ and $C_{yz} = C_{zy}$.

If the conductivity is isotropic or if the direction of the material anisotropy coincides with the coordinate axes, all off-diagonal terms are 0, and the tensor can be expressed as

$$\mathbb{C}^e = \begin{bmatrix} C_{xx} & 0 \\ 0 & C_{yy} \end{bmatrix}. \tag{2.58}$$

If the material is isotropic, then $C_{xx} = C_{yy}$.

The operator for the isotropic case shown in (2.44) is $\sigma^e \nabla \cdot \nabla = \nabla^2$, but the operator for anisotropic cases is $\nabla \cdot (\mathbb{C}^e(x, y)\nabla)$. The computations for the $\mathbf{k}^e$ matrix must take into account the individual tensor components. In calculating the operator (L contribution of the functional, we must calculate

$$\mathbf{k}^e = \int_R \left((\nabla \mathbf{N}^e)^T \mathbb{C}^e \nabla \mathbf{N}^e \right) dA. \tag{2.59}$$

The operator ∇ here can be thought of as a matrix, that is,

$$\nabla = \begin{bmatrix} \frac{\partial}{\partial x} \\ \frac{\partial}{\partial y} \end{bmatrix} \tag{2.60}$$

Recall that $\mathbf{N}^e$ is a $1 \times X$ matrix, where X is the number of nodes in the element. The result of applying (2.60) to $\mathbf{N}^e$ is a $2 \times X$ matrix. If we multiply the 2×2 matrix $\boldsymbol{\sigma}$ by the $2 \times X$ $\nabla \mathbf{N}^e$, we obtain another $2 \times X$ matrix. Premultiplying this result by the $X \times 2$ matrix $(\nabla \mathbf{N}^e)^T$ results in an $X \times X$ matrix. An example for the triangular shape function where $X = 3$ is shown in (2.61).

$$\mathbf{k}^e = \int_{R^e} \left(\left(\begin{bmatrix} \frac{\partial}{\partial x} \\ \frac{\partial}{\partial y} \end{bmatrix} \begin{bmatrix} L_A & L_B & L_C \end{bmatrix} \right)^T \mathbb{C}^e \begin{bmatrix} \frac{\partial}{\partial x} \\ \frac{\partial}{\partial y} \end{bmatrix} \begin{bmatrix} L_A & L_B & L_C \end{bmatrix} \right) dA$$

$$= \int_{R^e} \left(\left(\begin{bmatrix} \frac{\partial L_A}{\partial x} & \frac{\partial L_B}{\partial x} & \frac{\partial L_C}{\partial x} \\ \frac{\partial L_A}{\partial y} & \frac{\partial L_B}{\partial y} & \frac{\partial L_C}{\partial y} \end{bmatrix} \right)^T \mathbb{C}^e \begin{bmatrix} \frac{\partial L_A}{\partial x} & \frac{\partial L_B}{\partial x} & \frac{\partial L_C}{\partial x} \\ \frac{\partial L_A}{\partial y} & \frac{\partial L_B}{\partial y} & \frac{\partial L_C}{\partial y} \end{bmatrix} \right) dA$$

$$= \int_{R^e} \left(\begin{bmatrix} \frac{\partial L_A}{\partial x} & \frac{\partial L_A}{\partial y} \\ \frac{\partial L_B}{\partial x} & \frac{\partial L_B}{\partial y} \\ \frac{\partial L_C}{\partial x} & \frac{\partial L_C}{\partial y} \end{bmatrix} \begin{bmatrix} C^e_{xx} & C^e_{yx} \\ C^e_{xy} & C^e_{yy} \end{bmatrix} \begin{bmatrix} \frac{\partial L_A}{\partial x} & \frac{\partial L_B}{\partial x} & \frac{\partial L_C}{\partial x} \\ \frac{\partial L_A}{\partial y} & \frac{\partial L_B}{\partial y} & \frac{\partial L_C}{\partial y} \end{bmatrix} \right) dA. \tag{2.61}$$

As you can see, the resulting expression gets large quite quickly. But the result is a 3×3 matrix. Let's just look at one entry, for k^e_{AA}. We find that

$$k^e_{AA} = \int_{R^e} \left(C^e_{xx} \frac{\partial L_A}{\partial x} \frac{\partial L_A}{\partial x} + C^e_{yx} \frac{\partial L_A}{\partial y} \frac{\partial L_A}{\partial x} + C^e_{xy} \frac{\partial L_A}{\partial x} \frac{\partial L_A}{\partial y} + C^e_{yy} \frac{\partial L_A}{\partial y} \frac{\partial L_A}{\partial y} \right) dA \tag{2.62}$$

If the material is isotropic, we recover (2.39).

2.13 Grading

Recall that the solution within each element is typically a low-order polynomial. Depending on the boundary conditions, the shape of the boundary itself, and the positions of any sources, the solution may be more active (that is, change more rapidly) in different areas of the domain. Therefore, if elements are uniformly sized, this will result in reduced accuracy near such areas. To maintain uniform solution accuracy throughout the solution space, it is often necessary to grade the size of elements, using smaller elements where the solution is most active. This can be done automatically when the mesh is created, by specifying a grading function that has large values where solution activity is expected to be highest. Meshing will usually be finer (smaller elements) near regions of higher curvature, and this is where solutions may also be expected to be more active. An alternative technique is to bias a coarsely graded mesh according to the expected solution activity in order to make the accuracy uniform throughout and then to increase the fineness of the mesh uniformly up to the number of elements required to meet the target accuracy in the solution.

Of course, while it is straightforward to determine the accuracy of a model where an exact analytic solution is available, in practice, the accuracy of a particular complex model is difficult to establish. To determine the influence of the finite element mesh on the solution, it is usual to solve the problem on meshes with a range of element numbers (a "mesh refinement study") and to trust models when increasing the number of elements further does not change solutions beyond a specified tolerance.

2.14 Higher-Order Elements

A method of increasing the solution accuracy while maintaining the same number of elements is by increasing the order of the approximating polynomial inside each element. Often this will require specification of internal nodes. For instance, in the case of the triangular element, increasing the order of the approximating polynomial from 1 to 2 requires the specification of three extra nodes—resulting in a complete second-order polynomial of the form

$$\phi^e(x, y) = a_0 + a_1 x + a_2 y + a_3 xy + a_4 x^2 + a_5 y^2. \tag{2.63}$$

The three extra nodes are chosen to be the midpoints of each side of the triangle as in Fig. 2.8. For a tetrahedron, the extra nodes are inserted in a similar way.

The shape functions for quadratic triangles or tetrahedra are derived from the simple linear triangle or tetrahedral shape functions, and a 6×6 or 10×10 $\mathbf{k}^e$ matrix results.

2.15 Segmentation of Image Data into Realistic Geometry Models

The closer a model is to a real experimental situation, and the larger the number of elements, the more the solution should be expected to follow

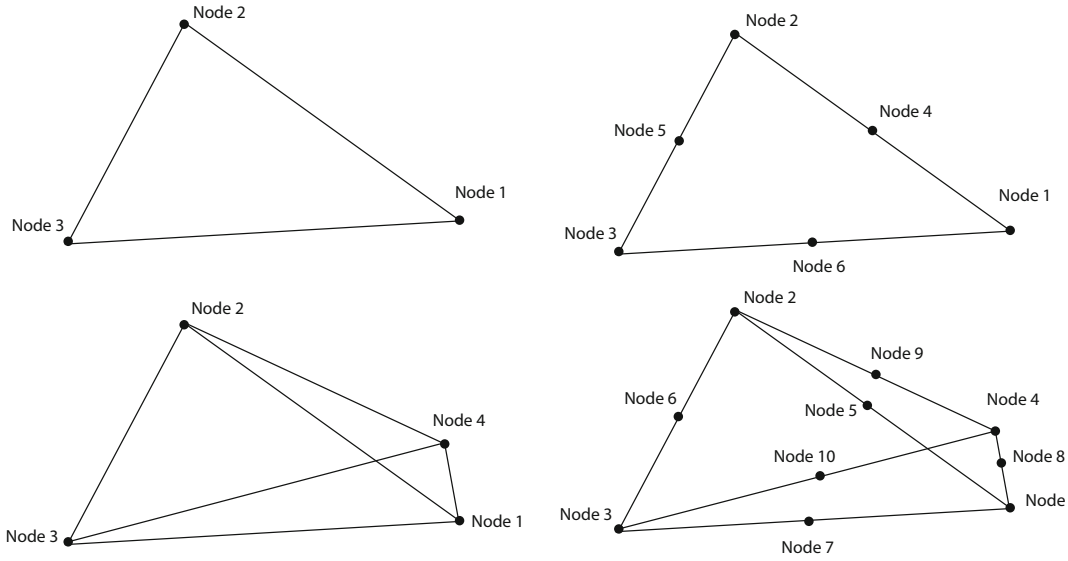

Fig. 2.8 Linear and quadratic triangular and tetrahedral elements. Nodes in linear elements are placed on vertices. Extra nodes for quadratic elements are placed halfway along edges

the real-world solution. Recreation of accurate model geometries usually depends on imaging data, whether they be photographs or medical images. In our area, MR magnitude images are the principal source of the data used to produce realistic models, since they are a convenient byproduct of MREIT or EPT data collection. In the sections that follow, we will consider segmentation of a three-dimensional neuroimaging volume for electromagnetic simulations, but the general principles can easily be extensible to images of other data and modeling other phenomena.

The simplest model that could be created from MRI magnitude images of the head is a solid volume showing its outer shape. The outer shape of a volume is a strong determinant of the current pathways formed within it, even more than the internal conductivity distribution [1]. Models with the correct outer boundary shape and a uniform conductivity are used in calculating the projected current density described in Chap. 6. Determination of the outer boundary shape of the volume can be performed just using simple thresholding. Note that thresholding alone might not result in a perfect volume because there may be regions of low signal (e.g., air or bone) within the head that may have lower values than the threshold you determine divides the scalp from the external air. All segmentation, whether manual or automatic, must always be checked as a final step.

Now we move to the concept of determining the domain extent. Given that you have a discrete image volume, it is natural to consider modeling as much tissue (using as much of the data) as possible. But remember that the larger the model is, the longer it will take to solve and the more storage space it will need once solved. Consider how much you need to model while still providing a good solution in the regions or subdomains you are interested in. For example, in neurological image-based models, Indahlastari et al. [4] found that if the model is truncated below the skull base, this did not significantly affect current densities predicted within the cortex.

The next concept is which tissues to segment. Only electrically distinct tissues need to be segmented, since only these properties appear in the PDE. Therefore, if you only have conductivity for "gray matter" or "white matter," there would normally be no need to segment, say, the substantia nigra or dorsolateral prefrontal cortex. Where it *may* be useful to segment these structures is in postprocessing, to see what the predicted fields are in these specific regions.

In the next section, we describe a typical workflow for constructing a model that satisfies the principles above. There are of course many more tools available than one can describe in one document, and you are encouraged to explore the range of resources available in constructing models.

2.15.1 Segmentation Procedures

In the simplest (and most time-consuming) situation, you could entertain the idea of methodically working through a volume "coloring in" each voxel according to the tissue you believe it must be, based on the voxel's intensity. This might be possible for simple images or in two dimensions, but to segment a structure as complex as the brain, some automatic processes must be used. Luckily, there are many freely available software tools that enable you to automatically segment brain tissue, but at present there are fewer that segment the entire head or other body parts. Many of the automatic processing steps are intended to differentiate gray and white matter and cerebrospinal fluid (CSF) only and are not intended to segment the entire head. There are also some tools available to find the skull and scalp. Other electrically important tissues such as muscle, fat, the eyes, and blood must be segmented manually, i.e., by working through voxel by voxel and determining which tissue is which, referring to an atlas such as [13]. Manual segmentations must be checked comprehensively by viewing segmented structures in all three planes (XY, YZ, and ZX) of the volume as errors can result from segmenting in only one plane set. Regardless of the method used to segment the model, it will always be necessary to check the final segmentation and make sure there are no holes (voxels with unassigned tissues) or errors in tissue assignments.

Figure 2.9 (from [5]) shows the procedure used to segment a human head based on T1-weighted MRI data. The procedure first involves using FreeSurfer to segment white and gray matter, followed by SPM to segment scalp and skull. The resulting masks are combined in software to make a whole volume where each head voxel is tagged in terms of tissue type. While you can do this in MATLAB, specialized software such as Simpleware ScanIP[1] (Synopsys, Inc. Mountain View, CA), Mimics[2] (Materialise, NV, Leuven, Belgium), or ITK-Snap[3] provide more convenient means of making final manual segmentations or corrections before segment definitions are exported to a FEM solver.

Major automated segmentation tools in neuroscience applications include FreeSurfer[4] and SPM.[5] The emphasis of both FreeSurfer and SPM is fMRI analysis, but each has extensions enabling automatic processing of subject-specific data to find specific tissues or regions of interest. The ROAST tool that can be used to automatically segment MRI data and simulate electric fields for transcranial electrical stimulation [3] uses elements of SPM 12. The SimNIBS [14] package used to simulate fields in transcranial electric and magnetic stimulation applications uses elements of both FreeSurfer and FSL,[6] and more recently, some parts of SPM12 have been implemented in SimNIBS to aid skull segmentation [8].

Commonly applied operations in segmentation include painting, thresholding, and region growing operations. While these functions can be performed using MATLAB, programs like ScanIP, Mimics, or ITK-SNAP are specialized toward segmentation operations. They also make it possible to easily add additional structures such as electrodes.

When each image voxel has been tagged as a particular type, all voxels of that type can then be assigned a property (conductivity, permittivity, or both, maybe specified as a function of frequency). If it is appropriate to specify a particular tissue as anisotropic, the six parameters describing the conductivity tensor in each voxel can be determined by finding the principal direction of the

[1] https://www.synopsys.com/simpleware/software/scanip.html.

[2] https://www.materialise.com/en/medical/mimics-innovation-suite/mimics.

[3] www.itksnap.org.

[4] https://surfer.nmr.mgh.harvard.edu.

[5] https://www.fil.ion.ucl.ac.uk/spm.

[6] https://fsl.fmrib.ox.ac.uk.

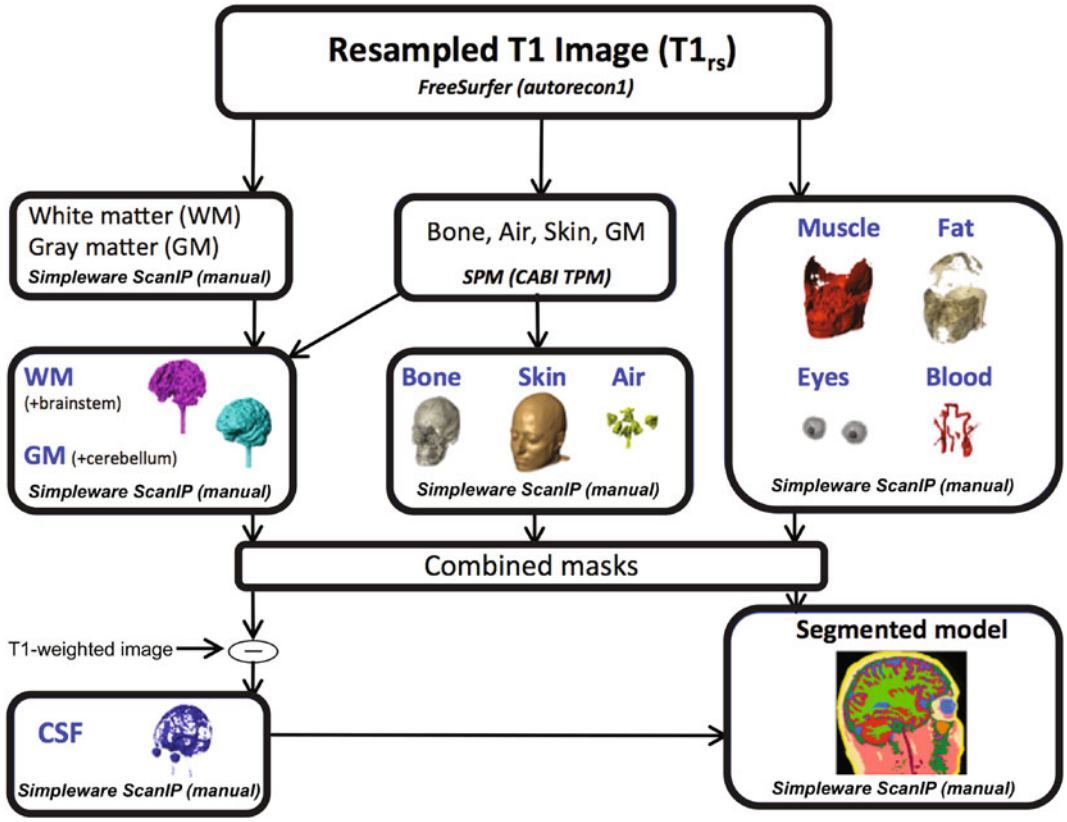

Fig. 2.9 The segmentation pipeline involved both manual and automatic segmentation processes. The pipeline is shown in terms of the three major operation types (FreeSurfer, SPM, and manual segmentation and checking). Results from each operation type were finally combined to produce a single head model containing ten tissue types

diffusion tensor data and rotating a principal conductivity tensor describing the tissue to align with it. More details on this process are below.

2.15.2 Exporting Segmentation Information to a Finite Element Solver

There are a number of options in exporting segmentation information to a FEM solver. You can save the external shape of the head, that is, save the surface definition. This can be done by exporting the surface to an `stl` (stereolithography) file. The `stl` file format is the same one as used in 3D printers.

This sort of idea is good if you just want to calculate the homogeneous contribution to the projected current density (see Chap. 6). But what if you want to create an inhomogeneous model? If you save just the surface, you could specify the property distribution as a function (using interpolation based on the conductivities assigned at the center of each voxel). In this case, you could import the homogeneous conductivity model into your FEM program and import the volume defining conductivities, and everything is set. The three-dimensional solid defined by the .stl file would be meshed by the FEM program, and calculations would proceed from there.

A second approach would be to generate a mesh compatible with your FEM program that recognizes the boundaries of the different tissue types. This is important because we typically assume that the properties within one element are constant. The actual property values could

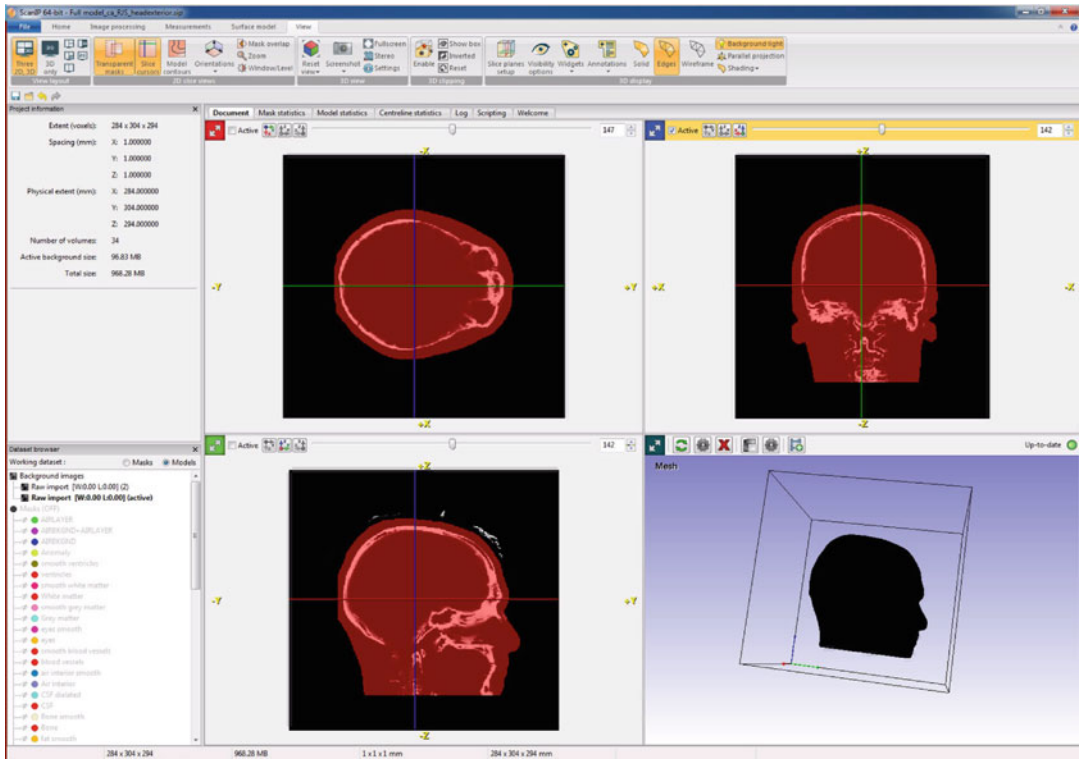

Fig. 2.10 Interface of manual segmentation program. The example shown includes masks for skull and entire head compartments viewed in three planes and rendered in three dimensions

be set before or after mesh export. This type of option is possible with ScanFE (Synopsys) and Mimics. An example screenshot from the ScanFE interface is shown in Fig. 2.10. In the case shown in Fig. 2.10, entire head and skull compartment masks are displayed. A combined mesh that respects each compartment's boundaries can be generated and exported to compatible file formats including NASTRAN, ABAQUS, and COMSOL model files.

Going back a step, seeing as the segmented T1-weighted model is made of voxels, which are hexahedrons, it is also perfectly acceptable to construct a mesh based on this structure. This method was implemented in [11] using C and MATLAB code. Starting from the voxelwise segmentation, each hexahedral element was split into six quadratic tetrahedrons, and global $\mathbf{K}$ and $\mathbf{F}$ matrices were assembled. The system was then solved using the preconditioned conjugate gradient method. The platform was extended to add anisotropy in [12]. This approach is quite inflexible but can work well if you are only working with a limited range of problem types. For this reason, we will now describe use of a commercially available modeling platform to solve PDEs arising in this area.

2.15.3 Adding Anisotropy to Models

Anisotropy can be added to models using an interpolation function. There are a number of ways of doing this. If diffusion tensor information is available, the (appropriately co-registered) tensor components for each voxel can be overlaid on the model. There are two approaches that can be used to model the full conductivity tensor in the model. Rullmann et al. [10] suggested calculating a scaling factor (s identical to the factor η reconstructed in DT-MREIT) in the white and gray matter compartment of the brain using a weighted mean of

isotropic literature conductivities and averaged diffusivities. The scaling factor was multiplied by the diffusion tensor to produce the conductivity tensor applied to the model. An alternative approach [7, 12] involves computing the principal eigenvector within each diffusion tensor voxel and using it to re-orient a tensor assumed for the tissue type. In both cases, the result can be imported into the model and incorporated in the stiffness matrix using the method described in Sect. 2.12. If only white matter anisotropy needs to be incorporated, the operation can easily be masked to only apply to the white matter compartment.

2.16 COMSOL Modeling

Solving finite element problems of any reasonable size quickly becomes tedious to program on your own. This is where use of commercially available software packages becomes advantageous. In the sections below, we describe three approaches that are of use in solving or verifying electromagnetic properties mapping, using COMSOL Multiphysics (Burlington, MA, USA). The COMSOL platform is designed to solve general "multiphysics" problems, that is, problems governed by multiple PDEs. An example of a multiphysics problem is electromagnetic heating. If an external current flows through a conductor, with the solution to the problem given by the Laplace equation (2.8), energy will be dissipated within the conductor. The energy distribution throughout the conductor is given by $Q_s = \mathbf{J} \cdot \mathbf{E}$. This measure is in J/m^3. This heating distribution can be used as a source term in the PDE governing heat diffusion (without convection)

$$\rho c_p \frac{\partial T}{\partial t} + \nabla \cdot (-\varkappa \nabla T) = Q_s \qquad (2.64)$$

where ρ is the density of material, c_p is its specific heat capacity, $\varkappa$ is its thermal conductivity, and T denotes temperature. You could consider that this coupling is unidirectional, since the eventual heat distribution within the conductor does not influence current flow. However, temperature does influence material electrical properties. If you wished, you could define conductivity or permittivity as a function of temperature and solve the two PDEs together at each time step of the diffusion problem. This is bidirectional coupling.

COMSOL has numerous modules that are instances of PDEs specific to particular physical contexts. It also allows modeling of generic PDEs in a mathematics module. The benefits of the modules are that multiple derived variables and common application environments are conveniently predefined. The modules most commonly used in electrical properties mapping are the electric currents (`ec`), magnetic and electric fields (`mef`), and magnetic fields (`mf`) modules. In the sections below, we show examples of models using these modules and outline how they may be used in mapping or reconstructing electrical properties.

2.16.1 Electric Current Modeling

The images in Fig. 2.11 show a geometry, mesh, and finite element results found when solving the Laplace equation using a uniform model. This model was created by exporting an .stl (stereolithography) file from a segmentation program (in this case, Simpleware ScanIP) and importing it into COMSOL. Export from ScanIP incorporated triangle smoothing. Import of three-dimensional surface structures into COMSOL is usually tricky to do. In this case, the model was exported by combining the head and electrodes into one mask and exporting it as a single part `stl` mesh. The electrode boundaries were then defined by adjusting the surface mesh import to only generate distinct boundary faces when the change in angle was greater than around 15°. This was sufficient to generate clear boundaries where the electrodes met the scalp. However, even with triangle smoothing, this generated a large number of faces that needed to be combined. The extraneous faces on the surface geometry were concatenated to produce the three faces defining the electrodes and the remainder of the head. The `stl` mesh is not used as the finite element mesh. After import, the region defined with the surface

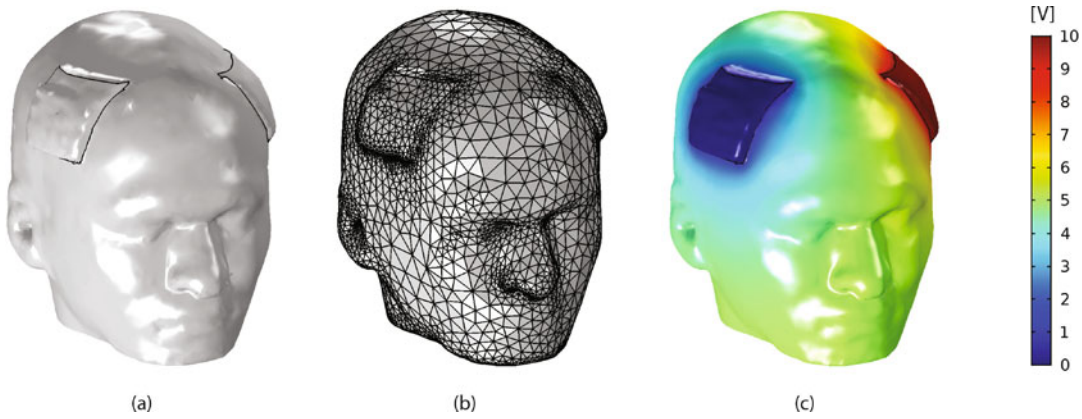

Fig. 2.11 Images illustrating uniform-conductivity COMSOL model constructed using an `stl` surface mesh including electrodes only. (**a**) shows the model surface, including electrode faces, (**b**) illustrates surface of final volume mesh, and (**c**) shows voltage distribution formed within the model

mesh was transformed into a solid geometry object, and a new volume mesh was defined to solve the problem.

The conductivity of the entire model was defined as 1 S/m, and the boundary conditions were specified as +10 V on the right electrode (F4) and 0 V on the left electrode, and insulation was specified on the remainder of the boundary. Normally, transcranial stimulation parameters are defined in terms of a current, so you may wonder why voltage was specified. Why not just specify a normal current density (an $\bar{\mathbf{f}}$ contribution) on each electrode? If the boundary conditions are specified only using normal current density, the matrix $\mathbf{K}$ that is inverted to solve the problem is still singular. In fact, if there is no voltage solution specified in addition to the current flow, there are an infinite number of possible solutions if only a boundary flow (current) is stipulated. As an alternative, you could set one electrode to be at ground (0 V) and specify a normal current density on another electrode. A final option is to stipulate a normal current density on both as long as a voltage is specified at one of the nodes in the mesh. The integral of the normal current density over each electrode should match. Some COMSOL options will also allow you to specify a total current (in A) flowing through a boundary `terminal`.

Although the model shown in Fig. 2.11 was exported as a surface mesh and a uniform conductivity of 1 S/m was used for the entire volume, the model could also be used to solve for a heterogeneous conductivity distribution by defining a conductivity distribution on a grid overlaid on the volume. This grid could inform an interpolation function used for the conductivity of the object. This approach is useful because the mesh is not constrained by the compartment boundaries which would typically make the mesh larger (and the solutions longer and its storage requirements larger).

A second example derived from the same image data is shown in Fig. 2.12. In this case, the structure was exported directly as a COMSOL mesh from Simpleware, using ScanFE, and the model contains no geometry, only a mesh. The mesh contained multiple compartments for the different tissues within the head as well as the electrodes and wires delivering current to the electrodes. Each compartment mesh was exported with a different material definition (conductivity or permittivity for time- or frequency-dependent models), and these can be changed or defined as a function of frequency within COMSOL if required. If one compartment material (white matter) needs to be defined as anisotropic, the volumes for each component of the conductivity tensor can be imported as a grid and values can be interpolated, in a similar way as noted above for importing and interpolating conductivity functions. Because the mesh is predefined, it is not

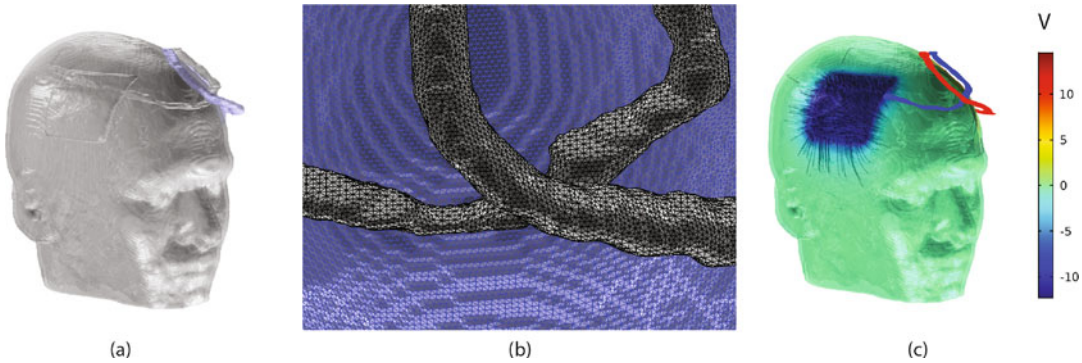

Fig. 2.12 Image of full mesh exported from ScanIP including wires as well as electrodes. Part (**a**) shows the mesh exterior, (**b**) shows mesh detail, and (**c**) shows voltage formed on the mesh surface as well as streamlines in left (red) and right (blue) wires and emanating from electrodes (black) into interior

possible to add extra geometry features (e.g., electrodes) to the model. Anything needed must be added to the Simpleware environment before the COMSOL mesh is exported. After the mesh is imported, there is some limited availability to break up face definitions if those automatically created within Simpleware are not acceptable, but this flexibility is limited.

If you wished, you could simulate the effect of current administration from the end of one wire to the end of another, and the wires have been included in Fig. 2.12. However, the increase in the level of detail required to do this is probably too large, and there is not much point. For example, you would need to account for the insulation on the wires; otherwise, the wire structures lying directly on the head here may result in conduction directly into the scalp rather than into the electrodes. One way of avoiding this is to model each wire-electrode combination separately using a separate electric currents module and feed the current density resulting on the electrodes into the head using a third module that includes head tissues only, and this strategy has been used here.

A useful reason for modeling current in the wires is to account for the magnetic flux density it contributes to MRI phase recorded within the head. Depending on the wire geometry and the slices chosen, these effects can exceed internal current flow effects. Therefore, careful modeling and correction of these fields are required. The flux density can be directly calculated from the simulated current density distribution (see the section on the fast Fourier transform method used for Biot-Savart calculation in Chap. 6) or modeled directly using the COMSOL magnetic and electric fields module (`mef`), as described in Sect. 2.16.2.

2.16.2 Magnetic and Electric Fields Modeling Combined

If the COMSOL AC/DC model is used, it is possible to extract both the information available in the electric currents module and compute the **B** fields together with **J** data. Unfortunately, it is not easily possible to manually add a postprocessing step to compute **B**, and adding this step is not very efficient. The image shown in Fig. 2.13 is of the z-component of magnetic flux density calculated in a model created from the same `.stl` data as Fig. 2.11 but with the wires added to the model export. Because there are multiple PDEs solved in the `mef` module, if a model with the number of mesh elements used for the model in Fig. 2.12 were to be used, the number of degrees of freedom involved (i.e., the number of values solved for in total) would likely be too large to be solved on desktop computer. Therefore, constructing the model from `.stl` data is the best option. In this simple case, the wires were simulated with a high conductivity, and the remainder of the head compartment had a conductivity of 1 S/m.

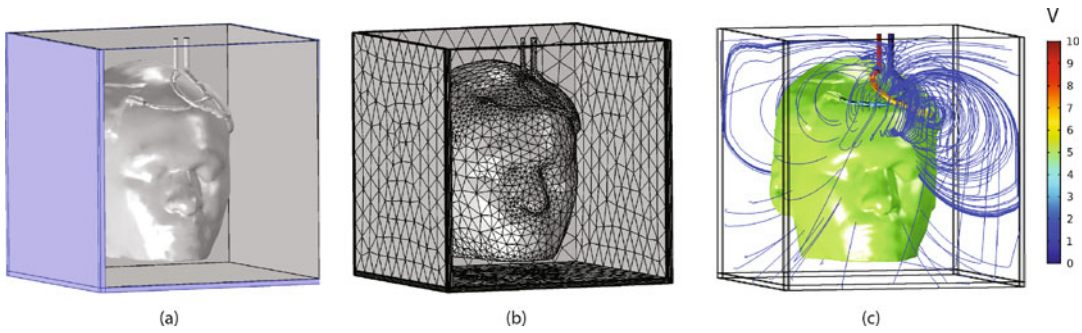

Fig. 2.13 Images from a model constructed using the COMSOL `mef` module and an `.stl`-based model, with extended wires and using infinite elements. Part (**a**) shows the model geometry, including the air box and infinite elements, (**b**) illustrates the mesh, and (**c**) shows the model result with the surface color representing voltage and blue streamlines indicating magnetic flux density distribution

The figure shown in Fig. 2.13 includes an air compartment within which magnetic fields can be calculated. The wires have been extended in the axial (z) direction to ensure that boundary conditions ($V_{left} = 10\,\text{V}$; $V_{right} = 0\,\text{V}$) can be applied at the wire ends and that there will be no B_z component created by the extension. Notice also that there is a "fishtank" surrounding the air compartment, but not on the top where the boundary conditions were applied. This edge contains "infinite elements" which are elements that have a length scale different from the main model. This results in the effective volume of air modeled to be much larger than the small box surrounding the head and reduces any distortion of the magnetic flux density distribution that might result from the box edges. The infinite element domain faces are subject to a perfect magnetic conductor boundary condition ($\mathbf{n} \times \mathbf{H} = 0$, $\mathbf{n} \cdot \mathbf{J} = 0$) to solve the problem. You can see at the right edge of Fig. 2.13c that the flux density distribution looks like it is truncated at the model edge, but the lines of flux do not appear distorted by its presence. Apparent kinks in the distribution at top left and bottom right result from the streamline calculation process at the model boundary.

2.16.3 Modeling of High-Frequency Electromagnetic Properties

EPT measures tissue electrical properties at the resonant (Larmor) frequency of an MRI system. For a 1.5 T system, this is around 64 MHz, and at 3 T, properties are measured at around 128 MHz. To model these effects, it is necessary to solve the Maxwell equations in wave form. In (2.65), μ_r denotes the relative permeability of the medium—this is 1 for most tissue, and ε_r is the relative permeability at the frequency in question—at 64 MHz, it may be around 50 (in the model example, it is set to 40), and the average conductivity at this frequency may be around 1 S/m; k_0 is the free space wavenumber of the fundamental mode of the solution. Losses and phase shifts caused by non-zero conductivity are accounted for by the term in brackets on the right-hand side of (2.65).

$$\nabla \times \nabla \times \mathbf{E} = \mu_r k_0^2 \left(\varepsilon_r - \frac{i\sigma}{\omega \varepsilon_0} \right) \mathbf{E} \qquad (2.65)$$

A relevant example is shown in Fig. 2.14. This example illustrates solution of the equation within a resonant birdcage MRI coil 64 MHz. The birdcage coil can be used to produce a circularly polarized magnetic field if it is excited with voltage waveforms that are 90° out of (wave) phase and applied at ports that are rotated 90° with respect to each other. The resonant frequency of the coil can be adjusted by changing the capacitance of elements located along each of the coil's rungs. The birdcage coil can be used to both transmit and receive RF energy into the body to excite MRI signals, or transmit them only, with reception being performed by surface coils. The presence of the body within the coil can affect the coil

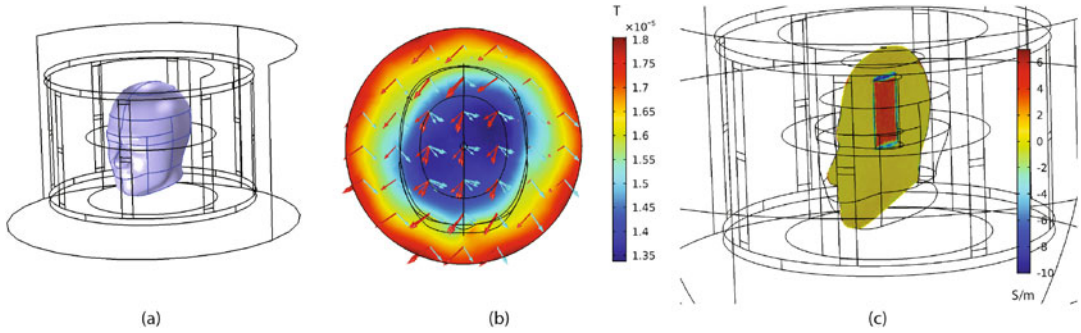

Fig. 2.14 Images from a model constructed using the COMSOL `mf` module of a birdcage coil at 64 MHz. Part (**a**) shows the model geometry, including the air box and coil rungs. (**b**) shows a cross section through the tuned coil showing the magnitudes and directions of the left- and right-polarized magnetic fields within the coil and its distortion by the presence of the head tissues. (**c**) shows the conductivity computed from the B^p phase data

resonance, and it is normally necessary to adjust the capacitors to improve the tuning after the subject or object to be imaged is in place. You can see some of the effect of the head tissue properties manifest in Fig. 2.14 where the vectors indicating the real or imaginary part of the magnetic flux density distribution are oriented differently with respect to each other compared to the surrounding air. The quantity used in reconstructing the electrical properties is the transmitted flux density $\mathbf{B}_1^+$. In the simplest case, the Laplacian of the measured transmit *phase* (φ^+) can be used to compute conductivity distributions. However, this phase cannot be measured directly in $\mathbf{B}_1$ images because it is combined with the receive phase φ^-. Therefore, in many approaches to EPT, the *transceive* phase approximation is used, wherein the transmit phase is approximated as half of the measured transceive phase $\varphi_0 = \varphi^+ + \varphi^-$. If it is assumed that the conductivity varies slowly, it is possible to calculate it directly via the approximation

$$\sigma(\mathbf{r}) \approx \frac{\nabla^2 \varphi^+(\mathbf{r})}{\mu_0 \omega}. \tag{2.66}$$

More details on EPT data acquisition, algorithms, and processing can be found in Chap. 8. We will use this equation to illustrate use of the finite element model in the remainder of this section.

As we noted above, in the example shown in Fig. 2.14, the head is specified with an overall relative permittivity of 40. Most of the head conductivity is 0.9 S/m, but there is a cylindrical inclusion that has a conductivity of 5 S/m. It is possible to calculate the conductivity distribution within the head directly from the simulated $\mathbf{B}^+$ phase, where $\mathbf{B}^+ = \mathbf{B}_x + i\mathbf{B}_y$. The plot in Fig. 2.14c shows the conductivity calculated according to (2.66). This involves first computing B^+ by defining a new variable within COMSOL, finding its phase, and then calculating the Laplacian. Because the full Maxwell equations are based on derivatives, special shape functions, known as curl shape functions, are used to solve these problems [6]. COMSOL does not make derivatives based on the solutions available, and if you tried to compute a derivative of an electromagnetic quantity (**E**, **D**, **B**, or **H**) within the COMSOL RF module, the answer will default to zero. In order to process the data further, it is necessary to interpolate the solution onto a more standard shape function (e.g., a quadratic tetrahedron) and base further calculations based on that. In the model shown in Fig. 2.14, it was necessary to define a new general PDE $a\mathbf{u} = \mathbf{f}$ and set $a = 1$ and **B** and then calculate the Laplacian based on **u** operations involving the COMSOL derivative operators $d(\cdot, x)$ or $d(\cdot, y)$. Note that the assumptions involved in (2.66) result in large discontinuities at the anomaly boundary. There

are a number of ways of avoiding this assumption, also discussed in Chap. 8.

Appendix 1: Formulation of the Functional for Laplace or Poisson Equations

Before application of any boundary conditions, the functional (denoted I) for a PDE $L\phi = f$, where L is linear self-adjoint and positive definite operator such as the Laplacian ∇^2, in a two-dimensional region R can be expressed as [2]

$$I[\phi] = \iint_R (\phi L\phi - 2f\phi)\, dxdy \tag{2.67}$$

If we assume general, Robin-type boundary conditions are applied on the boundary C, for example,

$$\frac{\partial \phi}{\partial \mathbf{n}} + \lambda(s)\phi = h(s). \tag{2.68}$$

where $\mathbf{n}$ denotes the boundary normal and the functions λ and h are parameterized using distance along the boundary s, the functional form becomes

$$I[\phi] = \iint_R (\phi L\phi - 2\phi f)\, dxdy - \int_C \left(\lambda(s)\phi^2 - 2\phi h(s)\right) ds \tag{2.69}$$

If the operator L is ∇^2, the full expression is

$$\begin{aligned} I[\phi] &= \iint_R (\phi L\phi - 2\phi f)\, dxdy - \int_C \left(\lambda(s)\phi^2 - 2\phi h(s)\right) ds \\ &= \iint_R \left(|\nabla\phi|^2 - 2\phi f\right) dxdy - \int_C \left(\lambda(s)\phi^2 - 2\phi h(s)\right) ds \\ &= \iint_R \left(\frac{\partial \phi}{\partial x}^2 + \frac{\partial \phi}{\partial y}^2 - 2\phi f\right) dxdy - \int_C \left(\lambda(s)\phi^2 - 2\phi h(s)\right) ds \end{aligned} \tag{2.70}$$

Formulation of the Functional for a Finite Element Mesh

We have that the overall solution for the problem, Φ, is (in 2D)

$$\Phi^e(x, y) = \sum_{e=1}^{E} \phi^e(x, y) = \sum_{e=1}^{E} \mathbf{N}^e \delta^e \tag{2.71}$$

where E is the total number of elements in the finite element mesh.

Recall that the solution vector (displacement vector) for the element δ^e is

$$\delta^e = \begin{bmatrix} \phi_A \\ \phi_B \\ \vdots \\ \phi_X \end{bmatrix} \tag{2.72}$$

where $\phi_A \cdots \phi_X$ are the values of the finite element solution at each node within the element.

Then, substituting (2.70) into the expression, we obtain

$$\begin{aligned} I[\Phi] &= \iint_R \left\{ \left(\frac{\partial}{\partial x}\sum_{e=1}^{E}\phi^e\right)^2 + \left(\frac{\partial}{\partial y}\sum_{e=1}^{E}\phi^e\right)^2 - 2\sum_{e=1}^{E}\phi^e f \right\} dxdy \\ &\quad + \int_C \left\{ \lambda(s)\left(\sum_{e=1}^{E}\phi^e\right)^2 - 2\sum_{e=1}^{E}\phi^e h(s) \right\} ds \\ &= \sum_{e=1}^{E} \iint_R \left\{ \left(\frac{\partial \phi^e}{\partial x}\right)^2 + \left(\frac{\partial \phi^e}{\partial y}\right)^2 - 2\phi^e f \right\} dxdy \\ &\quad + \sum_{e=1}^{E} \int_{C^e} \left\{ \lambda(s)(\phi^e)^2 - 2\phi^e h(s) \right\} ds \\ &= \sum_{e=1}^{E} I^e = I\left(\phi^1, \phi^2, \ldots, \phi^E\right) = I\left(\phi_1, \phi_2, \ldots, \phi_N\right) \end{aligned} \tag{2.73}$$

where N indicates the total number of nodes within the finite element mesh. The key point to take away from (2.73) is to note that the functional can be calculated for each individual element (line 2) and that the functional depends on the solution at the individual nodes, because functions within each element depend on nodal values, as in (2.72).

Minimizing the Functional

From (2.73), the functional depends only on the nodal values of the solution. To minimize the functional, it is then necessary to compute the derivative of the functional with respect to each

nodal value and determine where the derivative is zero. This gives rise to N equations that are solved simultaneously.

Consider the derivative of I with respect to the nodal value ϕ_i. This node may appear in more than one element, so the derivative is written as

$$\frac{\partial I}{\partial \phi_i} = \sum_{e=1}^{E} \frac{\partial I^e}{\partial \phi_i} \tag{2.74}$$

Now let's consider the derivative of I^e with respect to all the nodal values

$$\frac{\partial I^e}{\partial \Phi} = \left\{ \frac{\partial I^e}{\partial \phi_1}, \frac{\partial I^e}{\partial \phi_2}, \ldots, \frac{\partial I^e}{\partial \phi_N} \right\}. \tag{2.75}$$

The value of these derivatives will be 0 for nodes that are not in element e.

Now look at one non-zero entry in this vector, $\frac{\partial I^e}{\partial \phi_i}$. Expanding the derivative using (2.70), we find

$$\begin{aligned} \frac{\partial I^e}{\partial \phi_i} = &\iint_{R^e} \left\{ \frac{\partial}{\partial \phi_i} \left(\frac{\partial \phi^e}{\partial x} \right)^2 + \frac{\partial}{\partial \phi_i} \left(\frac{\partial \phi^e}{\partial y} \right)^2 - 2 \frac{\partial \phi^e}{\partial \phi_i} f \right\} dxdy \\ &+ \int_{C^e} \left\{ \lambda(s) \frac{\partial}{\partial \phi_i} \left(\phi^e \right)^2 - 2 \frac{\partial \phi^e}{\partial \phi_i} h(s) \right\} ds \end{aligned} \tag{2.76}$$

Note that the integral over the boundary C^e will only be non-zero if the element is on a boundary. Let us break up (2.76) even further and examine individual terms. The first term can be expanded using the definition of ϕ^e.

$$\frac{\partial}{\partial \phi_i} \left(\frac{\partial \phi^e}{\partial x} \right)^2 = 2 \frac{\partial \phi^e}{\partial x} \frac{\partial}{\partial \phi_i} \left(\frac{\partial \phi^e}{\partial x} \right) = 2 \frac{\partial \phi^e}{\partial x} \frac{\partial}{\partial x} \left(\frac{\partial \phi^e}{\partial \phi_i} \right). \tag{2.77}$$

Recall that, expanding (2.71)

$$\begin{aligned} \phi^e(x, y) = \mathbf{N}^e \delta^e &= \begin{bmatrix} \mathbf{N}_A^e & \mathbf{N}_B^e & \ldots & \mathbf{N}_X^e \end{bmatrix} \begin{bmatrix} \phi_A \\ \phi_B \\ \vdots \\ \phi_X \end{bmatrix} \\ &= \mathbf{N}_A^e \phi_A + \mathbf{N}_B^e \phi_B + \cdots + \mathbf{N}_A^X \phi_X. \end{aligned} \tag{2.78}$$

We see from this that

$$\frac{\partial \phi^e}{\partial \phi_i} = N_i^e, i \in A, B, \ldots, X \tag{2.79}$$

and using (2.78) and (2.79)

$$\begin{aligned} \frac{\partial}{\partial \phi_i} \left(\frac{\partial \phi^e}{\partial x} \right)^2 &= 2 \frac{\partial}{\partial x} \left(\mathbf{N}^e \delta^e \right) \frac{\partial N_i^e}{\partial x} \\ &= 2 \begin{bmatrix} \frac{\partial N_A^e}{\partial x} \frac{\partial N_i^e}{\partial x}, \ldots, \frac{\partial N_X^e}{\partial x} \frac{\partial N_i^e}{\partial x} \end{bmatrix} \begin{bmatrix} \phi_A \\ \vdots \\ \phi_X \end{bmatrix}. \end{aligned} \tag{2.80}$$

The final term on the first line term corresponds to N_i^e, and the term multiplied by $\lambda(s)$ is similarly expanded to be

$$\frac{\partial}{\partial \phi_i} \left(\phi^e \right)^2 = 2 \begin{bmatrix} N_i^e N_A^e & N_i^e N_B^e & \ldots & N_i^e N_X^e \end{bmatrix} \begin{bmatrix} \phi_A \\ \phi_B \\ \vdots \\ \phi_X \end{bmatrix} \tag{2.81}$$

Overall, then

$$\begin{aligned} \frac{\partial I^e}{\partial \phi_i} = &\iint_{R^e} \left[\left\{ \frac{\partial N_i^e}{\partial x} \frac{\partial N_A^e}{\partial x} + \frac{\partial N_i^e}{\partial y} \frac{\partial N_A^e}{\partial y} \right\} \cdots \right. \\ &\left. \left\{ \frac{\partial N_i^e}{\partial x} \frac{\partial N_X^e}{\partial x} + \frac{\partial N_i^e}{\partial y} \frac{\partial N_X^e}{\partial y} \right\} \right] \begin{bmatrix} \phi_A \\ \vdots \\ \phi_X \end{bmatrix} dxdy \\ &- 2 \iint_{R^e} f N_i^e dxdy \\ &+ 2 \int_{C^e} \lambda(s) \begin{bmatrix} N_i^e N_A^e & \ldots & N_i^e N_X^e \end{bmatrix} \begin{bmatrix} \phi_A \\ \vdots \\ \phi_X \end{bmatrix} ds \\ &- 2 \int_{C^e} h(s) N_i^e ds. \end{aligned} \tag{2.82}$$

The four terms in (2.82) can then be reexpressed in matrix form as

$$\frac{\partial I^e}{\partial \phi_i} = 2 \sum_{j \in e} k_{ij}^e \phi_j + 2 \sum_{j \in e} \bar{k}_{ij}^e - 2 f_i^e - 2 \bar{f}_i^e \tag{2.83}$$

where $i, j \in A, B \ldots, X$ and

$$
\begin{aligned}
k_{ij}^e &= \iint_{R^e} \left(\frac{\partial N_i^e}{\partial x} \frac{\partial N_j^e}{\partial x} + \frac{\partial N_i^e}{\partial y} \frac{\partial N_j^e}{\partial y} \right) dxdy \\
\bar{k}_{ij}^e &= \int_{C^e} \lambda(s) N_i^e N_j^e ds \\
f_i^e &= \iint_{R^e} f N_i^e dxdy \\
\bar{f}_i^e &= \int_{C^e} h(s) N_i^e ds.
\end{aligned}
\tag{2.84}
$$

Note that the matrices formed of k_{ij}^e and $\bar{k}_{ij}^e$ entries($\mathbf{k}^e$ and $\bar{\mathbf{k}}^e$) have dimension $X \times X$ where X is the number of nodes in each element and that the matrices formed by f_i and $\bar{f}_i$ entries ($\mathbf{f}^e$ and $\bar{\mathbf{f}}^e$)) are $X \times 1$.

Finally, requiring that $\frac{\partial I^e}{\partial \phi_i} = 0$ and rearranging the equations, we find that for each element

$$
\left[\mathbf{k}^e + \bar{\mathbf{k}}^e \right] \delta^e = \mathbf{f}^e + \bar{\mathbf{f}}^e. \tag{2.85}
$$

Assembly of all matrices for each element and matrix type are then combined to form the global stiffness matrix

$$
\mathbf{K\Delta} = \mathbf{F}. \tag{2.86}
$$

where the global displacement vector contains all of the nodal solutions.

Appendix 2: Extraction of Data from Finite Element Models

This chapter has detailed extensively how to simulate the results of electromagnetic measurements. However, before these results can be used in formulating reconstructions, or just to synthesize data to compare results, the simulated data has to be sampled at a resolution matching the experimental data. In this appendix, we will describe an approach that can be used to appropriately sample $\mathbf{J}$, $\mathbf{E}$, σ, or any other data defined on a model.

Partial Volume

First, consider the nature of the data recovered from an MR experiment. Reconstructed MR or MREIT images are specified in voxel (or pixel) array form. Within each slice, there may be NX voxels in one direction and NY in the other. Each voxel has dimensions $\Delta x \times \Delta y$ and fields of view (FOV) of $FOV_x = \Delta x \times x$ and $FOV_y = \Delta y \times y$. MR image volumes contain NZ slices, each slice having a thickness Δz. The volume of each voxel is $\Delta x \times \Delta y \times \Delta z$. Whatever value is reported as the representative magnitude or phase, or any other quantity derived from it, is necessarily an *average* of the quantities existing within the entire voxel region. Figure 2.15a shows a simple voxel layout and an individual voxel dimension.

Regardless of the voxel layout, it is inevitable that some voxels will include tissues from multiple tissue types. The voxel shown in Fig. 2.15b is an exaggerated example of this, with one voxel including gray matter, white matter, CSF, and bone. Any properties derived from this voxel will reflect this. The value recovered will not be representative of a point in the center of the voxel.

Finite Element Sampling

When retrieving data from a finite element model for use in reconstructions using MRI data, we must take care to sample from the model in a similar way to the way the MRI data were gathered. That is, to correctly compare modeled and imaged data, we must sample the model over many points and compute model output values as averages (or integrals) over each simulated voxel. Figure 2.16a again shows a voxel array, but now this voxel array must be overlaid on the finite element domains. Consider the voxel highlighted in blue. The mesh in Fig. 2.16b covers this voxel. It may be the case that mesh elements are in more than one of the voxels.

We now overlay a voxel sampling grid (Fig. 2.16c) over this part of the mesh. Recall that the finite element solution is recovered as

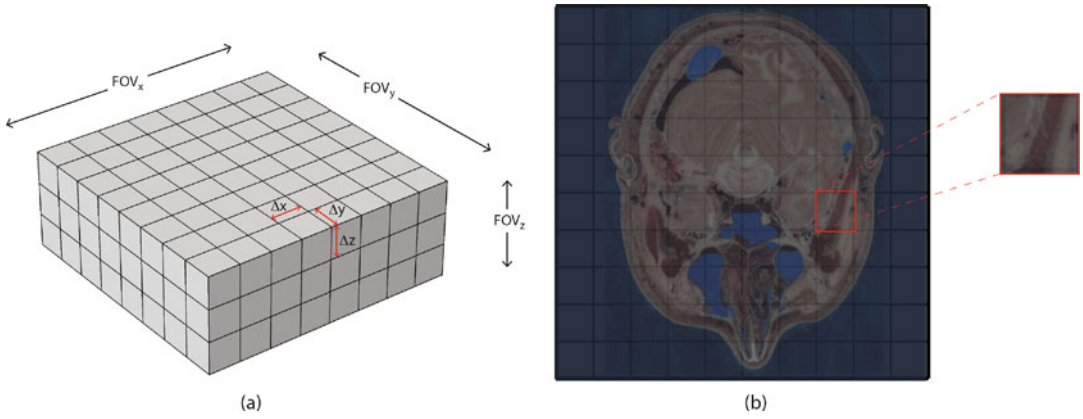

Fig. 2.15 Voxel layout and partial volumes. (**a**) shows an $8 \times 8 \times 3$ voxel array; the field of view (FOV) along x, y, and z directions; and the voxel dimensions Δx, Δy, and Δz. (**b**) illustrates partial volume concept with top view of grid overlaid on tissue structure

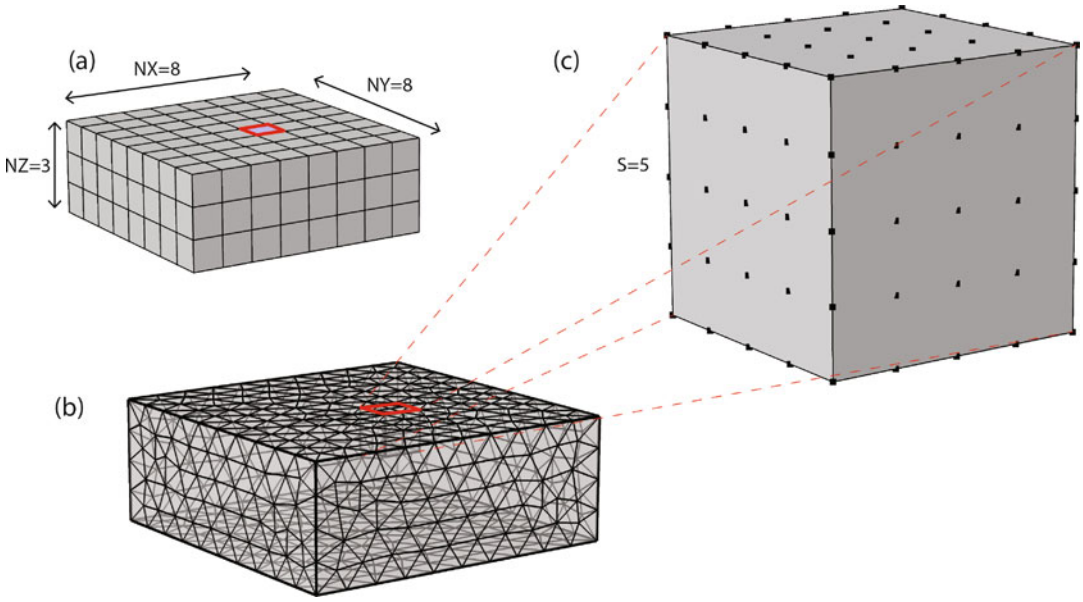

Fig. 2.16 Illustration of sampling finite element model data. (**a**) Representative $NX \times NY \times NZ$ voxel layout, showing individual voxel highlighted in red. (**b**) Finite element mesh over voxel region, and (**c**) sample grid with $S = 5$ defined over candidate voxel

the values at each of the mesh nodes within the domain. But we also know that if we nominate any point within the domain, locate the element containing this point, and then multiply this solution vector within the element by the shape function matrix for this element (see (2.13)), then it is possible to determine the interpolated solution there.

Consider the sampling grid shown in Fig. 2.16c. To calculate a representative value for a quantity over this voxel, we take the following steps:

1. Define the regular grid within each voxel.
2. Recover values at each value of the grid

(a) If the grid is regular, the values may simply be averaged to produce the representative value.
(b) If the grid is a free mesh, you must integrate the quantities over the mesh and divide by the voxel volume.

Example Code Using COMSOL

COMSOL provides means of sampling the solution at arbitrary points. These points can be nominated arbitrarily within the graphical user interface. Alternatively, using MATLAB and COMSOL together, it is possible to use the `mphinterp` command to extract the value of a model parameter at any point. Here is some example code that demonstrates how to perform the steps above. In this case, we define a fine regular grid with $S = 11$, giving 1331 points within each voxel. The sampled values are averaged over each voxel to produce the result.

```
% EXAMPLE CODE FOR SAMPLING FINITE ELEMENT
SOLUTION
% Code samples electric field components Ex
and Ey.
ex128=zeros(NX,NY,NSLICE); ey128=ex128;

fov_xy=8.96;
fov_z=NSLICE*5e-1;

halfwidth=fov_xy/2;
halfwidthz=fov_z/2;

deltaxy=fov_xy/NX; % assumes NX=NY
deltaz=fov_z/NSLICE;

%discretize each voxel to (S)*(S)*(S) GRID.
S SHOULD BE ODD AND >= 3
S=11;
inc=deltaxy/(S-1);
jinc=deltaxy/(S-1);
kinc=deltaz/(S-1);

% assumes no transverse (x,y) offset
[Xfine,Yfine]=meshgrid(-
halfwidth:iinc:halfwidth,-
halfwidth:iinc:halfwidth);
zlist=0:kinc:(NSLICE)*deltaz+OFFSETZ;

fov_z_new=max(zlist)-min(zlist);
sizefine=size(Xfine);

slicefine=size(zlist,2); % number of fine
slices
sizeall=[sizefine slicefine];
ex=zeros(sizeall); ey=ex; % define fine sam-
pling arrays

for fs=1:slicefine
mygrid = [Xfine(:), Yfine(:), ones(size(Xfine(:)))*
 zlist(fs)];
% use COMSOL command mphinterp
[d1, d2]=       mphinterp(model,'ec.Ex','ec.
Ey','coord',mygrid','recover','pprint');
ux(:,:,fs)  =  reshape(d1(:),  sizefine(1),
sizefine(2));
uy(:,:,fs)  =  reshape(d2(:),  sizefine(1),
sizefine(2));
end

NPOINTS=S**3;
HS=(S-1)/2;

for i=1:NX
for k=1:NSLICE
for j=1:NY
count=0;
mydUX=zeros(1,NPOINTS);
mydUY=zeros(1,NPOINTS);
% modify loop to sample points on arbitrary
grid
for ii=-HS:1:HS
for jj=-HS:1:HS
for kk=-HS:1:HS
count=count+1;
mydUX(count)=ux((i-1)*(S-1)+ii+HS+1,(j-
1)*(S-1)+jj+HS+1,(k-1)*(S-1)+kk+HS+1);
mydUY(count)=uy((i-1)*(S-1)+ii+HS+1,(j-
1)*(S-1)+jj+HS+1,(k-1)*(S-1)+kk+HS+1);
end
end
end
ux128(i,j,k)=mean(mydUX(:));
uy128(i,j,k)=mean(mydUY(:));
end
end
end
```

Acknowledgments RJS thanks Aprinda Indahlastari and Enock Boakye for their assistance in preparing material on segmentation and modeling methods used in this chapter.

References

1. A. Boyle, W.R.B. Lionheart, C. Gomez-Laberge, A. Adler, Evaluating deformation corrections in electrical impedance tomography, in *Proceedings of the 19th International Conference on Clinical Applications of Electrical Impedance Tomography*, ed. by R. Halter (2008), p. 4
2. P. Davies, *The Finite Element Method: A First Approach*, 2nd edn. (Academic Press, London, 2000)
3. Y. Huang, A. Datta, M. Bikson, L.C. Parra, Realistic volumetric-approach to simulate transcranial electric stimulation - ROAST - a fully automated open-source pipeline. J. Neural Eng. **16**, 056006 (2019)
4. A. Indahlastari, M. Chauhan, B. Schwartz, R.J. Sadleir, Changing head model extent affects finite element predictions of transcranial direct current stimulation distributions. J. Neural Eng. **13**, 066006 (2016)

5. A. Indahlastari, M. Chauhan, R.J. Sadleir, Benchmarking transcranial electrical stimulation finite element simulations: a comparison study. J. Neural Eng. **16**(2), 026019 (2019)
6. J.-M. Jin, *The Finite Element Method in Electromagnetics*, 3rd edn. (Wiley-IEEE Press, 2014)
7. M.K. Metwally, S.M. Han, T.S. Kim, The effect of tissue anisotropy on the radial and tangential components of the electric field in transcranial direct current stimulation. Med. Biol. Eng. Comput. **53**, 1085–1101 (2015)
8. J.D. Nielsen, K.H. Madsen, O. Puonti, H.R. Siebner, C. Bauer, C.G. Madsen, G.B. Saturnino, A. Thielscher, Automatic skull segmentation from mr images for realistic volume conductor models of the head: Assessment of the state of the art. NeuroImage **174**, 587–598 (2018)
9. W.H. Press, S.A. Teukolsky, W.T. Vetterling, B.P. Flannery, *Numerical Recipes in C* (Cambridge University Press, 1992)
10. M. Rullmann, A Anwander, M. Dannhauer, S.K. Warfield, F.H. Duffy, C.H. Wolters, EEG source analysis of epileptiform activity using a 1 mm anisotropic hexahedra finite element head model. NeuroImage **44**, 399–410 (2008)
11. R.J. Sadleir, A. Argibay, Modeling skull electrical properties. NeuroImage **35**(10), 1699–1712 (2007)
12. R.J. Sadleir, T.D. Vannorsdall, D.J. Schretlen, B. Gordon, Target optimization in transcranial direct current stimulation. Front. Psychiatry **3**, 90 (2012)
13. V.M. Spitzer, D.G Whitlock, *National Library of Medicine Atlas of the Visible Human Male: Reverse Engineering of the Human Body*, 1st edn. (Jones & Bartlett Learning, 1997)
14. A. Thielscher, A. Antunes, G.B Saturnino, Field modeling for transcranial magnetic stimulation: a useful tool to understand the physiological effects of TMS? in *Proc. Annu. Int. Conf. IEEE Eng. Med. Biol. Soc.* (2015), pp. 222–225

Magnetic Resonance Imaging Basics

3

Atul Singh Minhas and Ruth Oliver

Abstract

In this chapter, we will discuss the basic principles of signal generation and image formation in magnetic resonance imaging (MRI). We will start with a description of nuclear magnetic resonance (NMR) phenomenon and then gradually arrive at the mathematical expressions for MRI signal in spatial domain and k-space domain. Then we describe the image reconstruction methods typically used in MRI, the signal-to-noise ratio calculation methods in MRI, and common MR image formats. A key focus of the contents of this chapter is on the formation of phase images in MRI. We do not intend to provide a comprehensive overview of MRI. Instead, the contents are intended for readers interested in performing research in electromagnetic properties mapping using MRI. Nevertheless, considering the generality of the contents, any reader interested in developing a quick understanding of the physical and mathematical background of MRI can find this chapter helpful.

A. S. Minhas (✉) · R. Oliver
School of Engineering, Macquarie University, Wallumattagal Campus, Macquarie Park, NSW, Australia
e-mail: atul.minhas@mq.edu.au; ruth.oliver@mq.edu.au

3.1 Introduction

Magnetic resonance imaging (MRI) is playing an ever-growing role in modern life, through its widespread use as the most prominent medical imaging modality for high-quality soft tissue imaging. It has come a long way since Raymond Damadian performed the first full-body scan of a human being in 1977 [4]. While the credit of making the first MRI scanner goes to Raymond Damadian, his idea is not the one used in modern clinical MRI scanners. That credit goes to the American chemist, Paul C Lauterbur, and the British physicist, Sir Peter Mansfield, for their discoveries of using gradient magnetic fields to create MR images. Their discoveries are the foundation of MRI scanners used till today and earned them the 2003 Nobel Prize in Physiology and Medicine [4].

Multiple improvements have taken place over the past four decades in the hardware, software, and new applications of MRI. Bespoke designs are now available to cater to different settings such as clinical imaging centers for medical diagnosis, pre-clinical research centers for animal imaging, and research laboratories to image chemical or biological samples. The basics of MRI presented in this chapter are applicable for any of the these aforementioned settings.

R. Sadleir, A. S. Minhas (eds.), *Electrical Properties of Tissues*, Advances in Experimental Medicine and Biology 1380, https://doi.org/10.1007/978-3-031-03873-0_3

3.2 MRI Hardware

MRI hardware is a combination of multiple electrical and mechanical components mounted in an optimal manner to acquire superior-quality MR images. The locations of various components with respect to each other are illustrated in Fig. 3.1 for a cylindrical-shaped design of MRI system. Magnet is the outermost component of MRI. There are multiple electromagnetic coils used in MRI such as gradient coils, shim coils, and transmit/receive radiofrequency (RF) coils. In general, a coil is an electrical device consisting of multiple loops of wire that can either generate a magnetic field or detect an oscillating magnetic field through Faraday's principle of electromagnetic induction. Each of these hardware components is explained in detail in subsequent sections.

3.2.1 Magnet

The magnet in MRI scanner is responsible for the generation of uniform magnetic field. The strength of magnetic field is measured in Tesla (T) and field homogeneity in parts-per-million (ppm). MRI scanners are built with various types of magnets such as superconducting, electromagnetic, or permanent magnets depending on the strength of the required magnetic field. For example, clinical MRI scanners with field strength of 0.2 T use permanent magnets, but those with field strength $\geq$1.5 T use superconducting magnets. The most recent designs of superconducting magnets use technologies such as *zero helium boil-off* and *nitrogen-free*, which enable longer maintenance intervals.

While high-field (HF) MRI scanners are a desired choice for better image quality, their accessibility is limited due to the exponential increase in scanner's cost with increase in FS [20]. Therefore, the low-field (LF) MRI scanners of $\leq$1.5 T FS are still a preferred choice in urban and rural/remote areas of emerging and developing countries (EDC). MRI scanners with field strengths $\geq$7 T are typically referred to as "ultra-high-field (UHF)" MRI scanners.

The inner diameter (ID) of magnet controls the patient bore diameter of an MRI scanner. Diameter of spherical volume (DSV) is a spherically shaped volume where the homogeneity specifications are defined. For example, for Bruker 9.4 T pre-clinical MRI scanner (BioSpec 94/20), magnet specifications for homogeneity are $\pm$10 ppm in a 120 mm DSV. Likewise, for Siemens 3 T scanner (Magnetom Prisma), the magnet homogeneity specifications are 1.1 ppm in 500 mm DSV.

3.2.2 Gradient and Shim Coils

The gradient coils in MRI scanner are responsible for the generation of spatially varying magnetic fields. There are three gradient coils in MRI, one in each of the three directions, X, Y, and Z, and accordingly named as X-gradient coil, Y-gradient coil, and Z-gradient coil. Being electromagnetic

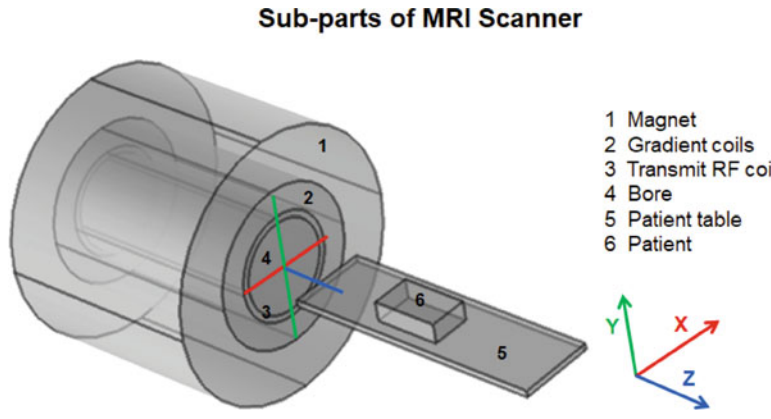

Fig. 3.1 Location of different hardware components used in MRI scanners

coils, they produce magnetic fields when electric current flows through them. Typical specifications for gradient coils are gradient strength (of the order of 45 mT/m) and slew rate (of the order of 200 T/m/s). Gradient coil designers aim to achieve these two specifications by minimizing the resistance and inductance of coils.

The shim coils produce second-order (or higher-order) magnetic fields and, as their name suggests, used to do shimming or correction of inhomogeneity in the magnetic field produced by magnet [18]. Typically, there are five shim coils in MRI for 1.5 T and 3 T MRI scanners, but higher magnetic field scanners can have more than five shim coils (typically along Z0, Z^3). The five shim coils produce second-order magnetic fields proportional to XY, X^2-Y^2, XZ, YZ, and Z^2 [10, 11]. Since shim coils produce second-order magnetic fields, their strengths are measured in mT/m^2.

Gradient and shim coils are typically made of stranded copper strips or copper plates arranged in a particular pattern around the coil surface. For a cylindrical coil surface, which is a typical structure in MRI scanners, the copper strips (or plates) are arranged around a cylinder. The patterns of copper strips (or plates) in X- and Y-gradient coils are of the same shape except that they are arranged orthogonal to each other. Likewise, the patterns of XZ and YZ shim coils are also orthogonal to each other. The patterns of copper strips (or plates) in Z-gradient coil and Z^2 shim coil are arranged as circular rings along the surface of the cylindrical structure. Multiple such rings are placed along $z-$direction and distanced optimally to achieve a desired gradient field strength [10, 11].

Most of the MRI scanners these days use self-shielded (or actively shielded) gradient coils. This means that there are two types of coils for each of the three gradient coils: primary and secondary coils. The secondary coil carries current opposite to the primary current and lies away from the isocenter ($(x, y, z) = (0, 0, 0)$) of MRI with the radius of secondary coil > radius of primary coil. The purpose of secondary coil is to cancel the primary coil's magnetic field outside the gradient coil surface (where other structures of magnet such as thermal shield and vacuum chamber lie). While the secondary coil aims to create the net magnetic field outside the gradient coil surface close to "zero," it also reduces the net magnetic field inside the bore of MRI scanner. Therefore, the number of turns used in primary coil is always higher than the number of turns used in secondary coil.

Mechanical Structure of Gradient Coil

The gradient and shim coils are located inside a cylindrical-shaped structure. This structure is typically made of epoxy to provide rigidity but doped with other materials to control its elasticity. The shim coils are located underneath the shield-gradient coils in the epoxy structure. This means that the radius of shield-gradient coils > radius of shim coils. Cooling pipes are embedded in epoxy, close to the locations of passive shim tokens, to dissipate the heat produced by gradient switching. The epoxy structure with gradient/shim coils and cooling pipes embedded inside it is collectively given a generic name of *gradient coil* as it is a standalone component of MRI. The *gradient coil* is mounted inside magnet using brackets, wedges, or air-filled balloons. The center of *gradient coil* must be aligned to the isocenter of MRI along $z-$direction. Care must be taken during mounting to avoid any misalignment in the orientation of *gradient coil* in azimuth direction; otherwise, this might lead to geometric distortions.

3.2.3 Radiofrequency Coils

There are two types of RF coils used in MRI: the transmit RF coils and the receive RF coils. As implied by their names, the transmit RF coil transmits RF magnetic field to the imaging object (such as the human body), and the receive RF coil detects the oscillating magnetic field emerging from within the imaging object. The goal of a transmit RF coil designer is to design the coil with

a highly homogeneous RF excitation field (B_1) across the entire volume covered. A receive RF coil designer aims to design the coil with better signal-to-noise ratio (SNR) of the received signal.

There are two options for placement of transmit and receive RF coils [7]. In the first case, transmit RF coil is located underneath the gradient coil and typically called as volume coil or body coil. The receive signal is detected by a separate receive coil located close to the imaging object. While a volume coil can receive the signal, its received signal is only used for calibration purposes. In the second case, the transmit and receive coils are designed as a single unit called transceive RF coil. The transceive RF coil is located in close proximity to the imaging object which increases the signal-to-noise ratio (SNR) of the received signal.

Many designs exist for receive RF coils [7]. For example, the surface coils used for spine imaging are located on the patient table, but those used for abdomen and cardiac imaging are flexible and placed on top of the abdomen and thorax. These days, parallel imaging has become a routine practice in MRI, and this is enabled by phase-array receive coils. These coils consist of small coil elements that are grouped together or fed into separate receive channels, and combining these large groups of smaller-sized coil elements enhances the overall SNR of the received signal. When surface coils and phase-array coils are used as receive coils, the body coil is used as transmit coil.

3.2.4 Spectrometer

Spectrometer in MRI refers to the hardware component which acts as an interface between the software present in the MRI console computer and the power amplifiers used in MRI. Spectrometer takes instructions about the shapes of gradient and transmit RF waveform from the MRI console computer and generates the corresponding voltage signals to be sent to the gradient and RF amplifiers. Spectrometer also records the data acquired by the receive RF coils and shares it with the computer running the reconstruction algorithms.

3.2.5 Power Amplifiers

Three different types of power amplifiers are used in MRI to drive the three hardware components: gradient coils, transmit RF coils, and shim coils. The designs of all these amplifiers must adhere to the IEC 60601-2-33 standards for the basic safety and essential performance of MRI equipment if the MRI equipment is intended for medical diagnosis.

A set of three high-power amplifiers independently drive each of the three channels of gradient coils. They take the voltage signals from spectrometer and amplify them to produce current signals as input to the gradient coils. The inductance of gradient coils govern the choice of gradient amplifier specifications. For example, the typical gradient amplifier specifications to achieve a gradient strength of 45 mT/m and slew rate of 200 T/m/s in a whole body MRI scanner are an operating current/voltage of 800 A/2000 V.

The power rating of shim amplifiers is much lower than the gradient amplifiers. For example, typical power ratings for a shim amplifier are 5–10 A and 15–30 V. There is an independent amplifier for each of the shim coils. The shim amplifiers are typically built in a single multichannel unit, with a dedicated channel (electronic circuit board) for each amplifier. Therefore, an important specification of a shim amplifier is the combined maximum output power (typically 650 W). The shim amplifiers should be robust against the induced voltage from gradients.

The RF amplifiers take the shape of transmit RF pulse from spectrometer and amplify it to drive the transmit RF coil. The operating frequency of RF amplifier is the same as the resonance frequency of the MRI scanner (e.g., 127.74 MHz for a 3 T MRI scanner). The output impedance of the transmit RF coil should be matched with the input impedance of the RF amplifier to enable the maximum power transfer from the power amplifier to the coil, by minimizing the reflected power from the coil.

This ensures that the greatest possible fraction of the power is delivered to the spins and enhances SNR. The matching/tuning of the transmit RF coil is a routine process before starting the imaging in ultra-high-field MRI scanners such as $\geq$4.7 T pre-clinical MRI scanners.

3.2.6 Preamplifier

The analog signals received by the receive RF coil are very low signals (of the order of mV) and therefore amplified using a preamplifier. This increases the amplitude of the received signal to a level that can be digitized. Since the transmit RF power is much higher than the received signal, the preamplifier of the receive RF coil has to be protected from damage. This is done by minimizing the coupling from the transmit coil to the receive coil using a detuning circuit [7].

3.3 Nuclear Magnetic Resonance

Nuclear magnetic resonance (NMR) is the fundamental phenomenon behind signal generation in MRI. As the name suggests, the *nuclear* in NMR relates to the nuclei of atoms in the imaging object, the *magnetic* is named for the external magnetic field which is applied to generate the desired behavior, and the *resonance* describes the emission of electromagnetic radiation due to interactions between the magnetic field of the nuclei and external magnetic field. Therefore, to understand the signal generation in MRI, we need to first understand the magnetic properties of nuclei and the NMR phenomenon.

History of NMR

Before describing the NMR phenomenon in detail, it is worth knowing about some of the seminal research works done in the field of NMR. The credit of describing and measuring the NMR phenomenon for the first time goes to Isidor Rabi who performed the NMR measurements in molecular beams in 1938 by extending the Stern-Gerlach experiment. Isidor Rabi won the 1944 Nobel Prize in Physics for this work. Later in 1946, Felix Bloch and Edward Mills Purcell expanded the NMR technique for use on liquids and solids, and they were awarded the 1952 Nobel Prize in Physics for this contribution. Felix Bloch also proposed the *Bloch equations* which determine the time evolution of nuclear magnetization.

3.3.1 Spin System of Hydrogen Nucleus

Spin System

The physical principles at nuclear level can be described by quantum mechanics as well as classical mechanics. *Spin* is an intrinsic property of elementary particles and defined in quantum mechanics. NMR discoveries have revealed that nuclei with odd atomic number (number of protons) and/or odd mass number, such as ^{1}H, ^{13}C, ^{19}F, and ^{31}P, possess an *angular momentum* $\overrightarrow{J}$, which is often called *spin*. In classical mechanics, *spin* is visualized as a physical rotation analogous to the rotation of a top about its axis. It is worth noting here that the concept of an elementary particle having a *spin* is the same as the concept of an electron having a mass. Just like an electron is indicated as a *point particle* occupying no volume of space at all, *spin* in reality is just a concept without any physical motion of nucleus.

An ensemble of spins of the same type is referred to as a *spin system* or *nuclear spin system*. For example, each of the nuclei ^{1}H, ^{13}C, ^{19}F, and ^{31}P represents a separate spin system. The signal in MRI comes from a voxel which is a finite volume with a

(continued)

large number of nuclei. It is assumed during a typical MRI scan that a voxel contains similar type of nuclei. Therefore, MRI signal from a voxel can be modeled as a signal of a spin system. Moreover, the MRI principles can often be described accurately using classical mechanics with the help of vectors.

Hydrogen Nucleus

Quantum theory tells us that atomic nuclei have specific energy levels due to the property known as spin quantum number, I. For example, the hydrogen nucleus, with its single unpaired proton, has a spin quantum number I of 1/2. The number of possible energy states N of a nucleus is given by the relationship:

$$N = 2I + 1 \tag{3.1}$$

For a single proton with $I = 1/2$, we have:

$$N = 2(1/2) + 1 = 2 \tag{3.2}$$

It follows that a hydrogen nucleus can have two energy states which we denote as $-1/2$ or $+1/2$. As per quantum mechanics, any particle with non-zero spin quantum number should have spin. As per classical mechanics, when a charged particle is moving, it creates a magnetic field. Therefore, the hydrogen protons with a net positive charge are spinning about their axis and creating a magnetic field (Fig. 3.2a). The direction of the magnetic field depends on the direction of spin of the proton and follows the "right-hand grip" convention. Note that the two energy states of hydrogen proton lead to two possibilities of the directions of magnetic field.

The magnetic field of a spin is somewhat like that from a bar magnet (Fig. 3.2b), with flux lines running from the south to the north pole (inside the magnet) and from the north pole to the south pole (outside the magnet), forming closed loops. As is the convention, the field direction of the bar magnet is taken to be outward from the north pole and in to the south pole.

(continued)

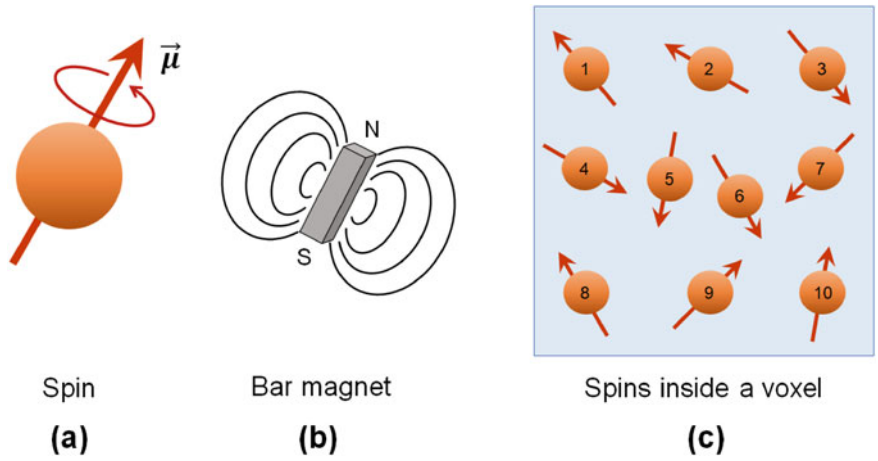

Fig. 3.2 (**a**) Magnetic field of a spin rotating in anti-clockwise direction. (**b**) Magnetic field of a bar magnet (which is analogous to a spin). (**c**) A spin system spins inside an MRI voxel

Table 3.1 Gyromagnetic ratios and spin quantum number for various nuclei

Nucleus	Spin quantum number (I)	Gyromagnetic ratio (MHz/T)
^{1}H	1/2	42.6
^{13}C	1/2	10.7
^{17}O	5/2	5.8
^{19}F	1/2	40.0
^{23}Na	3/2	11.3

It is worth noting that if there were an even number of protons in the nucleus, every proton would be paired, meaning that for every "spin-up" proton, there would be a "spin-down" proton and the magnetic fields would cancel out, leaving no net magnetic field. However, when a nucleus contains an odd number of protons, there exists an unpaired proton which points either up or down giving rise to a net magnetic field (Table 3.1).

3.3.2 Magnetic Moment and Magnetization

Magnetic Moment

The magnetic field of a nuclei is represented by a vector quantity $\vec{\mu}$ and known as *nuclear magnetic dipole moment* or *magnetic moment*. As per particle physics, the *angular momentum* of spin is related to the *magnetic moment* as:

$$\vec{\mu} = \gamma \vec{J} \tag{3.3}$$

where γ is a physical constant known as *gyromagnetic ratio*. *Gyromagnetic ratio* is sometimes also represented with the symbol $\gamma\!\!\!^{-}$ which is related to γ as:

$$\gamma\!\!\!^{-} = \frac{\gamma}{2\pi} \tag{3.4}$$

When expressed as γ, the unit of *gyromagnetic ratio* is rad/T/s, and when expressed as $\gamma\!\!\!^{-}$, the unit is MHz/T. Note that both γ and $\gamma\!\!\!^{-}$ are nucleus-dependent, which means that the NMR-active nuclei such as ^{1}H, ^{13}C, ^{19}F, and ^{31}P would each have its unique value of γ or $\gamma\!\!\!^{-}$. For ^{1}H, $\gamma\!\!\!^{-} = 42.58$ MHz/T, and $\gamma = 2.675 \times 10^{8}$ rad/T/s (Table 3.1).

Following on from previous discussion, a *magnetic moment* is found in any nucleus with an odd number of protons, neutrons, or both. As such, any element with these properties can be used for MR imaging, not just hydrogen. Other nuclei sometimes imaged in MRI are fluorine (^{19}F) and sodium (^{23}Na). However, hydrogen is the usual element under investigation due to its abundance in the human body—almost two thirds of the human body is water.

Magnetization

Consider a spin system containing N_{spins} number of spins. Considering that this is a linear system and applying systems engineering principles, the collective behavior of this spin system can be described using a magnetization vector $\vec{M}$ as:

$$\vec{M} = \sum_{n=1}^{N_{spins}} \vec{\mu}_n \tag{3.5}$$

where $\vec{\mu}_n$ is the magnetic moment of n^{th} spin. Note that since $\vec{\mu}_n$ is a vector, $\vec{M}$ is the vector sum of $\vec{\mu}_n$.

In the descriptions that follow, we will use a systems engineering approach where the imaging object acts as a linear system of magnetized nuclear spins. The system is excited by a

radiofrequency (RF) signal as input, which drives the system to a resonance state. When the system reverts to its original state, a signal is generated which can be detected using receive coils. We will discuss this further in the following sections.

3.3.3 Interaction of Magnetic Moments with External Magnetic Field

Consider a spin system of ^{1}H nuclei, where each spin has a magnetic moment $\overrightarrow{\mu}_n$. Since $\overrightarrow{\mu}_n$ is a vector, it has both magnitude and direction, the direction being along the axis of rotation (Fig. 3.2a). In the absence of any external magnetic field ($\mathbf{B} = 0$), the direction of $\overrightarrow{\mu}_n$ will be random due to the thermal random motion. Therefore, the combined effect of magnetic moments will cancel out, and the net magnetization will be zero ($\overrightarrow{M} = 0$). This is illustrated in Fig. 3.3a.

If an external magnetic field $\mathbf{B} = B_0\mathbf{a_z}$ is applied, this has the effect of causing the spins to behave like bar magnets and tend to align along the direction of the applied field ($\mathbf{a_z}$). However, unlike bar magnets, the $\overrightarrow{\mu}$ vector does not align exactly along the external magnetic field. Instead, it can only take one of a discrete set of orientations with respect to $\mathbf{a_z}$. As per quantum theory, the z-component of $\overrightarrow{\mu}$ becomes:

$$\mu_z = \gamma m_I \hbar \tag{3.6}$$

where m_I is the *magnetic quantum number* and $\hbar$ is Planck's constant. As mentioned earlier, since the number of energy states of a given nucleus is given by $2I + 1$, there are $2I + 1$ possible orientations of $\overrightarrow{\mu}$ with respect to the external magnetic field. Therefore, the ^{1}H nuclei with $I = 1/2$ has two possibilities for the orientation of the ^{1}H spins with respect to $\mathbf{a_z}$. The energy of spins in the $2I + 1$ states is given by:

$$E = -\overrightarrow{\mu} \cdot \overrightarrow{B} = -\mu_z B_0 = -\gamma m_I \hbar B_0 \tag{3.7}$$

For ^{1}H nuclei with $m_I = 1/2$ (spins pointing up), the energy becomes:

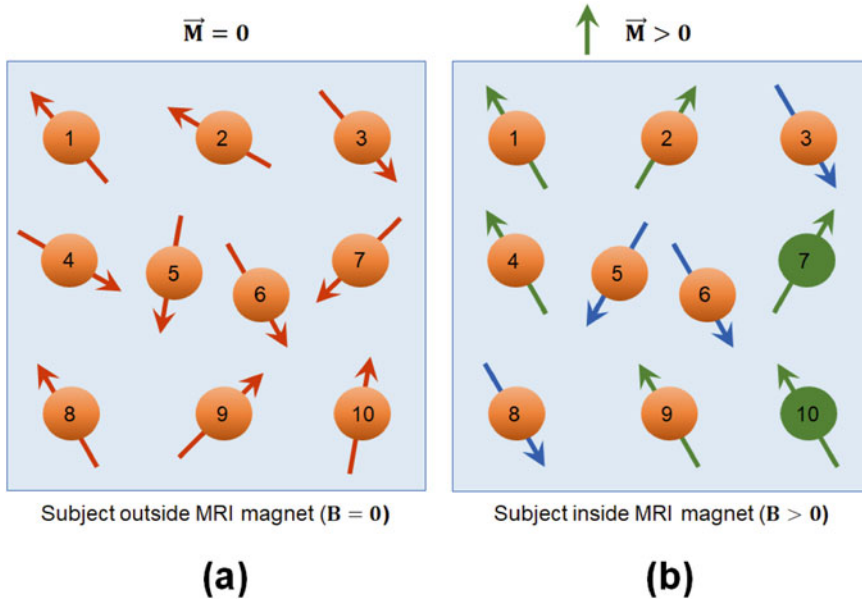

Fig. 3.3 Alignment of spins in a magnetic field (N_{spins}=10). (**a**) In the absence of an external magnetic field, the spins are randomly oriented, and there is no net magnetization. (**b**) With an applied field, the spins align with or against the field, with slightly more aligning with the field, leading to a net non-zero magnetization

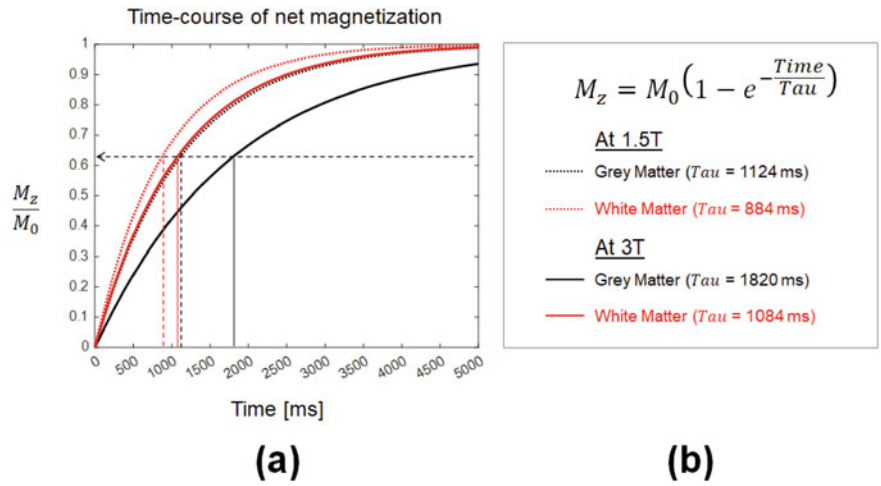

Fig. 3.4 (**a**) Time-course of exponentially increasing net magnetization for gray matter and white matter at 1.5 T and 3 T. (**b**) The time constants of the exponentially increasing net magnetization curves for gray matter and white matter at 1.5 T and 3 T. The values of time constants (the T1-relaxation times) were taken from [22]

$$E_{\uparrow} = -\frac{1}{2}\gamma\hbar B_0 \tag{3.8}$$

Likewise, for the ^{1}H nuclei with $m_I = -1/2$ (spins pointing down), the energy becomes:

$$E_{\downarrow} = \frac{1}{2}\gamma\hbar B_0 \tag{3.9}$$

Equations (3.8) and (3.9) indicate that spins pointing up have lower energy than the spins pointing down. Therefore, there are slightly more spins, about one in one million, aligning up (parallel) in the stable state with lower energy than aligning down (anti-parallel) with higher energy. As hydrogen is so plentiful in the human body, despite this tiny ratio, we are left with a net magnetization which is aligned along $\mathbf{a_z}$, the direction of applied magnetic field. This is illustrated in Fig. 3.3b where the total of $\vec{\mu}_{1,2,4,9}$ cancels the total of $\vec{\mu}_{3,5,6,8}$ leaving the net magnetic moments of $\vec{\mu}_7$ and $\vec{\mu}_{10}$ pointing up (parallel to $\mathbf{a_z}$).

Time-Course of Magnetization

Let us try to understand the time-course of development of magnetization since time $t = 0$ when the imaging object is outside MRI scanner. At $t = 0$, with no externally applied magnetic field, the spins are distributed randomly with no net magnetization. Upon application of $\mathbf{B}$ for $t > 0$, spins start aligning with the magnetic field, eventually resulting in a net non-zero magnetization along $\mathbf{a_z}$, the direction of $\mathbf{B}$. If we were to plot the net magnetization against time, it would look like the graph in Fig. 3.4a. This is an exponential growth curve with the time constant depending on the tissue that we are imaging and the strength of $\mathbf{B}$, i.e., B_0 (see Fig. 3.4b). The fact that the time constant is specific to the tissue being imaged is what contributes to the exquisite tissue contrast we are familiar with in MR imaging.

Spin Density

The net magnetization $\vec{M}$ is also dependent on a quantity known as *proton density* or *spin density N(H)*, which refers to the number of protons (or spins) present per unit volume in the tissue under investigation.

(continued)

Proton density differs for each tissue in the body and therefore contributes to the exquisite soft tissue contrast we are familiar with in MRI. However, it is important to note that it is not purely the *density* but the *number of mobile protons* aligning with the external field, which contribute to $\overrightarrow{M}$.

Free Precession (Larmor Precession)
Consider a spin rotating about its axis and interacting with an external magnetic field. In addition to the spin aligning along $\mathbf{a_z}$, the direction of **B**, it also undergoes *precession*. The *precession* refers to a rotation around the axis of the external magnetic field. The rate at which a spin precesses around the external magnetic field is described by the Larmor equation:

$$\omega_0 = \gamma B_0 \tag{3.10}$$

where ω is the angular precessional frequency of the spin (measured in rad/s), γ is the gyromagnetic ratio (measured in rad/s/T), and B_0 is the strength of the external magnetic field (measured in T). The Larmor or precessional frequency in MRI refers to the rate of precession of the magnetic moment of the spin around the external magnetic field. The direction of *precession* is determined using the *left-hand rule*. For example, when left thumb represents **B** and points along $\mathbf{a_z}$, the rotation of spins is clockwise (the direction of movement of fingers).

3.3.4 Susceptibility and Magnetic Materials

Magnetic susceptibility is a material property measuring the tendency of a material to become magnetized in an applied magnetic field. Therefore, it is the magnetic susceptibility of a material which controls the effective magnetic field **B** experienced by spins present in a material. Magnetic susceptibility is typically represented as χ and measured as:

$$\chi = \frac{\mathbf{M}}{\mathbf{H}} \tag{3.11}$$

where **M** is the magnetization normalized to a unit volume and **H** is the applied magnetic field intensity.

Measuring the magnetic susceptibility of a material gives us an indication of whether the material is going to be attracted into or repelled out of the applied magnetic field. This allows for a simple classification of materials into two categories: paramagnetic and diamagnetic. Paramagnetic materials with $\chi > 0$ align with the applied field and get attracted toward the regions of higher magnetic field. On the other hand, the diamagnetic materials with $\chi < 0$ align opposite to the applied field and therefore pushed away from the higher-field regions toward the regions of lower fields.

3.3.5 Radiofrequency Excitation

Previous section discussed how a net longitudinal magnetization $\overrightarrow{M_z}$ arises in an imaging object in the presence of an external magnetic field. By discussing about the "magnetic field of spin" and its "precession," we covered the *nuclear* and *magnetic* part of the NMR phenomenon. In this section, we discuss the effect of exciting an imaging object with RF magnetic field. This covers the *resonance* part of NMR phenomenon.

B_1 Field
The alignment of the longitudinal magnetization along the direction of external magnetic field does not create a measurable signal in NMR. The primary reason for

(continued)

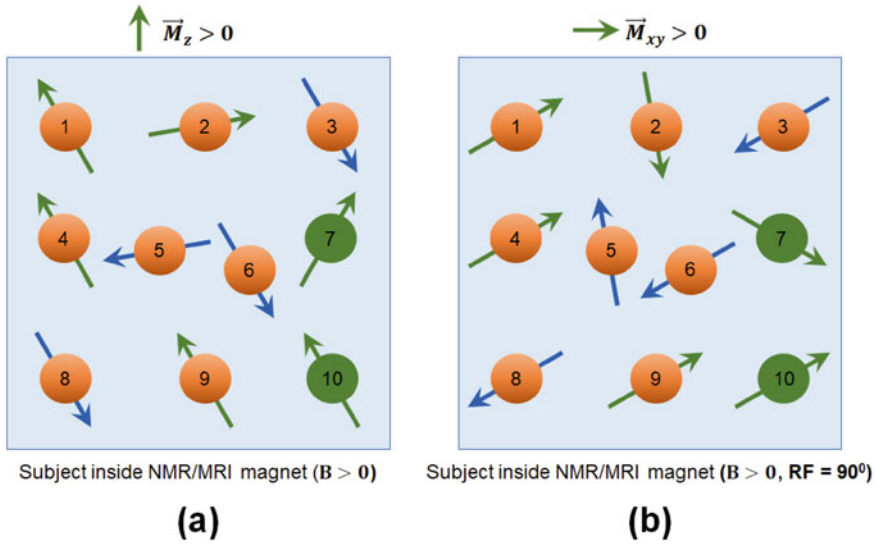

Fig. 3.5 Components of net magnetization before and after applying RF pulse to a spin system with N_{spins}=10. (**a**) $\vec{M}_z$ after the subject is placed inside NMR/MRI magnet. (**b**) $\vec{M}_{xy}$ after a 90° RF pulse is applied. The net magnetization due to the magnetic moment vectors $\vec{\mu}_{1,2,3,4,5,6,8,9}$ cancel out and the only magnetization contributing magnetic moments vectors are $\vec{\mu}_{7,10}$

this is because the design of receive RF coils can only permit receiving a signal in transverse plane. While individual spins do have a transverse component of $\vec{\mu}_n$, the combined transverse component of a *spin system* is "zero" due to randomly distributed directions of the transverse component. This means that $\vec{M}_z \neq 0$ but $\vec{M}_{xy} = 0$ after placing an imaging object inside NMR/MRI scanner. This is illustrated in Fig. 3.5a.

To create a signal in transverse plane, the random directions of the transverse components of spins should be re-oriented to prevent cancellation of the $\vec{M}_{xy}$ signal. *Resonance* in NMR/MRI refers to the establishment of a phase coherence which enables the spins in a spin system to start precessing in synchronization with each other, leading to the development of a non-zero $\vec{M}_{xy}$ component. *Resonance* is achieved by exciting a spin system with an RF magnetic field of a particular frequency. This RF magnetic field is called $\mathbf{B_1}$ field in NMR/MRI and delivered to an imaging object in the form of RF pulses of short duration. The development of a non-zero $\vec{M}_{xy}$ component after RF pulse is illustrated in Fig. 3.5b.

Resonance Condition

When an RF pulse of energy $E_{rf} = \Delta E = E_{\downarrow} - E_{\uparrow}$ is received by spins, they move from their low-energy state ($E_{\uparrow}$) to their excited sate ($E_{\downarrow}$), creating a *resonance condition*. Since $E_{rf} = \hbar\omega_{rf}$ and $\Delta E = \gamma\hbar B_0$, the frequency of this RF pulse is given by:

$$\hbar\omega_{rf} = \gamma\hbar B_0 \implies \omega_{rf} = \gamma B_0 = \omega_0 \tag{3.12}$$

This implies that the *resonance condition* in NMR/MRI occurs when spins are excited by an RF pulse of the same frequency as that of the Larmor frequency of spins.

Bloch Equations

The changes in magnetization during the RF pulse are governed by the *Bloch equations*. These equations are based on classical mechanics and described as:

$$\frac{d\vec{M}}{dt} = \gamma \vec{M} \times \mathbf{B} = \gamma \begin{bmatrix} (M_y B_z - M_z B_y)\mathbf{a_x} \\ +(M_z B_x - M_x B_z)\mathbf{a_y} \\ +(M_x B_y - M_y B_x)\mathbf{a_z} \end{bmatrix} \tag{3.13}$$

Here, the x-, y-, and z-components of magnetization vector $\vec{M}$ and the total external magnetic field $\mathbf{B}$ are given by $\vec{M} = [M_x\mathbf{a_x}, M_y\mathbf{a_y}, M_z\mathbf{a_z}]$ and $\mathbf{B} = [B_x\mathbf{a_x}, B_y\mathbf{a_y}, B_z\mathbf{a_z}]$. Recall that the total external magnetic field is composed of the static magnetic field $\mathbf{B_0}$ which points along z-direction and the RF magnetic field $\mathbf{B_1}$ which points orthogonal to the z-direction. Considering a circularly polarized RF pulse in x-direction, the total external magnetic field becomes:

$$B_x = B_1 cos\omega t$$

$$B_y = B_1 sin\omega t$$

$$B_z = B_0$$

Interaction of the Magnetization Vector with $\mathbf{B_1}$ Field

The detailed derivation of mathematical expressions governing the interaction between $\vec{M}$ and $\mathbf{B_1}$ are out of the scope of this book. We strongly encourage readers to look at alternate resources such as [13] to make themselves familiar with the rotating frame of reference and derivations of the time-dependent behavior of magnetization vector in the rotating frame. Here, we just briefly discuss the mechanisms behind flipping of $\vec{M}_z$ from z-direction to x-y plane, leading to the generation of $\vec{M}_{xy}$.

According to the *Bloch equation*, the time variation of the magnetization is directly proportional to the *curl* between the magnetization $\vec{M}$ vector and the external magnetic field. Therefore, if RF pulse is transmitted along the x-axis, the time variation of the magnetization will not occur along the x-axis, but will have components along the y- and z-axis. This indicates that the net magnetization vector $\vec{M}$ will precess in y-z plane, which is orthogonal to the x-axis. We can therefore say that the on-resonance condition leads to the precession of spins about the x-axis, which is the direction of delivery of RF pulse. The frequency of precession is given by $\omega_1 = \gamma B_1$.

In summary, prior to the application of RF pulse, the spins were precessing about the z-axis and were out of phase with one another, resulting in no net $\vec{M}_{xy}$. On being exposed to the $\mathbf{B_1}$ field emanating from the RF pulse, spins begin to precess about the x-axis and start aligning along this axis, thereby creating phase coherence. This is the origin of $\vec{M}_{xy}$. As the phase coherence grows, so does the net $\vec{M}_{xy}$. The magnitude of $\mathbf{B_1}$ field (B_1) is much weaker than B_0, somewhere in the order of 50mT compared to 1.5 T or 3 T on modern clinical scanners. It follows that $B_1 \ll B_0 \implies \omega_1 \ll \omega_0$, indicating that ω_1 can be ignored and the precession frequency of spins could still be considered as ω_0. Since the protons precess around the z- and x-axis at the same time, this results in the "flipping" of M_z from the z-axis into the x-y plane with a spiral motion.

Flip Angle

Let us denote the angle between the z-axis and $\vec{M}$ as α. This angle is called *flip angle* and controls the movement of $\vec{M}$ from z-axis onto the x-y plane. *Flip angle* is given

(continued)

by:

$$\alpha = \int_0^{\tau_{rf}} \omega_1(t)dt = \int_0^{\tau_{rf}} \gamma B_1(t)dt$$
$$= \gamma \int_0^{\tau_{rf}} B_1(t)dt \qquad (3.14)$$

where $B_1(t)$ is the envelope (or shape) of RF pulse and τ_{rf} is its duration. As an example, when RF pulse is of rectangular shape, $B_1(t) = B_1$, and the *flip angle* becomes:

$$\alpha = \omega_1 \tau_{rf} = \gamma B_1 \tau_{rf} \qquad (3.15)$$

Equations (3.14) and (3.15) indicate that the *flip angle* depends on the area under the B_1 envelope and the duration of this envelope. Note that the *flip angle* for two different RF shapes would be the same as long as the area under their time curves remains the same. In actual NMR/MRI scanning, *flip angle* and RF pulse duration are chosen by the user, and B_1 amplitude (or RF power) is calculated using Eq. (3.14).

3.3.6 Relaxation

After the delivery of RF pulse to an imaging object, its spins get excited. However, since this is an unstable state, they start returning to their normal state as soon as the delivery of RF pulse is stopped. The return of spins to their normal state from the excited state is called *relaxation*. The process of *relaxation* is characterized by two types of times, the *transverse relaxation time* and the *longitudinal relaxation time*. It is worth noting here that while the RF energy is absorbed by individual spins, the *relaxation times* are average quantities measured for a spin system. Therefore, these two times are the unique properties of tissues and characterize different species/tissues in NMR/MRI. In this section, we elaborate on these two times.

Longitudinal Relaxation Time, T_1

The *longitudinal relaxation time*, also referred to as T_1 time, is the time spanned by the M_z in recovering to 63% of the value it had before the delivery of RF pulse. We can note from Fig. 3.6a that for a 3 T MRI, the T_1 of gray matter and white matter in the human brain are 1820 ms and 1084 ms, respectively. We can also note from Fig. 3.6a that M_z is growing exponentially with a time constant of T_1 until it reaches a limit, which we denote as M_0. Considering this, the T_1 relaxation curve can be represented as:

$$M_z = M_0(1 - e^{-t/T_1}) \qquad (3.16)$$

The T_1 value of tissues varies with B_0. Reducing B_0 shortens the T_1 of tissues indicating that the T_1-induced contrast among tissues will deteriorate at lower B_0.

Transverse Relaxation Time, T_2 and T_2^*

After the RF pulse is stopped, the M_z begins to recover, and M_{xy} starts decaying. The *transverse relaxation time*, also referred to as T_2 time, is the time after which M_{xy} falls to 37% of the value it had attained after the delivery of RF pulse. As illustrated in Fig. 3.6b, M_{xy} is an exponentially decaying curve with a time constant T_2. Denoting the peak value before the beginning of decay as $M_{xy_{max}}$, the T_2 relaxation curve can be represented as:

$$M_{xy} = M_{xy_{max}} e^{-t/T_2} \qquad (3.17)$$

It is important to understand that the recovery of the longitudinal magnetization along the z-axis and the decay of the magnetization in the x-y plane are occurring at different rates. While it might seem intuitive that the rate of decay in the x-y plane

(continued)

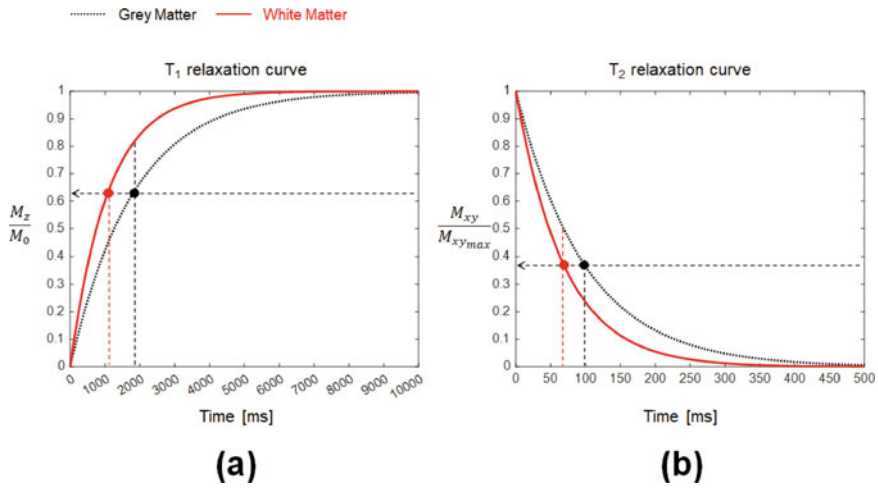

Fig. 3.6 (**a**) T_1 and (**b**) T_2 relaxation curves for gray matter and white matter at 3 T. The T_1 values for gray matter and white matter were taken as 1820 ms and 1084 ms, respectively [22]. The T_2 values for gray matter and white matter were taken as 99 ms and 69 ms, respectively [22]. Note that the time points corresponding to the 63% value of M_z/M_0 in (**a**) indicate the T_1 values of the two tissues. Likewise, the time points corresponding to the 37% values of $M_{xy}/M_{xy_{max}}$ in (**b**) indicate the T_2 values of the two tissues

would be matched by growth in the z-axis, the change in magnetizations is not a simple exponential process. T_2 decay actually occurs about five times more rapidly than T_1 recovery, and this is due to the "loss of phase coherence," also called *dephasing*

One of the major mechanisms behind this *dephasing* is the spin-spin interaction because of which the transverse relaxation is also called spin-spin relaxation. The spin-spin interaction refers to the transfer of energy from an excited spin to a spin in neutral state. This is possible when the spins involved in energy exchange are belonging to the same spin system and lie in close proximity to each other. The spins satisfying this condition will be oscillating with the same frequency ω_0 and will have phase coherence as long as the external magnetic field remains B_0. However, the inter-molecular and intra-molecular interactions (vibrations or rotations) cause transient fluctuations in B_0, leading to the loss of phase coherence over time.

When the B_0 field is inhomogeneous, different spins of a spin system experience different B_0 field leading to different ω_0 for the spins. In this case, the *dephasing* of spins is much quicker than T_2, and the relaxation time is denoted as T_2^*. Multiple sources can contribute to field inhomogeneity because of which the T_2^* can be represented as:

$$\frac{1}{T_2^*} = \frac{1}{T_2} + \frac{1}{T_2^{\Delta B}} + \frac{1}{T_2^{\Delta B_{susceptibility}}} + \frac{1}{T_2^{\Delta B_{gradients}}} + others \quad (3.18)$$

Here, $T_2^{\Delta B}$, $T_2^{\Delta B_{susceptibility}}$, and $T_2^{\Delta B_{gradients}}$ are the time constants induced due to B_0 inhomogeneity, magnetic susceptibility, and gradients, respectively. Note that the T_2 in Eq. (3.17) should be replaced with T_2^* when the B_0 field is inhomogeneous. Also note that the $T_2^{\Delta B_{gradients}}$ term in Eq. (3.18)

(continued)

can be compensated by properly designing the gradient shapes in MRI. Moreover, the $T_2^{\Delta B}$ term in Eq. (3.18) can be compensated either by using a 180° RF pulse (see Sect. 3.3.8) or by correcting for the inhomogeneity using higher-order shim coils.

3.3.7 Bloch Equations in General Form with T_1 and T_2

As discussed earlier, the changes in magnetization during the RF pulse are governed by the *Bloch equations*. A general form of these equations includes the effect of T_1 and T_2 relaxation times on the magnetization. Equation (3.13) can then be modified as:

$$\frac{dM_x}{dt} = \gamma(M_y B_0 + M_z B_1 sin\omega t) - \frac{M_x}{T_2}$$

$$\frac{dM_y}{dt} = \gamma(M_x B_1 cos\omega t - M_x B_0) - \frac{M_y}{T_2}$$

$$\frac{dM_z}{dt} = \gamma(M_x B_1 sin\omega t + M_y B_1 cos\omega t) - \frac{M_z - M_0}{T_1}$$

If we assume that immediately after the RF pulse is switched off, B1 = 0, we can solve:

$$M_x(t) = (M_x(0)cos\omega_0 t + M_y(0)sin\omega_0 t).e^{\frac{-t}{T_2}}$$

$$M_y(t) = (M_y(0)cos\omega_0 t - M_x(0)sin\omega_0 t).e^{\frac{-t}{T_2}}$$

$$M_z(t) = M_z(0)e^{\frac{-t}{T_1}} + M_0[1 - e^{\frac{-t}{T_1}}]$$

Furthermore, for a system initially in equilibrium and a 90° RF pulse applied along the x-axis, $M_x(0) = M_z(0) = 0$ and $M_y(0) = M_0$, which implies:

$$M_x(t) = (M_0 sin\omega_0 t).e^{\frac{-t}{T_2}}$$

$$M_y(t) = (M_0 cos\omega_0 t).e^{\frac{-t}{T_2}}$$

$$M_z(t) = M_0(1 - e^{\frac{-t}{T_1}})$$

These relationships inform us that the magnetizations in the x- and y-directions oscillate at the Larmor frequency, decaying with time constant T_2, while the magnetization in the z-direction grows with time constant T_1, from zero to M0.

3.3.8 Signal Generation in NMR

FID Signal

As discussed in Sect. 3.3.5, if RF pulse is transmitted to an imaging object along $x - direction$, the spin magnetization flips to y-direction and then starts precessing around z-direction in x-y plane. We can split the spin magnetization into two components: transverse magnetization (M_{xy}) and longitudinal magnetization (M_z). After the RF pulse is stopped, the M_{xy} component starts dephasing in x-y plane, and the M_z component starts recovering along z-direction. If we place a RF coil in a plane orthogonal to the z-direction, the exponentially decaying and oscillating M_{xy} magnetization will induce current in the coil. The induced current will create an exponentially decaying and oscillating signal called a free induction decay (FID) signal in MRI. The FID signal requires demodulation with ω_0 to recover the exponentially decaying signal.

Refocusing RF Pulse and Spin Echo

The FID signal reduces to 37% of its peak value after time T_2. Therefore, we should aim to receive this signal way before T_2 to achieve higher SNR. Recall that although T_2 is a characteristic of each tissue, the time constant of decaying FID signal is T_2^*, and not T_2, due to multiple sources of field inhomogeneity (see Eq. (3.18)). A 180° RF pulse, called *refocusing RF pulse*, is applied after the 90° RF pulse to recover the lost

(continued)

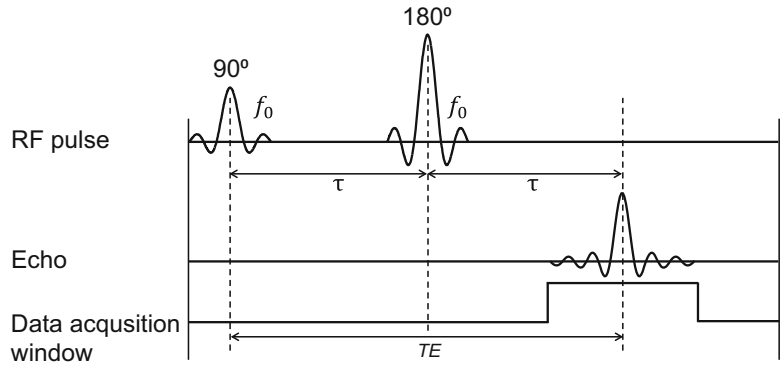

Fig. 3.7 Generation of *spin echo* by applying 180° RF pulse of the same frequency f_0 as that of the 90° RF pulse. Data acquisition window is time synchronized with the time duration of echo

coherence in spin phases. As its name indicates, the *refocusing RF pulse* refocuses the transverse component of magnetization. The mechanism behind this is that the 180° RF pulse reverses the phase of spins. The phase reversal leads to the arrival of phase coherence after a time equal to the time between 90° and 180°. The onset of phase coherence leads to a signal called *echo* in NMR/MRI. The time instant at which echo appears is called *echo time (TE)*. A typical 90–180 RF experiment leading to the generation of a *spin echo* is shown in Fig. 3.7. Note that a *spin echo* appears at $TE = 2\tau$, where τ is the time after which a 180° RF pulse is applied.

3.4 Magnetic Resonance Imaging

Section 3.3 described the physical principles of NMR and generation of FID signal in spin echo. The idea of using spatially varying magnetic fields (or gradient fields) to change the proton frequency as a function of position along the direction of the gradient was a remarkable discovery that helped in transforming the NMR field into the field of MRI. This discovery earned the 2003 Nobel Prize in Physiology and Medicine to Paul Lauterbur and Sir Peter Mansfield. In this section, we will describe how an image is formed by MRI scanners in both k-space and spatial domain using a combination of multiple sequences of RF and gradient pulses, called "pulse sequence" in MRI. Figure 3.15 shows the complete pulse sequence diagram of spin echo pulse sequence.

3.4.1 Initial Condition Inside an MRI Scanner

Consider an MRI scanner with its main magnetic field $\mathbf{B} = B_0\mathbf{a_z}$. Initially, when an imaging object is outside MRI scanner, the spin phases are aligned in random directions. This is illustrated in Fig. 3.8a. When we place an object inside MRI scanner, the magnetic moment of protons (spin magnetization) inside the object aligns along $\mathbf{a_z}$, as illustrated in Fig. 3.8b, and starts precessing around $B_0\mathbf{a_z}$. The Larmor or precessional frequency is proportional to the strength of $\mathbf{B}$ and depends on the environment in which protons are located. If protons are located in water environment such as muscle, the precessional frequency $f_w = \frac{\gamma}{2\pi}B_0$, where γ is the gyromagnetic ratio of protons. Likewise, if protons are placed in other environment such as fatty tissue, the precessional frequency $f_f = \frac{\gamma}{2\pi}(B_0 + \delta B_0)$, where δB_0 is the variation of magnetic field due to the electronic shielding of the protons in fatty tissue.

3.4.2 Application of Magnetic Field Gradients

In MRI, the constant magnetic field $B_0\mathbf{a_z}$ inside the bore of magnet is spatially varied through the

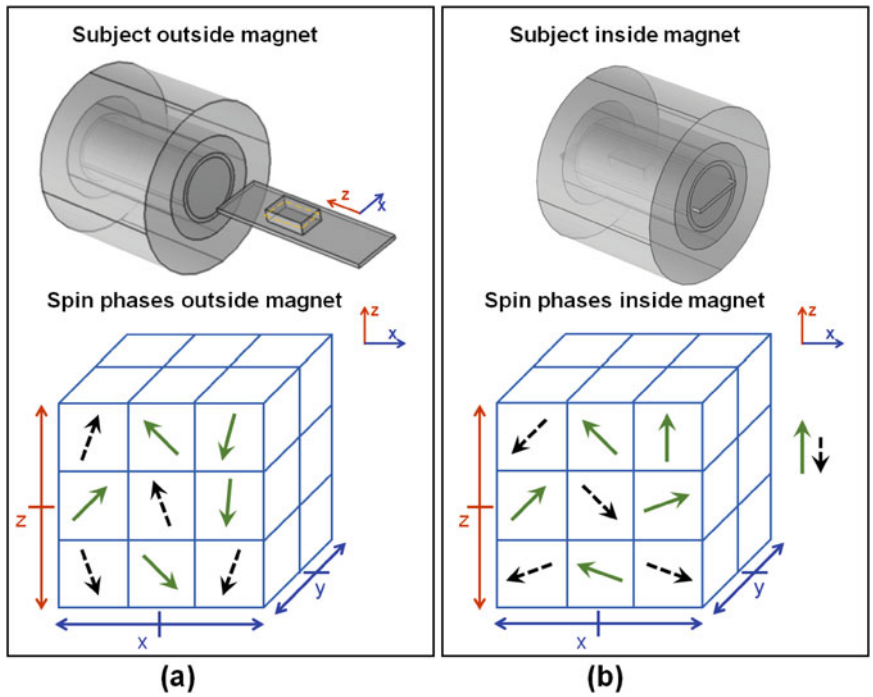

Fig. 3.8 Spin phases when subject is placed (**a**) outside and (**b**) inside an MRI scanner. The green colored (solid lines) and black colored (dashed lines) indicate two groups of spins. In each of these groups, the net magnetization is "zero" in (**a**) when spins are outside the magnet. When the subject is placed inside magnet in (**b**), then the group of spins with green color (solid lines) attain a net magnetization along $z-$direction, the direction of main magnetic field. However, the group with black color (dashed lines) attain their net magnetization opposite and with slightly less magnitude than the other group. Therefore, the net magnetization of spins is along $\mathbf{a_z}$

application of gradient magnetic fields independently in three directions: x, y, and z. This makes the total magnetic field B linearly dependent on the location (x, y, z) inside the magnet and can be expressed in terms of the gradient field strength G_x, G_y, and G_z as:

$$B(x, y, z) = B_0 + G_x x + G_y y + G_z z$$

Gradient fields are applied for a short period of time during the data acquisition cycle and referred to as gradient pulses. There are three such gradient pulses: slice selection, phase encoding, and frequency encoding. A combination of these pulses creates images in MRI. The slice selection gradient is responsible for the selection of an imaging slice in two-dimensional MRI or imaging volume in three-dimensional MRI. The phase-encoding gradient is responsible for the creation of extra phase in the spins present in the imaging plane or volume. The frequency-encoding gradient is responsible for the creation of difference in frequency in the spins lying in an imaging plane or volume. For imaging of axial slices in two-dimensional MRI, these gradients are applied along z-, y-, and x-direction for slice selection, phase encoding, and frequency encoding, respectively. These gradients are explained in detail in subsequent sections considering that axial slices are acquired. Note that if slices are acquired in sagittal or coronal planes, then the directions for slice selection, phase-encoding, and frequency-encoding gradient would change.

Slice Selection Gradient

When slice selection gradient $\mathbf{G_z}$ is turned on in z-direction, the magnetic field becomes $(B_0+G_z z)\mathbf{a_z}$. This variation of mag-

(continued)

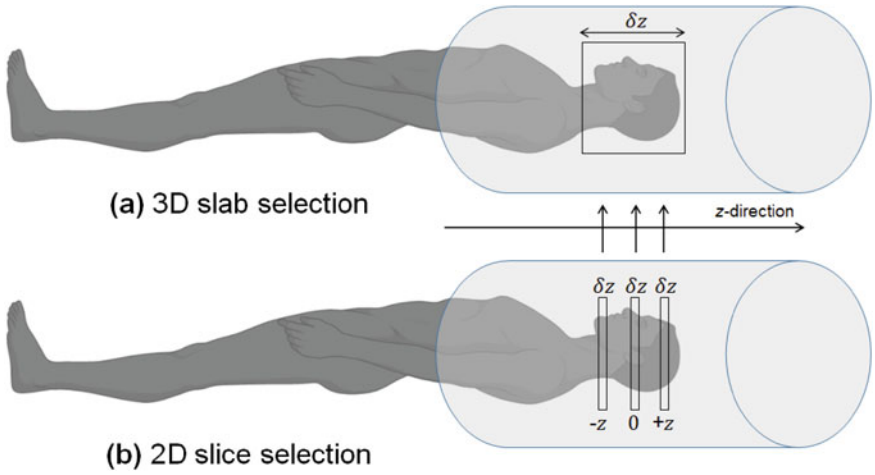

Fig. 3.9 (**a**) Slab and (**b**) slice selection process in three- and two-dimensional MRI, respectively. In slab selection, a thick 3D volume is selected, and in slice selection, a thin 2D slice is selected

netic field as a function of z-direction leads to a change in the precession frequency of protons along z-direction which is given by:

$$f(z) = f_0 + \gamma G_z z \tag{3.19}$$

where f_0 is the center frequency (or frequency without any z-gradient). In a two-dimensional (2D) data acquisition, a small section (typically called a "slice") of the imaging object is selected, and in a three-dimensional (3D) data acquisition, a larger section (typically called a "slab") is selected. The process of slice and slab selection is illustrated in Fig. 3.9. The excitation RF pulse (see Fig. 3.10a) is time synchronized with the slice selection gradient. Therefore, only the protons lying in the selected slice (or slab) get excited. The excitation RF pulse is frequency-selective, which means that it has certain frequency and bandwidth. The frequency of excitation RF pulse is chosen as per the location of slice (or slab) using Eq. (3.19). Typically, the bandwidth of excitation RF pulse (BW_{ss}) is fixed in a given pulse sequence program, which enables the user to change the slice thickness by varying the amplitude of slice selection gradient inside the pulse program. The required slice selection gradient (G_z) in a pulse program is calculated from the following equation:

$$G_z = \frac{BW_{ss}}{\gamma \Delta z}, \qquad \because BW_{ss} = \gamma G_z \Delta z \tag{3.20}$$

Phase-Encoding Gradient

When phase-encoding gradient $\mathbf{G_y}$ is turned on in the y-direction, the magnetic field becomes $(B_0 + G_y y)\mathbf{a_z}$. This variation of magnetic field along y-direction leads to a change in the precession frequency of protons which is given by:

$$f(y) = f_0 + \gamma G_y y \tag{3.21}$$

The evolution of spin phase and frequency under the influence of phase-encoding gradient is illustrated in Fig. 3.11. The phase-encoding gradient is applied for a fixed duration τ. Therefore, a constant phase $\theta(y)$

(continued)

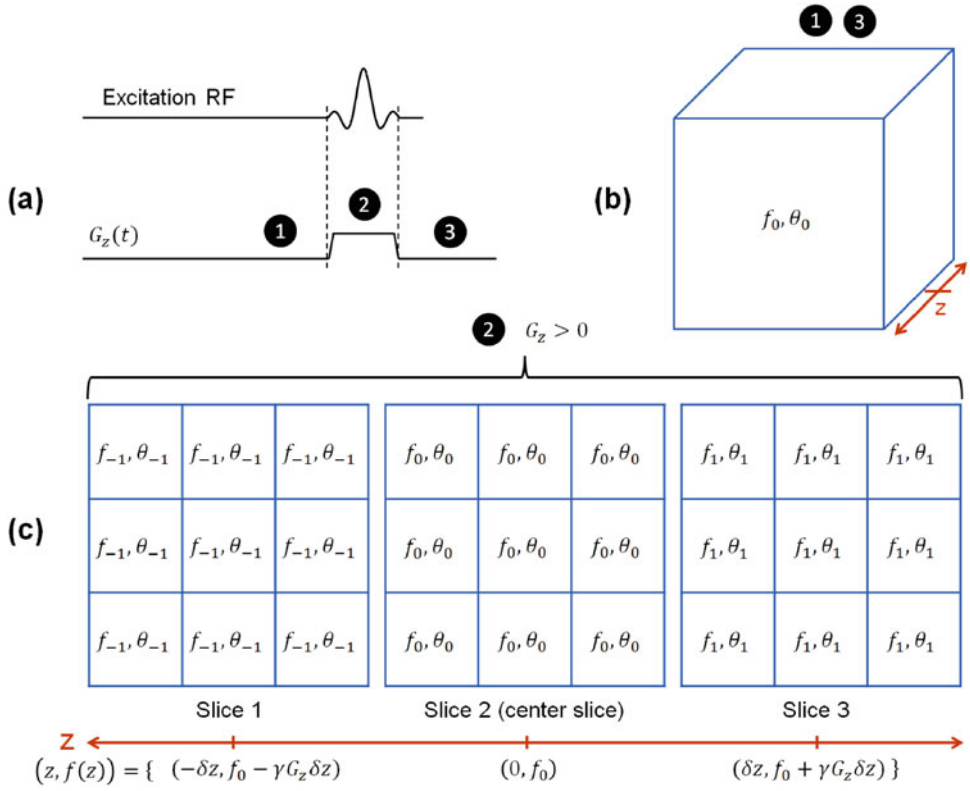

Fig. 3.10 Effect of slice selection gradient on spin phases. (**a**) Gradient pulse applied along $z-$direction in synchronization with a slice-selective RF pulse. (**b**) The frequency f_0 and phase θ_0 of spins at the time instants ❶and ❸before and after applying the slice selection gradient, respectively. (**c**) The frequency and phase of spins for three slices at the time instant ❷when a positive gradient is applied. Note that the frequency and phase of slice at z=0 remain the same as that without gradient because the gradient-induced change in magnetic field B_0 is equal to zero (see Eq. (3.19))

is introduced to the precessing protons as a function of y and can be expressed as:

$$\begin{aligned}\theta(y) &= 2\pi \int_0^{\tau} f(y)dt \\ &= 2\pi f_0 \int_0^{\tau} dt + 2\pi\gamma \int_0^{\tau} G_y y dt \\ &= 2\pi\tau(f_0 + \gamma G_y y)\end{aligned} \tag{3.22}$$

Frequency-Encoding Gradient

When the frequency-encoding gradient $\mathbf{G_x}$ is turned on in the x-direction, the magnetic field becomes $(B_0 + G_x x)\mathbf{a_z}$. Varying the magnetic field along x-direction leads to a change in the precession frequency of protons along the x-direction, which is given by:

$$f(x) = f_0 + \gamma G_x x \tag{3.23}$$

(continued)

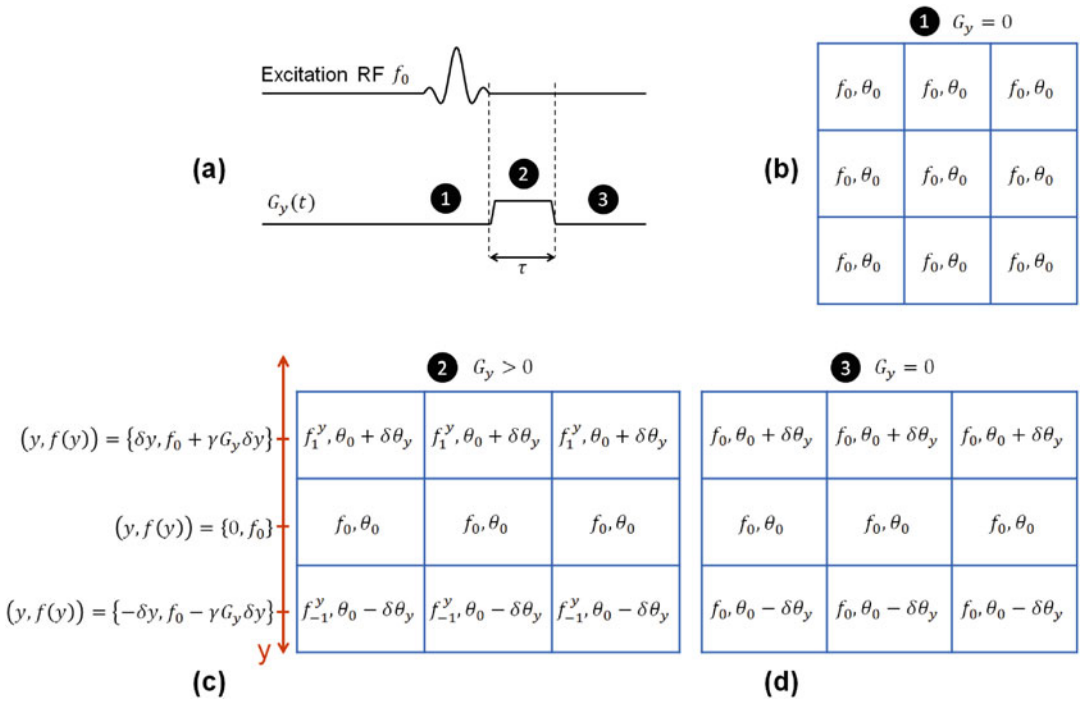

Fig. 3.11 Effect of phase-encoding gradient on spin phases located within a 3×3 grid of voxels. (**a**) Gradient pulse applied along $y-$direction after the end of an RF pulse of frequency f_0. (**b**) The frequency f_0 and phase θ_0 of spins at the time instant ❶before applying the phase-encoding gradient, assuming that center slice with spin frequency f_0 was selected by slice selection gradient. (**c**) The frequency and phase of spins at the time instant ❷when a positive gradient is applied. Note the change in frequency and phase along the $y-$direction. (**d**) The frequency and phase of spins at the time instant ❸when the gradient returns to zero. Note that the frequency is now the same for spins in all the voxels but they have accumulated a phase due to the $y-$gradient

The evolution of spin phase and frequency under the influence of frequency-encoding gradient is illustrated in Fig. 3.12. The frequency-encoding gradient is bipolar with the area (A) of negative gradient being half of the area (2A) of the positive gradient. Moving along the time from t_2 to t_4, the phase induced by the negative gradient starts getting cancelled by the phase due to the positive gradient. When the area (A) of negative gradient balances the half of the area (2A) of positive gradient at t_3, the phase of all the spins becomes θ_0, which is the same phase as that of the spins at the time instant ❶. Note that it is just the phase of spins which varies along t_2 to t_4; the distribution of spin procession frequencies remains the same along t_2 to t_4. An illustration of this phenomenon is presented in Fig. 3.12e using a 3×3 grid where phases vary with time but frequencies do not.

The sampling duration of one data sample within a data acquisition window is typically called dwell time Δt. Considering that N_x data samples are acquired within this data acquisition window, its duration is given by:

$$Data\_Acquisition\_Window = N_x \times \Delta t \tag{3.24}$$

(continued)

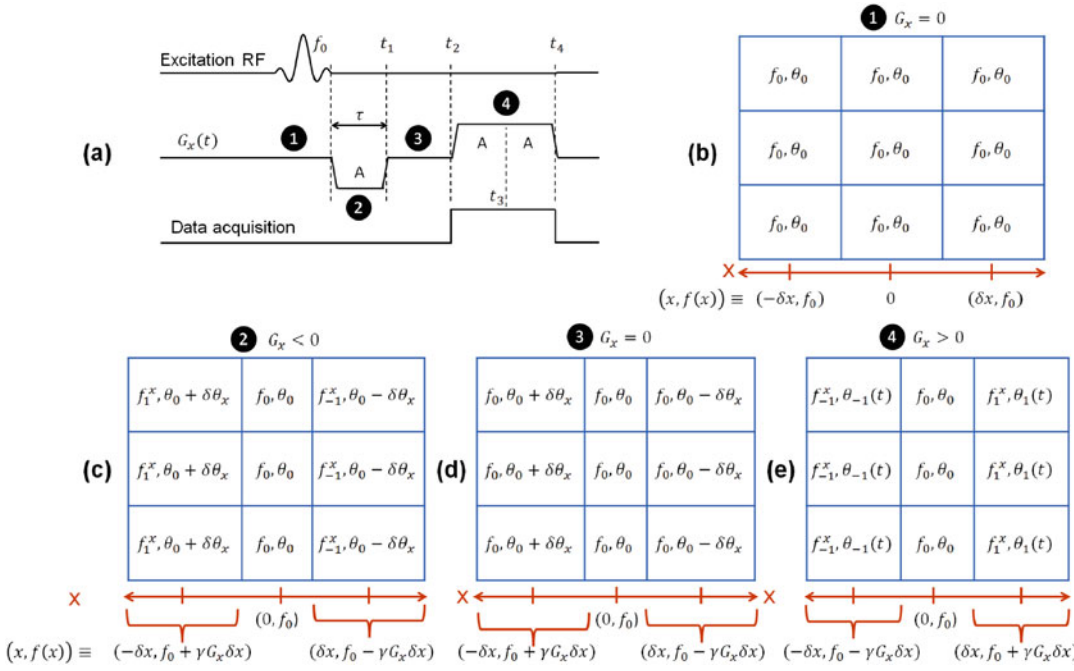

Fig. 3.12 Effect of frequency-encoding gradient on spin phases located within a 3 × 3 grid of voxels. (**a**) Bipolar gradient pulse applied along $x-$direction after the end of an RF pulse of frequency f_0 and the data acquisition window. (**b**) The frequency f_0 and phase θ_0 of spins at the time instant ❶before applying the frequency-encoding gradient, assuming that center slice with spin frequency f_0 is selected by the slice selection gradient. (**c**)–(**d**) The frequency and phase of spins at the time instants ❷and ❸when negative and zero gradients are applied, respectively. Note that the frequency and phase change along the $x-$direction at the time instant ❷but the frequency reverses back to f_0 when gradient returns to zero at ❸. However, the phase at the time instant ❸stays the same as that at ❷in the absence of any gradient. (**e**) The frequency and phase of spins at the time instant ❹when the positive gradient is applied. Note the variation of phase with respect to time at the time instant ❹

The time span ❹in Fig. 3.12 is also the duration when the data acquisition takes place in MRI. Therefore, different data samples acquired during the time span ❹have different phases depending on the difference in the areas between the positive and negative gradients. This leads to a change in the signal amplitude along the time span ❹with the signal peaking at t_3.

3.4.3 K-Space in MRI

The signal acquired in MRI during data acquisition window is in Fourier domain, also called k-space. The k-space image is not something many of us are familiar with as radiologists do not use it for diagnosis of abnormalities. However, it is the starting point for reconstruction of the most familiar spatial domain image which displays the structure of body tissues and typically used for diagnostic purposes. It is very important to understand how k-space data is formed in an MRI scanner to develop new MRI methods for novel MRI applications. While a brief description is provided in this section, we strongly recommend that readers should make themselves familiar with the Fourier domain and Fourier transform to gain a better understanding of the k-space in MRI.

Fourier Analysis and K-Space

Fourier theory tells us that any signal or waveform can be decomposed into a series

(continued)

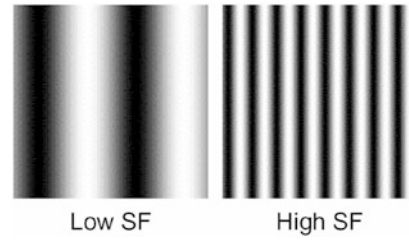

Fig. 3.13 Low and high spatial frequencies

of components at different frequencies and amplitudes. Such a representation is known as a spectrum in the frequency domain. As an analogy, consider the case of an acoustic signal such as a song. This is a 1D waveform in the time domain. When decomposing this song into its constituent components, we *Fourier transform (FT)* this signal to create a spectrum in the frequency domain, where we have a peak at each frequency contained in the song, with the amplitude of the peak reflecting the "loudness" of that frequency. An image is simply a 2D signal in the spatial domain, and k-space is the 2D FT of the anatomical image we are hoping to create. Note that MRI k-space signals are sometimes acquired in 3D, in which case 3D FT represents the series of concatenated 3D image slices acquired in MRI.

Spatial Frequency

The MRI k-space is a 2D/3D matrix containing spatial frequency information about the slice/slab we are imaging. Spatial frequency can be a difficult concept when first encountered, as frequencies are normally encountered in time domain rather than image domain. Let us consider two test images, as shown in Fig. 3.13, to better understand this concept. We can notice that there are alternating light and dark bands in the two images, with the narrower bands occurring more *frequently* than the wider bands in the same area. A spatial frequency is a periodic variation in image brightness, which can be measured in cycles per unit distance. The higher spatial frequencies correspond to the finer detail in a given image, and the lower spatial frequencies correspond to the uniform regions in the given image.

Spatial Encoding to Generate K-Space

As described in Sect. 3.4.2, spatial encoding is accomplished in MRI through the use of gradient coils to impose spatially varying magnetic fields. Considering only 2D imaging in axial plane, we have G_x and G_y gradients for the frequency- and phase-encoding directions. Referring to Sect. 3.4.2 again, we can notice that each voxel in our resultant image contains protons which have a distinct frequency and phase. Each time a frequency-encoding step is performed after phase encoding, we get a signal for each row of our data space. Each phase shift fills a different row in k-space. The ordering of filling the k-space rows could be arbitrary, so it is important to realize that the center of k-space does not represent the center of the spatial domain (which most of us are familiar with).

Looping in K-Space

K-space is created by a unique combination of multiple RF and gradient pulses, played in a certain order over a fixed period of time. This fixed time period is repeated

(continued)

in loops to fill the k-space, which gives it a unique name of repetition time (TR). The spin echo pulse sequence in Fig. 3.15 shows that the phase-encoding gradient varies from one TR to another by stepping from a negative value, through zero, to an equal positive value. Thus, each row of k-space experiences a different magnitude of phase-encoding gradient, which affects the magnitude of the received signal. The reason for this is that the phase-encoding gradient introduces additional dephasing to that caused by spin-spin interactions and B_0 inhomogeneity. When the gradient is at its maximum, we have maximum dephasing of spins. Therefore, the largest gradient used for phase encoding produces the lowest magnitude of signal. The highest signal is observed when the phase-encoding gradient is zero. This signal is placed at the center of k-space. Accordingly, the outer rows of k-space are filled with signal acquired with the strongest gradients, producing the least signal.

Properties of K-Space

The center of k-space contains the maximum signal. Additionally, each signal has maximum amplitude in the center column as this corresponds to the center of each echo, with more peripheral columns referring to more peripheral parts of the echo, either toward the maximum signal or away from it. This means that both the center row and center column contain maximum amplitude and therefore the highest signal-to-noise ratio. Multiple images of k-space are shown in Fig. 3.14. Note the high intensity in the center and what may be described as a series of concentric rings alternating in high and low intensities, but with a distinct decrease in intensity from the

(continued)

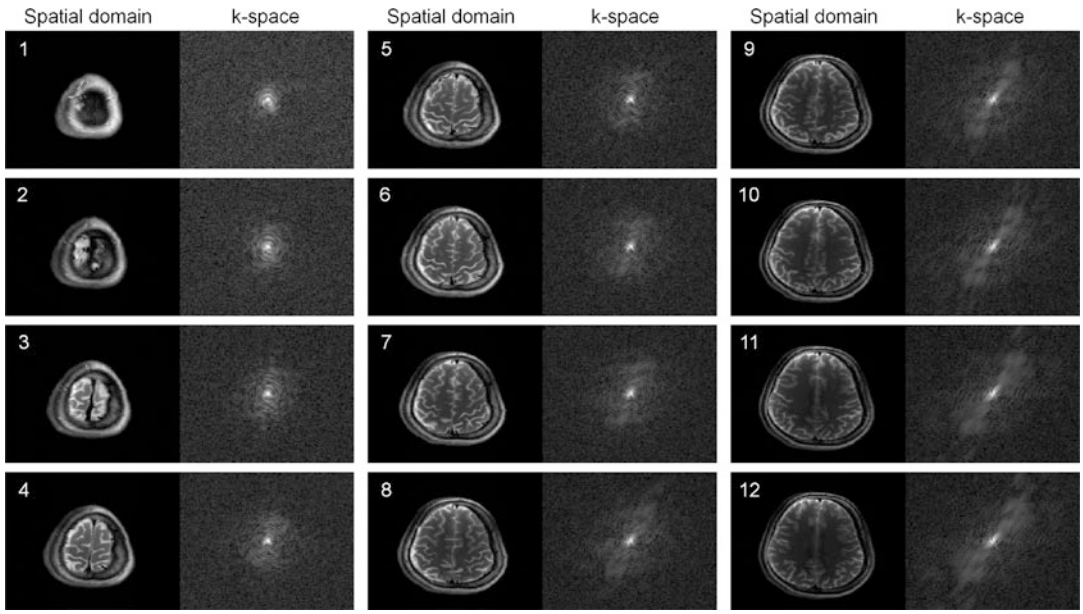

Fig. 3.14 Twelve consecutive MRI slices acquired from a healthy adult human brain with a slice thickness of 2 mm and a slice gap of 2 mm. Only the magnitude images of the spatial domain and the k-space domain are shown. The k-space images are shown after applying $|S(k_x, k_y)|^{0.4}$ filter

center to the edge of k-space. Also note that these concentric rings are more prominent in images where the spatial domain image is primarily uniform such as in images 1–4. As the contrast (or detailed structures) start appearing in images (from 5 to 12), the k-space intensities start becoming higher in the off-center regions as well.

Although on first thought it may seem appealing to construct an image from the high SNR center of k-space and neglect the periphery, if we were to do so, we would lose the fine detail in the final reconstructed image. This is because the periphery of k-space contains the high spatial frequencies which upon transform to the image domain produce clarity and fine structures such as boundaries. It is important to realize that all points in the k-space contribute to the entire image with lesser or greater SNR depending on their distance from the center. However, there is no direct relationship between the center of k-space and the center of the reconstructed image, and accordingly, the edges of k-space do not correspond to the image edges.

3.4.4 Mathematical Expression of MRI K-Space Signal

The raw k-space MRI data is acquired either in two dimensions (x-y plane) or in three dimensions (x-y-z plane). Let us understand the mathematical model of representing this two- and three-dimensional signal k-space signal. After slice selection (see Fig. 3.10), the combination of phase- and frequency-encoding gradients creates a phase- and frequency-dependent encoding of spin-ensemble present in a given voxel (see Figs. 3.11 and 3.12). The corresponding k-space signal acquired during the data acquisition window is then given by a summation of the signal from all the voxels present in the selected slice:

$$S(k_x) = \int M(x, y) e^{i\delta(x,y)} e^{-i(xk_x + \delta y k_y)} dx \tag{3.25}$$

Here, $M(x, y)$ is the proton-, T_1-, and T_2-dependent signal from a voxel located at (x, y), and $\delta(x, y)$ is the systematic phase artifact at (x, y). The k_x and k_y are given by $k_x = \int \gamma G_x t$ and $k_y = \int \gamma G_y t$. Note that Eq. (3.25) represents only one k-space line acquired at $y = \delta y$. Since phase-encoding gradient is incremented in a loop during the acquisition of multiple lines in k-space, the 2D k-space signal can be represented mathematically as:

$$S(k_x, k_y) = \int\int M(x, y) e^{i\delta(x,y)} e^{-i(xk_x + yk_y)} dx dy \tag{3.26}$$

In 3D data acquisition, there is one additional phase increment along the slice selection direction. This makes the signal in 3D k-space as:

$$S(k_x, k_y, k_z) = \iiint M(x, y, z) e^{i\delta(x,y,z)} e^{-i(xk_x + yk_y + zk_z)} dx dy dz \tag{3.27}$$

3.4.5 Discrete K-Space

The mathematical models of 2D and 3D k-space signals presented in Sect. 3.4.4 are continuous domain signals. However, the k-space data acquired by MRI scanners is in discrete domain. Considering 2D k-space data acquisition, Eq. (3.26) can be represented in discrete domain as:

$$S(k_x^m, k_y^n) = \sum_{m=1}^{N_x} \sum_{n=1}^{N_y} M(m\Delta x, n\Delta y) \times e^{i\delta(m\Delta x, n\Delta y)} e^{-i(m\Delta x k_x^m + n\Delta y k_y^n)} \Delta x \Delta y \tag{3.28}$$

Here, $k_x^m = \gamma G_x m \Delta t$, and $k_y^n = \gamma n \Delta G_y \tau$. Note that the G_x term in k_x^m corresponds to the gradient applied at the time instant ❹ in Fig. 3.12 and Δt is the dwell time. Additionally, ΔG_y is the increment, and τ is the duration of phase-encoding gradient. Note that since k_x^m and k_y^n in Eq. (3.28) are only the mth and nth voxels in k-space, the full k-space must be filled by acquiring data spanning from $m = 1$ to N_x and $n = 1$ to N_y.

3.4.6 Pulse Sequences in MRI

Pulse sequence is a generic name given to a combination of RF and gradient pulses. Many pulse sequences are used in MRI; some are generic, and others are named based on the kind of contrast they create. Generic MRI pulse sequences include spin echo and gradient echo or their multi-echo versions such as multi-spin-multi-echo (MSME) and multi-gradient-multi-echo (MGRE). Other common pulse sequences include fast spin echo (FSE) and echo planar imaging (EPI) for T_2-weighted imaging and the diffusion-weighted imaging (DWI) or diffusion-tensor imaging (DTI) pulse sequences to image diffusion of water molecules in an imaging object. Chapter 5 describes various pulse sequences used for MREIT and MR current density imaging (sometimes also referred by MRCDI). Chapter 8 describes the pulse sequence widely used for MREPT.

MRI Data Acquisition Steps

A typical spin echo pulse sequence used to acquire two-dimensional k-space data, as represented in Eq. (3.26), is shown in Fig. 3.15. Let us review this sequence in detail to better understand the MRI data acquisition steps. The order of events in this sequence are listed below:

1. Apply a 90° RF pulse using a suitable slice selection gradient, G_z.
2. Apply a 180° RF pulse, and after time TE, receive an echo.
3. During this time, apply the frequency-encoding gradient G_x (also called read-out gradient).

(continued)

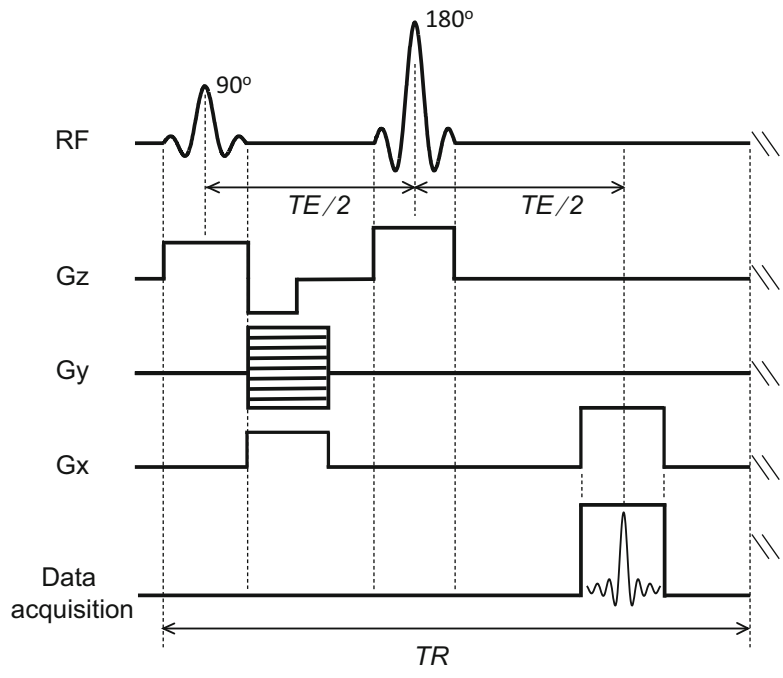

Fig. 3.15 Spin echo pulse sequence for two-dimensional data acquisition

4. Sample this echo, and place it into one of the rows of k-space, which means k-space is acquired one row at a time (at least for conventional imaging).
5. For a 256 × 256 matrix, we would use 256 samples. Note that the k-space does not have to be square and the frequency-encoding dimension is *usually* the first set of numbers, followed by the number of phase encode steps.
6. The number of samples dictates the number of columns in k-space.
7. For the next row, change the phase-encoding gradient, and repeat.
8. The number of phase encode steps dictates the number of rows in k-space and, accordingly, the scan duration. One phase encode step is achieved in each TR.

3.5 Image Reconstruction in MRI

Multiple image reconstruction algorithms exist in MRI depending on the way k-space data is acquired by a pulse sequence. In this section, we will only focus on the reconstruction algorithms considering that k-space data is acquired in Cartesian coordinates. The reader should note that there could be other pulse sequences in MRI acquiring data in spiral and radial coordinates. We encourage readers to look for other resources if their MRI data is to be reconstructed from non-Cartesian k-space.

3.5.1 Fourier Reconstruction of MRI Data

Once all the k-space data is collected in Cartesian coordinates, we reconstruct an anatomical image by performing the inverse Fourier transform (IFT) of the k-space data. This is possible because there is a one-to-one relationship between frequency and position in the x-direction and between phase-encoding gradient strength and position in the y-direction. In other words, the frequency- and phase-encoding gradients provide the position of a signal in image space (spatial domain).

Depending on whether the k-space data is acquired in 2D or 3D, we apply either 2D or 3D IFT. The so-called fast Fourier transform (FFT) is the most widely used algorithm to implement IFT due to its computational efficiency. The current state-of-the-art in MRI is to use phase-array coils and acquire multiple snapshots of the same location from different angles. Since multiple images are available for the same location, the conventional Fourier reconstruction is no longer a suitable method of image reconstruction. Instead, the final reconstructed image must be a weighted combination of the individual channel images because the signal received by a given channel is sensitive only to the area closer to that channel. This is illustrated in Fig. 3.16 for multi-channel images acquired with a 52-channel receive RF coil. Note that only 48 of the 52 channel images are displayed. The magnitudes of their corresponding k-space images are shown in Fig. 3.17.

The most common method to combine multi-channel images is the so-called *sum-of-squares* method [12]. In this method, the root-mean-square average of the channel images is taken to create a combined image. All the 12 brain slices shown in Fig. 3.14 are created by using *sum-of-squares* method. Note that the phase information is lost in this method because the root-mean-square averages could be calculated only for the magnitude images and not for the phase images. Chapter 8 describes a method to combine the multi-channel phase images when data is acquired using multi-echo-spin-echo pulse sequence.

3.5.2 Parallel Imaging

One of the major issues with MR imaging is the longer time of data acquisition. Parallel imaging is a commonly used technique to reduce the scan time in MRI. In parallel imaging, some of the phase-encoding lines in k-space are skipped to reduce the scan time. If we directly apply IFT on

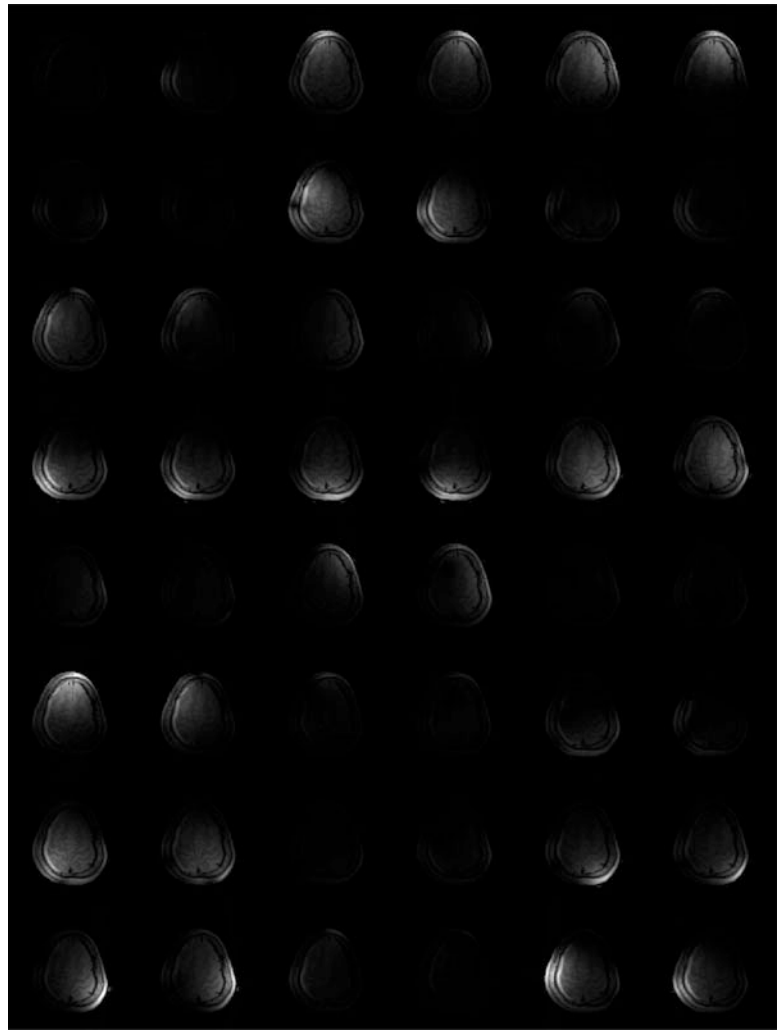

Fig. 3.16 Forty-eight spatial domain images of a single slice (slice 6 in Fig. 3.14) acquired with a multi-channel receive RF coil. Only the magnitude images are shown

this undersampled data, we would get overlapping/aliased images. As an illustration, refer to Fig. 3.18a where every alternate phase-encoding line is skipped and a direct application of IFT leads to aliasing as is evident from Fig. 3.18b. Therefore, more sophisticated image reconstruction algorithms are necessary to correct for these artifacts. In this section, we are briefly introducing SENSitivity Encoding (SENSE) [19] and GeneRalized Autocalibrating Partial Parallel Acquisition (GRAPPA) [6], which are the two most widely used algorithms for image reconstruction on the clinical scanners using parallel imaging. A nice summary of SENSE and GRAPPA is provided by Deshmane et al. [2]. While SENSE and GRAPPA are important, we strongly encourage readers to study other parallel imaging algorithms such as SMASH [21], PILS [5], and others [9,15].

Parallel Imaging Algorithms

The SENSE algorithm exploits the encoding effect produced by using the sensitivity of phase-array coils. Since this encoding effect is complementary to the Fourier preparation created by linear field gradients, utilizing it compensates for the aliasing produced by the skipping of k-space lines. It is worth noting that the SENSE

(continued)

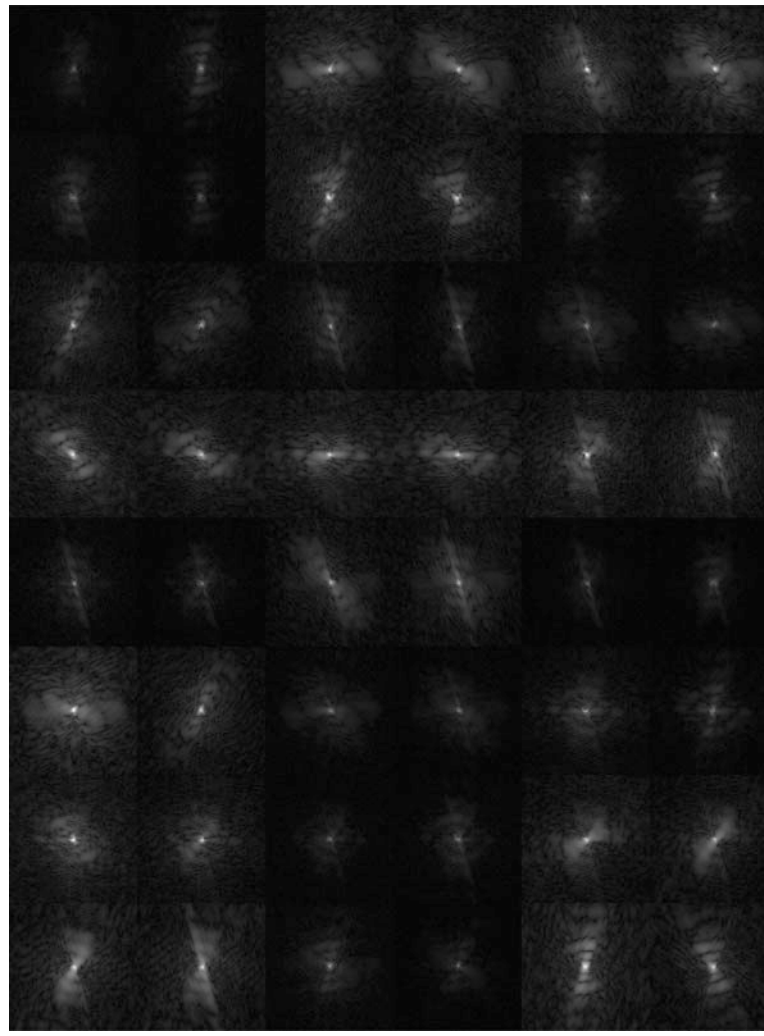

Fig. 3.17 Forty-eight k-space images of a single slice (slice 6 in Fig. 3.14) acquired with a multi-channel receive RF coil. Only the magnitude images are shown after applying $|S(k_x, k_y)|^{0.4}$ filter

algorithm uses coil sensitivities to sort out the overlapping/aliased signals in the image domain (spatial domain) after applying IFT. In contrary to SENSE, the GRAPPA algorithm corrects for the overlapping/aliased signals in image domain by regenerating the missing phase-encoding lines in k-space and then applying IFT to create the final image. Because of the difference in these two methods, GRAPPA is said to work with the undersampled k-space, whereas SENSE works on the aliased image [2]. Because GRAPPA does not rely on exact knowledge of the coil sensitivities, it is robust in applications where measuring coil sensitivity maps is difficult. This is especially the case in regions of low signal and in regions that are subject to patient motion.

The weighting factors (or weights) used to generate the missing phase-encoding lines in GRAPPA are determined by using a patch of k-space with the same desired k-space spacing/image FOV as the final reconstructed image. This patch of lines is called autocalibration signal (ACS) and acquired at the center of k-space. The pat-

(continued)

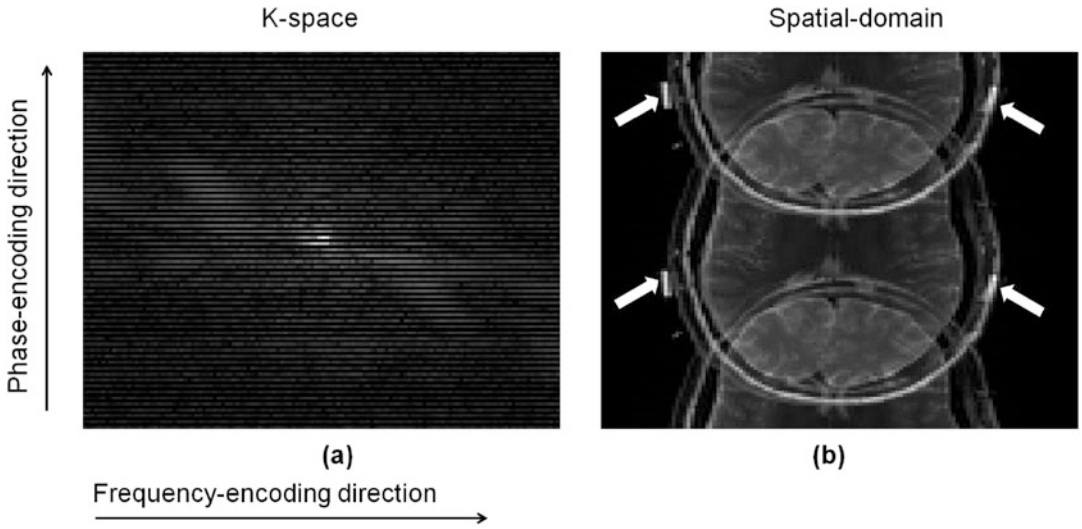

Fig. 3.18 Illustration of aliasing effect when IFT is directly applied on data acquired with parallel imaging. (**a**) K-space data acquired by skipping every alternate line in phase-encoding direction. (**b**) Reconstructed spatial domain image after applying IFT. The arrows indicate a hyper-intense signal from gel which was placed on the head while acquiring these images. Placing gel on the scalp is a typical experimental setup in MREIT and MRCDI (see Chap. 4)

tern of phase undersampling is governed by the so-called acceleration factor (AF). The AF = 2 means skipping of every alternate line, and AF = 3 means skipping every two lines. Therefore, increasing the AF reduces the scan time, but poses challenges for image reconstruction due to the enhanced ghosting associated with the missing phase-encoding lines.

3.6 Magnitude and Phase Images in MRI

It is common for MR signals to be detected in quadrature by two coils which are sensitive to signal in orthogonal directions. These signals are demodulated, processed, and recombined to create the anatomical image we want to see. The quadrature receiver coils are both measuring the same net precessing magnetization, but from different perspectives. In theory, the signal is identical from either coil, except for a phase shift of 90°. In reality, this will not be the case due to noise, which is independent in each coil and uncorrelated with the other.

We can represent the net magnetization as a vector with real and imaginary parts recorded from the two coil channels (see Fig. 3.19). Complex notation can be used for this, and it is an arbitrary choice to consider one of the signals as *real* and the other *imaginary*. From this *real* and *imaginary* data, we can construct a *magnitude* and a *phase* image as:

$$Magnitude(M) = \sqrt{Re^2 + Img^2} \tag{3.29}$$

$$Phase(\phi) = tan^{-1}(Img/Re) \tag{3.30}$$

Significance of Phase Images in MRI

Phase images are something most of us are not familiar with because they are not used for clinical diagnosis. However, they play a significant role in the design of MRI system and improving the image quality. Phase images are utilized for the calculation of the so-called B_0 inhomogeneity which is

(continued)

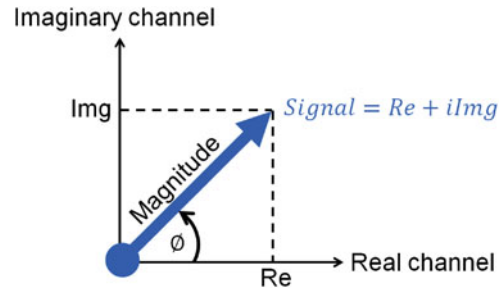

Fig. 3.19 Representation of the MRI signal in real and imaginary terms

then used to calculate the currents in shim coils to correct for the field inhomogeneity. Phase images are also used in certain MRI applications such as susceptibility-weighted imaging (SWI) [8, 17] and quantitative susceptibility mapping (QSM) [23]. The phase images are a central focus of this book and widely discussed in Chap. 5 for MREIT and MRCDI applications and in Chap. 8 for and MREPT applications.

3.7 MRI Applications Exploiting Imaging Artifacts

In this section, we discuss two applications of MRI which exploit artifacts in images to create new types of images with diagnostic capability.

Susceptibility Artifact in MRI

Referring to Sect. 3.3.4, we can note that the magnetization of a material augments the applied field $\mathbf{B_0}$ with its own χ-dependent magnetic field, causing the field lines of the applied field to concentrate in paramagnetic materials or be excluded in diamagnetic materials. Either way, if the susceptibility-induced field distortion is strong enough, it will create artifacts in MRI. Susceptibility artifacts are especially problematic at interfaces between materials with different susceptibilities, such as near metal implants or at air-brain interfaces near the paranasal sinuses [1]. Nevertheless, susceptibility-weighted imaging (SWI) is an application in MRI which exploits the χ-dependent change in MRI signal and produces quantitative maps of the magnetic susceptibility of body tissues. These maps provide insights into the structure of body tissues and demonstrated to have diagnostic capability [14].

Chemical Shift Artifact in MRI

Section 3.4.4 described the mathematical model of the MRI k-space signal in 2D and 3D when protons are located in water. However, when protons are located in an environment (or medium) other than water, these equations need modification. Under a specific condition when protons are located in a fatty environment, an artifact called chemical shift artifact appears in MR images. In the description that follows, we explain the mathematical model of MRI k-space signal when this artifact appears.

Let us assume that protons are located in both fat and water environments. Considering that a read gradient G_x is applied in the x-direction, the water and fat frequencies are expressed as:

$$f_w = \frac{\gamma}{2\pi} G_x x \tag{3.31}$$

and

(continued)

$$f_f = \frac{\gamma}{2\pi}(G_x x + \delta B_0) = f_w + \frac{\gamma}{2\pi}\Delta B_0 \tag{3.32}$$

where ΔB_0 is 3.5 ppm of B_0. The phase accumulated by water protons at time t is given by:

$$\phi_x^w = \frac{\gamma}{2\pi} G_x x t = k_x x \tag{3.33}$$

where $k_x = \frac{\gamma}{2\pi} G_x t$ is a spatial frequency. The phase accumulated by fat protons at time t is given by:

$$\begin{aligned}\phi_x^f &= \frac{\gamma}{2\pi} G_x x t + \frac{\gamma}{2\pi}\Delta B_0 t \\ &= k_x x + \xi = k_x(x + x')\end{aligned} \tag{3.34}$$

where $x' = \frac{\Delta B_0}{G_x}$ is a given constant indicating the pixel shift.

Let $W(x, y)$ and $F(x, y)$ be the proton densities of the water and fat, respectively. The k-space signal is assumed to be a linear combination of water and fat signals. Using the pulse sequence as shown in Fig. 3.15, we can obtain the following k-space signals $S^{\pm}$, respectively:

$$\begin{aligned}S(k_x, k_y) = &\int\int W(x, y) e^{i\delta(x,y)} \\ &\times e^{-i(xk_x + yk_y)} dx dy \\ &+ \int\int F(x, y) e^{i\delta(x,y)} \\ &\times e^{-i(k_x(x+x') + yk_y)} dx dy\end{aligned} \tag{3.35}$$

where δ is any systematic phase error. Through the change of variable $x + x'$ in the second term, we get:

$$\begin{aligned}S(k_x, k_y) = &\int\int W(x, y) e^{i\delta(x,y)} \\ &\times e^{-i(xk_x + yk_y)} dx dy \\ &+ \int\int F(x - x', y) e^{i\delta(x-x',y)} \\ &\times e^{-i(xk_x + yk_y)} dx dy.\end{aligned} \tag{3.36}$$

Equation (3.36) represents the signal model for chemical shift in MRI when protons are present in fatty tissues. Taking inverse Fourier transform, we obtain the complex MR image of water and fat as:

$$\begin{aligned}\mathcal{M}(x, y) = &W(x, y) e^{i\delta(x,y)} \\ &+ F(x - x', y) e^{i\delta(x-x',y)}.\end{aligned} \tag{3.37}$$

While Eq. (3.37) describes an artifact in images, Dixon [3] leveraged this artifact to separate water and fat images. Modified versions of Dixon's method are widely used these days in various applications including MREIT [16].

3.8 Signal and Noise in MRI

The signal-to-noise ratio (SNR) is an important metric used in MRI during the various stages of development of an MRI scanner. During hardware development, SNR is calculated by designers of RF coil, gradient coil, and magnet. Once the different hardware components are integrated together to form MRI system, SNR is calculated during MRI pre-scans such as center frequency adjustment and linear shim calculations. The SNR is also used to compare the quality of images obtained from different pulse sequences.

Sometimes, we want to compare the quality of images acquired from same pulse sequence but with different scan parameters, and SNR is a good metric for this purpose. We can also use SNR to compare the quality of images from different image reconstruction algorithms.

3.8.1 SNR Calculation Methods

Different SNR calculation methods have been described in MRI. We can differentiate them based on methods that use a single image, two images, or a series of images for SNR calculation. The mathematical expressions for SNR calculation vary for each of these methods. Consider an image voxel at position $\mathbf{r} = (x, y, z)$. If "true" MR image intensity $S(\mathbf{r})$ at position $\mathbf{r}$ is corrupted with noise, the signal intensity $S_\eta(\mathbf{r}, n)$ in the presence of noise in a series of N repeated acquisitions can be described as:

$$S_\eta(\mathbf{r}, n) = S(\mathbf{r}) + \eta(\mathbf{r}, n) \tag{3.38}$$

where $\eta(\mathbf{r}, n)$ is the noise at position $\mathbf{r} = (x, y, z)$ for the nth acquisition ($n = 1, 2, \ldots, N$). For simplicity, we will assume that $\eta(\mathbf{r}, n)$ is normally distributed in space (that is with respect to $\mathbf{r}$) and time (that is with respect to n) and described by mean = 0 and standard deviation = σ. It should be noted that the assumption of normal distribution of noise is valid only for large SNRs, i.e., $S(\mathbf{r}) >> \sigma$; otherwise, noise has more complicated distributions such as the Rician distribution or non-central chi distribution.

The SNR of a single image voxel at position $\mathbf{r} = (x, y, z)$ can be defined as:

$$SNR(\mathbf{r}) = \frac{S(\mathbf{r})}{\sigma} \tag{3.39}$$

To calculate the SNR at position $\mathbf{r} = (x, y, z)$, the statistical measurement of signal intensity $S(\mathbf{r})$ and the standard deviation σ of noise distribution are necessary.

SNR Calculation from a Series of Images

The signal intensity $S(\mathbf{r})$ can be calculated as the mean value of the signal over all N repetitions,

$$S(\mathbf{r}) = mean(S_\eta(\mathbf{r}, n)), \quad n = 1, 2, \ldots, N \tag{3.40}$$

If we prefer to choose a group of voxels in an image, called region of interest (ROI), then the signal in this ROI can be calculated as the mean value of the signal over all the voxels of the ROI and over all N repetitions.

$$S(ROI, n) = mean(S_\eta(ROI, n))_{r \in ROI}, \quad n = 1, 2, \ldots, N \tag{3.41}$$

Although the signal calculation is easy, the σ calculation is not straightforward. If we have N repeated and "identical" measurements of the signal, then

$$\sigma(\mathbf{r}) = stdev(S_\eta(\mathbf{r}, n)) = stdev(\eta(\mathbf{r}, n)), \quad n = 1, 2, \ldots, N \tag{3.42}$$

Therefore, SNR_{mult} of a voxel at position $\mathbf{r} = (x, y, z)$ for N repeated and "identical" measurements of the voxel signal is given by

$$SNR_{mult} = \frac{S_{mult}}{\sigma_{mult}} = \frac{mean(S_\eta(\mathbf{r}, n))}{stdev(S_\eta(\mathbf{r}, n))}, \quad n = 1, 2, \ldots, N \tag{3.43}$$

If we prefer to choose an ROI, then we should select a region with uniform signal within ROI, i.e., the spatial variation of the signal can be neglected within the ROI. In this case, the $SNR_{mult, r \in ROI}$ is given by:

$$SNR_{mult, \mathbf{r} \in ROI} = \frac{S_{mult, \mathbf{r} \in ROI}}{\sigma_{mult, \mathbf{r} \in ROI}}$$

(continued)

$$= \frac{mean(S_\eta(ROI, n))}{mean(stdev(S_\eta(ROI, n)))},$$
$$n = 1, 2, \ldots, N \qquad (3.44)$$

In Eq. (3.44), the numerator is calculated by taking the mean value of the signals for each voxel and for all the N repetitions. The denominator is calculated by first finding, for each voxel with ROI, the standard deviation of the voxel signal varying across N repetitions and then taking the mean of the standard deviations of all the voxels in the ROI.

SNR Calculation from Two Images

The SNR calculation method described in Sect. 3.32 is generic and not suitable for practical applications as the increase in the number of repetitions increases the MRI scan time. Additionally, signals from multiple repetitions may be affected by systematic signal variations due to motion of imaging object or due to underlying physiological phenomenon which changes the signal over time. To overcome these issues, a method using just two repetitions n_1 and n_2 has been developed for SNR calculation. Using this method, the SNR is calculated as:

$$SNR_{diff}(n_1, n_2) = \frac{S_{diff}}{\sigma_{diff}} = \frac{\frac{1}{2}\ mean_{\mathbf{r}\in ROI}(S_\eta(\mathbf{r}, n_1)) + (S_\eta(\mathbf{r}, n_2))}{\frac{1}{\sqrt{2}}\ stdev(S_\eta(\mathbf{r}, n_1)) - (S_\eta(\mathbf{r}, n_2))} = \frac{mean(S_\eta(ROI, n_1) + S_\eta(ROI, n_2))}{\sqrt{2}\ \ stdev(S_\eta(ROI, n_1) - S_\eta(ROI, n_2))} \qquad (3.45)$$

The numerator in $SNR_{diff}(n_1, n_2)$ is calculated by first taking the sum of the two images at the two repetitions n_1 and n_2 and then taking the mean value of the ROI voxels within the summed image. The denominator is calculated by taking the standard deviation of the ROI voxels for the difference image (difference is taken between the two images at two repetitions n_1 and n_2). Note the scaling of denominator with $\sqrt{2}$. It should also be noted that this method assumes a Gaussian noise distribution within the ROI in the difference image. Therefore, the ROI must be placed on a tissue with sufficiently high signal and the regions with low signal or the background should not be used for SNR calculation using this method.

SNR Calculation Using NEMA Method

The National Electrical Manufacturers Association (NEMA) has developed some standard methods to determine SNR in diagnostic MRI (NEMA Standards Publication MS 1-2008 (R2014)). While the methods described in the document are applicable for multi-channel receive coils, the document description only restricts to single-channel receive systems. We describe one method from this document which is primarily used during prototype MRI development but can also be used in clinical scanners if the manufacturer permits data acquisition under the specified conditions.

In this method, two images are acquired. First of all, a normal image is acquired, and the mean value of the ROI voxels is calculated (S_{NEMA}). Then, a noise image is acquired without any RF excitation (i.e., either the RF amplifier is turned off or the RF excitation is suppressed). The TR may be decreased to accelerate the data acquisition for noise scan, but other parameters such as bandwidth, matrix size, and number of signal averages must be held constant. It

(continued)

must be ensured that the system receiver attenuation (or gain control) and any scaling of the image reconstruction are identical to that of the first scan (normal image scan). Except for TR, the noise image should be acquired under the same conditions as those for the normal image scan, i.e., no system adjustment or calibration should be performed between the scans. An ROI is placed at the same location as that of the normal image, and the standard deviation of the ROI voxels in the noise image is calculated (σ_{NEMA}). The SNR is then calculated as:

This noise image obtained in this process will not have a Gaussian distribution but Rician distribution which must be compensated during SNR calculation. The factor of 0.66 ($= \sqrt{(4-\pi)/2}$) accounts for the Rayleigh distribution of the noise in the magnitude image (Henkelman, R. M. 1985, Medical Physics, 12, 232–233).

$$SNR_{NEMA}(image, noise) = \frac{SNR_{NEMA}}{\sigma_{NEMA}} = 0.66\,\frac{mean_{\mathbf{r}\in ROI}(S_\eta(\mathbf{r}, image))}{stdev_{\mathbf{r}\in ROI}(S_\eta(\mathbf{r}, image))} \tag{3.46}$$

While a preferred method during prototyping of MRI scanners, this SNR calculation method is not suitable for clinical scanners as most clinical scanners do not permit the acquisition of pure noise image (without any transmit RF pulse) with standard pulse sequences.

SNR Calculation from a Single Image

The most widely used technique for SNR calculation just takes a single image ($n = 1$) and relies on signal statistics from two separate ROIs drawn on this image. One ROI is in foreground of image on the tissue of interest (ROI_{tissue}), and the other ROI is in the background of image (ROI_{tissue}). The SNR is then calculated as

$$SNR_{image}(n_1) = \frac{SNR_{image}}{\sigma_{image}} = \frac{mean_{\mathbf{r}\in ROI_{tissue}}(S_\eta(\mathbf{r}, n_1))}{\sqrt{\frac{2}{4-\pi}}\,stdev_{\mathbf{r}\in ROI_{air}}(S_\eta(\mathbf{r}, n_1))} \tag{3.47}$$

The correction factor ($\sqrt{2/(4-\pi)} = 1.53$) is required because of the Rayleigh distribution of the background noise in the magnitude image.

3.8.2 SNR Formulation in MRI

Consider the x, y, and z to be the readout, phase-encoding, and slice selection directions, respectively, in a typical MRI data acquisition protocol. The SNR/voxel of MRI data acquired using this protocol can be controlled by carefully selecting imaging parameters such as the voxel dimensions (Δx, Δy, Δz), the number of acquisitions (or repetitions) N_{acq}, the bandwidth BW_{read}, and the number of k-space samples (k_x, k_y, k_z). The following expression describes the SNR/voxel dependence on imaging parameters selected in this protocol:

$$SNR/voxel \propto \frac{\Delta x \Delta y \Delta z \sqrt{N_{acq}}}{\sqrt{\frac{BW_{read}}{N_x N_y N_z}}} \tag{3.48}$$

Choosing the scan parameter as data sampling rate Δt instead of BW_{read}, since $BW_{read} = \frac{1}{\Delta t}$, the SNR/voxel is given by:

$$SNR/voxel \propto \Delta x \Delta y \Delta z \sqrt{N_{acq} N_x N_y N_z \Delta t} \tag{3.49}$$

Since the readout time T_s is given by $T_s = N_x \Delta t$, the SNR/voxel becomes:

$$SNR/voxel \propto \Delta x \Delta y \Delta z \sqrt{N_{acq} N_y N_z T_s} \tag{3.50}$$

Since the bandwidth per voxel BW is given by $BW = BW_{read/N_x}$, the SNR/voxel becomes:

$$SNR/voxel \propto \Delta x \Delta y \Delta z \sqrt{\frac{N_{acq} N_y N_z}{BW}} \tag{3.51}$$

Further variations of the expression for SNR/voxel are possible by substituting the following relations:

$$FOV_x = N_x \Delta x$$

$$FOV_y = N_y \Delta y$$

$$FOV_z = N_z \Delta z \tag{3.52}$$

3.9 Common MR Image Formats

In this section, we describe two most commonly used image formats used in MRI: DICOM, which stands for Digital Imaging and Communications in Medicine, and NIfTI, which stands for Neuroimaging Informatics Technology Initiative.

3.9.1 DICOM

DICOM is the standard for communication and management of medical information and related data. It is a standard developed by the American College of Radiology (ACR) and the NEMA. It is most commonly used for storing and transmitting medical images which enables the integration of medical imaging devices and *picture archiving and communications systems* (PACS) from multiple manufacturers. DICOM incorporates standards for imaging modalities such as ultrasound, CT, PET, as well as MRI. It also includes protocols for image exchange, for example, by portable media, image compression, 3D visualization, image presentation, and results reporting. To promote identical grayscale values on different monitors and viewing devices, the DICOM committee developed a lookup table (LUT) to display digitally assigned values.

DICOM format groups information into datasets with a file consisting of a *header* and *image dataset* packed into a single file. The first few packets of information in a DICOM file constitute the header which stores demographic information about the patient, acquisition parameters, and image formation:

- Image dimensions—pixel/voxel size
- Sequence specifics—TE, TR, flip angle size
- Date of birth
- Patient name
- And lots of other fields

A disadvantage of the DICOM format is that there can be inconsistencies in the header filling between image creation sites.

3.9.2 NIfTI

NIfTI was designed under the auspices of the National Institutes of Health (NIH) to improve interchangeability between processing packages. Image analysis can be much more straightforward with the NIfTI format as many standard software packages (certainly of the neuroimaging community) work directly with this format, for example, the ubiquitous FMRIB Software Library (FSL) from Oxford University.

NIfTI files also contain a header and image dataset. An important difference to the DICOM header format is the inclusion of two affine coordinate definitions relating voxel index (i, j, k) to spatial location (x, y, z): one affine transform to indicate the mapping to normal space and another to indicate orientation and location of the data in scanner coordinates. The header also contains fields for MRI parameters such as:

- Image dimensions—pixel/voxel size
- Spatiotemporal order of fMRI slices
- Spiral acquisitions
- Interleaving
- And some other fields

NIfTI headers do not contain patient-specific information and often few acquisition parameters. Therefore, the end user must take care when converting from DICOM to NIfTI that all relevant acquisition parameters are either copied to a NIfTI header field or stored elsewhere. Failure to do so can be a tremendous source of frustration if the original DICOM images are no longer available, as is often the case with PACS after a set interval.

References

1. R. Cusack, B. Russell, S.M. Cox, C. De Panfilis, C. Schwarzbauer, R. Ansorge, An evaluation of the use of passive shimming to improve frontal sensitivity in fMRI. Neuroimage **24**, 82–91 (2005)
2. A. Deshmane, V. Gulani, M.A. Griswold, N. Seiberlich, Parallel MR imaging. J. Magn. Reson. Imag. **36**(1), 55–72 (2012)
3. W.T. Dixon, Simple proton spectroscopic imaging. Radiology **153**(1), 189–194 (1984)
4. R.R. Edelman, The history of MR imaging as seen through the pages of radiology. Radiology **273**(2S), S181–S200 (2014)
5. M.A. Griswold, P.M. Jakob, M. Nittka, J.W. Goldfarb, A. Haase, Partially parallel imaging with localized sensitivities (PILS). Magn. Reson. Med. **44**(4), 602–609 (2000)
6. M.A. Griswold, P.M. Jakob, R.M. Heidemann, M. Nittka, V. Jellus, J. Wang, B. Kiefer, A. Haase, Generalized autocalibrating partially parallel acquisitions (GRAPPA). Magn. Reson. Med. **47**(6), 1202–1210 (2002)
7. B. Gruber, M. Froeling, T. Leiner, D.W.J. Klomp, RF coils: A practical guide for nonphysicists. J. Magn. Reson. Imag. **48**(3), 590–604 (2018)
8. E.M. Haacke, S. Mittal, Z. Wu, J. Neelavalli, Y.-C.N. Cheng, Susceptibility-weighted imaging: Technical aspects and clinical applications, part 1. Am. J. Neuroradiol. **30**(1), 19–30 (2009)
9. J. Hamilton, D. Franson, N. Seiberlich, Recent advances in parallel imaging for MRI. Progr. Nuclear Magn. Reson. Spectr. **101**, 71–95 (2017)
10. C. Juchem, R.A. de Graaf, B0 magnetic field homogeneity and shimming for in vivo magnetic resonance spectroscopy. Analy. Biochem. **529**, 17–29 (2017)
11. C. Juchem, B. Muller-Bierl, F. Schick, N.K. Logothetis, J. Pfeuffer, Combined passive and active shimming for in vivo mr spectroscopy at high magnetic fields. J. Magn. Reson. **183**(2), 278–289 (2006)
12. E.G. Larsson, D. Erdogmus, R. Yan, J.C. Principe, J.R. Fitzsimmons, SNR-optimality of sum-of-squares reconstruction for phased-array magnetic resonance imaging. J. Magn. Reson. **163**(1), 121–123 (2003)
13. Z.-P. Liang, P.C. Lauterber, *Principles of Magnetic Resonance Imaging: A Signal Processing Perspective*. (Wiley/IEEE Press, New York/Piscataway, 2000), pp. 1–416
14. C. Liu, W. Li, K.A. Tong, K.W. Yeom, S. Kuzminski, Susceptibility-weighted imaging and quantitative susceptibility mapping in the brain. J. Magn. Reson. Imag. **42**(1), 23–41 (2015)
15. M. Lustig, J.M. Pauly, SPIRiT: Iterative self-consistent parallel imaging reconstruction from arbitrary k-space. Magn. Reson. Med. **64**(2), 457–471 (2010)
16. A.S. Minhas, Y.-T. Kim, W.-C. Jeong, H.-J. Kim, S.-Y. Lee, E.-J. Woo, Chemical shift artifact correction in MREIT. J. Biomed. Eng. Res. **30**(6), 461–468 (2009)
17. S. Mittal, Z. Wu, J. Neelavalli, E.M. Haacke, Susceptibility-weighted imaging: technical aspects and clinical applications, part 2. Am. J. Neuroradiol. **30**(2), 232–252 (2009)
18. A. Phair, M. Brideson, L.K. Forbes, A cylindrical basis set for shim coil design in magnetic resonance imaging. Concepts Magn. Reson. Part B Magn. Reson. Eng. **48B**(3), e21400 (2018)
19. K.P. Pruessmann, M. Weiger, M.B. Scheidegger, P. Boesiger, SENSE: sensitivity encoding for fast MRI. Magn. Reson. Med. **42**(5), 952–962 (1999)
20. M. Sarracanie, N. Salameh, Low-field MRI: how low can we go? a fresh view on an old debate. Front. Phys. **8**, 172 (2020)
21. D.K. Sodickson, W.J. Manning, Simultaneous acquisition of spatial harmonics (SMASH): fast imaging with radiofrequency coil arrays. Magn. Reson. Med. **38**(4), 591–603 (1997)
22. G.J. Stanisz, E.E. Odrobina, J. Pun, M. Escaravage, S.J. Graham, M.J. Bronskill, R.M. Henkelman, T1, T2 relaxation and magnetization transfer in tissue at 3T. Magn. Reson. Med. **54**(3), 507–512 (2005)
23. Y. Wang, T. Liu, Quantitative susceptibility mapping (QSM): decoding MRI data for a tissue magnetic biomarker. Magn. Reson. Med. **73**(1), 82–101 (2015)

4 Phantom Construction and Equipment Configurations for Characterizing Electrical Properties Using MRI

Munish Chauhan and Rosalind Sadleir

Abstract

Phantom objects are commonly employed in MRI systems as stable substitutes for biological tissues to ensure systems for measuring images are operating correctly and safely. For magnetic resonance electrical impedance tomography (MREIT) and magnetic resonance electrical property tomography (MREPT), conductivity or permittivity phantoms play an important role in checking MRI pulse sequences, MREIT equipment performance, and algorithm validation. The construction of these phantoms is explained in this chapter. In the first part, materials used for phantom construction are introduced. Ingredients for modifying the electromagnetic properties and relaxation times are presented, and the advantages and disadvantages of aqueous, gel, and hybrid conductivity phantoms are explained. The devices and methods used to confirm phantom electromagnetic properties are explained. Next, different types of MREIT electrode materials and the constant current sources used for MREIT studies are discussed. In the last section, we present the results of previous MREIT and MREPT studies.

M. Chauhan · R. Sadleir (✉)
School of Biological and Health Systems Engineering, Arizona State University, Tempe, AZ, USA
e-mail: mchauha4@asu.edu; rosalind.sadleir@asu.edu

4.1 Introduction

In recent years, magnetic resonance electrical impedance tomography (MREIT) and electric properties tomography (EPT) have emerged as important new tools for imaging electromagnetic parameters including current density and electric fields as well as conductivity and permittivity distributions within objects. These distributions may provide better differentiation of the state of tissues and organs and are expected to result in enhanced diagnosis and treatment of disease.

The raw signals used in either MREIT or EPT are the result of small perturbations in MRI measurements created by intrinsic tissue properties (EPT) or by the flow of external currents (MREIT). There is therefore always a need for phantoms to help validate data quality and evaluate reconstruction algorithm performance. The most important property of phantom materials is that they should have *known, controllable, and stable* electrical properties.

Of course, the need for phantoms is not specific to MREIT and EPT. MRI phantoms are frequently used to test signal and reconstruction quality in all scanners. Although modern MRI systems show good technical quality (e.g., high signal-to-noise ratio, good image homogeneity, and minimal ghosting) and differentiation be-

R. Sadleir, A. S. Minhas (eds.), *Electrical Properties of Tissues*, Advances in Experimental Medicine and Biology 1380, https://doi.org/10.1007/978-3-031-03873-0_4

tween tissue classes (i.e., image contrast), absolute signal intensities of acquired images are not reproducible between systems of the same or different make and type [57, 72]. Image values and contrast are dependent on the sequence parameter settings and on MR scanner hardware properties [72]. Additionally, MRI artifacts such as intensity non-uniformity introduce spatial variations in the image intensity. Magnetic field inhomogeneities or fluctuations in SNR may cause intensity variations. This might be a problem for longitudinal studies, as changes in acquisition protocols and scanner upgrades may lead to inaccuracies of measurements over time [72]. Especially when MRI data is collected at multiple sites or with several different scanners, vendor-specific differences in scanners, use of different RF coils, and pulse sequence characteristics should be taken into account. To ensure consistent MRI interpretation at participating facilities, it is essential to have a means for system comparison beyond basic imaging parameters. A commonly used multi-purpose phantom is the ACR (American College of Radiology) phantom, but it is not suitable for evaluating MREIT or EPT [8, 13, 81]. Construction of a phantom suitable *both* for quality assurance purposes and for evaluating new imaging techniques and sequences is not feasible [23]. We therefore require a combination of phantoms, each one chosen or tailored to best evaluate the question at hand. Examples in related fields are ones specific to functional imaging [13] and diffusion imaging [23].

While EPT does not require any additional hardware, most methods for reconstructing low-frequency electrical conductivity require external current injection [75, 76, 82]. Thus, MREIT experiments involve three additional challenges: the need to construct phantoms that can be physically connected to current sources (and where the internal parts of the phantom are electrically connected to each other); constructing or sourcing appropriate current sources for use with these phantoms; and synchronizing current injection with measurement pulse sequences. In this chapter, we consider methods for constructing electrical property phantoms, current sources, and the electrodes that form the interface between them. Current injection protocols and source controls will be examined in Chap. 5.

4.2 Electrical Property Phantoms

Materials used in phantoms to mimic soft tissues with respect to one or more MRI properties include aqueous solutions of paramagnetic salts (most commonly NaCl), water-based gels of various forms, and ex vivo tissues [25, 43, 56]. In the case of MREIT, current must be distributed throughout the entire phantom and compartments with different conductivities and electrolyte concentrations are in diffusive communication with each other. One problem with this sort of phantom is therefore that they are intrinsically unstable and diffusion processes will ultimately limit their lifetime [20]. In MREPT, different property materials can be enclosed in insulating containers, and problems caused by diffusion do not occur.

Important characteristics of MRI phantoms for MREIT and MREPT are [50]:

1. **Electric properties** equivalent to human tissues
2. **Relaxation times** equivalent to human tissue
3. **Homogeneous** relaxation times and dielectric properties throughout the phantom
4. Sufficient **strength** to allow fabrication without the use of physical reinforcement
5. Ability to fabricate the **shape** of a human organ
6. Ease of **handling**
7. Chemical and physical **stability** over extended time periods.

We consider four classes of MREIT phantom: aqueous, gel, hybrid, and anisotropic. Ingredients used to change the properties of the phantom are shown in Table 4.1. As well as NaCl, water, agar or agarose, and TX-151 are the most commonly used phantom materials for MREIT [33, 61, 75, 82]. As we noted above, MREIT phantoms require electrical connectivity between the different gels or tissues used to construct the phantom. This makes MREIT phantoms more complex to

construct than MREPT phantoms, although the same phantom materials and chemicals can be used for both MREIT and MREPT.

4.2.1 Phantom Types

Aqueous Phantoms

Aqueous solutions of paramagnetic salts are commonly used in MRI phantoms to produce a desired value of either T1 or T2. Aqueous phantoms are easy and safe to handle, but may require a 10 min settling time before commencing MRI scanning to eliminate any remaining convective motion. Although purely aqueous phantoms have good homogeneity and can have long-term stability, water is easily influenced by vibration during scans, and it is difficult to image any inclusions without incurring motion artifacts. More importantly for MREIT, imaging of aqueous phantoms at high fields or current densities (caused by using small electrodes), or both, may produce magneto-hydrodynamic artifacts [55].

Gel Phantoms

Gel phantoms are constructed by stabilizing aqueous electrolyte solutions with the use of gelling agents. Gelling agents make it possible to conveniently construct phantoms with realistic shapes. These types of phantoms usually require addition of preservative to make it stable over time. Because they are more solid, no settling time is required before starting MRI scanning, and they are not subject to vibration problems. The time that conductivity contrasts are maintained depends on the viscosity of the gel and the contrast itself, but lifetimes of several hours may be possible [20].

Hybrid Phantoms

Hybrid phantoms may be made by combining aqueous or gel materials and vegetable or animal tissues that have different electrical properties. Hybrid phantoms are useful in testing algorithms on their ability to reconstruct more realistic biological environments. As for gel phantoms, phantoms containing tissues can never be considered stable, and conductivity and permittivity properties may change between construction and scanning because of diffusion and osmosis. However, in using tissues in either MREIT or MREPT phantoms, the tissue electrical properties may also change over time because of decomposition processes.

Anisotropic Phantoms

Many biological tissues are also anisotropic. The best examples of this are muscle and white matter. The technique of diffusion tensor MREIT (DT-MREIT) provides a means of determining the full anisotropic tensor of these complex tissues. You can find more information about the differences between isotropic and anisotropic tissues in Chap. 2. Stable anisotropic properties are particularly difficult to recreate in phantoms. Of course, muscle tissue or other biological anisotropic material can be incorporated in hybrid phantoms, but it is very difficult to reliably estimate their properties if tissue is used, even on the benchtop. Attempts have been made to construct anisotropic properties in phantoms by incorporating thin fibers [63] or by layering gels of different conductivities [71], but the properties must be truly anisotropic at the measurement (voxel) scale to be usable in MREIT. Again, any anisotropic electrical properties are likely to diffuse away over time. Phantoms used for characterizing

(continued)

diffusion MRI could notionally be used in EPT [78], but the cell membranes responsible for tissue anisotropy at low frequencies do not manifest any directional properties at the high frequencies of EPT measurements.

4.2.2 T1, Conductivity, and Permittivity Modifiers

The electrical properties of biological tissues depend on the frequency of the electromagnetic field to which they are exposed. The characteristic electrical properties for many tissue types have been measured over a wide range of frequencies [15]. Pure fluids and gels tend to have MR relaxation times much longer than tissues. Therefore, paramagnetic salts are commonly added to phantoms to reduce T1 and T2 values. Common salts such as NaCl and KCl are often use to control conductivity, and sucrose or polyethylene may be used to control permittivity. Ingredients that can change the electromagnetic properties of the phantom to those found in biological tissues are listed in Table 4.1. Among relaxation time modifiers, copper sulfate ($CuSO_4$), nickel chloride ($NiCl_2$), and manganese chloride ($MnCl_2$) are frequently used because they are water soluble and have high stability [31]. Gelling materials may also slightly affect relaxation times. Gadolinium, as either $GdCl_3$ salt or chelated diethylenetriaminepentacetate (DTPA), may also be used [22], but is more expensive to procure.

4.2.3 Properties of Different Gelling Agents

Phantom stability is enhanced by using gels instead of conductive fluids. Use of agar, TX-151, and gelatin as gelling agents is very common in MRI and MREIT studies because of their useful physical properties and the short preparation times involved [61, 75, 82]. The following gelling agents have been used in MR imaging studies [9, 51, 52, 68].

1. Agarose or agar-agar
2. TX-151
3. Gelatin
4. Hydroxyethyl cellulose (HEC)
5. Polyacrylamide

In the following sections, we consider the properties of each and outline the pros and cons and possible utility of each.

Agarose or Agar-Agar

Agar (agar-agar) is a heterogeneous mixture of agaropectin and agarose. Agarose has more consistent properties and is much more expensive than agar. Luckily, experiments show that agar is well-suited for making phantoms, as it does not appear to influence the overall conductivity or permittivity of phantom materials. However, the T2 times observed in phantoms depend inversely on the concentration of the gelling agent. The T2 relaxation time of both agarose and agar gel at about 2% concentrations is similar to that of human tissue (40–150 ms), and it can be adjusted by altering the consistency of the gel (i.e., the concentration of agarose or agar) [25, 56]. Use of very high concentrations of agar will lead to very short T2 times, making imaging problematic [50].

In addition to MR research, agarose is widely used as a brain mimicking gel for infusion studies because of its structural properties [1, 8]. For example, porcine brain in vivo and agarose gel have similar pressure profiles, penetration transients, and drag forces associated with the advancement of a catheter into the tissue [8]. Agarose gel also mimics the brain in its ability to create a seal against the outer wall of a delivery device inserted into it [8]. Drag forces of agarose gels are within 5–10% of living human brain tissue [8, 24]. Agarose gels may therefore also be useful in constructing electric property measurement phantoms for use with implanted

(continued)

Table 4.1 Properties of conductivity and relaxation time modifiers used in electric property phantoms

Ingredients	Purpose	Pros	Cons
Copper (II) sulfate pentahydrate ($CuSO_4 \cdot 5H_2O$)	T1, T2 modifier	–Ease of handling	–Cannot be used with live tissue –Biohazard, disposal complicated
Manganese (II) chloride tetrahydrate ($MnCl_2 \cdot 4H_2O$)	T1, T2 modifier	–Ease of handling	–Biohazard
Gadolinium(III) chloride hexahydrate ($GdCl_3 \cdot 6H_2O$)	T1, T2 modifier	–High susceptibility	–Difficult to handle, as tiny quantities are required –Harmful
Nickel(II) sulfate hexahydrate ($NiSO_4 \cdot 6H_2O$)	T1,T2 modifier	–Ease of handling	–Biohazard –Disposal complicated
Sodium chloride (NaCl)	Conductivity modifier	–Ease of handling –Harmless	–Also influences relaxation times
Sucrose (saccharose)	Permittivity modifier	–Ease of handling –Harmless	–Sticky –Large amounts required
Polyethylene powder	Permittivity modifier	–Ease of handling	–Does not dissolve in water but can be mixed through gels

electrodes. However, agar materials are likely not suitable for forming complex phantoms such as contrast-resolution phantoms or anthropomorphic phantoms.

Agar or agarose gels require some care in handling. Agarose gel phantoms often have sodium azide added to retard mold formation [13]. Because sodium azide is poisonous, extreme caution is needed for phantoms employing a large amount. Another problem with sodium azide is that it also affects the conductivity of the final gel. So, precise calculations or measurements of the conductivity should be done during recipe design and after the gel has been formed to confirm actual values.

There is also the risk of bubbles forming in the gel. Ohno et al. [67] explained a two-stage heating method to dissolve the ingredients of magnetic resonance (MR) imaging phantoms to overcome issues of uneven quality and bubbles in conventional MR imaging phantoms and also evaluated uniformity and the reproducibility of their method. Alternatively, a vacuum pump may be used on the solution before the gel sets.

Pros Agarose or agar is cheap, easy to handle, and easily dissolved in warm or hot water.

Cons Agarose or agar gels suffer water loss over time, and apart from diffusion changes, gel breakdown can make agar-based phantoms unstable for long-term use. Another disadvantage of using agarose or agar gel in phantom material is the fact that these are natural products. Therefore, gelling and relaxation properties may differ somewhat between different product batches.

Agarose or Agar Gel Preparation Steps

Figure 4.1 shows the ingredients and steps in making an example agarose or agar gel for an MREIT conductivity phantom. It is recommended to dissolve any electric parametric modifiers like NaCl or $CuSO_4$ (used to reduce T2 values) before adding agar. Heating can be performed using a microwave or an induction heater. The mixture will start to solidify into a gel upon cooling once it has been heated to over

(continued)

Material	Quantity
Deionized Water (18.2 MΩ)	1000 mL
$CuSO_4$	1 g
Agar	25 g
NaCl	3.5 g ≈ 0.71 S/m

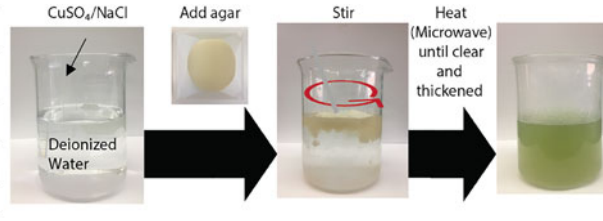

Fig. 4.1 Agarose- or agar gel-making process, showing (left) basic recipe for MREIT gel phantom and (right) preparation steps

approximately 80 °C. At high temperatures, care has to be taken to avoid incorporating air bubbles. As noted above, the amount of agarose or agar used directly influences the brittleness of the gel.

TX-151

TX-151 is a polysaccharide material that has commonly been used, together with water, agar, and NaCl, to create a tissue-equivalent gel for making realistic, inexpensive, conveniently moldable, and temporally stable tissue-equivalent MRI phantoms. The amount of TX-151 material added to a phantom can be varied over about 5–20% W/V, resulting in convenient sample preparation and gelling times. Within this range, use of TX-151 also has a slight influence on T1 and T2 values [52]. Additionally, sodium chloride and copper sulfate can be used to increase the conductivity and T1 (and T2), respectively. As for agar gels, sodium azide can be added as a preservative, with the same precautions as noted above.

Pros TX-151 gels are more durable than agarose gels. TX-151 gels are also more rigid than agar gels but are soft enough to be cut easily. They are relatively stable when immersed in saline solutions.

Cons It solidifies in cold water. Fast mixing may cause unwanted air bubbles within the gel.

TX-151 Gel Preparation Steps

Parametric modifiers such as NaCl and $CuSO_4$ should be dissolved in water, and the solution must be heated before adding TX-151. Heating can be performed using a microwave or induction heater. After adding the TX-151, mix the solution slowly to avoid the incorporation of air bubbles. At the same time, mixing must be fast enough to completely mix the solution before it gels. Solidification of the mixture will start upon cooling once it has been heated to over 80°C. At higher temperatures, extra care has to be taken to avoid adding air bubbles. Finally, the hot solution should be filtered using a steel mesh strainer to remove any unwanted lumps and air bubbles. Figure 4.2 shows the ingredients and steps involved in making a TX-151 gel for an MREIT conductivity phantom.

Animal Hide Gelatin (AHG)

Animal hide gelatin (AHG) gels have been used in MRI phantoms [2, 23]. Blechinger et al. [2] reported a modified version of materials and recipe used to construct a gelatin-agar phantom. In the modified recipe, glycerol was used to control T1

(continued)

Material	Quantity
Deionized Water (18.2 MΩ)	1000 mL
$CuSO_4$	1 g
TX-151	15 g
Agar	15 g
NaCl	3.5 g ≈ 0.7 S/m

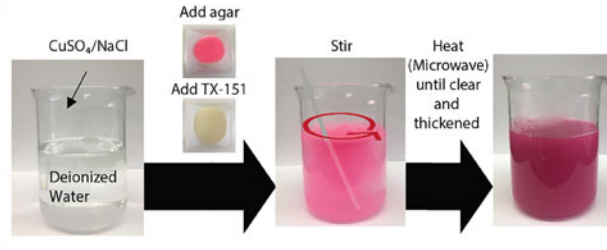

Fig. 4.2 TX-151 gel-making process, showing (left) basic recipe for MREIT gel phantom and (right) preparation steps

instead of a paramagnetic salt ($CuSO_4$). In this recipe, the solution used in making the tissue-mimicking material varied the glycerol/water ratio depending on the T1 value desired. One important observation of this study was that the glycerol/water ratio had little effect on the T2 value of the material. These gels can therefore be made to have specific T1/T2 ratios, as well as T1 and T2 values themselves, spanning the ranges found in normal and abnormal soft tissues. The frequency dependencies found for these gels also appear to simulate that found in nonfat-type soft tissues, and it is of great importance that the materials exhibit long-term stability in their MRI properties. In [2], it was reported that drying could be controlled by sealing the container using petroleum gel. Unfortunately, a long-term instability manifested itself in this study where a very slow rise in T1 value was observed over a period of months. This rise in T1 value was possibly due to the slow formation of a metal-organic complex, removing the Cu^{++} paramagnetic ions responsible for decreasing T1 [2].

Pros As with TX-151-based gels the gel recipe shown in Fig. 4.3 is less likely to shrink or leak from molds while setting and is therefore a good candidate for use in complex phantoms.

Cons In gelatin phantoms, bubbles are a very common problem, and therefore their preparation is more complicated. Gelatin is more sticky than agar or TX-151.

Animal Hide Gelatin Gel Preparation Steps

The ingredients (parts 1 and 2) and preparation steps involved in constructing a gelatin gel are shown in Fig. 4.3. Mix all materials in part 1 and part 2 separately, and heat up each solution using a microwave oven or induction heater. As each solution boils, keep watching it as an overflow may occur rapidly. After a few minutes, you will see that the bubbling reduces, and this is a signal to stop heating and combine the solutions. Mix both solutions slowly, and then add the amount of NaCl required. Gelatin gels are generally useful in forming the background of hybrid phantoms. When forming the background, it is advisable to pour the gel into the mold after the solution has cooled down to at least 50 °C.

Polyacrylamide Gels

Polyacrylamide (PAA) is a polymer formed from acrylamide subunits. It is often used in place of agar in electrophoresis gels, and it has similar physical properties. How-

(continued)

	Material	Quantity
Part 2	Distilled Water (~18.2Mohm)	490 mL
	Glycerol	210ml
	Agar	20 g
Part 1	Distilled Water (~18.2Mohm)	490 mL
	Glycerol	210ml
	Animal Hide Gelatin	100g
	NaCl	1.2 g ≈ 0.7 S/m

Fig. 4.3 Components of two-component animal hide gelatin gel-making process

ever, because some unpolymerized acrylamide, which is a neurotoxin, can always be present even in the usually nontoxic polyacrylamide gel, it must been treated with great caution [85]. Preparation of PAA gels is significantly more tedious than with agarose or TX-151 gels. Therefore, use of polyacrylamide is not recommended for electric property phantoms as large quantities of PAA will probably be required. However, it may have advantages in terms of stability and resistance to diffusion.

Pros: Polyacrylamide gel is durable and can be more stable than agar over time even when placed inside a saline solution.

Cons: Polyacrylamide gels are rigid, quite brittle, and poisonous. Preparation of PAA gels is difficult.

Hydroxyethyl Cellulose (HEC)

Hydroxyethyl cellulose, also called Natrosol, is a non-ionic water-soluble polymerizing agent [21]. It can be used to increase viscosity by simply mixing it into a fluid background, without the need for heating. Natrosol and similar cellulose compounds are safe for use with live biological tissues and can be dissolved to hot or cold water to create gels with a large range of viscosities. Since a rigid gel is desired for MRI phantoms, Natrosol 250 Pharm HEC HX (Ashland Global, Wilmington, DE, USA), which has one of the highest viscosity ranges of the different Natrosol gelling agents [50], can be useful. A related compound, methylcellulose powder, was used at 0.2 g/20 ml to increase the viscosity of artificial sea water surrounding an *Aplysia* abdominal ganglion imaged using MREIT at 800 MHz to minimize magneto-hydrodynamic effects [14, 55].

Pros: Biocompatible and nontoxic, heating not required.

Cons: Gelling occurs rapidly, even at room temperature. It is difficult to create a uniform mix, especially at high concentrations. Large volumes are required, so it cannot easily be used to make large phantoms.

4.2.4 Phantom Body

The bodies (containers) used for MRI phantoms are often made of acrylic plastic, glass, or silicone rubber. The material used for many custom-designed MREIT phantoms has been acrylic plastic. Some examples are illustrated in Fig. 4.4. Acrylic plastic phantom bodies are very hardy and can be reused multiple times. However, acrylic plastic materials are expensive and require precision machining. A specialized workshop has been used in the past to construct components used in these phantoms. Components required may include separate parts for electrode ports, a top and bottom plates for each face of the phantom, and gaskets and plastic screws to seal the phantom once it is assembled and filled.

Another alternative to acrylic plastic phantoms is 3D printed (polylactic acid or PLA) phantoms. Printing technology capable of producing three-dimensional (3D) objects has evolved rapidly in recent years and provides a means of quickly developing reproducible and complex MRI physical phantoms. Simple geometrical 3D phantoms

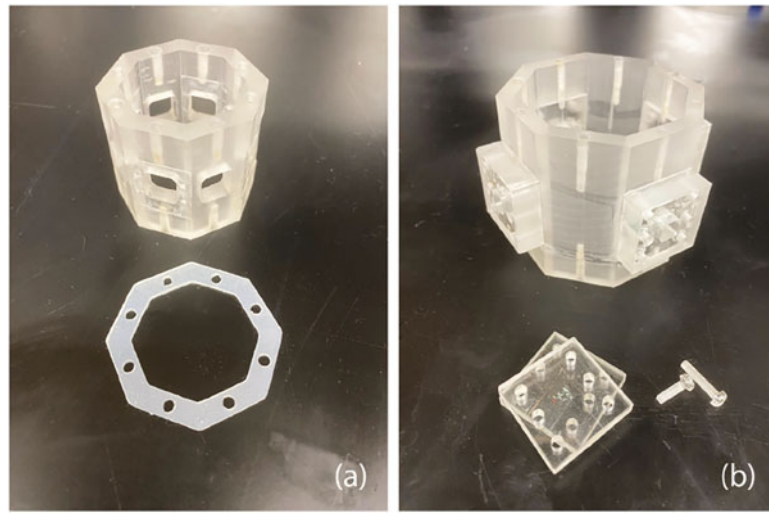

Fig. 4.4 Components of acrylic phantoms. Part (**a**) shows a small phantom with silicone gasket used to seal end face; (**b**) is a larger phantom with a recessed electrode and plastic screws to hold component in place

can be directly designed within 3D printer software or CAD software such as SolidWorks (Dassault Systèmes, France). An example is shown in Fig. 4.5. A big advantage of using computer-aided design is that reference CT or MRI data sets can be imported into the design interface and used to construct phantoms mimicking human body shapes.

A segmentation design approach can be used to classify tissues within a source CT or MRI data set. This segmentation process requires the developer to have the guidance of an expert in physiology or a physiological atlas in order to properly classify the tissues. Software that offers automatic or manual classification or segmentation algorithms can be used to perform the process (described in Chap. 2). To obtain a geometric mesh representing the segmented tissues, the data are output in a format compatible with CAD and 3D printing software. One commonly used format is the stereolithography (`.stl`) surface triangle specification. Figure 4.5 shows a human head mold and agarose gel with conductive inclusions. The mold shown here only included the external head geometry. However, tissues within the body could be segmented using similar methods, formed into gels, and incorporated within this outer shell. The gel volume required to make a human head is large, and handling such a large element is difficult. However, only the top mold sections need to be removed to apply electrodes and perform imaging.

4.3 Measuring Electrical Parameters

Measuring the electrical characteristics of gels created for phantoms is important, as it provides us reference values which can later be compared with values determined using MREIT or EPT imaging methods. Contact methods are the simplest way of measuring the low-frequency conductivity of biological tissues or phantom materials. The basic methods used are the two- and four-electrode methods shown in Fig. 4.6.

4.3.1 Two-Probe Method

The simplest method for measuring conductivity is the two-electrode (bipolar) measuring method. This method uses two electrodes. The electrodes both apply a constant current excitation I in the sample circuit and measure the voltage V between them, as shown in Fig. 4.6a. The resulting impedance Z is the sum of the resistance of the tissue sample and the parasitic resistances and capacitances at the electrode-electrolyte interface [17]. These parasitic resistances are due to electrode polarization. Two-probe methods are

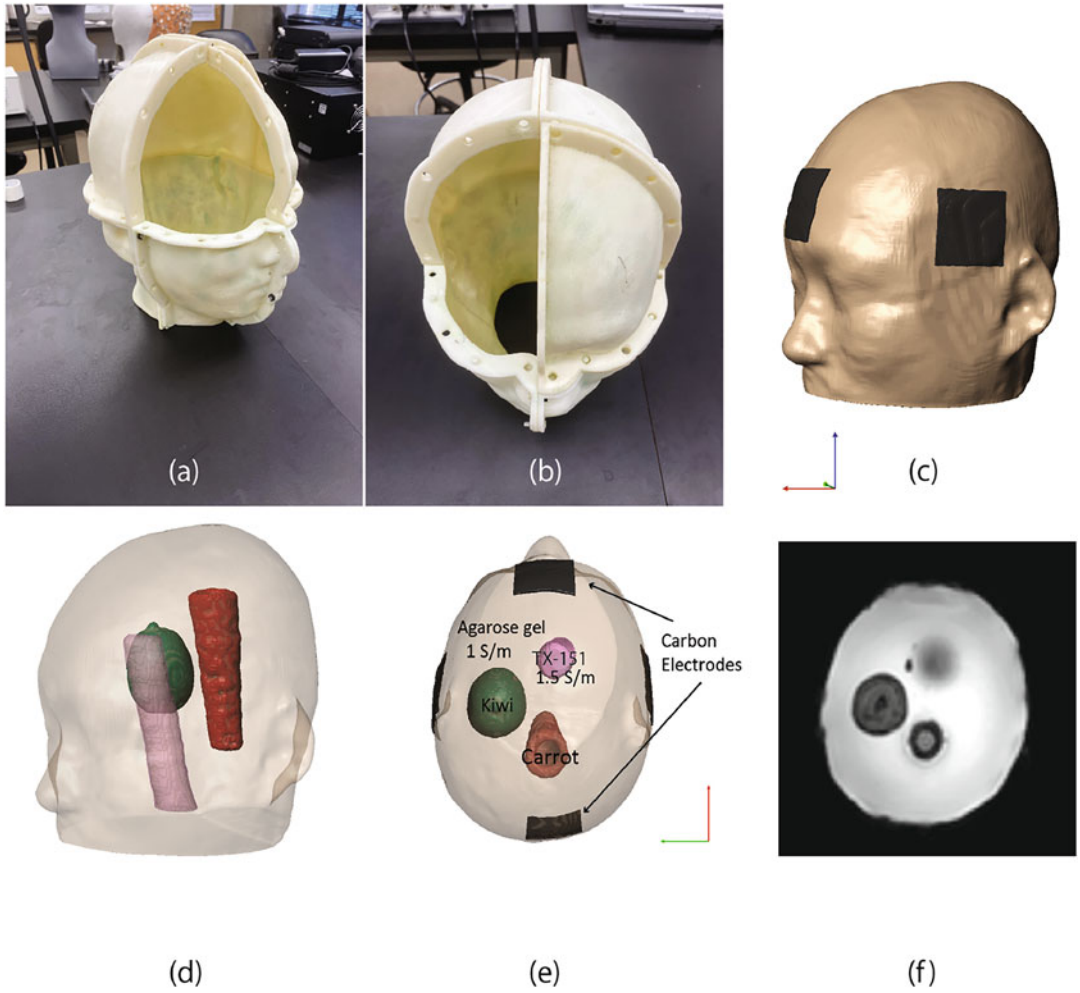

Fig. 4.5 3D printed human head phantom. Parts (**a**–**b**) show views of the phantom. It is printed in eight sections. A studded flange (**b**) and plastic screws are used to hold the segments together. Part (**c**) illustrates the phantom exterior (generated from MR magnitude images) with added carbon electrodes, and the interior of the phantom is shown in (**d, e**) including the agarose gel phantom background (1 S/m) and conductive inclusions of kiwi fruit, TX-151 gel (1.5 S/m), and carrot. Part (**f**) is a magnitude image slice containing all three anomalies

problematic because the parasitic impedances depend on electrode area, electrode type, and the electrolytes in the gel or solution. They are difficult to estimate directly, and methods that avoid including their effects are preferred. In addition, measured values may vary as a function of time as ions redistribute nearby the electrode-electrolyte interface. However, if a large electrode area is used, or if an approximate value is required, a two-probe method may be considered sufficient.

4.3.2 Four-Probe Method

One way of avoiding measuring parasitic resistances is to generate a zero current in the measuring circuit. This can be achieved by using a four-electrode measurement method. In the four-electrode measurement, the current I is flowing through two outer current (injection) electrodes, and the voltage V is measured by a vector voltmeter connected to the inner two measuring (voltage) electrodes (Fig. 4.6b). Due to the high input resistance of the voltmeter, no current flows

through the electrodes, and therefore the resulting impedance Z should not be affected by electrode properties [17].

Figure 4.7 demonstrates a practical four-electrode measurement procedure. Two central circular electrodes and low resistance metallic (copper) plates are used for the current(I) injection and voltage (V) measurements, respectively (Fig. 4.7a). Figure 4.7b shows the four-probe conductivity measurement setup using an LCR meter (ST2830, Sourcetronic, Bremen, Germany); it allows direct connection of the current (injection) and voltage (measuring) electrodes, making it possible to measure the impedance Z and the phase angle so that both conductivity and permittivity characteristics can be determined. Constructing electronic equipment that is capable of making true four-electrode measurements is difficult. Although many impedance measurement devices provide four terminals, it is often the case that circuitry within the devices does not truly isolate current and voltage measurement operations. The Solartron 1260 Impedance Analyzer (Solartron Analytical, Bognor Regis, UK) can make true four-terminal measurements, but is more expensive than many other devices. As shown in Fig. 4.7b, a cubic container can be used to contain the gel or tissue. This makes calculation of conductivity directly from the container dimensions straightforward. However, any sample container can be used as long as the impedance of the container is first measured when it contains a conductivity standard, as described in Chap. 1.

Recall that phantom impedance characteristics should be measured at a frequency relevant to the MR measurement performed. In MREIT, phase measurements are characteristic of tissue or phantom electrical properties at the frequency of the current waveform that is applied, and MREPT measurements reflect properties at the Larmor frequency. MREIT waveform frequencies are very low. For example, in Chauhan et al. [5], the principal frequency of the waveform used was 10 Hz. Measurements at very low frequencies (<10 Hz) may be variable because impedance

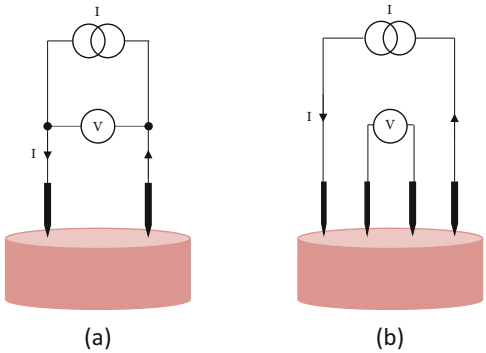

Fig. 4.6 Two- and four-electrode impedance measurement configurations. The two-electrode configuration shown in (**a**) will include electrical characteristics at the electrode-electrolyte interface. The four-electrode configuration in (**b**) measures voltage independent of current-carrying electrodes

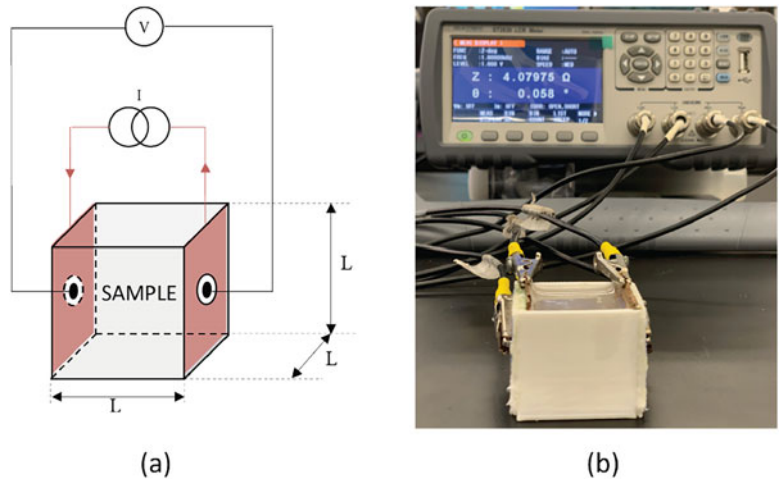

Fig. 4.7 Experimental four-electrode impedance measurement using a cubic sample chamber. Current is applied through large copper electrodes and measured via the central electrodes shown in the schematic of (**a**). An impedance analyzer or LCR meter can be used to measure the impedance, as in (**b**)

analyzers may not be designed to operate in this range or due to changes occurring at the electrode-electrolyte interface [16, 19]. In practice, measurements of phantom properties for use in MREIT are usually performed over the range 10–1000 Hz.

4.3.3 Temperature Dependence

The conductivities estimated for phantom materials in Sect. 4.2 are measured at ambient room temperatures (ca. 22 °C), but values measured in vivo are at body temperature (ca. 37 °C). Conductivity of the gels/tissues increases with temperature, due to increased mobility of charge carriers. Many studies have measured the temperature dependence of conductivity in gels or tissues [19, 29]. Kandadai et al. [29] measured AC conductivity of gelatin, agar, and agarose at room (22 °C) and physiological temperatures (37 °C) in the 100–500 Hz frequency range. In this study, the dependence of gel conductivity on NaCl concentration and temperature was measured. As expected, the conductivity increased by about 2%/°C [19]. Gelatin-based gels were found to be much more conductive (almost twice) than agar or agarose gels with the same concentration of NaCl when measured at the same temperature.

Conducting experiments at 37 °C is important for accurately mimicking human biological systems. However, when using phantom materials, it is also important to consider that differences observed between MREIT-measured conductivities and those found in the laboratory may be due to differences between laboratory temperature and temperatures inside the scanner bore. If possible, it is recommended to measure the MRI scanner room temperature.

4.4 MREIT Electrodes

In MREIT, we typically inject currents into the object to be imaged through surface electrodes. Each current produces a distribution of magnetic flux density within the object. The conventional MREIT electrode configuration utilizes two electrodes—one source (anode) and one sink (cathode) positioned on the object perimeter. Technically, an **electrode** is the surface of metal or conductive rubber that makes proper contact with an electrolyte such as saline or conductive gel [53]. In MREIT, consideration must be given to properties of all elements associated with the electrodes including the electrode body (copper, carbon), electrolyte (hydrogel, saline, conductivity paste), electrolyte carrier material (e.g., sponge for liquid electrolyte), and the mechanism holding electrodes in place, including any connectors or connecting wires.

In phantom experiments, the choice of electrode is mostly determined by MR imaging factors. However, for human experiments, current stimulation can produce unnecessary and possibly dangerous skin irritation or burns [11] when established electrode protocols are not followed or poor electrode design is used. Careful attention to MREIT electrode design and application is therefore needed to understand prevent adverse events and minimize MRI-related artifacts.

4.4.1 Copper Electrodes

In early MREIT studies, a non-magnetic copper foil was often used as an electrode material in phantom experiments [33, 58, 83]. However, when copper electrodes are directly attached to the surface of objects inside the bore of the MRI scanner, these electrodes shield the RF signal and produce severe image artifacts in the region near the conductor (Fig. 4.8a).

In order to shift these artifacts away from the materials of interest, Lee et al. [49] and Oh et al. [59] suggested using recessed electrodes for MREIT. Each recessed electrode shown in Fig. 4.8b is a cylindrical extension of the acrylic phantom container and is filled with a conductive gel such as agar, animal hide gelatin, or TX-151 [49]. The gel in contact with the main phantom body is in electrical contact with the object to be imaged, and a copper electrode is attached to the gel on the outer edge of the recessed electrode. An MREIT current source is connected to the copper electrode via a lead wire

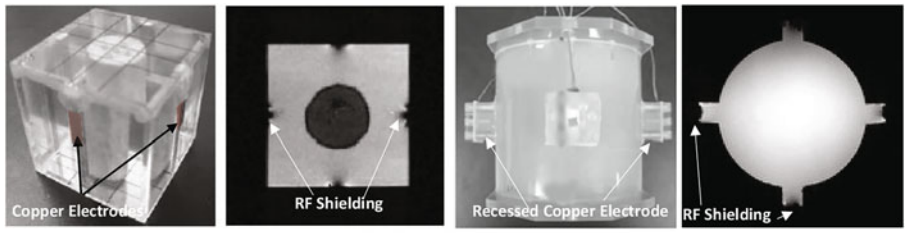

Fig. 4.8 Copper surface electrode and recessed electrodes. (**a**) Copper electrodes attached to saline phantom and MR magnitude image showing shielding artifact. (**b**) Phantom with recessed electrode and respective MR magnitude image. The shielding artifact is moved away from the imaged domain [49, 61]

to introduce the MREIT imaging current. Since the copper is moved away from the phantom surface, the RF shielding artifacts occur inside the recessed electrode container in the gel region near the copper conductor. This makes the data gathered within the object of interest free from any shielding artifact.

Though the recessed electrodes proved very successful in phantom and some animal experiments, they have some disadvantages [35,36]. For example, they are bulky and rigid and require an electrode holder to attach them onto the object's surface. It may be difficult to fit them inside RF coils. To make good contact, there must also be sufficient force attaching them to phantom or sample surfaces. This can end up distorting the shape of the object.

4.4.2 Carbon-Hydrogel Electrodes

To avoid problems associated with copper or recessed electrodes, Minhas et al. [54] introduced thin and flexible carbon-hydrogel electrodes that attached to objects using a conductive adhesive (also known as **self-adhesive electrodes**) for in vivo animal and human experiments [37, 38, 54]. The carbon-hydrogel electrodes comprise a custom-designed thin carbon electrode and a layer of adhesive conductive hydrogel (HUREV Co. Ltd., Korea) (Fig. 4.9). The size of the carbon electrodes used in [37, 38, 54] was $80 \times 60 \times 0.0596$ mm^3, and the conductivities of the carbon and hydrogel used in these electrodes were 2.857×10^4 and 0.17 Sm^{-1}, respectively. The lead wires attached to the carbon electrode were also made of carbon fiber. The larger resistance of the electrodes meant that any coupling between the current source and the MRI scanner was minimized. The overall electrical resistance of each carbon-hydrogel electrode, including wires, was about 300 Ω. Because the electrodes were self-adhesive, they required minimal preparation. However, when they are used on animals, it is easiest to use them at locations with little hair [70].

Minhas et al. [54] reported the performance of the carbon-hydrogel electrodes. It was observed that a thicker hydrogel layer was minimized artifacts near the boundary of the imaged object as the more conductive carbon still produced some RF shielding effect. This type of carbon-hydrogel electrode is inexpensive and requires almost no skin preparation. As noted above, these type of electrodes require a clean surface and secure connection to be most effective. The high resistance of these carbon-hydrogel electrodes may not be suitable for all montages (electrode placements), and they are only usable once. In the next section, we describe a more useful and economical approach to applying currents to phantoms or human subjects.

4.4.3 Carbon Rubber Electrodes

Nonadhesive **carbon rubber electrodes** are made of medical-grade conductive carbon rubber and are designed to be robust and durable. Carbon rubber electrodes are made in many

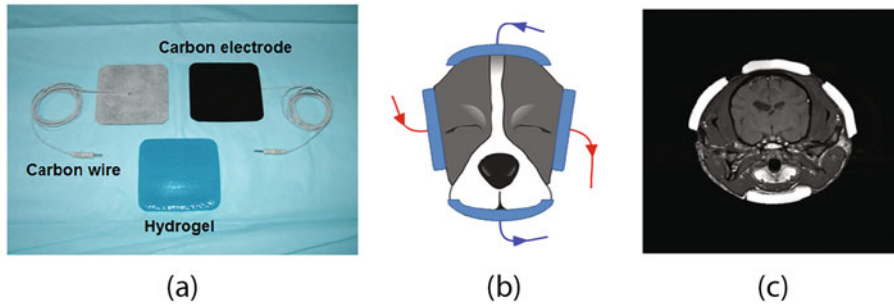

Fig. 4.9 Carbon-hydrogel electrodes. (**a**) Electrodes with lead wires and hydrogel (HUREV Co. Ltd., Korea) [54], (**b**) carbon-hydrogel electrode attached to canine head, and (**c**) resulting MR magnitude image [38]

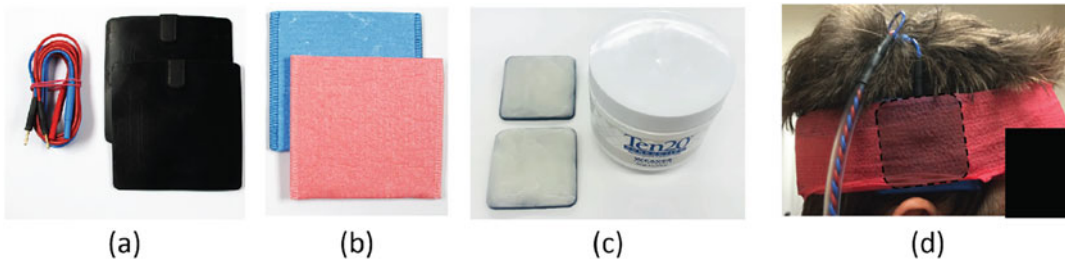

Fig. 4.10 Carbon rubber electrode setup. (**a**) Carbon rubber electrode with lead wire, (**b**) sponge insert, (**c**) conductivity paste applied to electrode, and (**d**) electrode attachment on human head

different sizes and shapes. For current injection applications, carbon rubber electrodes can be used with saline-soaked sponges or conductive gel to securely attach the electrodes to the skin for maximum conductivity and current distribution. These electrodes are particularly useful for applying current to human subjects in mapping transcranial electrical stimulation (tES) current flow in MREIT. Two instances of carbon rubber electrode use in humans are described below.

In the **first method**, carbon rubber electrodes may be connected to the head using a **sponge**. The electrode assembly comprises a carbon rubber electrode that is molded to accept a wire terminated with a metal pin connector and a sponge into which the electrode is inserted. The sponges must be soaked in an isotonic saline solution before use. This setup can be used to easily attach electrodes over thick hair areas [84]. The sponges and electrodes used in neuroConn tES electrodes (neuroCare, Munich, Germany) are shown in (Fig. 4.10a, b). The major disadvantage of this method is that a band or bandage is required to hold the sponge electrodes in place during a current injection session. Also, during long imaging sessions, sometime these electrodes dry out.

In the **second method**, the carbon rubber electrodes may be used with a conductive gel (e.g., Ten20 paste (Weaver and Company, Aurora, CO, USA) or Elefix paste (Nihon Kohden, Tokyo, Japan)) to both affix the electrode securely and provide a good conductive contact (Fig. 4.10c) [84]. Around 5 mm of conductive gel should be introduced on the carbon electrodes to provide good contact. The gel needs to be applied liberally and must make full contact with the area being targeted. Even though the gel is thick and somewhat adhesive, a headband should still be used to secure the electrodes, to prevent them from moving or sliding around. This method is good for long sessions because the gel is unlikely to dry out. After sessions, the area should be cleaned using a wet cloth or by washing the hair. Figure 4.10d shows the attachment of carbon rubber electrode on a human head for use in current density mapping during tES treatments using MREIT.

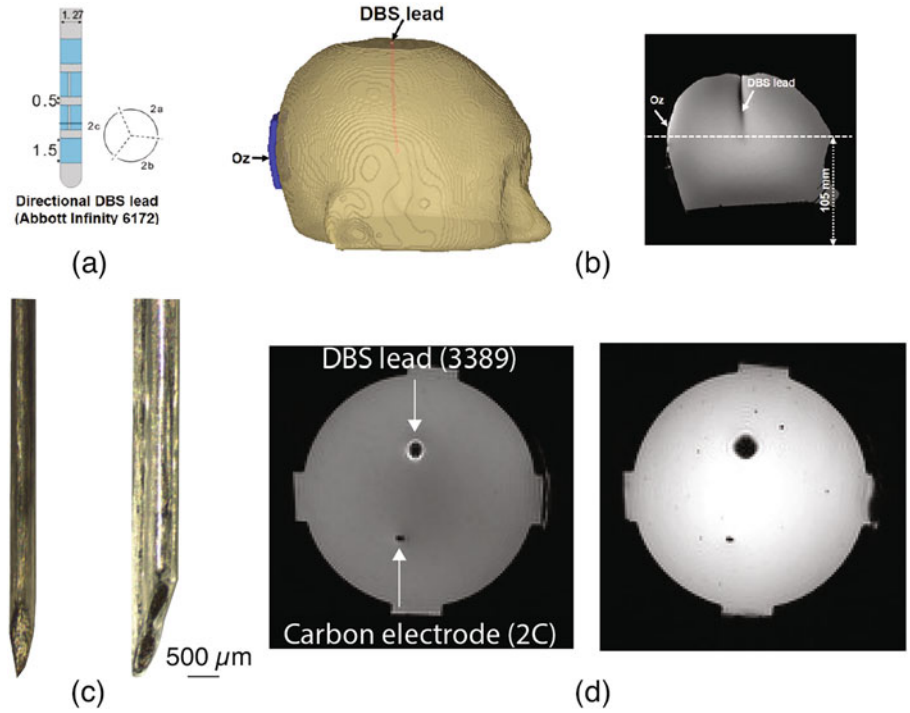

Fig. 4.11 Internal electrodes used in MREIT. (**a**) Directional DBS electrode (Abbott Infinity 6172, Abbott Laboratories, IL, USA), (**b**) sagittal model view showing location of DBS electrode in phantom head and sagittal T1-weighted MR magnitude image of DBS lead imaged at 3 T, (**c**) novel carbon electrodes with (left) single "1C" and (right) two contacts "2C," and (**d**) spin echo (left) and gradient echo (right) 7 T images of a phantom containing both a DBS lead (Medtronic 3389, Minneapolis, MN, USA) and a 2C electrode placed in a gel phantom

4.4.4 Internal Electrodes

MREIT need not be performed using external electrodes, and experiments have been performed to map currents or measure conductivity during deep brain stimulation (DBS), electroporation treatments, or radiofrequency (RF) ablation [3, 7, 44, 73]. MREIT images of current density distribution or conductivity distributions may be an important factor in determining mechanisms of neural excitation, characterizing tissue damage, and confirming correct electrode implantation [40]. Because MREIT signals are concentrated nearby, use of internal electrodes mostly improves the quality of the MREIT images in their neighborhood, although reconstruction even in this region can be challenging [7, 73]. Just as with surface electrodes discussed in Sect. 4.4.1, problems can be caused RF shielding or susceptibility artifacts caused by metal electrodes. One strategy to avoid this is to construct electrodes using carbon, which has a lower conductivity and susceptibility and should result in reduced artifact [45, 46].

Figure 4.11 illustrates use of internal electrodes in phantoms. Figure 4.11a, b shows a schematic of a directional DBS electrode and sagittal model and MR magnitude views of its location in the human head phantom described in Sect. 4.2.4. In Fig. 4.11c, single (1C) and double (2C) novel carbon fiber electrodes are illustrated, and images of both a DBS lead and a 2C electrode placed in a gel phantom and imaged at 7 T are shown in transverse cross section in Fig. 4.11d for (left) spin echo and (right) gradient echo sequences. Image artifacts generated for each electrode type were quantified by measuring full width at half maximum (FWHM) signal for each electrode and sequence type and determining the ratio of the FWHM to actual electrode diameter. The ratios found for the 2C carbon electrode

were 1.34 and 1.00 for spin echo and gradient echo, respectively, while the corresponding ratios found for the DBS lead were 2.34 and 4.69 [46]. This indicates that carbon fiber electrodes may potentially be useful in imaging fields nearby internal electrodes and should not be as affected by artifacts found with metal electrodes.

4.4.5 Electrode Preparation and Placement

For typical MREIT experiments involving two independent current administrations using four electrodes, electrodes are conventionally placed in diametrically opposed pairs [5]. For experiments on human subjects, the preparation and placement of electrodes remain the most critical and hence prone-to-error step in tDCS and in vivo MREIT experiments [10]. During in vivo experiments, monitoring of electrode resistance before and during current injection is considered important for tolerability [10, 32] as unusually high electrode resistance is indicative of undesired electrochemical changes or poor skin contact. In this section, we will discuss the steps involved in attachment of electrodes on a human head for MREIT experiments during tES treatment.

Step 1: Clean the surface or skin with saline or skin prep gel (Nuprep, Weaver and Company, Aurora, CO, USA) in the area where electrodes are to be placed.

Step 2: Precisely locate the electrode position. As head size and shape vary from person to person, it is important to use a fixed protocol such as the international 10–20 Electrode Placement System [42, 69] to determine electrode position for tES treatments and MREIT measurements on humans.

Step 3: *If using sponge electrodes*, place the sponge in isotonic (0.9%) saline solution until saturated. Remove excess saline from the sponge and place electrodes within them (see Fig. 4.10a, b) and place them at the target location [84]. Oversaturated sponges will be leaky, and this may lead to contacts shorting across the material used to secure them. In addition, since saline-soaked sponges are exposed to the room air and are in contact with the human body, the saline can evaporate over the imaging time period, and dehydration will cause an increase in contact resistance. The voltage across current electrodes should therefore be monitored closely during imaging.

If using a conductive gel applied to carbon rubber electrodes to form contacts [84], first apply some gel to the head approximately where the electrode is to be placed, and massage it in gently. Combined with Nuprep, this will prepare the surface to make a good contact with electrode, especially when there is hair in this area. Next, apply a thick layer of gel to the carbon rubber electrodes (∼3–5 mm). A thick layer is required to ensure flexible and consistent electrode-skin contact impedance and is less likely to result in skin irritation and discomfort [84].

Step 3: Use elastic straps or flexible athletic bandage to fasten the conventional saline-soaked or gel-layered rubber electrodes over the desired location. Be aware that the force applied to secure the electrodes over the skin might increase pressure over the electrode and pressure-induced erythema (redness) may appear either under or around the edges of the electrode after current injection.

Step 4: Attach the lead wires and check the contact impedance using the stimulator or constant current source. If impedance is not in desired range, check the electrode connection to the scalp and the lead wires. The best and most stable contacts will develop after electrodes have been in place for at least 10 minutes.

4.5 MREIT Constant Current Sources

A specialized constant current source is required in order to perform MREIT experiments. In most MREIT studies, currents have been injected as rectangular pulses synchronized with a specific MR pulse sequence. Care must be taken in the

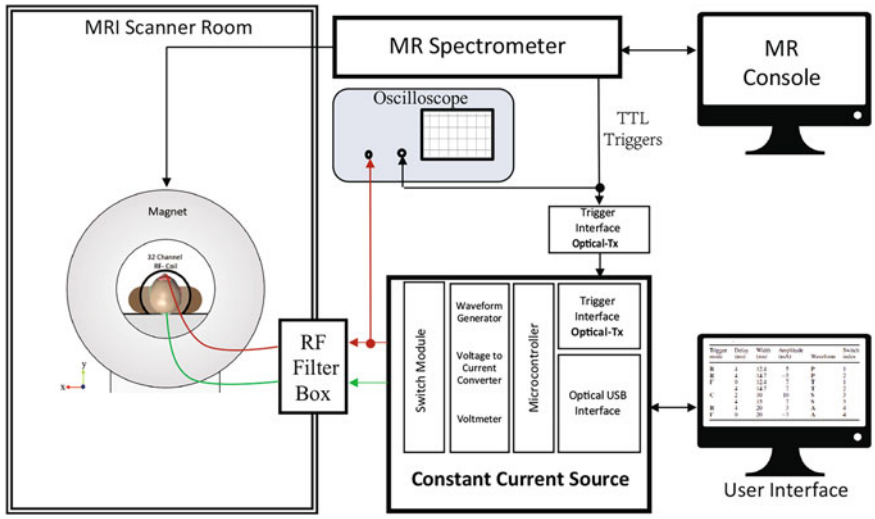

Fig. 4.12 A constant current source comprises a PC interface module, spectrometer interface module, RF pulse detector with trigger interface module, micro-controller, constant current source, switch module, and voltmeter as in [39]

design and arrangement of both the current source and lead wires to minimize the amount of artifact and noise that is ultimately measured in B_z images. This means that the current source must have very precise timing and excellent reproducibility in current amplitude, pulse shape, and width. There should also be no uncontrolled DC offset at the output of the current source. The current source must accept trigger signals from the spectrometer so that current injections can be synchronized with the pulse sequence. Users should be able to adjust current pulse widths T_C so that current injection can be set appropriately for given MR pulse sequence parameters. As discussed in Chap. 5 to avoid chemical changes occurring in phantoms, or to avoid skin irritation in vivo, the net charge of current waveforms must be zero, i.e., equal for both positive and negative current injections. For use in human subjects, the possibility of subject perception at different current frequencies and amplitudes also must be taken into account when designing current waveforms.

In the early stages of MREIT, Kim et al. [34] and Oh et al. [62] designed basic constant current sources (CCS) for MREIT studies used for initial experimental MREIT studies [60, 61]. In later years, Kim et al. designed improved MREIT CCS versions [39]. They described an MREIT current source with features including interleaved current injection, arbitrary current waveform setting, electrode switching to discharge any stored charge from previous current injections, a versatile PC control program, optical isolation from the MR spectrometer and controller PC, and precise current injection timing control for typical MR pulse sequences. Figure 4.12 shows the basic building blocks of a MREIT constant current source. We will discuss the components of the MREIT CCS described in [39] in detail, as they illustrate many important features of any current source used for MREIT.

4.5.1 Constant Current Source (CCS-KHU)

4.5.2 Control Program

To accommodate a range of pulse sequence parameters, Kim et al. [39] developed a current source setup program running on a PC with Microsoft Windows operating system (Microsoft, USA). User interface software was designed in Microsoft Visual Studio to control the CCS from a host computer. Users could control the current

source by editing a script file containing a sequence of commands. These commands might be predetermined based on a chosen pulse sequence to be used in a certain imaging experiment. The command sequence in each line of the script file was initiated by a trigger signal. After each trigger, users could insert a delay period before the current injection started. Each current pulse was specified by its width, amplitude, and waveform type (sine or square). At least one trigger signal for each TR cycle was required as input. This allowed a single trigger signal to initiate multiple current injections (positive or negative) per TR when delay times were specified.

4.5.3 PC Interface

Since the current source described in [39] was designed to be located inside the shielded room while the PC interface was outside, careful design was required to reject electromagnetic interference spreading into the shielded room through the connection. To achieve this, an optically isolated USB port was constructed using a USB controller and fiber-optic diodes. On the PC interface side, a custom USB-optical converter was designed. The optically isolated data communication link between the PC and CCS was established using 10 m optical fiber cables.

4.5.4 Constant Current Source

A micro-controller controlled all circuits in the current source, including a digital waveform generator, voltage-to-current converter, and switch module. Each control parameter could be adjusted by modifying commands in the script file. The digital waveform generator was implemented using a 16-bit digital-to-analog converter (DAC). A separate 8-bit DAC and a digital potentiometer could be employed to adjust the waveform amplitude and offset. An improved Howland constant current circuit was used as the voltage-to-current converter [12]. For either in vitro or in vivo experiments, a user might require different dynamic ranges of current outputs. Therefore, in this constant current source, two separate voltage-to-current converters were designed: one for a 5 mA maximum current output and the other for 50 μA.

4.5.5 Voltmeter

To reconstruct absolute conductivity images, users must measure at least one boundary voltage induced by an injected current [26,47]. Therefore, a voltmeter was also implemented in this design. This allowed users to measure surface voltage differences on the object on non-current-carrying electrodes or to monitor the injected current. To monitor current, the voltmeter measured a voltage drop across a known-value resistor inserted in series with the imaged object.

4.5.6 Discharge Circuit

During current injection, there may be capacitance at electrode-electrolyte interfaces and also within the imaged object. Charge may accumulate in the circuit, and if it is not completely discharged before injecting subsequent current pulses, this may produce erroneous extra currents and therefore changes in B_z images. Therefore, as suggested by Oh et al. [62], a discharge circuit was implemented to momentarily connect the chosen pair of current-injection electrodes to circuit ground after each current injection.

4.5.7 Switch Module

In many MREIT experiments, users use two pairs of electrodes to apply current injections in two independent directions. The design in [39] was able to address and switch currents among up to four electrodes connected to the switch module via multiple photo-MOS switches. The micro-controller set the switches so that the user could inject current between any chosen pair of electrodes. After each current injection, the discharge circuit was triggered. For voltage measurements, the switch module also enabled the user to mea-

sure voltage between a chosen pair of electrodes or across the current-sensing resistor.

4.5.8 Trigger Pulse Interface

The current source obtained trigger signals from the MR spectrometer, which is typically located outside the shielded room containing the magnet bore. Trigger pulses from the MR spectrometer may be contaminated with switching and RF noise generated elsewhere in the system. In order to prevent this noise from entering the current source, the trigger pulse interface was based on an optical coupling device. Trigger signals entered the shielded room through a separate 10 m optical fiber cable and arrive at the current source, where they were converted back to electrical signals. Users could also configure the CCS to accommodate and ignore a preset number of dummy triggers (pulses produced before the main imaging sequence commences).

4.5.9 Commercial Current Sources for MREIT

Apart from the Kyung Hee University (KHU) research current source just described, in recent MREIT studies, commercial stimulators have also been used for constant current administration [5,14,30,46]. Some examples are provided below.

DC-STIMULATOR MR (neuroConn GmbH, Ilmenau, Germany)
In recent studies, researchers have used the neuroConn DC-STIMULATOR MR stimulator as a current source in studies mapping the current density in the brains of humans during tES current administration [5,30]. The system has also been employed in fMRI studies performed inside scanners. Other certified tES stimulators are available from manufacturers such as Brainstim, Magstim, Neuroelectrics, Newronika, and Soterix Medical [84]. The DC-STIMULATOR MR is an MRI-compatible stimulator that is an extension of the neuroConn DC-STIMULATOR PLUS. This stimulator uses RF filter modules with MRI-compatible cables and electrodes to ensure there is no interference between the scanner and stimulator during MRI sequences (Fig. 4.13). While it has a nominal maximum output amplitude of 4.5 mA, MREIT studies have used 1.5 mA current amplitudes to minimize subject perception during pulsed MREIT current administrations.
Adapting the neuroConn DC MC stimulator posed two major challenges for MREIT research. First, it was not feasible for the stimulator to be triggered by the MRI spectrometer, and therefore it was not possible to synchronize current delivery with pulse sequences. Second, the stimulator did not allow for sub-second stimulation durations, which meant that the minimum TR usable in the MR acquisitions was at least one second. This would have drastically increased the scanning time. To address these shortcomings, a custom-made switching circuit was constructed. This enabled users to capture a TTL (transistor-transistor logic) signal programmed to output from the MRI spectrometer to gate DC electrical stimulation as required, including switching polarity of the applied stimulation. The switching circuit was controlled by a separate microprocessor program that could be adapted for use with different pulse sequence types.

IZ2M/IZ2MH Stimulator (Tucker-Davis Technologies, Alachua, FL, USA)
The IZ2M/IZ2MH can be used as part of a larger TDT framework that monitors neural signals over multiple channels. The IZ2M/IZ2MH stimulators (the difference between IZ2M and IZ2MH is the maximum output current and precision permitted) can be used to output constant-current stimulation on up to ten electrodes simultaneously and provide feedback of actual voltages delivered to each electrode. IZ2MH stimulator can deliver a maximum of 3 mA (300 μA for the IZ2/IZ2M) of current per electrode up to 12 V. The TDT framework provides an interface that can be used to program arbitrary

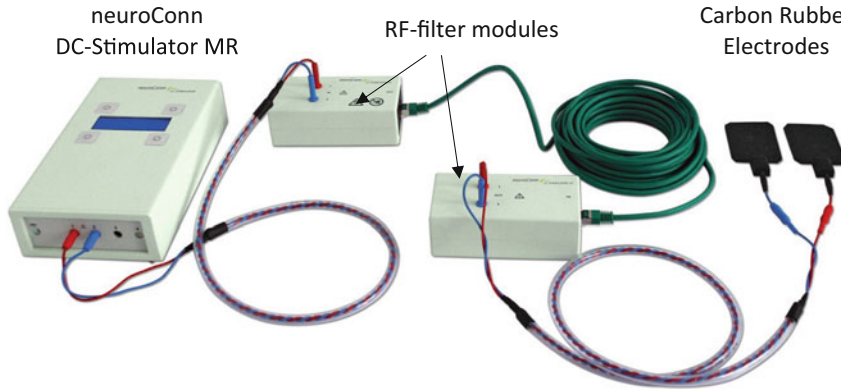

Fig. 4.13 neuroConn DC Stimulator MR. The stimulator source is shown to the left, with the two RF filter modules at the center. The RF filter closest to the stimulator is placed in the scanner console room. The RF filter module closest to the carbon rubber electrodes (right) is placed in the magnet bore near the subject's head

Fig. 4.14 IZ2M stimulator with RZ5D processor base station (left) and MR-compatible non-ferrous headstage connectors (right)

stimulation waveforms (with a sampling rate up to 50 kHz), and waveforms can be triggered from an external MR spectrometer TTL output (Fig 4.14). The stimulator can be also operated using Li-poly battery power, which improves safety and the possibility of interference between stimulator and scanner. However, there is full medical-grade isolation between mains power and electrode outputs.

4.6 Steps in a Typical MREIT or MREPT Study

1. **ACR phantom:** Validation using a standard MRI phantom is important when modifications have been made to an existing pulse sequence or reconstruction algorithm. The performance of the modified MR sequence, for example, in terms of factors such as geometric accuracy, signal-to-noise ratio (SNR), or the presence of magnitude or phase dispersion artifacts should be evaluated before testing using current injection. This can be done using a American College of Radiology (ACR) phantom provided with the MRI scanner [27].
2. **Gel phantom:** After performance of the pulse sequence has been validated using the ACR phantom, the next step is check the MR magnitude and phase quality using a uniform known-conductivity phantom. For MREIT, this step should be done both with and without external current injection and using non-magnetic (carbon) electrodes. The uniform gel phantom can be useful in evaluating the quality of current-induced phase images (phase artifacts, phase noise analysis) and magnetic flux density (B_z or B_1).
3. **Tissue or hybrid phantom:** As our final goal is to implement electrical property imaging technique on animal or human subjects, more complex phantoms are required to further validate the (B_z or B_1) de-noising methods and current density or conductivity reconstruction

algorithms. These types of phantom can be designed using anomalies made different conductivity gels or ex vivo animal tissues in a gel or saline backgrounds.

4. **In vivo animal experiment:** After satisfactory performance has been obtained using the sequences or algorithm tested in the previous step, we can move to in vivo animal experiments. If the animal is anesthetized, there will be little likelihood of motion, and methods can be evaluated to determine effects of physiological noise. Animal ethics approvals from the Institutional Animal Care and Use Committees will be required before any imaging can be done.
5. **In vivo human experiment:** The final step is to perform in vivo human experiments to validate the method or algorithm. This step is critical, as it also requires ensuring the safety of the human subject. Additional approvals may require before performing in vivo human subject imaging. Because of the need to apply external currents in MREIT, careful calculations and tests should be conducted prior to imaging subjects in the scanner to confirm that current or charge densities are lower than recommended and that the frequencies of stimulations are also in a range tolerable by subjects. Ethical approval must be obtained from institutional review boards before imaging human subjects.

4.7 Previous MREIT Studies

4.7.1 MREIT

In this section, we will discuss some specific examples of previous MREIT studies, starting from initial MREIT phantoms and progressing to in vivo measurements.

4.7.2 Non-biological Phantoms

In the early stages of MREIT development, non-biological phantoms were exclusively used to test current density and conductivity reconstruction algorithms. Saline doped with $CuSO_4$ or gels (described in Sect. 4.2.3) were used to construct these phantoms. Figure 4.15 shows some examples of non-biological phantoms used for MREIT. Oh et al. [64] and Kim et al. [41] constructed novel phantoms using saline as a background and thin plastic films pierced by small holes as anomalies, to demonstrate effects of ionic mobility and the apparent conductivity contrast mechanism in MREIT, shown in Fig. 4.15a, b. Kim et al. [41] used the same phantom to compare MREIT- and MREPT-generated conductivity contrasts. The thin film phantom, with or without holes, was also used by Oh et al. [65] to determine temperature distributions via electrical conductivity images obtained using MREIT. Later, Chauhan et al. [5] used an agarose gel phantom to evaluate efficiency of single and multi-shot echo planar imaging (EPI)-based MREIT sequences. In this study, a conductivity contrast was created by placing a hollow insulating cylindrical object at the center of the phantom (Fig. 4.15c). Hybrid non-biological phantoms are also frequently used for MREIT studies. Jeong et al. [28] used a hybrid phantom to optimize magnetic flux density measurement using multiple RF receiver coils and multi-echo in MREIT. To evaluate the method, a cylindrical phantom was designed with saline background with three anomalies (agarose, TX-151, and gelatin), shown in Fig. 4.15d. Other hybrid non-biological phantoms have been used in studies for magnetic flux density measurement optimization [3, 66].

4.7.3 Biological Phantoms

Ideally, MREIT reconstruction algorithm validation should also be performed using a biological phantom, that is, one containing biological material with very similar MR properties to human tissues. In these cases, samples easily obtained at a market, such as chicken breast or porcine muscle, are a convenient substitute for human muscle and other tissues. These tissues also contain little fat and are therefore not likely to complicate MREIT evaluations with MRI fat-shift artifacts. Further, they provide a simple way

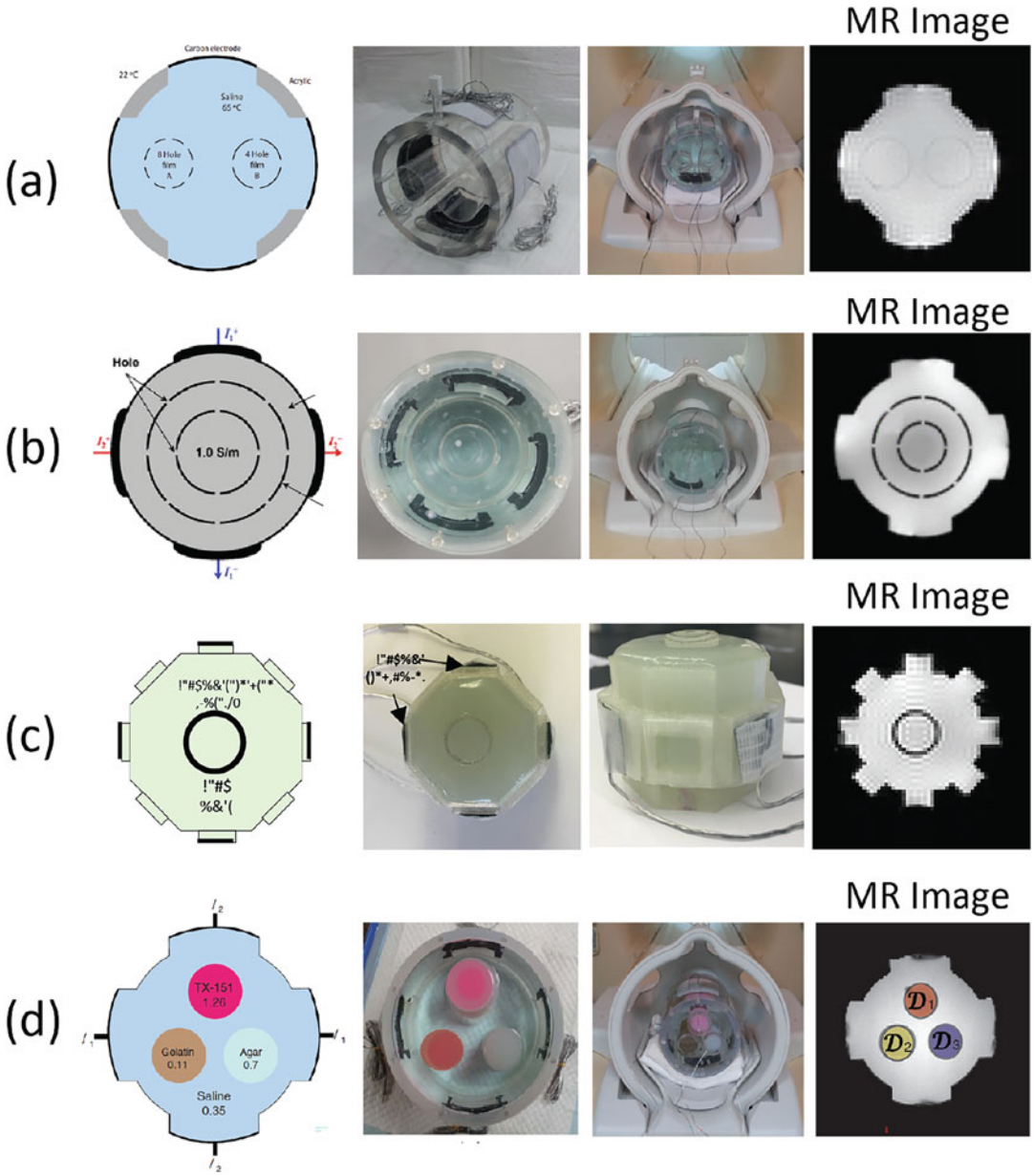

Fig. 4.15 Examples of non-biological phantoms used in MREIT. Shown are (**a, b**) thin film phantoms [41, 64], (**c**) hollow object phantom [5], and (**d**) hybrid phantom [28]

of creating anisotropic MREIT phantoms. Oh et al. [61] constructed a biological tissue phantom containing porcine muscle, chicken breast, and bovine tongue to demonstrate electrical conductivity measurement of biological tissue phantoms using MREIT. These tissues were placed in a agar background as shown in Fig. 4.16a. In 2008, Minhas et al. [54] suggested a carbon-hydrogel electrode for MREIT in vivo experiments and used an ex vivo swine leg to verify its perfor-

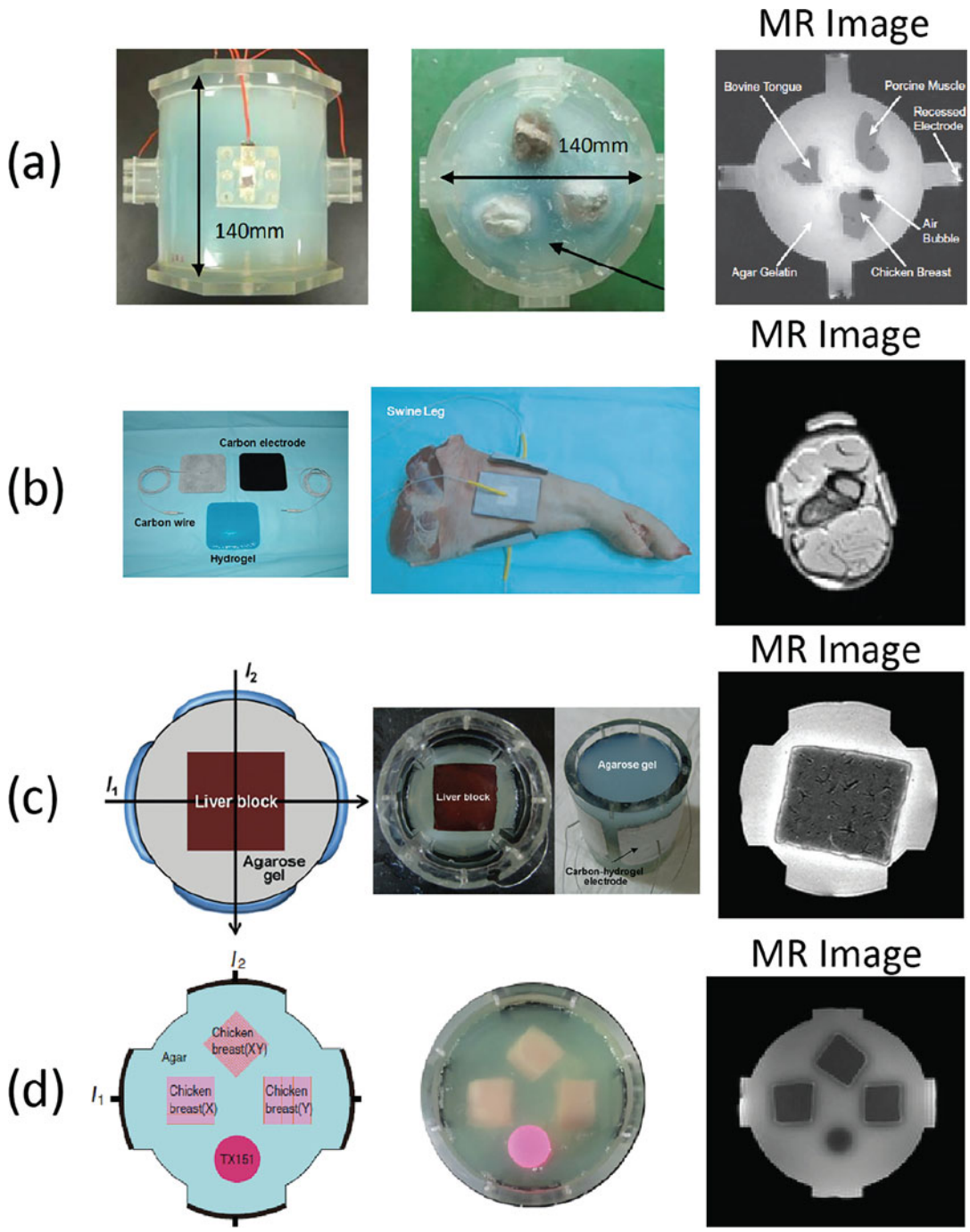

Fig. 4.16 Examples of biological phantoms used in MREIT. Shown are (**a**) early biological tissue phantom [61], (**b**) swine leg phantom [54], (**c**) liver phantom [4], and DT-MREIT phantom [48]

mance in MR and reconstructed conductivity images (Fig. 4.16b). Chauhan et al. [4] demonstrated feasibility of MR-based electrical conductivity imaging to detect RF ablation lesions (Fig. 4.16c) using radiofrequency (RF)-ablated bovine liver samples in agar gel. This study demonstrated that MREIT imaging based on the conductivity distribution of tissues can be used to monitor liver RF ablation without using any contrast media or additional MR scans.

In 2014, Kwon et al. [48] proposed a new method, called DT-MREIT, for absolute conductivity tensor image reconstructions based on a linear relationship between the water diffusion tensor and the electrical conductivity tensor by combining diffusion tensor (DT)-MRI and MREIT techniques. This required an anisotropic phantom. To validate this, Kwon et al. used three pieces of an anisotropic biological tissue (chicken breast) each oriented along a different axis, inside an agar gel phantom, shown in Fig. 4.16d. The method was able to quantitatively recover the direction and magnitude of the anisotropic conductivity tensors as well as isotropic conductivity values. The same phantom has subsequently been used in validating other DT-MREIT-based reconstruction methods [74].

4.7.4 In Vivo Studies

With the advancement of efficient reconstruction algorithms and MR imaging methods, in vivo animal and human MREIT experiments have been increasingly performed to visualize current flow and both isotropic and anisotropic conductivity images. Kim et al. [36] described an in vivo MREIT animal imaging experiment using a 3T MRI scanner (Fig 4.17a). They injected pulsed 5 mA currents into the head of an anesthetized dog and imaged the canine brain *pre-* and *post-mortem*. Later, in 2009, the first in vivo high-resolution MREIT imaging of the human leg was reported by Kim et al. [37] (Fig 4.17b). Because of the large surface area of the carbon-hydrogel electrodes used, it was possible to inject pulse-type currents with an amplitude as high as 10 mA into the leg without producing peripheral nerve stimulation.

Recently, Kasinadhuni et al. [30] and Göksu et al. [18] used MR phase-based current density imaging techniques to compute current density maps of brain during tES treatment on in vivo human subjects. Using the phase data acquired by Kasinadhuni et al. [30] and diffusion tensor images, Chauhan et al. [6] were successfully able to generate conductivity tensor images of the human brain using DT-MREIT (Fig. 4.17(c)).

4.8 MREPT

The MR-based high-frequency (Larmor frequency) technique of magnetic resonance electrical properties tomography (MREPT) may be used to derive electric conductivity and permittivity distributions from the Laplacian of the B1 field map measured by MRI RF coils, specifically maps of the transmit RF field [77, 79, 80]. Because MREPT does require use of any external currents or to have compartments with different electrical properties connected, construction of MREPT phantoms is drastically simpler than for MREIT. Naturally, the phantom concepts used in MREIT can also be used for MREPT, but it must be considered that the electrical properties measured by MREPT are at a much higher frequency (128 MHz for 3 T) than for MREIT (ca. 10 Hz) and the material properties of phantom components should be confirmed using independent measurements at the Larmor frequency. Examples of an MREPT phantom and in vivo animal and human studies are demonstrated in Chap. 8.

4.9 Summary

With the development of faster MRI sequences and techniques, MREIT shows promising poten-

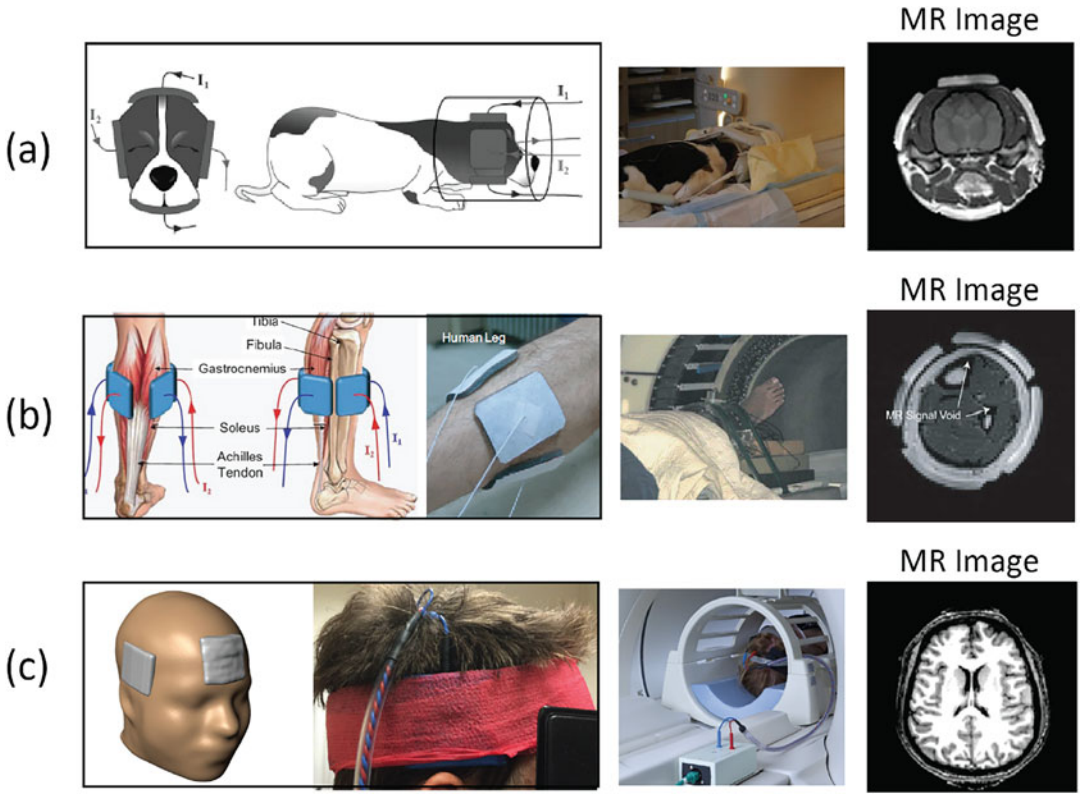

Fig. 4.17 In vivo examples of MREIT uses. Images show configurations used for (**a**) in vivo experiment measuring brain conductivity in the anesthetized dog [36], (**b**) human leg experiment [37], and (**c**) in vivo human brain imaging [6, 30]

tial for routine in vivo measurement of current density and conductivity distributions.

References

1. M.A. Bauman, G.T. Gillies, R. Raghavan, M.L. Brady, C. Pedain, Physical characterization of neurocatheter performance in a brain phantom gelatin with nanoscale porosity: steady-state and oscillatory flows. Nanotechnology **15**, 92 (2004)
2. J.C. Blechinger, E.L. Madsen, G.R. Frank, Tissue-mimicking gelatin–agar gels for use in magnetic resonance imaging phantoms. Med. Phys. **15**, 629–636 (1988)
3. M. Chauhan, W.C. Jeong, H.J. Kim, O.I. Kwon, E.J. Woo, Optimization of magnetic flux density for fast MREIT conductivity imaging using multi-echo interleaved partial Fourier acquisitions. Biomed. Eng. Online **12**, 82 (2013)
4. M. Chauhan, W.C. Jeong, H.J. Kim, O.I. Kwon, E.J. Woo, Radiofrequency ablation lesion detection using MR-based electrical conductivity imaging: a feasibility study of ex-vivo liver experiments. Int. J. Hyperthermia **29**(7), 643–652 (2013)
5. M. Chauhan, R. Vidya Shankar, N. Ashok Kumar, V.D. Kodibagkar, R.J. Sadleir, Multi-shot echo-planar MREIT for fast imaging of conductivity, current density, and electric field distributions. Magn. Reson. Med. **79**(1), 71–82 (2018)
6. M. Chauhan, A. Indahlastari, A.K. Kasinadhuni, M. Schär, T.H. Mareci, R.J. Sadleir, Low-frequency conductivity tensor imaging of the human head in vivo using DT-MREIT: first study. IEEE Trans. Med. Imag. **37**(4), 966–976 (2018)
7. M. Chauhan, S.Z.K. Sajib, S. Sahu, W.S. Kasoff, R.J. Sadleir, Imaging of electromagnetic field distribution in deep brain stimulation (DBS): a biological tissue phantom study, in *Proceedings of the 2021 ISMRM*, vol. 740 (2021)
8. C.C. Chen, Y.L. Wan, Y.Y. Wai, H.L. Liu, Quality assurance of clinical MRI scanners using ACR MRI phantom: preliminary results. J. Digit. Imag. **17**, 279–284 (2004)
9. C.K. Chou, G.W. Chen, A.W. Guy, K.H. Luk, Formulas for preparing phantom muscle tissue at various radio-frequencies. Bioelectromagnetics **5**(4), 435–41 (1984)

10. A. Da Silva, M.S. Volz, M. Bikson, F. Fregni, Electrode positioning and montage in transcranial direct current stimulation. J. Vis. Exp. **51**, e2744 (2011)
11. J.E. Dundas, G.W. Thickbroom, F.L. Mastaglia, Perception of comfort during transcranial DC stimulation: effect of NaCl solution concentration applied to sponge electrodes. Clin. Neurophysiol. **118**, 1166–1170 (2007)
12. S. Franco, *Design with Operational Amplifiers and Analog Integrated Circuits* (McGraw-Hill, New York, 2002)
13. L. Friedman, G.H. Glover, Report on a multicenter fMRI quality assurance protocol. Magn. Reson. Imag. **23**, 827–839 (2006)
14. F. Fu, Ultrahigh field functional magnetic resonance electrical impedance tomography (fMREIT) in neural activity imaging. PhD Thesis, School of Biological and Health Systems Engineering. Arizona State University, Tempe (2019)
15. S. Gabriel, R.W. Lau, C. Gabriel, The dielectric properties of biological tissues: II. Measurements in thefrequency range 10 Hz to 20 GHz. Phys. Med. Biol. **44**, 2251–2269 (1996)
16. C. Gabriel, A. Peyman, E.H. Grant, Electrical conductivity of tissue at frequencies below 1 MHz. Phys. Med. Biol. **54**, 4683–4878 (2009)
17. L.A. Geddes, *Electrodes and the Measurement of Bioelectric Events* (Wiley, New York, 1972)
18. C. Göksu, L.G. Hanson, H.R. Siebner, P. Ehses, K. Scheffler, A. Thielscher, Human in-vivo brain magnetic resonance current density imaging (MR-CDI). NeuroImage **171**, 26–39 (2018)
19. S. Grimnes, O.G. Martinsen, *Bioimpedance & Bioelectricity Basics*, 1st edn. (Academic Press, London, 2000)
20. M.J. Hamamura, L.T. Muftuler, O. Birgul, O. Nalcioglu, Measurement of ion diffusion using magnetic resonance elecrical impedance tomography. Phys. Med. Biol. **51**(11), 2753–2762 (2006)
21. G. Hartsgrove, A. Kraszewski, A. Surowiec, Simulated biological materials for electromagnetic radiation absorption studies. Bioelectromagnetics **8**, 29–36 (1987)
22. K. Hattori, Y. Ikemoto, W. Takao, S. Ohno, T. Harimoto, S. Kanazawa, M. Oita, K. Shibuya, M. Kuroda, H. Kato, Development of MRI phantom equivalent to human tissues for 3.0-T MRI. Med. Phys. **40**, 32303 (2013)
23. A. Hellerbach, V. Schuster, A. Jansen, J. Sommer, MRI phantoms – are there alternatives to agar? PLoS ONE **8**(8), e703430 (2013)
24. M.A. Howard, B.A. Abkes, M.C. Ollendieck, M.D. Noh, C. Ritter, G.T. Gillies, Measurement of the force required to move a neurosurgical probe through in vivo human brain tissue. IEEE Trans. Biomed. Eng. **46**, 891–894 (1999)
25. F.A. Howe, Relaxation times in paramagnetically doped agarose gels as a function of temperature and ion concentration. Magn. Reson. Imag. **6**, 263–270 (1988)
26. Y.Z. Ider, S. Onart, W.R.B. Lionheart, Uniqueness and reconstruction in magnetic resonance electrical impedance tomography (MREIT). Physiol. Meas. **24**, 591–604 (2003)
27. T.M. Ihalainen, N. Lönnroth, J. Peltonen, J. Uusi-Simola, M. Timonen, L. Kuusela, MRI quality assurance using the ACR phahtom in a multi-unit imaging center. Acta Oncol. **50**(6), 966–972 (2011)
28. W.C. Jeong, M. Chauhan, S.Z.K. Sajib, H.J. Kim, I. Serša, O.I. Kwon, E.J. Woo, Optimization of magnetic flux density measurement using multiple RF receiver coils and multi-echo in MREIT. Phys. Med. Biol. **59**, 4827–4844 (2014)
29. M.A. Kandadai, J.L. Raymond, G.J. Shawa, Comparison of electrical conductivities of various brain phantom gels: developing a 'Brain Gel Model'. Mater. Sci. Eng. C **32**(8), 2664–2667 (2012)
30. A.K. Kasinadhuni, A. Indahlastari, M. Chauhan, M. Schar, T.H. Mareci, R.J. Sadleir, Imaging of current flow in the human head during transcranial electrical therapy. Brain Stimul. **10**(4), 764–772 (2017)
31. H. Kato, M. Kuroda, K. Yoshimura, A. Yoshida, K. Hanamoto, S. Kawasaki, K. Shibuya, S. Kanazawa, Composition of MRI phantom equivalent to human tissues. Med. Phys. **32**, 3199–3208 (2005)
32. N. Khadka, D. Truong, M. Bikson, Principles of within electrode current steering. J. Med. Dev. **9**, 020947 (2015)
33. H.S. Khang, B.I. Lee, S.H. Oh, et al., J-substitution algorithm in magnetic resonance electrical impedance tomography (MREIT): phantom experiments for static resistivity images. IEEE Trans. Med. Imag. **21**(6), 695–702 (2002)
34. K.S. Kim, T.I. Oh, S.M. Paek, S.H. Oh, E.J. Woo, S.Y. Lee, J. Yi, Design and performance analysis of current source for 3.0T MREIT system. J. Biomed. Eng. Res. **25**, 165–169 (2004)
35. H.J. Kim, B.I. Lee, Y. Cho, Y.T. Kim, B.T. Kang, H.M. Park, S.Y. Lee, J.K. Seo, E.J. Woo, Conductivity imaging of canine brain using a 3T MREIT system: postmortem experiments. Physiol. Measur. **28**, 1341–1353 (2007)
36. H.J. Kim, T.I. Oh, Y.T. Kim, B.I. Lee, E.J. Woo, J.K. Seo, S.Y. Lee, O. Kwon, C. Park, B.T. Kang, H.M. Park, In-vivo electrical conductivity imaging of a canine brain using a 3T MREIT system. Physiol. Meas. **29**(10), 1145–55 (2008)
37. H.J. Kim, Y.T. Kim, A. Minhas, W.C. Jeong, E.J. Woo, In-vivo high-resolution conductivity imaging of the human leg using MREIT: the first human experiment. IEEE Trans. Med. Imag. **28**(11), 1681–1687 (2009)
38. Y.T. Kim, W.C. Jeong, A. Minhas, C.Y. Lim, H.M. Park, H.J. Kim, E.J. Woo, In vivo magnetic resonance electrical impedance tomography of canine brain: disease model study of ischemia and abscess. Biomed. Eng. Lett. **1**, 56–61 (2011)

39. Y.T. Kim, P.J. Yoo, T.I. Oh, E.J. Woo, Magnetic flux density measurement in magnetic resonance electrical impedance tomography using a low-noise current source. Meas. Sci. Technol. **22**, 105803–105812 (2011)
40. H.J. Kim, Z.J. Meng, S.Z.K. Sajib, M. Chauhan, W.C. Jeong, H. Wi, O.I. Kwon, E.J. Woo, T.I. Oh, Numerical simulation of electromagnetic field distribution induced in brain by electrical stimulation. Electron. Lett. **50**(15), 1045–1047 (2014)
41. D.-H. Kim, M. Chauhan, M.-O. Kim, W.C. Jeong, H.J. Kim, I. Serša, O.I. Kwon, E.J. Woo, Frequency-dependent conductivity contrast for tissue characterization using a dual-frequency range conductivity mapping magnetic resonance method. IEEE Trans. Med. Imag. **34**(2), 507–513 (2015)
42. G.H. Klem, H.O. Lüders, W.H. Jasper, C. Elger, The ten-twenty electrode system of the international federation. The international federation of clinical neurophysiology. Electroencephalograph. Clin. Neurophysiol. Suppl. **52**, 3–6 (1999)
43. K.A. Kraft, P.P. Fatouros, G.D. Clarke, P.R. Kishore, An MRI phantom material for quantitative relaxometry. Magn. Reson. Med. **5**, 555–562 (1987)
44. M. Kranjc, B. Markelc, F. Bajd, M. Čemažar, I. Serša, T. Blagus, D. Miklavčič, In situ monitoring of electric field distribution in mouse tumor during electroporation. Radiology **274**, 115–123 (2015)
45. N.A. Kumar, Neural activity mapping using electromagnetic fields: an in vivo preliminary functional magnetic resonance electrical impedance tomography (fMREIT) study. Ph.D. Thesis, School of Biological and Health Systems Engineering. Arizona State University, Tempe (2020)
46. N.A. Kumar, M. Chauhan, S.K. Kandala, S.-M. Sohn, R.J. Sadleir, Novel carbon electrodes for MREIT current density imaging of deep brain stimulation. Magn. Reson. Med. **84**, 2103–2116 (2018). https://doi.org/10.1002/mrm.28273
47. O. Kwon, E.J. Woo, J.R. Yoon, J.K. Seo, Magnetic resonance electrical impedance tomography (MREIT): simulation study of J-substitution algorithm. IEEE Trans. Biomed. Eng. **49**(2), 160–167 (2002)
48. O. Kwon, W.C. Jeong, S.Z.K. Sajib, H.J. Kim, E.J. Woo, Anisotropic conductivity tensor imaging in MREIT using directional diffusion rate of water molecules. Phys. Med. Biol. **59**(12), 2955–2974 (2014)
49. B.I. Lee, S.H. Oh, E.J. Woo, et al., Three-dimensional forward solver and its performance analysis for magnetic resonance electrical impedance tomography (MREIT) using recessed electrodes. Phys. Med. Biol. **48**(13), 1971–1986 (2003)
50. C. Leuze, Construction and testing of a realistic head phantom for assessment of radiofrequency power deposition in MRI. Diploma Thesis, Universität Leipzig (2008)
51. I. Mano, et al., New polyvinyl alcohol gel material for MRI phantoms. Magn. Reson. Med. **3**(6), 921–926 (1986)
52. G.P. Mazzara, R.W. Briggs, Z. Wu, B.G. Steinbach, Use of a modified polysaccharide gel in developing a realistic breast phantom for MRI. Magn. Reson. Imag. **14**, 639–648 (1996)
53. D.R. Merrill, M. Bikson, J.G.R. Jeffreys, Electrical stimulation of excitable tissue: design of efficacious and safe protocols. J. Neurosci. Methods **141**, 171–198 (2005)
54. A. Minhas, W.C. Jeong, Y.T. Kim, H.J. Kim, T.W. Lee, E.J. Woo, MREIT of postmortem swine legs using carbon-hydrogel electrodes. J. Biomed. Eng. Res. **29**:436–442 (2008)
55. A.S. Minhas, M. Chauhan, F. Fu, R.J. Sadleir, Evaluation of magnetohydrodynamic effects in magnetic resonance electrical impedance tomography at ultra-high magnetic fields. Magn. Reson. Med. **81**, 2264–2276 (2018)
56. M.D. Mitchell, H.L. Kundel, L. Axel, P.M. Joseph, Agarose as a tissue equivalent phantom material for NMR imaging. Magn. Reson. Imag. **4**, 263–266 (1986)
57. L.G. Nyul, J.K. Udupa, On standardizing the MR image intensity scale. Magn. Reson. Med. **42**, 1072–1081 (1999)
58. S.H. Oh, J.Y. Han,S.Y. Lee, M.H. Cho, B.I. Lee, E.J. Woo, Electrical conductivity imaging by magnetic resonance electrical impedance tomography (MREIT). Magn. Reson. Med. **50**(4), 875–878 (2003)
59. S.H. Oh, B.I. Lee, E.J. Woo, S.Y. Lee, M.H. Cho, O.I. Kwon, J.K. Seo, Conductivity and current density image reconstruction using harmonic B_z algorithm in magnetic resonance electrical impedance tomography. Phys. Med. Biol. **48**, 3101–3116 (2003)
60. S.H. Oh, B.I. Lee, E.J. Woo, S.Y. Lee, T.S. Park, M.H. Cho, O.I. Kwon, J.K. Seo, Magnetic resonance electrical impedance tomography at 3 Tesla field strength. Mag. Reson. Med. **51**, 1292–1296 (2004)
61. S.H. Oh, B.I. Lee, E.J. Woo, S.Y. Lee, T.S. Kim, O.I. Kwon, J.K. Seo, Electrical conductivity images of biological tissue phantoms in MREIT. Physiol. Meas. **26**, S279–S288 (2005)
62. T.I. Oh, Y. Cho, Y.K. Hwang, S.H. Oh, E.J. Woo, S.Y. Lee, Improved current source design to measure induced magnetic flux density distributions in MREIT. J. Biomed. Eng. Res. **27**, 30–37 (2006)
63. S.H. Oh, S.Y. Lee, M.H. Cho, T.-S. Kim, I.H. Kim, Electrical conductivity estimation from diffusion tensor and T2: a silk yarn phantom study, in *Proceedings 14th Annual Meeting International Society for Magnetic Resonance in Medicine*, vol. 3034 (2006)
64. T.I. Oh, Y.T. Kim, A. Minhas, J.K. Seo, O. Kwon, E.J. Woo, Ion mobility imaging and contrast mechanism of apparent conductivity in MREIT. Phys. Med. Biol. **56**, 2265–2277 (2011)
65. T.I. Oh, H.J. Kim, W.C. Jeong, M. Chauhan, O.I. Kwon, E.J. Woo, Detection of temperature distribu-

tion via recovering electrical conductivity in MREIT. Phys. Med. Biol. **58**(8), 2697–2711 (2013)
66. T.I. Oh, W.C. Jeong, J.E. Kim, S.Z.K. Sajib, H.J. Kim, O.I. Kwon, E.J. Woo, Noise analysis in fast magnetic resonance electrical impedance tomography (MREIT) based on spoiled multi gradient echo (SPMGE) pulse sequence. Phys. Med. Biol. **59**, 4723–4738 (2014)
67. S. Ohno, H. Kato, T. Harimoto, et al., Production of a human-tissue-equivalent MRI phantom: optimization of material heating. Magn. Reson. Med. Sci. **7**(3), 131–140 (2008)
68. T. Onishi et al., Biological tissue-equivalent agar-based solid phantoms and SAR estimation using the thermographic method in the range of 3–6 GHz. IEICE Trans. Commun. **E88-B**(9), 3733–3741 (2005)
69. R. Oostenveld, P. Praamstra, The five percent electrode system for high-resolution EEG and ERP measurements. Clin. Neurophysiol. **112**, 713–719 (2001)
70. B. Paneri, D. Adair, C. Thomas, et al., Tolerability of repeated application of transcranial electrical stimulation with limited outputs to healthy subjects. Brain Stimul. **9**, 740–754 (2016)
71. R.J. Sadleir, F. Neralwala, T. Te, A. Tucker, A controllably anisotropic conductivity or diffusion phantom constructed from anisotropic layers. Ann. Biomed. Eng. **37**(12), 2522–2531 (2009)
72. H.G. Schnack, N.E.M. vanHaren, H.E. HulshoffPol, M. Picchioni, M. Weisbrod, Reliability of brain volumes from multicenter MRI acquisition: a calibration study. Hum. Brain Map. **22**, 312–320 (2004)
73. S.Z.K. Sajib, T.I. Oh, H.J. Kim, O. Kwon, E.J. Woo, In vivo mapping of current density distribution in brain tissues during deep brain stimulation (DBS). AIP Adv. **7**, 015004 (2017)
74. S.Z.K. Sajib, M. Chauhan, O.I. Kwon, R.J. Sadleir, Magnetic-resonance-based measurment of electromagnetic fields and conductivity in vivo using single current administration - a machine learning approach. PLoS ONE **16**(7), e0254690 (2021)
75. G.C. Scott, M.L.G. Joy, R.L. Armstrong, R.M. Henkelman, Measurement of nonuniform current density by magnetic resonance. IEEE Trans. Med. Imag. **10**, 362–374 (1991)
76. G.C. Scott, M.L.G. Joy, R.L. Armstrong, R.M. Henkelman, Sensitivity of magnetic-resonance current-density imaging. Journal of Magnetic Resonance **97**, 235–254 (1992)
77. R. Stollberger, P. Wach, Imaging of the active B1 field in vivo. Magn. Reson. Med. **35**, 246–251 (1996)
78. S. Vellmer, D. Edelhoff, D. Suter, I.I. Maximov, Anisotropic diffusion phantoms based on microcapillaries. J. Magn. Reson. **279**, 1–10 (2017)
79. T. Voigt, U. Katscher, O. Dössel, Quantitative conductivity and permittivity imaging of the human brain using electic properties tomography. Magn. Reson. Med. **66**, 456–466 (2011)
80. J. Wang, M. Qiu, Q.X. Yang, M.B. Smith, R.T. Constable, Measurement and correction of transmitter and receiver induced non uniformities in vivo. Magn. Reson. Med. **53**, 408–417 (2005)
81. Z.L. Wang, Y. Seo, J.M. Chia, N.K. Rollins, A quality assurance protocol for diffusion tensor imaging using the head phantom from American College of Radiology. Med. Phys. **38**, 4415–4421 (2011)
82. E.J. Woo, J.K. Seo, Magnetic resonance electrical impedance tomography (MREIT) for high-resolution conductivity imaging. Physiol. Measur. **29**(10), R1 (2008)
83. E.J. Woo, S.Y. Lee, C.W. Mun, Impedance tomography using internal current density distribution measured by nuclear magnetic resonance, in *Proceedings of SPIE 2299, Mathematical Methods in Medical Imaging III*, vol. 2299 (1994)
84. A.J. Woods, A. Antal, M. Bikson, P.S. Boggio, A.R. Brunoni, P. Celnik, L.G. Cohen, F. Fregni, C.S. Herrmann, E.S. Kappenman, H. Knotkova, D. Liebetanz, C. Miniussi, P.C. Miranda, W. Paulus, A. Priori, D. Reato, C. Stagg, N. Wenderoth, M.A. Nitsche, A technical guide to tDCS, and related non-invasive brain stimulation tools. Clin. Neurophysiol. **127**, 1031–1048 (2016)
85. B. Xiong, R.D. Loss, D. Shields, T. Pawlik, R. Hochreiter, A.L. Zydney, M. Kumar, Polyacrylamide degradation and its implications in environmental systems. Clean Water **1**, 17 (2018)

MR Current Density and MREIT Data Acquisition

5

Munish Chauhan and Rosalind Sadleir

Abstract

Magnetic resonance electrical impedance tomography (MREIT) can provide internal conductivity distributions at low frequency (below 1 kHz) induced by an external injecting current. In MREIT, we inject current I using at least one pair of electrodes into an object to produce internal current density $\mathbf{J} = (J_x, J_y, J_z)$ and magnetic flux density $\mathbf{B} = (B_x, B_y, B_z)$ in the object. An MRI scanner with its main magnetic field pointing the z direction is used to measure the induced magnetic flux density (B_z) caused by external current injection. To avoid the interaction of external current injection with MRI acquisitions, it is important to synchronize the current injection with MRI sequence. In the first part of this chapter, we will discuss the practical aspects of a successful MREIT experiment. Following a brief introduction to the experiment setup, we will then summarize various MRI sequences used for MREIT, magnetic flux density measurement, and image reconstructions for MREIT experiments.

M. Chauhan · R. Sadleir (✉)
School of Biological and Health Systems Engineering, Arizona State University, Tempe, AZ, USA
e-mail: mchauha4@asu.edu; rosalind.sadleir@asu.edu

5.1 Introduction

The first step in MREIT reconstruction is phase data acquisition using an MRI scanner. We can think of an entire MREIT system as comprising an MRI scanner, constant current source, surface or internal electrodes, and current density or conductivity image reconstruction algorithms or software [1–5]. In this chapter, we will discuss factors related to to the MRI scanner and external current injection which directly affect the MREIT data quality. Examples of these are the magnet field strength, RF coil type, injected current magnitude and current injection time (T_c) and current source synchronization. We will go on to consider phase data preprocessing, noise corrections, and preparation of data for reconstruction procedures. Finally, some specific application examples are discussed.

5.2 Experiment Setup

In designing an MREIT experiment, the first design constraint will be the space available within the magnet bore, followed by the type of coil to be used. In many applications a transmit/receive volume coil is used, but many imaging procedures on animals or humans may involve use of special head or surface coils. It is critically important that

R. Sadleir, A. S. Minhas (eds.), *Electrical Properties of Tissues*, Advances in Experimental Medicine and Biology 1380, https://doi.org/10.1007/978-3-031-03873-0_5

equipment to be placed inside the magnet bore is MR-safe and will meet the space constraints. The second important choice to make is the image pulse sequence type. For example, standard spin echo pulse sequences can produce low artifact images, but the total time required for a full spin echo pulse sequence may be too long for practical use with human subjects. Electrode design and preparation can be performed following recommendations in Chap. 4. Once these factors are determined, image parameters can be adjusted to capture data within the body region of interest while maximizing the MREIT data signal-to-noise ratio (SNR). For MREIT data collection, the current source must also be synchronized with the imaging sequence. This section discusses these important initial steps.

5.2.1 System Configurations/Magnetic Resonance Imaging Scanner

MR magnitude image SNR is key to MREIT image quality, because the standard deviation in measured B_z noise is inversely proportional to the MR image SNR [6, 7]. The MR magnitude image SNR is dependent on the following factors [8]:

1. Magnetic field strength
2. Slice thickness and receiver bandwidth
3. Field of view (FOV)
4. Image matrix size
5. Number of acquisitions (averages)
6. Scan parameters (TR, TE, flip angle)
7. Selection of the transmit and receive coil (RF coil)

SNR is proportional to the degree of nuclear spin polarization, which scales approximately linearly with magnetic field strength. For example, the move to 3 T is driven mainly by its approximate doubling of the signal-to-noise ratio (SNR) compared to 1.5 T [9]. The improved SNR can be used to shorten acquisition times, to improve spatial resolution at a fixed scan time, or a combination of the two.

New human MR systems operating at static magnetic fields of 7 T or higher ($\geq$ 300 MHz proton frequency) have recently become available. Although this ultrahigh field increases the SNR, imaging human-sized objects at such high frequencies presents several challenges, including the presence of nonuniform RF fields, enhanced susceptibility artifacts, and higher tissue RF energy deposition (i.e., specific absorption rate (SAR)) [10]. Field nonuniformity is more likely to manifest at these high frequencies because the wavelength at the Larmor frequency (around 1 m) approaches the scale of the imaged objects, and thus their electrical property distribution greatly affects RF field distributions. RF inhomogeneity also produces the data required to reconstruct EPT images [11, 12]. However, it is important to note that the field may be distorted at these high frequencies by many other factors as well as the body's properties.

Parameters 2–6 listed above can be controlled during MR image acquisition. The selection of appropriate MRI RF coils can also improve the MR image SNR. Conventional RF coils, including multichannel phased array coils, can be adopted for MREIT as long as there is enough space for electrodes and lead wires within them.

Main magnetic field homogeneity and gradient linearity of MRI scanner are also important for MREIT. Main magnetic field inhomogeneity can be corrected by carefully shimming the field before starting imaging. There are normally many different shimming methods available in commercial MR scanners. These can be passive, active, or both. Clinical scanners typically perform automatic shimming as part of the preparation phase of each scan. Sensitivity and B_1-field uniformity of the RF coil significantly affect the image quality in MREIT. All possible means must be sought to minimize noise and artifacts in collected k-space data when configuring an MREIT system.

5.2.2 TTL Triggers

In order to perform MREIT experiments, a constant current source (CCS) (see Chap. 4) must

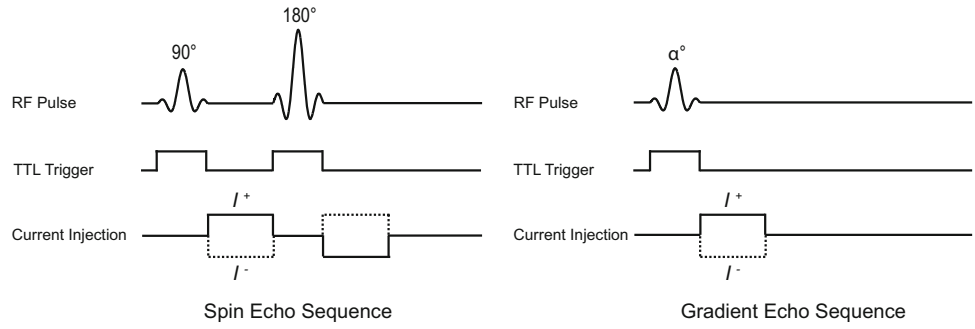

Fig. 5.1 MREIT TTL trigger setup for (left) spin echo and (right) gradient echo sequences. Two variants of each current injection protocol are presented

correctly inject current into the object or subject [1,3]. In most MREIT studies, these constant currents have been injected as rectangular pulses synchronized with a chosen MR pulse sequence. MR system spectrometers can be programmed to generate output TTL (transistor-transistor logic) pulses during a MRI scan. Similar pulses are often used in fMRI, where TTL pulses are synchronized with image acquisition, often to trigger the start of a user task. For MREIT experiments, it is desirable to avoid current injection during RF pulses as this may disturb phase images. For example, TTL triggers could be generated to indicate the *end* of every RF pulse and to initiate external current injection. More than one trigger TTL pulse per TR may be required. In spin echo (SE) MREIT sequences, two TTL trigger pulses can be used, to indicate the end of the 90° and 180° degree RF pulses, respectively. Gradient echo (GE) sequences require only one trigger pulse, as shown in Fig. 5.1. In the case shown in Fig. 5.1, note that current source operation is triggered by the *falling edge* of each TTL pulse, as the current is injected immediately after the TTL pulse ends. The same current injection pattern could be generated if the current source is programmed to be triggered by the rising edge of each TTL pulse but with a delay between detection of the rising pulse and the start of the current pulse. In general, the CCS should be able to accommodate rising or falling edge triggers and be able to insert a variable-width delay after each pulse.

5.3 Data Acquisition

Figure 5.2a shows a typical setup for MREIT imaging experiments. The oscilloscope is used to monitor TTL pulses and the level of injected output current. The inner and outer RF filters can be used to minimize propagation of external electromagnetic noise into or out of the scanner room. Ideally, current-carrying wires near the imaging object should be aligned parallel to the main magnetic field direction, to avoid any stray magnetic field induced by these current-carrying wires (as discussed in Chap. 6). Figure 5.2b shows an example of an SE pulse sequence commonly used in MREIT experiments. The injected current induces a magnetic flux density **B**. This produces a phase accumulation proportional to the z-component (B_z) of $\mathbf{B}=(B_x,B_y,B_z)$. Figure 5.2b–c shows example TTL pulses and corresponding positive-first current (I^+) injected during an MREIT experiment conducted using an SE sequence.

5.4 Measurement of B_z

As discussed in Chap. 3, the MR signal is denoted (S). For MREIT, the MR spectrometer provides complex k-space data $S^{\pm}$ corresponding to external current injections, I^+ and I^-, respectively. This signal is

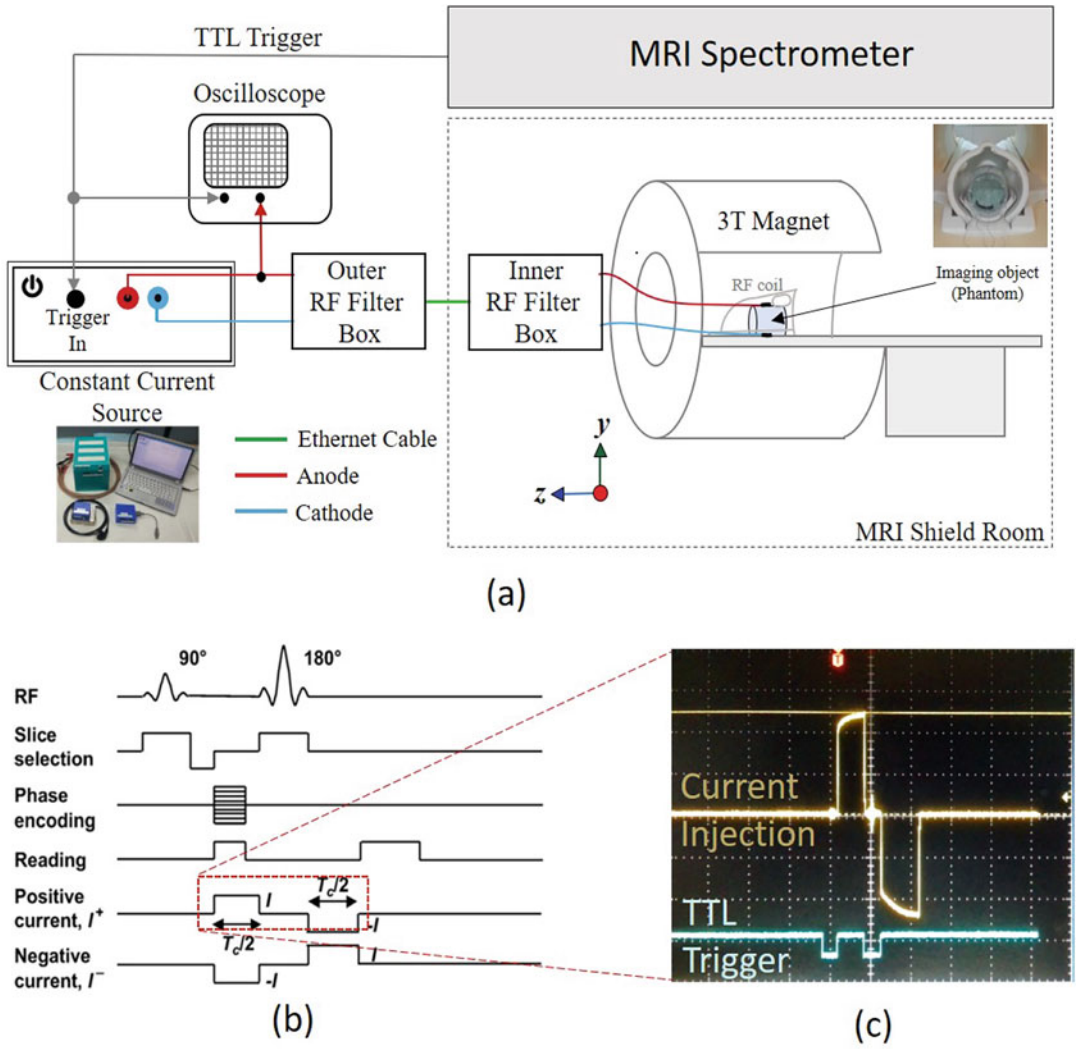

Fig. 5.2 Typical MREIT current injection configuration. (**a**) illustrates connections and position of the MREIT CCS with respect to the imaged object. Current injection may be monitored using an oscilloscope connected across a known resistor in the CCS, and RF filtering is employed to minimize noise pickup by the scanner or CCS. (**b**) shows the schematic for an example current injection pattern I^+. (**c**) is a photograph of the oscilloscope screen for an I^+ during an SE sequence

$$S^{\pm}(k_x, k_y) = \iint \rho(x, y) e^{i\delta(x,y)} e^{\pm i\gamma B_z(x,y)T_c} \times e^{-i(xk_x + yk_y)} dx dy \qquad (5.1)$$

where ρ is a conventional MR magnitude image, δ is any systematic phase artifact, $\gamma = 26.75 \times 10^7\ T^{-1}.s^{-1}$ is the gyromagnetic ratio of hydrogen, and T_c is the current pulse width in seconds.

Phase images acquired using positive-first and negative-first currents, I^+ and I^-, can be subtracted (or complex-divided) to cancel out the systematic phase artifact δ in images acquired by the MRI scanner.

Taking the two-dimensional discrete Fourier transform, we obtain the following complex MR images:

$$\mathcal{M}^{\pm}(x, y) = \rho(x, y) e^{i\delta(x,y)} e^{\pm i\gamma B_z(x,y)T_c} \qquad (5.2)$$

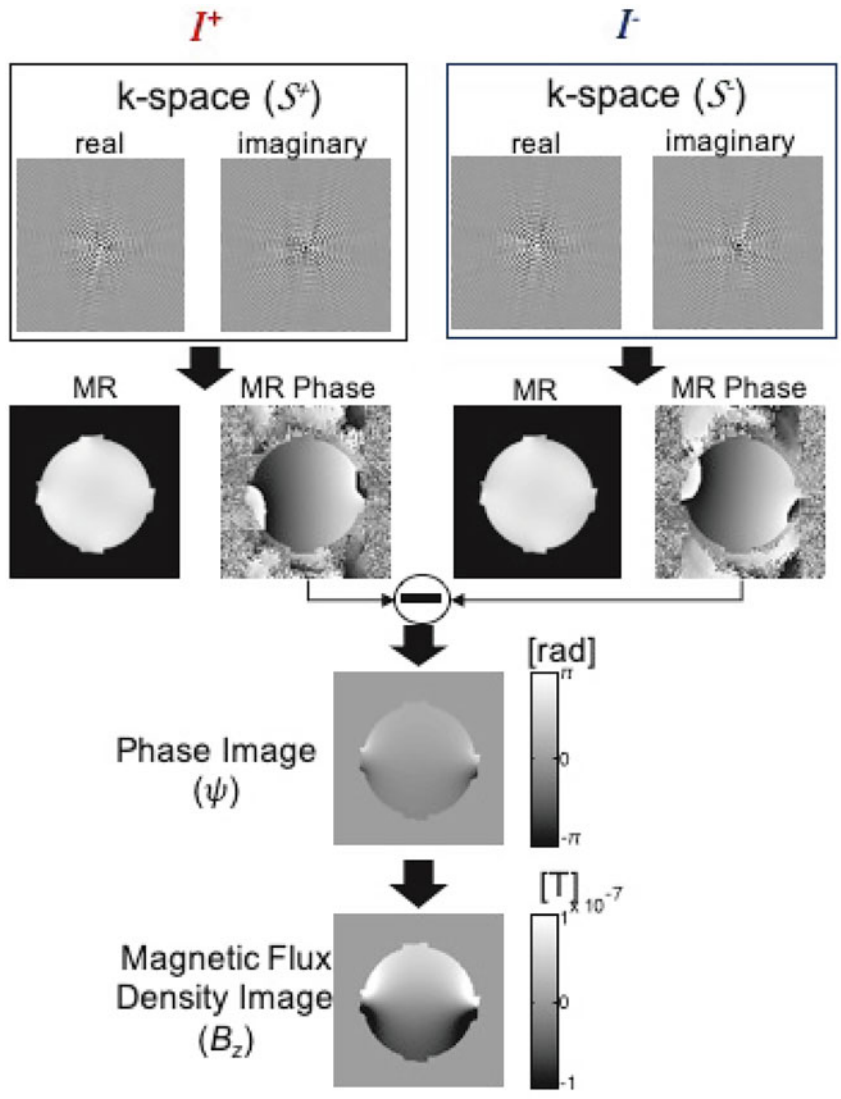

Fig. 5.3 MREIT data flow. Data acquired for I^+ or I^- images are Fourier transformed to produce complex spatial data. MR phase images from I^- are subtracted from I^+ images to obtain the net phase ψ. Images of ψ are then rescaled to obtain B_z

The net phase change, $\psi(x, y)$, is

$$\psi(x, y) = \arg\left(\frac{\mathcal{M}^+(x, y)}{\mathcal{M}^-(x, y)}\right) = 2\gamma B_z(x, y)T_c \tag{5.3}$$

where we assume that the operator $\arg(\cdot)$ includes any necessary phase unwrapping. By performing the complex division using I^+ and I^-, the systematic phase artifact term δ is eliminated, and the phase difference is doubled. Once ψ is obtained, we compute B_z as

$$B_z(x, y) = \frac{\psi(x, y)}{2\gamma T_c} = \frac{1}{2\gamma T_c}\arg\left(\frac{\mathcal{M}^+(x, y)}{\mathcal{M}^-(x, y)}\right) \tag{5.4}$$

The complete B_z reconstruction process from raw k-space MRI data is shown in Fig. 5.3 for a SE sequence. In practice, the data required to form ψ need not be obtained using separate scans, and all required phase data for any type of sequence can be collected during one scan using multiple dynamics or averages within the

pulse sequence. This is an important consideration in the presence of magnet drift and when using small currents. Drift in the main magnetic field B_0 can result in the effective phase artifact changing as a function of time. If this occurs then the resulting ψ data will be incorrect. Effects of magnet drift may be relatively minor when large injection currents are used, but at the amplitudes used in human tES experiments (ca. 1 mA), this drift may result in detrimental signal loss [13,14]. For example, in a Philips 3T Achieva system used in [13,14], it was observed that the main magnetic field drift was around 0.01 Hz/min. The magnetic fields due to ca. 1 mA currents correspond to frequency shifts only around four times this level (0.043 Hz). Therefore, data to be divided should be gathered as close together in time as possible. This may be done by reversing polarity in alternate averages of one phase encode line. Careful attention must thus also be paid to the order in which slices, averages, and phase encode lines are gathered. Multiple runs of the same sequence can be averaged to improve ultimate SNR while keeping each run a reasonable length for subjects [13–15].

5.4.1 Noise in MREIT

Noise in measured B_z data is the primary limiting factor in determining the spatial resolution of a reconstructed current density or conductivity image. The **first method** to estimate noise levels in B_z images was suggested by Scott et al. [6]. They showed that the noise standard deviation, s_{B_z}, in measured B_z data is inversely proportional to the signal-to-noise ratio (SNR) of the magnitude image, $\Upsilon_{\mathcal{M}}$, and the total current injection time, T_c as

$$s_{B_z} = \frac{1}{2\gamma T_c \Upsilon_{\mathcal{M}}} \tag{5.5}$$

To evaluate $\Upsilon_{\mathcal{M}}$, the most commonly used technique is based on the signal statistics in two separate regions of interest (ROIs) from a single image: one in the tissue of interest to determine the signal intensity and one in the image background to measure the noise intensity [16,17]. There are two important preconditions for SNR measurements based on this "two-region" approach: a spatially homogeneous distribution of noise over the whole image is required, and the statistical intensity distribution of the noise should be known so that the noise properties measured in a background area can be used to deduce the noise distribution overlaying the anatomic structures in the foreground. These assumptions have been valid for many MR images, particularly for images from standard *single-channel volume quadrature coils*.

The use of *phased array surface coils* and *parallel reconstruction techniques* can influence both the statistical and the spatial distribution of noise [18, 19]. Use of a sum-of-squares reconstruction for data from phased array coils [20] changes the statistical distribution of background noise. Dietrich et al. [21] evaluated the validity of the "two-region" approach in comparison with two alternative techniques in MRI experiments with multielement surface coils and parallel imaging techniques. Depending on the type of RF coil and imaging technique used, the method suggested by Dietrich et al. [21] is recommended to calculate $\Upsilon_{\mathcal{M}}$ in MREIT data.

A practical approach which calculates MREIT noise standard deviation directly from measured magnetic flux density (B_z) data was suggested by Sadleir et al. [7]. The following relation provides a way to experimentally estimate noise standard deviation $\hat{s}_{B_z}$ in measured B_z data by determining

$$\hat{s}_{B_z} = \frac{1}{\sqrt{\frac{20}{\Delta^4} + \frac{6}{\Delta_z^4}}} s_{\nabla^2 B_z} \tag{5.6}$$

where Δ is the distance between consecutive pixels along the x and y directions, Δ_z is the slice thickness, and $s_{\nabla^2 B_z}$ is the standard deviation of the Gaussian random noise in $\nabla^2 B_z$.

Acquiring B_z data using a homogeneous conductivity phantom, we can evaluate relation between theoretical and practical methods, described in Eqs. (5.5) and (5.6), respectively. If s_{B_z} in (5.5) and $\hat{s}_{B_z}$ in (5.6) are approximately equal to each other (within a factor of about two),

we can conclude that the MREIT experiment is consistent.

In MREIT, the measured raw data is the net phase change ψ in (5.3). This phase change is proportional to the product of B_z and T_c. Since B_z is directly proportional to I, we must optimize the MREIT pulse sequence to maximize the product of I and T_c in Fig. 5.1. During in vivo human imaging experiments, permissible values of I and T_c must be determined carefully considering the physiological effects of current injection [22].

5.4.2 MRI Pulse Sequences for MREIT

Spin Echo

In last two decades, many MRI-based methods have been developed to measure the effects of applied currents at various frequencies (i.e., near DC [2], at RF at the Larmor frequency of the scanner [23] and low-frequency AC currents up to 2 kHz [24,25]. Most of these methods use a standard spin echo (SE) pulse sequence, which acquires one line of k-space data per repetition time (TR). The SE pulse sequence shown in Fig. 5.4 has been widely used in MREIT, since it is most robust to many kinds of undesirable perturbations to the phase image. As described in Sect. 5.2.2, the SE pulse sequence requires two TTL triggers to indicate the end of 90° and 180° RF pulses. In the I^+ version of the scan, a positive current is injected between the end of the 90° and the beginning of 180° RF pulse. A negative current is injected after the 180° RF pulse and up to the beginning of the read gradient as the 180° pulse reverses the phase polarity. In the I^- scan the sequence is repeated but with an initial negative current.

A major drawback of the SE sequence is the long acquisition time. This limits

(continued)

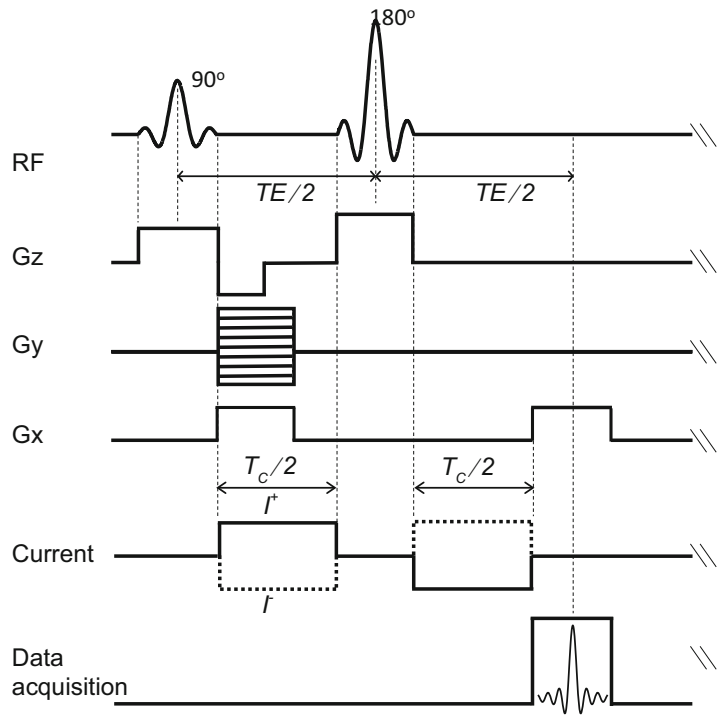

Fig. 5.4 Spin echo pulse sequence for MREIT. Current is injected for a total of T_c per TR. In a simple version of the scan phase data recorded with I^+ and I^-, current patterns are subtracted to remove systematic phase artifact

the number of the signal averages that can be measured and make the sequence susceptible to motion artifacts during in vivo studies [26]. More recent MREIT studies have therefore used multi-slice SE MRI sequences to allow simultaneous acquisition of several spin echo image slices and reduce overall scan time [4]. The pulse sequence diagram for MREIT data acquisition using a SE sequence is shown in Fig. 5.4.

SE Injected Current Nonlinear Encoding (SE-ICNE)

In the conventional SE current injection method shown above, currents are injected during the time segment between the end of the first RF pulse and the beginning of the read gradient in order to ensure gradient linearity. Since longer current injections accumulate more phase change [7], Park et al. [27] proposed a modified pulse sequence called injection current nonlinear encoding (ICNE) where the current pulse duration is extended until the end of the read gradient (Fig. 5.5). Since current injection during the read gradient disturbs gradient linearity, Park et al. [27] suggested a novel algorithm to extract the induced magnetic flux density from the acquired MR signal. Lee et al. [28] showed that the optimal current injection time T_c^* and the corresponding optimal data acquisition time T_s^* are

$$T_c^* = \frac{2}{3}\left(TE - \frac{3\tau_{RF}}{2}\right) \quad \text{and}$$
$$T_s^* = \frac{2}{3}\left(TE - \frac{3\tau_{RF}}{2}\right) \qquad (5.7)$$

where TE is the echo time and τ_{RF} is the RF pulse width. Compared with a conventional current injection method [6], the SE-ICNE method can theoretically reduce the noise level in measured magnetic flux

(continued)

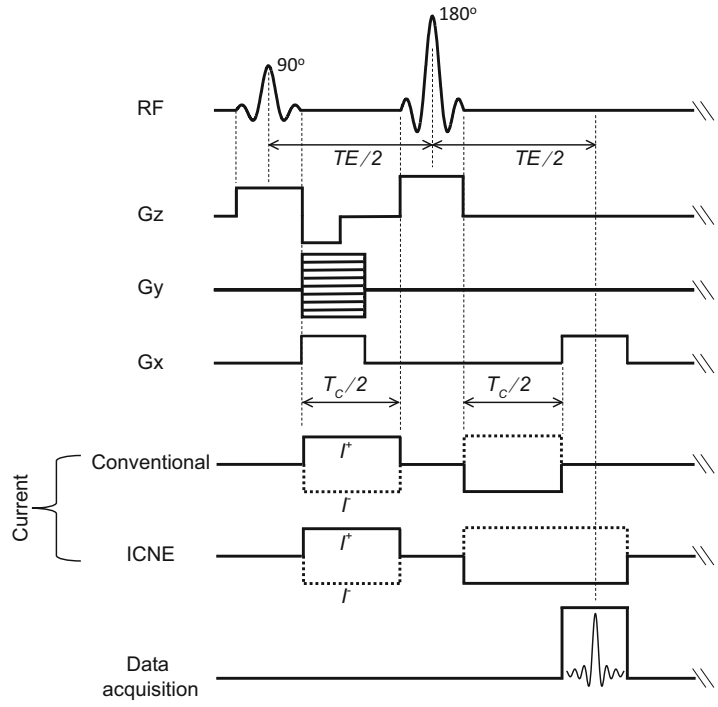

Fig. 5.5 Spin echo pulse sequence showing a comparison of conventional and ICNE injection currents

density up to 42% in the optimal case [28, 29]. Figure 5.5 shows the pulse sequence diagram for the SE-ICNE MREIT pulse sequence. The length of the current injection after 180° pulse is extended until the end of the read gradient (G_x).

Multi-Echo Spin Echo Injected Current Nonlinear Encoding Sequence (MESE-ICNE)

Another useful approach to effectively increase the T_c in MREIT is to use multi-echo SE (MESE) MRI sequences. The MESE pulse sequence generates multiple echoes by repeatedly applying 180° refocusing RF pulses within one TR [30,31]. Additionally, the ICNE approach can be used to improve B_z SNR by extending the current injection duration until the end of the read gradient. Figure 5.6 shows a current injection scheme that could be used in the MESE-ICNE sequence with three echoes. Since the multi-echo approach enables an increase in the total current injection time (T_c), it should produce advantages for MREIT. However, this approach cannot be used indefinitely, since T_2 signal decay will result in noisier images being recovered as larger numbers of echoes are recorded.

Minhas et al. [31] evaluated the performance of a multi-echo SE-ICNE sequence using data from phantom and animal studies. They found that the multi-echo MR magnitude image ($\mathcal{M}^{\pm}_{ME}$) for positive and negative current injection after combining N echo datasets can be represented as

$$\mathcal{M}^{\pm}_{ME}(x,y) = \frac{1}{N}\sum_{n=1}^{N} \rho(x,y) e^{-n\frac{TE}{T_2}} \tag{5.8}$$

The resulting total multi-echo phase change (ψ_{ME}) found by combining the n echoes is

$$\psi_{ME}(x,y) = \sum_{n=1}^{N} \psi_n(x,y) = 2\gamma B_z(x,y)\Delta T \tag{5.9}$$

where $\Delta T = \sum_{n=1}^{N}\left(\sum_{k=1}^{2n}\Delta k\right)$ is the total effective current injection duration for echo-combined data. The ICNE pulse sequence with a single echo described by Park et al. [27] is a special case of the multi-echo sequence where $n = 1$.

Gradient Echo and Multi-Echo Gradient Echo Sequences

The gradient echo (GRE) MR sequence is faster than the SE sequence and is widely used in MRI imaging. The difference between SE and GRE pulse sequences relates to elements used to generate the MR signal [32]. While two radio-frequency (RF) pulses (90° and 180°) are used for spin refocusing and spin echo generation in SE sequences, GRE imaging is based on only a single RF pulse applied at a *flip angle* that is typically <90°, in combination with readout gradient reversals [33,34]. The images thus retain T_2^* dephasing effects. The consequence of using low-flip angle excitations is faster recovery of longitudinal magnetization, which in turn allows for shorter repetition times (TR) and echo times (TE) and decreases overall scan times. Figure 5.7 shows a pulse sequence diagram for a GE MREIT acquisition.

As B_z noise standard deviation is inversely proportional to T_c [6, 7], the B_z standard deviation is higher for gradient echo sequences due the shorter TE, TR, and therefore T_C values. Because of its sensitivity to magnetic field inhomogeneity arising from susceptibility differences, GE-based MREIT has generally been avoided in MREIT data acquisitions where time restrictions are not present. However, multi-

(continued)

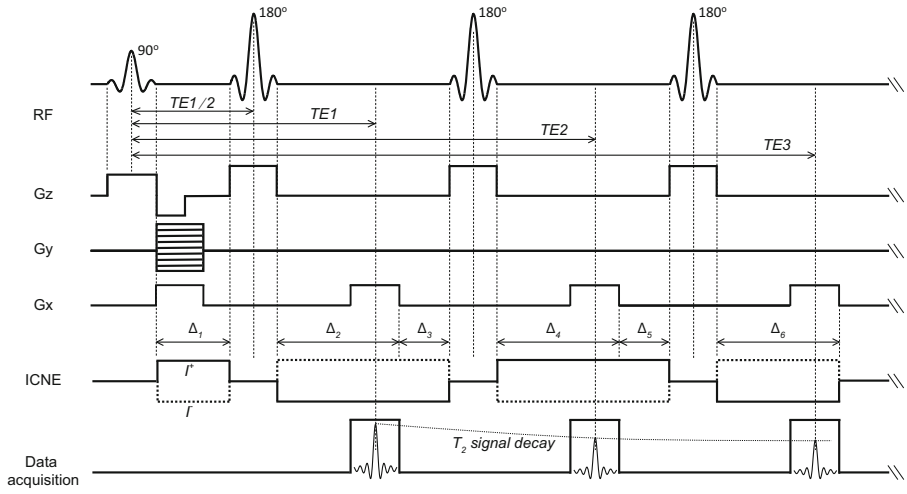

Fig. 5.6 Multi-echo spin echo ICNE pulse sequence with synchronized injection current pulses

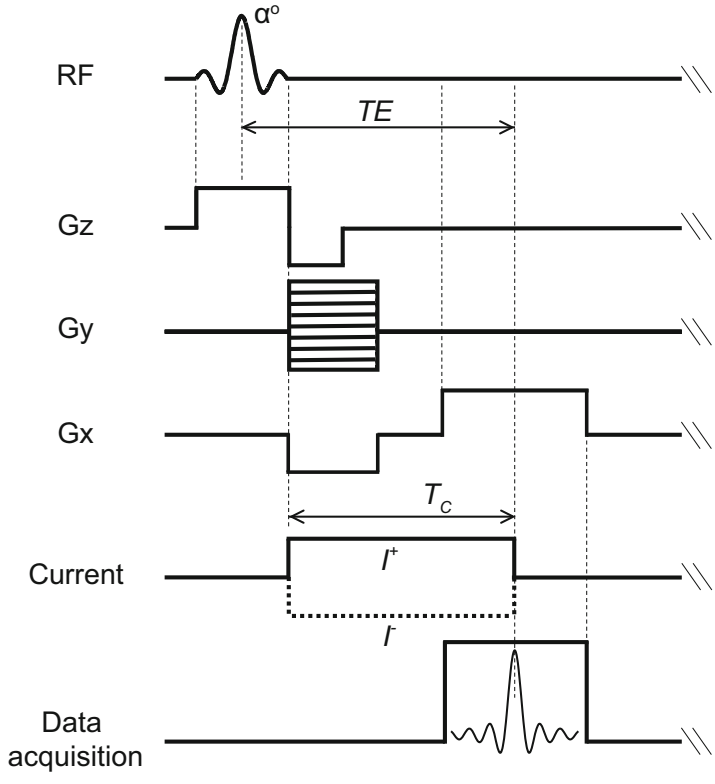

Fig. 5.7 Gradient echo pulse sequence with synchronized injection current pulses

echo gradient MREIT sequences have successfully been implemented in human studies [15, 35].

Multi-Echo GRE Use of multi-echo gradient echo (ME-GRE) MR sequences solve many problems observed in GRE sequences for MREIT and allow us to take advantage of their short TR times. In a normal GRE sequence, a gradient reversal process is used to create a single gradient echo and can be repeated to produce two or more additional gradient echoes after a single RF pulse. Multiple gradient echoes can be acquired using this process, but because of T_2^*-decay, the maximum usable number of echoes is limited [36].

Kim et al. [36] proposed an MREIT pulse sequence by combining a ME-GRE pulse sequence with the injected current nonlinear encoding (ICNE) approach, with current injection up to the end of the readout gradient, as shown in Fig. 5.8. The proposed method increases T_c almost up to TR as the multiple echoes are recorded.

Later, Oh et al. [37] suggested that estimated T_2^* relaxation times can be used to estimate noise levels in the multiple measured ${B_z}^j, j = 1, \ldots, N_E$ using the ICNE-MEGRE sequence and to determine an optimized magnetic flux density ${B_z}^{opt}$ by recovering weighting factors ω_j for each measured magnetic flux density echo ${B_z}^j$ that minimize the noise level of ${B_z}^{opt}$, where N_E is the number of echoes in T_R.

The optimal weighting factor $\omega_j(\mathbf{r})$ can be obtained by computing

$$\omega_j(\mathbf{r}) = \frac{\gamma_j(\mathbf{r})}{\sum_{j=1}^{N_E} \gamma_j(\mathbf{r})} \tag{5.10}$$

where $\gamma_j(\mathbf{r}) := T_{cj}^2 \mathrm{e}^{-\frac{2T_{cj}}{T_2^*(\mathbf{r})}}$ and T_{cj} is the current injection time at the j^{th} echo.

(continued)

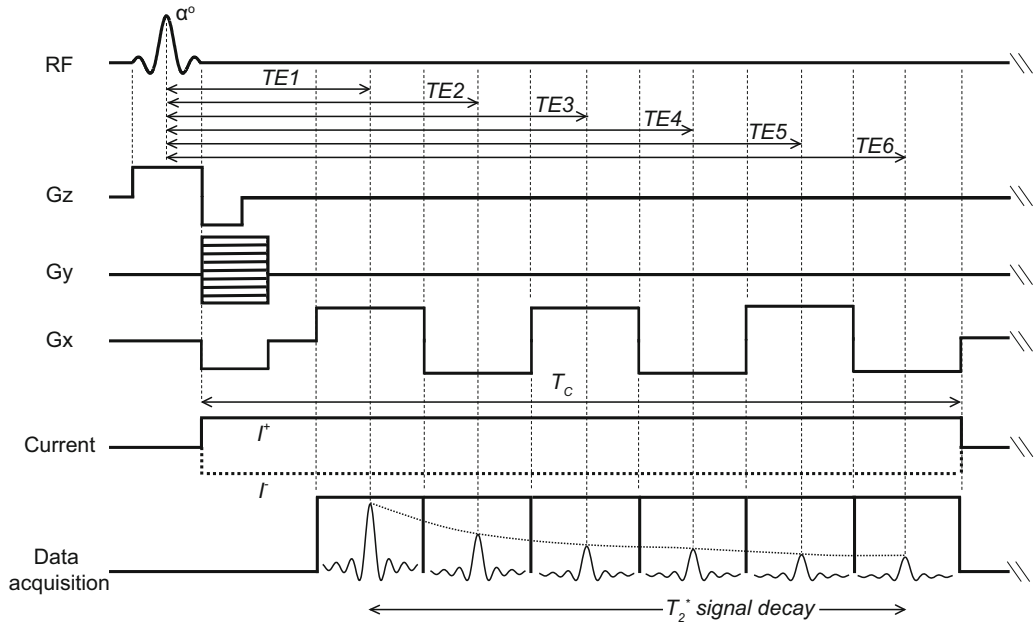

Fig. 5.8 Multi-echo gradient echo ICNE pulse sequence with synchronized injection current pulses

Once the weighting factors $\omega_j(\mathbf{r})$ have been determined, the optimized $B_z{}^{opt}(\mathbf{r}) = \sum_{j=1}^{N_E} \omega_j(\mathbf{r}) B_{zj}(\mathbf{r})$ can be obtained and used in further analysis.

Echo Planar Imaging

In recent years, many fast SE or GRE MR sequences have been developed for MRI data acquisition, including fast spin echo(FSE), ultrafast gradient echo (Turbo GRE), echo planar imaging (EPI), and ultra-short echo time (UTE) techniques. Immediate use of these sequences in MREIT is challenging because of the need to combine the pulse sequence structure and data readout method with external current injection. In some recent studies, researchers have investigated the use of a single-shot or multi-shot spin echo EPI pulse sequences for data acquisition in MREIT [26, 35]. These sequences acquire the entire k-space data in single (one shot) or multiple TRs and may thus be useful in MREIT data acquisition—decreasing the total scan time and reducing susceptibility to motion artifacts. They may also be useful in functional MREIT studies.

EPI is one of the most efficient and fast MRI techniques. Single or multi-shot EPI is widely used in functional MRI (fMRI) and diffusion tensor MRI (DT-MRI) imaging studies. However, EPI artifacts can result in severe image distortions. While EPI-based sequences can drastically decrease scan time, obtaining of artifact-free EPI data is intrinsically difficult [38, 39]. System imperfections and physical phenomena (e.g., eddy currents, asymmetric anti-aliasing filter response, B_0 inhomogeneity, chemical shift effect, mismatched gradient group delays, hysteresis) can lead to Nyquist ghosts and geometrical distortions in EPI images.

Nyquist ghosting observed in raw EPI reconstructions is the result of time-reversal asymmetry between even and odd echoes, and this reduces SNR and degrades image quality. These artifacts also result in inaccurate measurements of both magnitude and MREIT magnetic flux density data. Many methods to reduce effects of ghosting and geometrical distortion in EPI data have been suggested [40–44]. Chauhan et al. [35] used the techniques of Chen and Wyrwicz [43] and Chiou et al. [44] to apply ghost and geometric corrections, respectively, to phase images in EPI-based MREIT. They compared MREIT reconstructions for single- and multiple-shot EPI with a gold-standard SE sequence and concluded that EPI methods can be combined successfully with MREIT reconstruction algorithms to achieve fast imaging of current density, conductivity, and electric field. Figure 5.9 shows the MREIT current administration sequence used in [35] against the single-shot SE-EPI sequence.

5.4.3 MREIT Data Preprocessing

After collecting multiple sets of k-space data in (5.1), several processing tasks must be required to transform it into B_z data. First, the discrete inverse Fourier transformation is computed to obtain the complex MR image of (5.2). Though this step is straightforward, the second step of computing the net phase change in (5.3) requires a carefully implemented numerical phase-unwrapping algorithm. Recall that for the safety of subjects in in vivo experiments, the amount of injected current I should be small, which reduces B_z signal. The SNR of B_z data is also directly affected by the noise of $\mathcal{M}$. Therefore, attention must almost always be paid to denoising phase data prior to its use in reconstruction. Figure 5.3 shows the flow diagram for basic MREIT data processing. In the following subsections, we discuss unwrapping

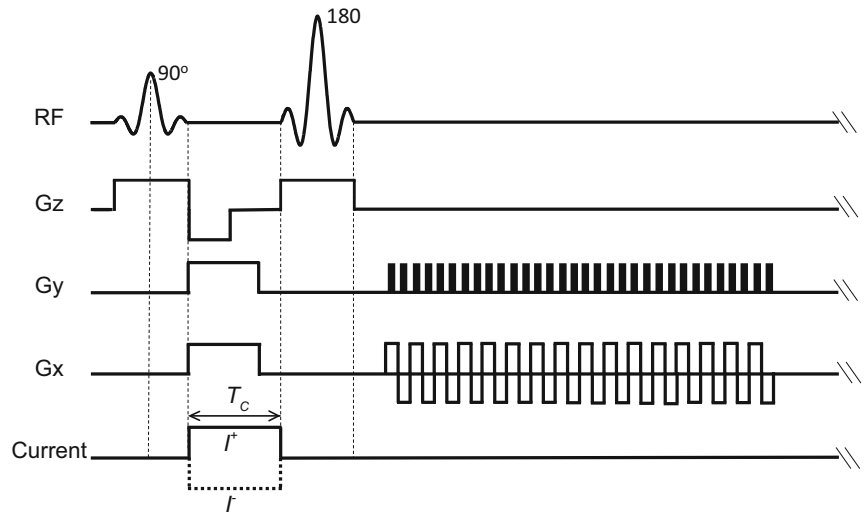

Fig. 5.9 Spin echo EPI pulse sequence with conventional injection currents. Because of the limited time between the 180° pulse and read gradients, no current is injected after the 180° pulse. Scans using positive current (I^+) or negative current first (I^-) may be combined to remove systematic phase artifact

and phase correction methods that can be applied to MREIT data.

5.4.3.1 MR Phase Corrections

Phase Unwrapping

As we know from Eq. (5.3), the phase change measured in MR phase images (ψ) depends on the duration of the applied current (T_c) [2,3]. The phase is usually first revealed using the arctan function (see (5.3)), which constrains the phase to the interval $[-\pi,\pi]$. However, the phase-unwrapping process in MREIT must extend the interval to its full correct range. If the total current is small, this may not be necessary. However, if large currents or very small electrodes that produce large current densities are used, the need for unwrapping is more likely. The unwrapping problem is an important aspect in MREIT, as in other fields using MR phase information such as EPT or quantitative susceptibility mapping (QSM).

As noted above, special care must be given to regions near current injection electrodes where current densities are high and phase changes may be very rapid (Fig. 5.10). Ghiglia and Pritt [45] explain details of numerous phase-unwrapping algorithms, and this is a useful general reference. To unwrap phase discontinuities in the phase images obtained with current injection, most MREIT studies have used Goldstein's branch cut algorithm [45].

Harmonic In-painting Using MR Data

MR images may contain regions where signals are weak due to low proton density or because the tissues may have very short T1 or T2 values. These MR signal voids usually occur in tissues such as the lungs, cortical bones and in gas-filled organs [46]. Within these regions, $\mathcal{M} \approx 0$ in (5.2). As the SNR in this region will be very low, by Eq. (5.5), the measured B_z data in (5.4) will be very noisy, even though the B_z sig-

(continued)

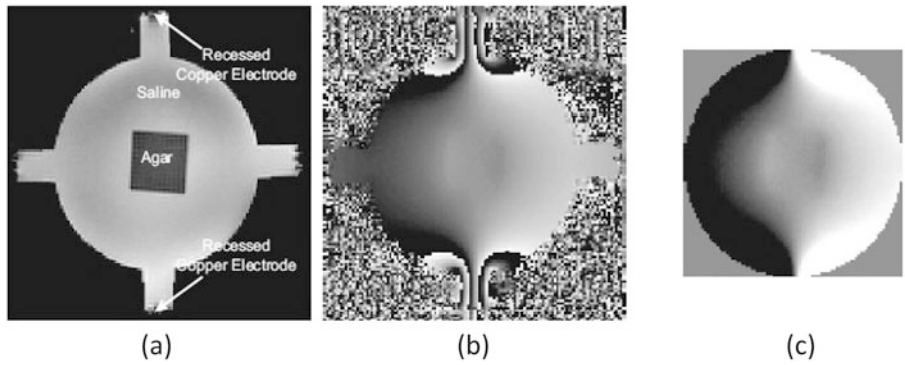

Fig. 5.10 (**a**) MR magnitude image M of a cylindrical saline phantom including an agar object. Conductivity values of the saline and agar were different. (**b**) Wrapped phase image subject to an injection current from the top to the bottom electrodes. (**c**) Corresponding image of induced B_z after applying a phase-unwrapping algorithm

nal itself may not be small there [3]. Lee et al. [47] termed this defective B_z data, since using it for conductivity reconstruction may result in errors. They proposed an **in-painting** method to recover B_z data in defective regions using Maxwell's equations combined with the adjacent higher-quality B_z data. The method is based on the fact that $\nabla^2 B_z = 0$ inside a region with zero conductivity. They first segmented out defective regions and their boundaries and solved the equation $\nabla^2 B_z = 0$ subject to boundary conditions of the B_z data along the region boundary. This computed synthetic B_z data then replaced the original noisy B_z data inside defective regions, and they will appear as locally homogeneous conductivities. If there are multiple small regions with low SNR, a harmonic decomposition denoising method [48] may be preferable to harmonic in-painting [3].

Research software called CoReHA (**Co**nductivity **Re**constructor using **H**armonic **A**lgorithms) is available to aid MREIT data processing. In older versions of CoReHA [49], a manual segmentation tool was provided for the extraction of boundaries and correction of B_z data in defective regions using the harmonic in-painting algorithm [48]. However, the manual segmentation required to identify the defective region boundary causes user-dependent reconstruction results. To deal with this situation, CoReHA2.0 [50] assumes that any defective region has low MR magnitude and that its conductivity distribution is homogeneous, so that $\nabla^2 B_z = 0$. CoReHA2.0 then automatically selects the defective region using a threshold of 10% of the maximum MR magnitude.

B_z Denoising

Images of magnetic flux density B_z include the core information about the conductivity contrast. These images also contain noise from the object itself as well as the MRI system [46, 51]. Denoising methods specific to MREIT can be attempted as the next step after phase unwrapping, taking caution not to distort the signal component. Lee et al. [48] suggested a **PDE-based denoising** technique for MREIT. They adopted a harmonic decomposition method specific to the relation between B_z and conductivity contrast to separate noise from the signal component. Other denoising techniques

(continued)

may also be applied as long as they preserve B_z signal components.

The B_z images typically present areas of sloped transitions, which may be described as "ramps." Conductivity contrasts change ramp slopes in B_z images, and it is critical to preserve the positions of ramp slope changes to correctly recover the position of edges in conductivity images. The **ramp-preserving denoising technique** [52] uses eigenvalue analysis to isolate parts of the image contaminated by random noise (contributed by the MR scanner) or salt and pepper noise (contributed by tissue structure) and applies an anisotropic filter that smooths ramps while preserving edge data.

Jeon et al. [49, 50, 74] integrated the functions of ramp-preserving denoising, harmonic in-painting, and ROI image reconstruction using the local harmonic B_z algorithm into the CoReHA conductivity image reconstruction software. Applying these methods together with the harmonic B_z algorithm, they confirmed that they could be used to improve the quality of conductivity images of phantoms and intact animals.

5.4.3.2 Current Density and Conductivity Image Reconstruction

Data acquired from MREIT experiments can be used for both current density and conductivity image reconstructions. In some MREIT algorithms, current density reconstruction (e.g., projected current density) is an intermediate step in computing conductivity images. While current density calculations can be done with single current injection (injecting current between one pair of electrodes) [53]; for reliable conductivity image calculations, most MREIT algorithms require more than one current injection. Current density and conductivity image reconstruction algorithms typically also need a three-dimensional finite element model of the imaged object. Multi-slice MR magnitude image volumes can be used for this task, and methods for constructing these models are described in Chap. 2. Even though MREIT data provides magnitude information, the voxel size may be larger than desired for constructing the computational model, and a finer-resolution scan (typically 1 mm isotropic) covering the entire domain of interest is often used for this purpose. Extraction of the object boundary from multi-slice MR magnitude images is relatively easy, since image values are close to zero outside the object. In addition, as discussed in Chap. 7, diffusion tensor-based MREIT (DT-MREIT) algorithms require diffusion tensor images (DTI) along with current-induced magnetic flux density (B_z) images to compute conductivity tensor images of anisotropic objects [54–56]. Coregistration of the structural scans used to construct computational models, and any diffusion tensor volumes with MREIT data is critical for correct reconstructions. This is most easily achieved by collecting all required data in a single session.

5.4.4 Clinical Applications of MREIT

5.4.4.1 MREIT During tES Therapy

Transcranial electrical stimulation (tES) techniques have emerged as an important modality for understanding the relationship between brain and behavior [57]. It has been assumed that effects caused by tES neuromodulation techniques are due to electric current flow within brain structures that are key to the processes being studied. MR current density imaging and diffusion tensor MREIT (DT-MREIT) methods have recently been used to reconstruct current density distributions [15, 58] and anisotropic conductivity images [56] during tES therapy using MREIT and diffusion tensor image data gathered from healthy human subjects. The experimental procedures used in an example study [15,56] are described in the sections below.

Subject Preparation and Electrode Attachments

Subjects were neurologically normal and right-handed. They completed brief questionnaires before and after interventions to assess mood and tES-related physical sensations. Prior to scans, neuroConn carbon-rubber electrodes (~25 cm^2), enclosed in sponges, were soaked in saline (0.9% NaCl) and squeezed to remove excess solution. Immediately before electrode placement on Fpz, Oz, T7, and T8 locations, a 5 ml volume of saline was applied to both sides of each sponge. Small amounts (ca. 1 ml) of saline were also applied to the scalp under hair at electrode sites. Electrodes were applied approximately 30 min before the current administration procedures began. Electrode positions, wiring and fastenings are shown in Fig. 5.11a, b. The process of electrode attachment is discussed in detail in Chap. 4.

Subjects were requested to report any stimulation-related side effects while in the scanner such as phosphenes, pain, or skin irritation. Phosphenes are light sensations appearing in the visual field that can be induced by external electrical stimuli. They were particularly likely to occur during the MREIT waveform used because its principal frequency was around 10 Hz [59]. Phosphene perception was rated on a 1–10 scale, with 1 corresponding to "no detectable flashing" and 10 corresponding to 'white field." Phosphene fields were recorded as either "peripheral" or "central." Any subject perceptions of cutaneous stimulation were also recorded. Using recorded phosphene perception data from multiple subject undergoing tES, Indahlastari et al. compared the predicted and observed

(continued)

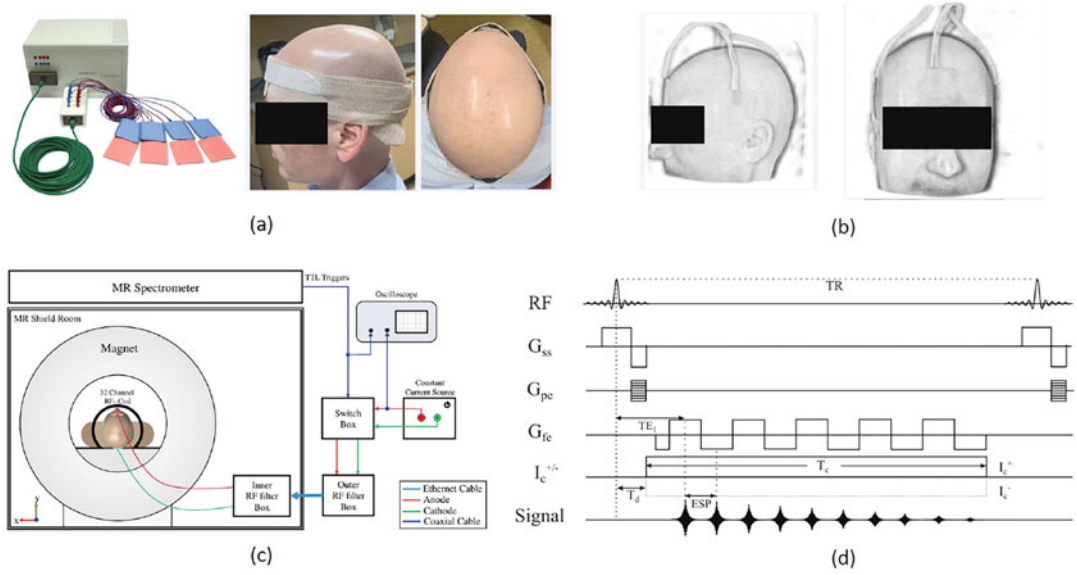

Fig. 5.11 tES MREIT experiment setup and pulse sequence. Part (**a**) shows the four-channel MR-safe stimulator with sponge electrodes, also showing electrodes secured using elastic bandaging, (**b**) is a rendering of the subject in 3D from MR (MPRAGE) images and illustrates wiring arrangement, (**c**) shows a schematic of tES electrical connections used in the experiment, and (**d**) shows the ten-echo multigradient echo sequence used to obtain subject data. Note that the current was applied until just after the last echo

phosphene experience using the finite element method [60] and found that this method, combined with modeling or direct measurement, could be used to explore the mechanism of phosphene generation.

Imaging Procedures

The complete experimental setup is shown in Fig. 5.11c. All data were measured using a 32-channel head coil in a 3T MRI Philips Achieva scanner. After pilot scan acquisition, a 3D FLASH T1-weighted structural image was acquired with a 240 mm (FH) × 240 mm (AP) × 160 mm (RL) field of view (FOV) and 1 mm isotropic resolution, centered laterally on the midbrain. Figure 5.11d shows the Philips `mffe` sequence modified for MREIT. MREIT datasets were acquired in three 5 mm contiguous slices (NS = 3) with an in-plane FOV of 224 mm (RL) × 224 mm (AP) and a data matrix size 100 × 100 × 3 (resolution 2.24 × 2.24 × 5 mm^3). MREIT slice positions were aligned to the T1-image volumes and chosen so that the volume contained as much of the electrode extent as possible.

MREIT scans for each slice were performed in sequence, each slice comprising 100 phase encode (PE) steps. For each PE step, ten echoes were acquired during a current injection time (T_c) of 32 ms within a TR of 50 ms, and then the current polarity was alternated during subsequent TR intervals. This sequence was repeated 12 times (NAV = 12) for each PE step. Therefore, the total acquisition time for each MREIT image acquisition was TR × 2 (polarity switching) × NAV × PE × NS = 6:00 min. The entire MREIT procedure was repeated and results averaged, for a total acquisition time of 12 min, to achieve better signal-to-noise ratio (SNR) and to reduce standard deviations($S_{D_{B_z}}$) in current-induced magnetic fields (B_z) [7]. "Positive" pulses were applied first to the first named electrode in each montage (Fpz or T7). An initial, no current (NC), MREIT scan was performed to verify system stability and produce baseline T_2^* maps. This required only 6 min since no polarity switching was used. The entire MREIT acquisition, comprising stimulation via both Fpz-Oz and T7–T8 electrode pairs and NC scans, lasted approximately 30 min.

Diffusion-weighted MR (DWI) data required to perform DT-MREIT reconstructions were then acquired using a HARDI (high angular resolution diffusion imaging) protocol, at b-values of 100 s/mm^2 (6 directions) and 1000 s/mm^2 (64 directions). Data were sampled at a 2 mm isotropic resolution, with a matrix size of 70 × 112 × 112. Two six-direction DWI datasets were acquired with reversed phase encode directions to remove effects of background magnetic inhomogeneity. These two datasets were then combined using the FSL topup procedure [61]. While T1-weighted, MREIT and DWI data were all referred to the same reference scan, the *S*0 (no diffusion gradient, $b = 0$ s/mm^2) DWI image registration was used to confirm alignment of T1-weighted and DTI data. Both the S0 and T1-weighted images were then resampled to a 100 × 100 × 44 matrix size to match MREIT resolution.

Electrical Stimulation Protocol

A 1.5 mA current intensity was used in all experiments, for both Fpz-Oz and T7–T8 montages. It was found that subjects tolerated this current amplitude well and there was good phase signal after averaging had been applied. Figure 5.11d shows that current was applied for periods of 32 ms of each 50 ms TR. Because current polarity re-

(continued)

versed after each TR, the stimulation waveform therefore corresponded to a sequence of rectangular pulses with a duty cycle of approximately 64% [15,56].

5.4.4.2 3D Head Model Generation

For segmentation, de-identified T1-weighted axial and sagittal datasets were resampled using FreeSurfer (Cambridge, MA) to a $1\,mm^3$ isotropic resolution. Segmentation was completed using resampled sagittal images. Figure 5.12 shows an outline of the segmentation procedures. A combination of automatic and manual steps was used to segment datasets into ten tissue compartments. White and gray matter segmentation was performed using FreeSurfer (http://surfer.nmr.mgh.harvard.edu/), while bone, ski,n and air segmentations were completed using MATLAB (Mathworks, Natick, MA) and the SPM12 module (Wellcome Trust Centre for Neuroimaging, London, UK). All automated segmented tissue masks were corrected manually in ScanIP v7.0 (Simpleware, Synopsys Inc., Exeter, UK) with reference to an anatomical atlas [62]. The remaining tissue compartments, comprising cerebrospinal fluid (CSF), the eyes, blood, fat, and muscle were segmented manually in ScanIP. Using thresholding in T1-weighted axial images, the temporal electrodes (T7, T8) were segmented to an electrode surface area of about $36\,cm^2$, in comparison to the $25\,cm^2$ carbon-rubber core. As a final step, segmented electrodes and tissues were combined into a single ScanIP model for each subject. Segmented models were then exported to COMSOL for subsequent calculations, as described in Chap. 2.

Current Density and Conductivity Tensor Imaging During tES

This study demonstrated the first MREIT current density images in human heads. To calculate current densities during tES treatment, the projected current density (J^P) algorithm was used. Details of projected current density reconstruction algorithms are described in Chap. 6.

The same data collected in the study were used to reconstruct the first in vivo anisotropic conductivity images of the human brain, using the combination of diffusion tensor and MREIT reconstruction techniques (DT-MREIT) [54]. A full discussion of the DT-MREIT algorithm is in Chap. 7. Because the external current in-

(continued)

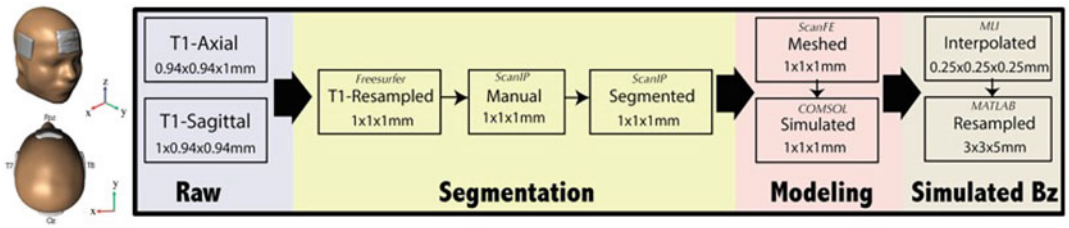

Fig. 5.12 Modeling simulation workflow. Outlined here is the general procedure used to process raw T1 datasets (left) into synthetic B_z (right). Raw T1 datasets were resampled prior to segmentation, and a combination of manual and automatic steps was used for the segmentation process. The segmented model was meshed in Simpleware ScanFE. All finite element simulation was performed using COMSOL, and simulation results were processed and analyzed in MATLAB

jection used for these experiments was at around 10 Hz, these measured conductivity distributions are also those relevant to brain activity frequencies (DC-250 Hz).

5.4.4.3 MREIT During Electroporation

Monitoring of electroporation processes could provide a path to safe and efficient applications of electroporation in clinical procedures such as electrochemotherapy and nonthermal irreversible electroporation [63]. Several methods of monitoring electroporation processes have already been suggested, particularly for irreversible (NTIRE), where immediate changes of tissue properties can be detected [64]. However, monitoring of reversible electroporation is more demanding task since there are almost no immediate visible physical changes in treated tissue. Electroporation-based treatment efficiency is correlated to electric field distribution [63]. More specifically, at a given number and duration of pulses, the local electric field is the critical factor determining tissue electroporation. Therefore, use of MREIT would benefit understanding of mechanisms and practice of electroporation if used intraoperatively.

Electric Field Measurement During Electroporation

As accurate coverage of the tissue with a sufficiently large electric field presents one of the most important conditions for successful electroporation, Kranjc et al. [53, 65] proposed a method for determining electric field distribution during electroporation based on magnetic resonance electrical impedance tomography (MREIT). They demonstrated that MREIT can be used to determine electric field distribution during electroporation in agar phantoms, and ex vivo tissues (chicken liver). Tissues were sectioned in flat and cylindrical-shaped samples with a diameter of 20 mm and placed in an acrylic glass container (Fig. 5.13a). Four cylindrical-shaped platinum-iridium electrodes with a diameter of 1 mm were placed inside. Samples were then inserted in a 25 mm RF probe and connected to the electric pulse generator using cables including a low-pass filter to avoid possible RF disturbances in the NMR signal. The sequence of four high-voltage electric pulses with an amplitude U_{el} of either 1000 V or 1500 V and a duration of 100 ms was delivered between opposing pairs of electrodes using an electric pulse generator Cliniporator Vitae (IGEA, Carpi, Italy) to establish electric field distribution below and above reversible electroporation threshold values for applied voltages of 1000 V and 1500 V, respectively.

For these studies, MR phase images of current-induced magnetic field changes were obtained using a two-shot RARE current density imaging (RARE CDI) sequence [66], shown in Fig. 5.13b, with the following scan parameters: imaging matrix 64×64, field of view 30 mm, inter-echo delay 2.64 mm, echo time of the current encoding period 20 ms, and the time interval between two RARE signal acquisitions 10 s. MR imaging was performed on a TecMag NMR spectrometer connected to an Oxford 2.35 T horizontal bore superconducting magnet. The MRI system was equipped with Bruker micro-imaging accessories with maximum gradients of 250 mT/m. Measured electric currents and voltages for liver tissues exposed to four 100-ms-long electroporation pulses at amplitudes of 1000 and 1500 V were presented in this study (Fig. 5.13c). Current densities were reconstructed directly from Ampere's law, since use of long electroporation electrodes resulted in there being no z component to the current density. Conductivity was reconstructed using J-substitution [67]. Further details of the J-

(continued)

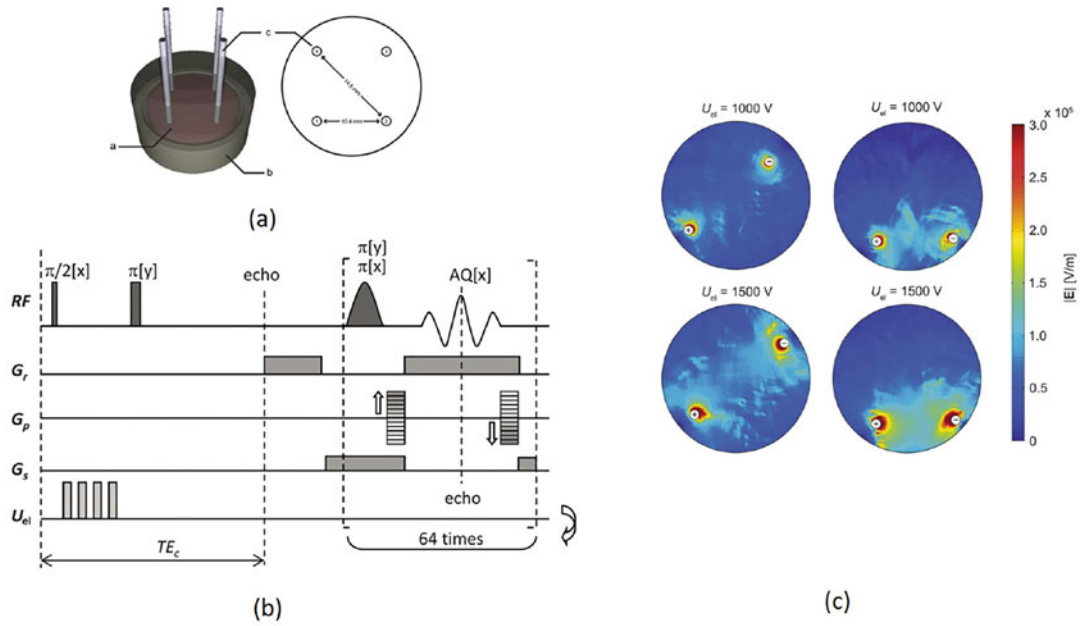

Fig. 5.13 Electroporation MREIT experiment setup and results. (**a**) Liver sample with inserted electrodes placed in an acrylic glass container. (**b**) Two-shot RARE CDI sequence. (**c**) Electric field distribution in the liver tissue obtained by MREIT

substitution algorithm are given in Chap. 7. Significant changes in the liver tissue electrical conductivity were observed when tissue was exposed to pulses with an amplitude of 1500 V. A region with a higher electrical conductivity between electrodes was established as a consequence of tissue changes associated with application of a high electric field in this region. Such changes were not detected in tissue exposed to pulses with an amplitude of 1000 V. In conclusion, monitoring of the electric field distribution during ECT and NTIRE by means of MREIT would thus enable detection of insufficient electric field coverage, potentially providing a means of avoiding treatment failure.

Conductivity Measurement During Electroporation

One benefit of measurement of electrical properties of tissues affected by electroporation would be a better characterization of numerical models of tissues in patient specific pre-treatment plans [68, 69]. Namely, the local electric field in tissues is affected by applied electroporation pulses, which depend on local electrical conductivity, and, vice versa, electroporation increases the conductivity and consequently alters the electric field distribution [70, 71]. Studies of these nonlinear effects are also important for understanding electrical safety.

In a later study, Kranjc et al. [72] demonstrated the feasibility of MREIT for

(continued)

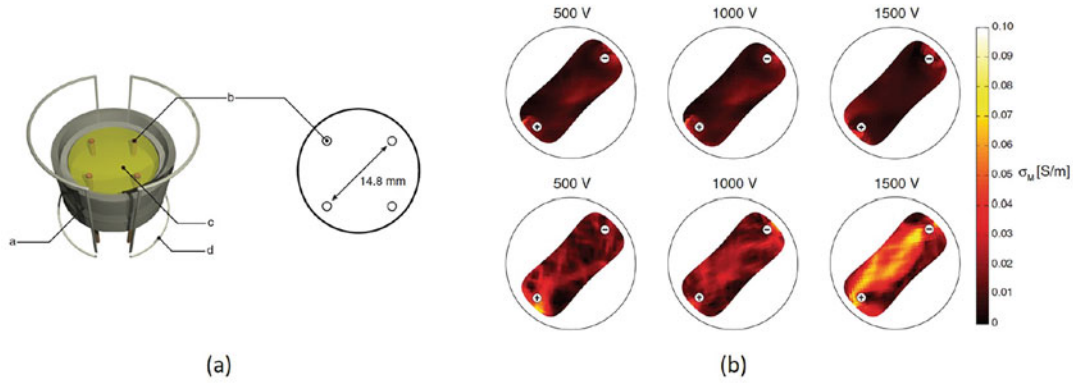

Fig. 5.14 (**a**) The container used in the study was made of acrylic glass with four holes for electrodes. Either an agar phantom or liver tissue was placed inside. The container was inserted in the radio-frequency (RF) probe. The distance between the active electrodes was 14.8 mm. Electrical conductivities of agar phantom (**b**, top row) and liver tissue (**b**, bottom row) exposed to electric pulses of different amplitudes (500, 1000, 1500 V). Electric pulses were delivered between two needle electrodes (marked with + and −)

assessing conductivity of tissues undergoing electroporation by placing agar anomalies or ex vivo liver tissue into a sample container. Samples were sliced into cylindrical shapes measuring 21 mm in diameter and 2 mm in height before being placed in in the acrylic container. The cylindrical electrodes were made of platinum-iridium and measured 1 mm in diameter. Both samples were exposed to short duration (100 μs) high-voltage electric pulses (500, 1000 or 1500 V), as are normally used in electroporation clinical applications. The electric pulses were delivered by a Cliniporator Vitae electric pulse generator (IGEA, Carpi, Italy) between two diagonal electrodes that were placed 14.8 mm apart in the tissues (Fig. 5.14a). The same MRI parameters described in the previous section were used for the MREIT experiments in [72], and, again, the measured current density distribution was then used to reconstruct the conductivity distribution using the *J*-substitution algorithm [67, 73].

Electrical conductivities of both measurement objects exposed to electric pulses of different amplitudes (500, 1000, 1500 V) within ROI are shown in Fig. 5.11b.

In conclusion, these findings suggest that MREIT can indeed be used for detecting electrical conductivity changes that occur in tissue exposed to short high-voltage pulses and that these methods can be used for assessment and prediction of the electroporation effect on tissue.

5.4.5 Summary

In this chapter, we have covered the technical aspects of integrating phantoms, MRI pulse sequences and MREIT measurements. Considerations required when converting phase to B_z signals and in dealing with noisy data were discussed, and some examples of key experiments and applications were presented. This material should enable a new MREIT experimenter to design and perform scans in novel settings.

References

1. M.L.G. Joy, G.C. Scott, R.M. Henkelman, In vivo detection of applied electric currents by magnetic resonance imaging. Magn. Reson. Imag. **7**, 89–94 (1989)
2. G.C. Scott, M.L.G. Joy, R.L. Armstrong, R.M. Henkelman, Measurement of nonuniform current density by magnetic resonance. IEEE Trans. Med. Imag. **10**, 362–374 (1991)
3. E.J. Woo, J.K. Seo, Magnetic resonance electrical impedance tomography (MREIT) for high-resolution conductivity imaging. Physiol. Meas. **29**(10), R1 (2008)
4. J.K. Seo, E.J. Woo, Magnetic resonance electrical impedance tomography (MREIT). SIAM Rev. **53**(1), 40–68 (2011)
5. J.K. Seo, E.J. Woo, Electrical tissue property imaging at low frequency using MREIT. IEEE Trans. Biomed. Eng. **61**(5), 1390–1399 (2014)
6. G.C. Scott, M.L.G. Joy, R.L. Armstrong, R.M. Henkelman, Sensitivity of magnetic-resonance current-density imaging. J. Magn. Reson. **97**, 235–254 (1992)
7. R.J. Sadleir, S. Grant, S.U. Zhang, B.I. Lee, H.C. Pyo, S.H. Oh, C. Park, E.J. Woo, S.Y. Lee, O. Kwon, J.K. Seo, Noise analysis in magnetic resonance electrical impedance tomography at 3 and 11 T field strengths. Physiolog. Meas. **26**, 875–884 (2005)
8. J.M. Froehlich, D. Nanz, K.P. Pruessmann, *How Does MRI Work? An Introduction to the Physics and Function of Magnetic Resonance Imaging*, 2nd edn. (Springer, New York, 2006), pp. 29–39
9. M.A. Bernstein, J. Huston, H.A. Ward, Imaging artifacts at 3.0T. J. Magn. Reson. Imag. **24**(4), 735–746 (2006)
10. E.L. Mark, B. Peter, M. Martin, M. Ewald, M.N. Armin, G.N. David, S. Sebastian, S. Oliver, S. Sina, Z. Moritz, Pros and cons of ultra-high-field MRI/MRS for human application. Progr. Nuclear Magn. Reson. Spectr. **109**, 1–50 (2018)
11. E.M. Haacke, L.S. Pepropoulos, E.W. Nilges, D.H. Wu, Extraction of conductivity and permittivity using magnetic resonance imaging Phys. Med. Biol. **36**, 723–734 (1991)
12. T. Voigt, U. Katscher, O. Doessel, Quantitative conductivity and permittivity imaging of the human brain using electric properties tomography. Magn. Reson. Med. **66**, 456–466 (2011)
13. A.K. Kasinadhuni, M. Chauhan, A. Indahlastari, C. Anderson, P. Carney, T.H. Mareci, R.J. Sadleir, Mapping of magnetic fields due to current injection in the human brain using MREIT: First measurements, in *Proceedings of the 24th Annual Meeting and Exhibition ISMRM, Singapore* (2016), p. 1107
14. A.K. Kasinadhuni, Mapping current density due to electrical stimulation using magnetic resonance electrical impedance tomography. PhD Thesis, University of Florida, 2016
15. A.K. Kasinadhuni, A. Indahlastari, M. Chauhan, M. Schär, T.H. Mareci, R.J. Sadleir, Imaging of current flow in the human head during transcranial electrical therapy. Brain Stimul. **10**(4), 764–772 (2017)
16. L. Kaufman, D.M. Kramer, L.E. Crooks, D.A. Ortendahl, Measuring signal-to-noise ratios in MR imaging. Radiology **173**, 265–267 (1989)
17. R.M. Henkelman, Measurement of signal intensities in the presence of noise in MR images. Med. Phys. **12**, 232–233 (1985)
18. D.K. Sodickson, W.J. Manning, Simultaneous acquisition of spatial harmonics (SMASH): fast imaging with radiofrequency coil arrays. Magn. Reson. Med. **38**, 591–603 (1997)
19. K.P. Pruessmann, M. Weiger, M.B. Scheidegger, P. Boesiger, SENSE: sensitivity encoding for fast MRI. Magn. Reson. Med. **42**, 952–962 (1999)
20. P.B. Roemer, W.A. Edelstein, C.E. Hayes, S.P. Souza, O.M. Mueller, The NMR phased array. Magn. Reson. Med. **16**, 192–225 (1990)
21. O. Dietrich, J.G. Raya, S.B. Reeder, M.F. Reiser, S.O. Schoenberg, Measurement of signal-to-noise ratios in MR images: Influence of multichannel coils, parallel imaging, and reconstruction filters. J. Magn. Reson. Imag. **26**, 375–385 (2007)
22. J.P. Reilly, *Applied Bioelectricity: From Electrical Stimulation to Electropathology* (Springer, New York, 1998)
23. G.C. Scott, M.L.G. Joy, R.L. Armstrong, R.M. Henkelman, RF current density imaging in homogeneous media. Magn. Reson. Med. **28**(2), 186–201 (1992)
24. Y.Z. Ider, L.T. Muftuler, Measurement of AC magnetic field distribution using magnetic resonance imaging. IEEE Trans. Med. Imag. **16**(5), 617–22 (1997)
25. U. Mikac, F. Demšar, K. Beravs, I. Serša, Magnetic resonance imaging of alternating electric currents. Magn. Reson. Imag. **19**(6), 845–56 (2001)
26. M.J. Hamamura, L.T. Muftuler, Fast imaging for magnetic resonance electrical impedance tomography. Magn. Reson. Imag. **26**, 739–745 (2008)
27. C. Park, B.I. Lee, O. Kwon, E.J. Woo, Measurement of induced magnetic flux density using injection current nonlinear encoding (ICNE) in MREIT. Physiol. Meas. **28**, 117–127 (2007)
28. B.I. Lee, C.J. Park, H.C. Pyo, O. Kwon, E.J. Woo, Optimization of current injection pulse width in MREIT. Physiol. Meas. **28**, N1–N7 (2007)
29. O.I. Kwon, B.I. Lee, H.S. Nam, C.J. Park, Noise analysis and MR pulse sequence optimization in MREIT using an injected current nonlinear encoding (ICNE) method. Physiol. Meas. **28**, 1391–404 (2007)
30. H.S. Nam, O.I. Kwon, Optimization of multiply acquired magnetic flux density B_z using ICNE-Multiecho train in MREIT. Phys. Med. Biol. **55**, 2743–2759 (2010)
31. A. Minhas, W.C. Jeong, Y.T. Kim, Y. Han, H.J. Kim, E.J. Woo, Experimental performance evaluation of

multi-echo ICNE pulse sequence in magnetic resonance electrical impedance tomography. Magn. Reson. Med. **66**, 957–965 (2011)
32. J. Hennig, Echoes-how to generate, recognize, use or avoid them in MR-imaging sequences. Part 2: Echoes in imaging sequences. Concepts Magn. Reson. **3**, 179–192 (1991)
33. W.A. Edelstein, J.M. Hutchison, G. Johnson, T. Redpath, Spin warp NMR imaging and applications to human whole-body imaging. Phys. Med. Biol. **25**, 751–756 (1980)
34. J. Frahm, A. Haase, D. Matthaei, Rapid NMR imaging of dynamic processes using the FLASH technique. Magn. Reson. Med. **3**, 321–327 (1986)
35. M. Chauhan, R.V. Shankar, N.A. Kumar, V.D. Kodibagkar, R.J. Sadleir, Multishot echo-planar MREIT for fast imaging of conductivity, current density, and electric field distributions. Magn. Reson. Med. **79**, 71–82 (2018)
36. M.N. Kim, T.Y. Ha, E.J. Woo, O.I. Kwon, Improved conductivity reconstruction from multi-echo MREIT utilizing weighted voxel-specific signal-to-noise ratios. Phys. Med. Biol. **57**, 3643–3659 (2012)
37. T.I. Oh, W.C. Jeong, J.E. Kim, S.Z.K. Sajib, H.J. Kim, O.I. Kwon, E.J. Woo, Noise analysis in fast magnetic resonance electrical impedance tomography (MREIT) based on spoiled multi gradient echo (SPMGE) pulse sequence. Phys. Med. Biol. **59**(16), 4723 (2014)
38. H. Fischer, R. Ladebeck, Echo-planar imaging image artifacts, in *Echo-Planar Imaging* (Springer, Berlin, 1998)
39. S.B. Reeder, E. Atalar, B.D. Bolster Jr, E.R. McVeigh, Quantification and reduction of ghosting artifacts in interleaved echo-planar imaging. Magn. Reson. Med. **38**(3), 429–439 (1997)
40. Q.X. Yang, S. Posse, D.L. Bihan, M.B. Smith, Double-sampled echoplanar imaging at 3 Tesla. J. Magn. Reson. **113**, 145–150 (1996)
41. M.H. Buonocore, L. Gao, Ghost artifact reduction for echo planar imaging using image phase correction. Magn. Reson. Med. **38**, 89–100 (1997)
42. X. Wan, G.T. Gullberg, D.L. Parker, G.L. Zeng, Reduction of geometric and intensity distortions in echo-planar imaging using a multireference scan. Magn. Reson. Med. **37**, 932–944 (1997)
43. N.K. Chen, A.M. Wyrwicz, Nyquist ghost artifacts with two-dimensional phase correction. Mag. Reson. Med. **51**, 1247–1253 (2004)
44. J.Y. Chiou, C.B. Ahn, L.T. Muftuler, O. Nalcioglu, A simple simultaneous geometric and intensity correction method for echo-planar imaging by EPI-based phase modulation. Magn. Reson. Med. **22**, 200–205 (2003)
45. D.C. Ghiglia and M. D. Pritt, *Two-Dimensional Phase Unwrapping: Theory, Algorithms and Software* (Wiley-Interscience, New York, 1998)
46. E.M. Haacke, R.W. Brown, M.R. Thompson, R. Venkatesan, *Magnetic Resonance Imaging: Physical Principles and Sequence Design* (Wiley, New York, 1999)
47. S.H. Lee, J.K. Seo, C. Park, B.I. Lee, E.J. Woo, S.Y. Lee, O.I. Kwon, J. Hahn, Conductivity image reconstruction from defective data in MREIT: numerical Simulation and animal experiment. IEEE Trans. Med. Imag. **25**(2), 168–176 (2006)
48. B.I. Lee, S.H. Lee, T.S. Kim, O. Kwon, E.J. Woo, J.K. Seo, Harmonic decomposition in PDE-based denoising technique for magnetic resonance electrical impedance tomography. IEEE Trans. Biomed. Eng. **52**(11), 1912–20 (2005)
49. K. Jeon, C.O. Lee, H.J. Kim, E.J. Woo, J.K. Seo, CoReHA: conductivity reconstructor using harmonic algorithms for magnetic resonance electrical impedance tomography (MREIT). J. Biomed. Eng. **30**(5), 279–287 (2009)
50. K. Jeon, C.O. Lee, CoReHA 2.0: a software package for in vivo MREIT experiments. Comput. Math. Methods Med. **2013**, 941745 (2013)
51. M.A. Bernstein, K.F. King, X.J. Zhou, *Handbook of MRI Pulse Sequences* (Elsevier, Burlington, 2004)
52. C.O. Lee, K. Jeon, S.M. Ahn, H.J. Kim, E.J. Woo, Ramp-preserving denoising for conductivity image reconstruction in magnetic resonance electrical impedance tomography. IEEE Trans. Biomed. Eng. **58**, 2038–2050 (2011)
53. M. Kranjc, F. Bajd, I. Serša, E.J. Woo, D. Miklavčič, Ex-vivo and in silico feasibility study of monitoring electric field distribution in tissue during electroporation based treatments. PLoS ONE **7**(9), e457371–8 (2012)
54. O. Kwon, W.C. Jeong, S.Z.K. Sajib, H.J. Kim, E.J. Woo, Anisotropic conductivity tensor imaging in MREIT using directional diffusion rate of water molecules. Phys. Med. Biol. **59**(12), 2955–2974 (2014)
55. W.C. Jeong, S.Z.K. Sajib, N. Katoch, H.J. Kim, O.I. Kwon, E.J. Woo, Anisotropic conductivity tensor imaging of in vivo canine brain using DT-MREIT. IEEE Trans. Med. Imag. **36**(1), 124–131 (2017)
56. M. Chauhan, A. Indahlastari, A.K. Kasinadhuni, M. Schär, T.H. Mareci, R.J. Sadleir, Low-frequency conductivity tensor imaging of the human head in vivo using DT-MREIT: First study. IEEE Trans. Med. Imag. **37**(4), 966–976 (2018)
57. R. Polania, M.A. Nitsche, C.C. Ruff, Studying and modifying brain function with non-invasive brain stimulation. Nat. Neurosci. **21**, 174–187 (2018)
58. C. Göksu, L.G. Hanson, H.R. Siebner, P. Ehses, K. Scheffler, A. Thielscher, Human in-vivo brain magnetic resonance current density imaging (MRCDI). NeuroImage **171**, 26–39 (2018)
59. P. Lövsund, P.A. Öburg, S.E. Nilson, Magneto- and electrophosphenes: a comparative study. Med. Biol. Eng. Comput. **18**, 758–764 (1980)
60. A. Indahlastari et al., Methods to compare predicted and observed phosphene experience in tACS subjects. Neuropsychologia **2018**, ID-8525706 (2018)

61. J.L.R. Andersson, S. Skare, J. Ashburner, How to correct susceptibility distortions in spin-echo echo-planar images: Application to diffusion tensor imaging. NeuroImage **20**(2), 870–888 (2003)
62. V.M. Spitzer, D.G. Whitlock, *National Library of Medicine Atlas of the Visible Human Male: Reverse Engineering of the Human Body*, 1st edn. (Jones & Bartlett Learning, Burlington, 1997)
63. D. Miklavčič, K. Beravs, D. Šemrov, M. Čemažar, F. Demšar, G. Serša, The importance of electric field distribution for effective in vivo electroporation of tissues. Biophys J. **74**(5), 2152–2158 (1998)
64. R.V. Davalos, L.M. Mir, B. Rubinsky, Tissue ablation with irreversible electroporation. Ann. Biomed. Eng. **33**, 223–231 (2005)
65. M, Kranjc, F. Bajd, I. Serša, D, Miklavčič, Magnetic resonance electrical impedance tomography for monitoring electric field distribution during tissue electroporation. IEEE Trans. Med. Imag. **30**(10), 1771–1778 (2011)
66. I. Serša, Auxiliary phase encoding in multi spin-echo sequences: application to rapid current density imaging. J. Magn. Reson. **190**, 86–94 (2008)
67. O. Kwon, E.J. Woo, J.R. Yoon, J.K. Seo, Magnetic resonance electrical impedance tomography (MREIT): simulation study of J-substitution algorithm. IEEE Trans. Biomed. Eng. **49**(2), 160–167 (2002)
68. D. Miklavčič, M. Snoj, A. Zupanic, et.al., Towards treatment planning and treatment of deep-seated solid tumors by electrochemotherapy. Biomed. Eng. Online **9**, 10 (2010)
69. A. Zupanic, B. Kos, D. Miklavčič, Treatment planning of electroporation-based medical interventions: electrochemotherapy, gene electro-transfer and irreversible electroporation. Phys. Med. Biol. **57**, 5425–40 (2012)
70. D, Sel, D. Cukjati, D. Batiuskaite, T. Slivnik, L. Mir, D. Miklavčič, Sequential finite element model of tissue electropermeabilization. IEEE Trans. Biomed. Eng. **52**, 816–27 (2005)
71. N. Pavselj, Z. Bregar, D. Cukjati, D. Batiuskaite, L. Mir, D. Miklavčič, The course of tissue permeabilization studied on a mathematical model of a subcutaneous tumor in small animals. IEEE Trans. Biomed. Eng. **52**, 1373–81 (2005)
72. M. Kranjc, F. Bajd, I. Serša, D. Miklavčič, Magnetic resonance electrical impedance tomography for measuring electrical conductivity during electroporation. Physiol. Meas. **35**(6), 985–996 (2014)
73. O. Kwon, J.K. Seo, E.J. Woo, J.R. Yoon, S.Y. Lee, M.H. Cho, Resistivity image reconstruction using J-substitution algorithm for MREIT, in *Proceedings of the 23rd Annual International Conference of the IEEE Engineering in Medicine and Biology Society* (2001)
74. K. Jeon, H.J. Kim, C.O. Lee, J.K. Seo, E.J. Woo, Integration of the denoising, inpainting and local harmonic B_z algorithm for MREIT imaging of intact animals. Phys. Med. Biol. **55**(24), 7541 (2010)

Magnetic Resonance Current Density Imaging (MR-CDI)

6

Saurav Z. K. Sajib and Rosalind Sadleir

Abstract

Current density imaging (CDI) was developed with the aim of determining the three-dimensional distribution of externally applied electric current pathways inside a conductive medium, using measurements of magnetic flux density $\mathbf{B} = \left(B_x, B_y, B_z\right)$ data. While the **B** field may be measurable using instruments such as a magnetometer, in magnetic resonance current density imaging (MR-CDI), an MRI scanner is used to measure the magnetic flux density data induced by current flow. In MR-CDI, the object must be rotated inside the MRI machine to find all three components of the **B**-field, as only the component of **B** parallel to the magnet main magnetic field can be measured. In principle, once the all three components of the **B** field have been obtained from an MR imaging experiment, the current density distribution $\mathbf{J} = \left(J_x, J_y, J_z\right)$ can be reconstructed from Ampere's law $\mathbf{J} = \frac{1}{\mu_0}\nabla \times \mathbf{B}$. However, the need to rotate the object within the MRI scanner limits the usability of this technique. To overcome this problem, researchers have investigated the current density reconstruction problem using only one component of the magnetic flux density B_q, where $q = x, y, z$. In this chapter, we discuss numerical algorithms developed to reconstruct the distribution of **J** information from the measured **B**-field.

6.1 Introduction

Magnetic resonance current density imaging (MR-CDI) seeks to visualize electrical current distributions within a biological medium caused by an externally impressed electrical current [10, 35, 36]. The MR-CDI method, first developed in early 90s, uses a magnetic resonance imaging (MRI) scanner as a tool to capture the internal magnetic flux density distribution generated by the injection current. However, MR imaging coils can only measure the component of the magnetic flux density along the direction of the main magnetic field. To obtain all three components requires successive rotations of the object to align with each of the three coordinate directions. Once the magnetic flux density component from each orientation is obtained, it is possible to combine these data $\mathbf{B} = (B_x, B_y, B_z)$ to produce an image of the corresponding internal current density distribution $\mathbf{J} = (J_x, J_y, J_z)$ using Ampere's law $\mathbf{J} = \nabla \times \mathbf{B}/\mu_0$, where

S. Z. K. Sajib (✉) · R. Sadleir
School of Biological Health System Engineering, Arizona State University, Tempe, AZ, USA
e-mail: ssajib1@asu.edu; rsadleir@asu.edu

R. Sadleir, A. S. Minhas (eds.), *Electrical Properties of Tissues*, Advances in Experimental Medicine and Biology 1380, https://doi.org/10.1007/978-3-031-03873-0_6

μ_0 is the magnetic permeability of free space [35, 36]. Unfortunately, the need to rotate the object inside the MRI machine often limits the usability of this elegant technique, especially in the case of human and animal studies. Moreover, rotations may ultimately cause registration or conformation errors in the combined data [13].

Roth et al. [25] developed a two-dimensional current density image reconstruction algorithm, using a Fourier form of the Bio-Savart law and assuming the current distribution is confined in a thin sheet of thickness $d \rightarrow 0$. Although this method assumed measurements were to be made with a magnetometer, it is still applicable to the MR-CDI problem [23]. Later, a similar approach was proposed by Gao and He [4]. They extended Roth et al. 's approach, assuming a three-dimensional distribution of the current density, to reconstruct the transverse current density components $\tilde{\mathbf{J}} := \left(\tilde{J}_x, \tilde{J}_y\right)$ data from the measured B_q, $q = x, y, z$ images, by discretizing the Bio-Savart law in the spatial domain. Pyo et al. [24] developed another iterative algorithm that accommodated both tissue anisotropy and non-transversal current flow. While their method can reconstruct non-transversal current flow within an anisotropic conductive medium, its initial steps require knowledge of an approximate isotropic conductivity distribution reconstructed using data from two independent current injections. Seo et al. [37] also developed an algorithm to reconstruct transverse current density distributions, with the assumption that the conductivity distribution within the object is isotropic and the current flow in the axial (z) direction is small, i.e., $J_z \approx 0$. As noted above, we can only measure the z component of the magnetic flux density using MRI. Therefore, components of the magnetic flux or current density which are perpendicular to the measured magnetic flux density direction are usually referred to as transverse components, whereas the parallel direction is called the longitudinal or non-transverse component of the current density. For example, if we acquire the z component of the magnetic flux density, i.e., B_z, the x and y current density components will be transverse, and the J_z will be the longitudinal current component.

By analyzing the relationship between the three-dimensional distribution of the current and measured one component of magnetic flux density data, Park et al. [22] later developed a method called projected current density $\mathbf{J}^P$ algorithm. This method is important because it makes no assumption about the conductivity distribution. The algorithm proceeds by decomposing the true current density vector field into contributions from the projected $\mathcal{P}$ and the null $\mathcal{N}$ space. It can be shown that the reconstructed projected current density $\mathbf{J}^P$ is uniquely determined as the three-dimensional distribution of current which can be measured from only one component of the magnetic flux density data. Later, Kim et al. [14] and Sajib et al. [28] extended this method to reconstruct the current density in local regions, to avoid propagation of noise from regions with lower signal quality throughout the image. Ider et al. [7] also considered the current density image reconstruction problem in the Fourier domain. Since it is possible to construct a three-dimensional computational model of the object from MR magnitude data, Jeong et al. [8] and Kwon et al. [15] suggested improving current density image reconstruction methods by comparing the model-predicted current density with that suggested by magnetic flux density data.

Several groups have explored the feasibility of using the MR-CDI method, in numerous biomedical applications. For example, Yoon et al. [41] proposed using MR-CDI in cardiac applications. They used CDI to image current density distributions in a postmortem pig torso subject to defibrillation. Their study confirmed predictions that the highest current density can be observed in the chest wall. Moreover, current streamline plots within the myocardium closely followed the fiber direction of the cardiac muscle. They suggested that MR-CDI method may be useful in characterizing and diagnose diseases of heart muscle [41]. MR-CDI has also been proposed for monitoring osteoporosis, since this condition lowers the mineralization of solid bone [1]. This study also proposed that CDI may be useful in identifying bone fractures.

The brain is also of great interest to researchers. Gamba and Delpy [3] produced the first study to evaluate current density distributions within the brain. They used a pair of surface electrodes attached on in vivo and postmortem piglet skulls and were able to reconstruct the current distribution inside the brain. Joy et al. [11] also demonstrate that CDI may be useful for monitoring the current pathway during transcranial electrical stimulation (tES) by demonstrating measurements in the brain of a rabbit in vivo. However, in reconstructing the current distribution, both these studies measured all three components of the magnetic flux density. The single-component projected current density method of Kwon et al. [15] was used to study current density distributions inside the in vivo human brain during tES [5, 9, 12].

Deep brain stimulation, where internal electrodes are placed inside a specific brain region to directly deliver a stimulating current [18], is used to treat neurological conditions such as Parkinson's disease, with newer indications suggesting it may also be beneficial in managing Parkinson's disease and depression [17]. Sajib et al. [30] demonstrated that it is also possible to image the current pathways during DBS therapy using one component of magnetic flux density data measured in the in vivo canine brain.

In irreversible electroporation ablation therapy [19], pairs of internal electrodes are used to deliver high-amplitude electric pulses to tissues. The single-component CDI technique has also been used to monitor local current density distributions during electroporation treatment [39].

While numerous clinical applications of MR-CDI methods based on single-component $\mathbf{B}$ measurements are being developed, there are several practical issues which need to be considered. Since current is delivered to the object through pairs of electrodes connected to a source via lead wires, it is important to constrain the wire traces so they are parallel to the measurement direction. For example, if the flux density component B_z is measured, wires must be arranged so they are aligned with the z-axis. However, in many experimental and clinical conditions, this constraint is not always possible. Therefore, in general the measured data must be understood as being a sum of the current-induced domain magnetic flux density and *stray* magnetic flux created by current flow in the lead wires and electrode surface currents. These stray fields must be corrected before reconstructing current density distributions. In this chapter, we aim to provide a solid foundation of various image reconstruction algorithms in MR-CDI. We also briefly explain a method to remove wire- and electrode-created stray magnetic fields using a computational model acquired during a standard structural imaging procedures.

6.2 Preliminaries

The flow of externally injected current throughout the domain $\Omega \in \mathbb{R}^3$ caused by a current I applied by a pair of surface electrodes $\mathcal{E}^{\pm}$ is described by the divergence-free condition $\nabla \cdot \mathbf{J} = 0$ with the following constraints [38]

$$\nabla \cdot \mathbf{J} = \nabla \cdot (-\sigma \nabla u) = 0 \quad \text{in} \quad \Omega \tag{6.1a}$$

$$I = \pm \int_{\mathcal{E}^{\pm}} \sigma \frac{\partial u}{\partial \mathbf{n}} \cdot d\mathbf{s}, \ \nabla u \times \mathbf{n} = 0 \quad \text{on} \quad \mathcal{E}^{+} \bigcup \mathcal{E}^{-} \tag{6.1b}$$

$$-\sigma \frac{\partial u}{\partial \mathbf{n}} = 0 \quad \text{on} \quad \partial\Omega \setminus \left(\mathcal{E}^{+} \bigcup \mathcal{E}^{-}\right) \tag{6.1c}$$

where σ and u denote the conductivity and voltage distributions within Ω, respectively, and $\mathbf{n}$ represents the outward normal vector at a position $\mathbf{r}$ on the domain boundary $\partial\Omega$.

The continuity relationship in Eq. (6.1a) guarantees that there will be no charge deposition or internal source. Also, Eq. (6.1c) ensures that the current density outside the object Ω is zero. Furthermore, requiring $\nabla u \times \mathbf{n} = 0$ on the electrodes guarantees a constant potential in this region. This condition is valid because electrodes are typically made of highly conductive materials. The other condition in Eq. (6.1b)—a Neumann boundary condition—relates to the total injected current inside the object, which is known. Numerical models are often used to create data used in reconstruction processes, and computational electromagnetic models may be solved on domains

approximating an experimental object, subject to the conditions of (6.1b). However, in numerical models it is impossible to define the Neumann data in a pointwise sense [38], and an alternative approach may be used. Since the total injected current entering Ω through the anode $\mathcal{E}^+$ must leave the sink electrode $\mathcal{E}^-$, it has been shown that Eqs. (6.1a)–(6.1c) can be converted to [38],

$$\begin{cases} \nabla \cdot (-\sigma \nabla \tilde{u}) = 0 & \text{in} \quad \Omega \\ \tilde{u}|_{\mathcal{E}^+} = 1 \quad \tilde{u}|_{\mathcal{E}^-} = 0 \\ -\sigma \frac{\partial \tilde{u}}{\partial \mathbf{n}} = 0 & \text{on} \quad \partial\Omega \setminus \left(\mathcal{E}^+ \bigcup \mathcal{E}^-\right) \end{cases} \tag{6.2}$$

Once the solution $\tilde{u}$ is obtained from the Eq. (6.2) with these Dirichlet boundary conditions, the actual voltage distribution u of the boundary value problem (6.1a) may be determined using

$$u = \beta \tilde{u} \tag{6.3}$$

where the scale factor β is the ratio of the experimentally injected current I and the total current $\int_{\mathcal{E}^+} \sigma \frac{\partial \tilde{u}}{\partial \mathbf{n}} \cdot d\mathbf{s}$ injected into the model. This ratio is

$$\beta = \frac{I}{\int_{\mathcal{E}^+} \sigma \frac{\partial \tilde{u}}{\partial \mathbf{n}} \cdot d\mathbf{s}}. \tag{6.4}$$

The current density distribution $\mathbf{J}$ within the object can then be obtained via Ohm's law:

$$\mathbf{J} = -\sigma \nabla u \tag{6.5}$$

and the magnetic flux density $\mathbf{B}_\Omega = \left(B_x, B_y, B_z\right)$ can be obtained using the Biot-Savart law:

$$\mathbf{B}(\mathbf{r}) = \frac{\mu_0}{4\pi} \int_\Omega \mathbf{J}(\mathbf{r}') \times \frac{\mathbf{r} - \mathbf{r}'}{|\mathbf{r} - \mathbf{r}'|^3} d\mathbf{r}' \tag{6.6}$$

where $\mu_0 = 4\pi \times 10^{-7}$ H/m is the permeability of free space. Expanding the term $\mathbf{J}(\mathbf{r}') \times \frac{\mathbf{r}-\mathbf{r}'}{|\mathbf{r}-\mathbf{r}'|^3}$ in Eq. (6.6), each component of the magnetic flux density can individually be expressed as

$$B_x(x,y,z) = \frac{\mu_0}{4\pi} \int_\Omega \frac{\left(z-z'\right) J_y\left(x',y',z'\right) - \left(y-y'\right) J_z\left(x',y',z'\right)}{\left((x-x')^2 + (y-y')^2 + (z-z')^2\right)^{3/2}} dx'\,dy'\,dz' \tag{6.7a}$$

$$B_y(x,y,z) = \frac{\mu_0}{4\pi} \int_\Omega \frac{\left(x-x'\right) J_z\left(x',y',z'\right) - \left(z-z'\right) J_x\left(x',y',z'\right)}{\left((x-x')^2 + (y-y')^2 + (z-z')^2\right)^{3/2}} dx'\,dy'\,dz' \tag{6.7b}$$

$$B_z(x,y,z) = \frac{\mu_0}{4\pi} \int_\Omega \frac{\left(y-y'\right) J_x\left(x',y',z'\right) - \left(x-x'\right) J_y\left(x',y',z'\right)}{\left((x-x')^2 + (y-y')^2 + (z-z')^2\right)^{3/2}} dx'\,dy'\,dz' \tag{6.7c}$$

The induced current density $\mathbf{J}$ and the magnetic flux density $\mathbf{B}$ also satisfy Ampere's law:

$$\mathbf{J} = \frac{1}{\mu_0} \nabla \times \mathbf{B} \tag{6.8}$$

In a typical MR-CDI experiment (see Fig. 6.1), an external current source is connected via the lead wires to deliver a low-amplitude current through the surface electrodes. The current-induced magnetic flux density is then collected using an MRI machine. Therefore, the total magnetic flux density measured in an MR-CDI experiment will be the sum of the current-induced magnetic flux density inside the imaging domain $\mathbf{B}^m_\Omega$ and magnetic flux density due to the current flow on the electrode surface $\mathbf{B}_\mathcal{E}$, and lead wire-created magnetic fields, $\mathbf{B}_\mathcal{L}$. Since only the component of the magnetic flux density which is parallel to the main magnetic field of the MRI machine $B_0 = \mathbf{B}_0 \cdot (0,0,1)$ can be measured, the magnetic flux density acquired during the MR-CDI experiment can be explicitly expressed as [16]

$$B^m_x = B^m_{x,\Omega} + B_{x,\mathcal{E}} + B_{x,\mathcal{L}} \tag{6.9a}$$

$$B^m_y = B^m_{y,\Omega} + B_{y,\mathcal{E}} + B_{y,\mathcal{L}} \tag{6.9b}$$

$$B^m_z = B^m_{z,\Omega} + B_{z,\mathcal{E}} + B_{z,\mathcal{L}} \tag{6.9c}$$

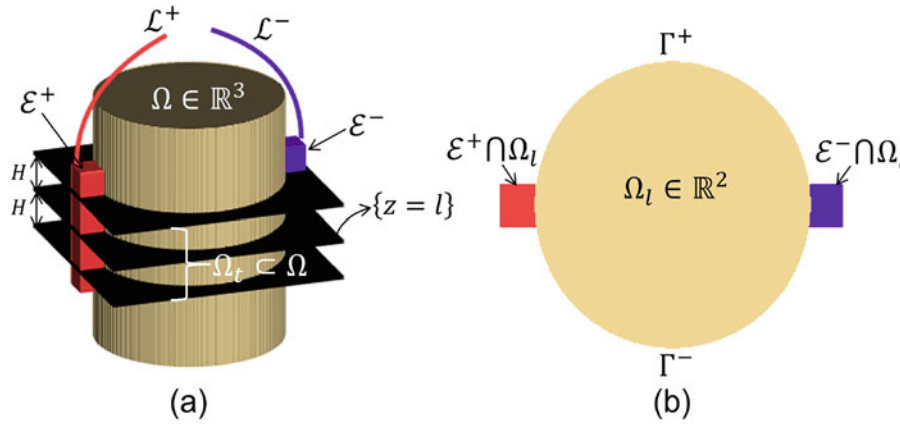

Fig. 6.1 (**a**) Illustration of a typical MR-CDI experimental setup. The surface electrodes $(\mathcal{E} = \mathcal{E}^+ \bigcup \mathcal{E}^-)$ with wires $(\mathcal{L} = \mathcal{L}^+ \bigcup \mathcal{L}^-)$ are used to deliver current inside the object domain Ω. In a typical MR-CDI experiment, the **B** field is collected from a portion of the whole imaging domain represented by $\Omega_t \subset \Omega$. (**b**) Central imaging slice $\Omega_l = \Omega_t \bigcap \left\{(x, y, z) \in \mathbb{R}^3|_{z=l\in(l-H,l+H)}\right\}$ with boundary notations $\mathcal{E}^{\pm} \bigcap \partial\Omega_l$ and $\Gamma^{\pm}$

From Eqs. (6.9a)–(6.9c), it is clear that the measured magnetic flux density may vary depending on the geometric arrangement of the lead wires and shape of the electrodes. However, the $\mathbf{B}^m_\Omega$ inside the domain Ω induced due to the external current injection depends only on the Neumann data applied on its boundary $\partial\Omega$, since as in [16]

$$\frac{1}{\mu_0}\nabla \times (\mathbf{B}_\mathcal{E} + \mathbf{B}_\mathcal{L}) = \frac{1}{4\pi}\nabla \int_{\partial\Omega} \frac{\mathbf{J}(\mathbf{r}') \cdot \mathbf{n}(\mathbf{r})}{|\mathbf{r} - \mathbf{r}'|} d\Omega' \tag{6.10}$$

Equation (6.10) clearly shows that two completely different sets of electrodes and lead wires produce the same current density **J** in Ω only if they establish the same Neumann boundary conditions on $\partial\Omega$. Therefore, the lead wire trajectories do not have any effect on the current density **J** within Ω. However, since the measured magnetic flux density using an MRI scanner is affected by lead wire and electrode-created stray magnetic fields (see Eqs. (6.9a)–(6.9c)), in some current density reconstruction algorithms, additional preprocessing steps are required to remove them. Fortunately, because of the superposition principle, a three-dimensional numerical model including wire and electrode surfaces can be used in this purpose. A detailed description can be found later in this chapter.

6.3 Current Density Imaging via Ampere's Law

As we have noted previously, only B_z can be measured by the MR machine. Therefore, to explicitly measure the other components of **B**, the imaging object must be rotated inside the MRI system bore. This process is explained in Fig. 6.2. Once the current-induced magnetic flux density $\mathbf{B}^m_\Omega = \left(B^m_{x,\Omega}, B^m_{y,\Omega}, B^m_{z,\Omega}\right)$ within Ω is measured, Ampere's law (Eq. (6.8)) can be used to reconstruct the current density images [35]:

$$J_x = \frac{1}{\mu_0}\left(\frac{\partial B^m_{z,\Omega}}{\partial y} - \frac{\partial B^m_{y,\Omega}}{\partial z}\right) \tag{6.11a}$$

$$J_y = \frac{1}{\mu_0}\left(\frac{\partial B^m_{x,\Omega}}{\partial z} - \frac{\partial B^m_{z,\Omega}}{\partial x}\right) \tag{6.11b}$$

$$J_z = \frac{1}{\mu_0}\left(\frac{\partial B^m_{y,\Omega}}{\partial x} - \frac{\partial B^m_{x,\Omega}}{\partial y}\right). \tag{6.11c}$$

Direct reconstruction of the current density vector field described in Eqs. (6.11a)–(6.11c) requires extraction of the $\mathbf{B}_\Omega$ information from the complex MR signal. For example, the two-dimensional complex MR image $\mathcal{M}^{\pm}_{c,q}$ with interleaved current injection $I^{\pm}$ [36] with a perfect rectangular pulse may be modeled as [36]

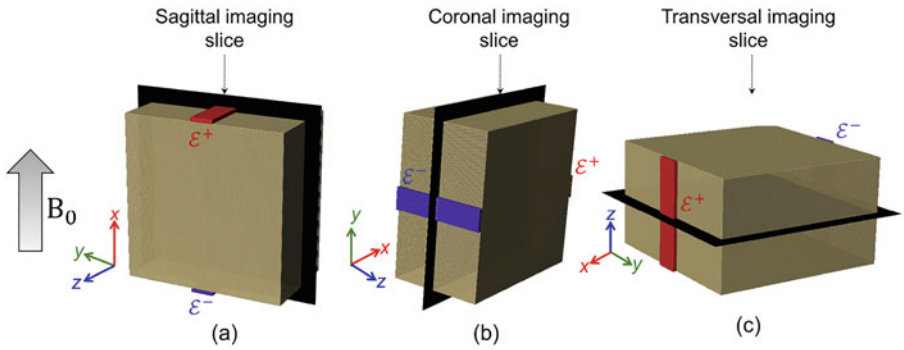

Fig. 6.2 Illustration of object rotation sequence inside the MRI scanner to sequentially measure components of $\mathbf{B} = (B_x, B_y, B_z)$ field. (**a**) Current is injected into yz plane to measure B_x. (**b**) Current is injected into zx plane and B_y is measured. (**c**) Current is injected into xy plane and induced B_z is measured. Coordinate system is relative to object. The arrow at left shows the direction of the main magnetic field of the MRI scanner

$$\mathcal{M}^{\pm}_{c,q}(x,y) = \mathcal{K}_{\mathcal{M}}\mathcal{M}(x,y)\, e^{i\delta(x,y)} e^{\pm i\gamma B^{m}_{q,\Omega}(x,y)T_c}, \quad q = x, y, z \tag{6.12}$$

where the subscript q in $B^{m}_{q,\Omega}$ denotes the x, y, z-coordinates, $\mathcal{M}(x, y)$ is the continuous real transverse magnetization expressed in the sample coordinate system, $\gamma = 26.7519 \times 10^7$ rad/T $\cdot$ s is the proton's gyromagnetic ratio, and current injection duration is represented by T_c. Any systematic phase artifact is denoted by a constant phase $\delta(x, y)$ which does not change with time, and the constant $\mathcal{K}_{\mathcal{M}}$ is related to imaging parameters such as the voxel size and the number of k-space lines sampled by the sequence. Comparing the two measurements, the component $B^{m}_{q,\Omega}(x, y)$ can be found as

$$B^{m}_{q,\Omega}(x,y) = \frac{1}{2\gamma T_c}\tan^{-1}\left(\frac{\mathcal{M}^{+}_{I,q}\mathcal{M}^{-}_{R,q} - \mathcal{M}^{-}_{I,q}\mathcal{M}^{+}_{R,q}}{\mathcal{M}^{+}_{I,q}\mathcal{M}^{-}_{I,q} + \mathcal{M}^{+}_{R,q}\mathcal{M}^{-}_{I,q}}\right), \quad q = x, y, z \tag{6.13}$$

where $\mathcal{M}^{\pm}_{R,q}$ and $\mathcal{M}^{\pm}_{I,q}$ are spatial components of the real and imaginary part of the measured MR complex signal $\mathcal{M}_{c,q^{\pm}}$ obtained using the interleaved current injections $I^{\pm}$. Since extraction of $B^{m}_{q,\Omega}$ involves the $\tan^{-1}$ operation, which may cause phase wrapping [35], an efficient phase unwrapping method may be required. To avoid this, one may use the exact definition of the phase derivative. For example, to compute the z component of the current density in Eq. (6.11c), the x and y derivatives of $B^{m}_{y,\Omega}$ and $B^{m}_{x,\Omega}$ data, respectively, must be evaluated. The exact definition of $\frac{\partial B^{m}_{y,\Omega}}{\partial x}$, $\frac{\partial B^{m}_{x,\Omega}}{\partial y}$ yields [35]

$$\frac{\partial B^{m}_{y,\Omega}}{\partial x} = \frac{\mathcal{M}^{+}_{R,y}\frac{\partial \mathcal{M}^{+}_{I,y}}{\partial x} - \mathcal{M}^{+}_{I,y}\frac{\partial \mathcal{M}^{+}_{R,y}}{\partial x} - \mathcal{M}^{-}_{R,y}\frac{\partial \mathcal{M}^{-}_{I,y}}{\partial x} + \mathcal{M}^{-}_{I,y}\frac{\partial \mathcal{M}^{-}_{R,y}}{\partial x}}{2\gamma T_c |\mathcal{M}_{c,y}|^2} \tag{6.14a}$$

$$\frac{\partial B^{m}_{x,\Omega}}{\partial y} = \frac{\mathcal{M}^{+}_{R,x}\frac{\partial \mathcal{M}^{+}_{I,x}}{\partial y} - \mathcal{M}^{+}_{I,x}\frac{\partial \mathcal{M}^{+}_{R,x}}{\partial y} - \mathcal{M}^{-}_{R,x}\frac{\partial \mathcal{M}^{-}_{I,x}}{\partial y} + \mathcal{M}^{-}_{I,x}\frac{\partial \mathcal{M}^{-}_{R,x}}{\partial y}}{2\gamma T_c |\mathcal{M}_{c,x}|^2}. \tag{6.14b}$$

To reconstruct the current density, the directional derivative of the measured data must be evaluated. However, discrete approximation of the numerical derivative is prone to truncation errors. For example, for the central difference approximation of the first derivative, the truncation error is approximately $O(\Delta^2)$, where Δ is the pixel dimension (see Appendix 1 for details). The advantage of Eqs. (6.14a)–(6.14b) is that one can directly apply the Fourier method [36] to evaluate the directional derivative, without needing to use any numerical approximation. Hence, this method is called the exact method in [36].

However, in practice it may not possible to determine the magnetic flux density within the domain $B^m_{q,\Omega}$, $q = x, y, z$ using an MRI system because of stray magnetic flux in lead wires and electrodes (see Eqs. (6.9a)–(6.9c)). Additional steps are therefore required to remove these effects from the measured phase data. As a consequence, discrete approximation of the numerical derivative is frequently used to find the current density in MR-CDI [35]. This is accomplished by convolving the measured phase data with directional derivative templates. In [35], Scott et al. proposed several different directional derivative templates. Though it is possible to design large filter templates to reduce the noise in the measured data, these may cause spatial blurring and edge effects. Therefore, use of such templates may lead to loss of important features of internal structures. In practice, 3×3 templates are most often used to evaluate the x and y directional derivatives of $\mathbf{B}$ components [36]. These may be written as

$$\frac{\partial}{\partial x} \approx \frac{1}{8\Delta}\begin{pmatrix} -1 & 0 & 1 \\ -2 & 0 & 2 \\ -1 & 0 & 1 \end{pmatrix}$$

$$\text{and } \frac{\partial}{\partial y} \approx \frac{1}{8\Delta}\begin{pmatrix} 1 & 2 & 1 \\ 0 & 0 & 0 \\ -1 & -2 & -1. \end{pmatrix} \quad (6.15)$$

Please refer to Appendix 1 for details.

6.4 Current Density Reconstruction Algorithms from one Component of Magnetic Flux Density data

Several methods have been developed to reconstruct current density images from only one component of the magnetic flux density data and avoid practical limitations on object or subject rotation. In this section we briefly discuss a few of them.

6.4.1 Current Density Reconstruction Using the Discretized Bio-Savart Law

Gao and He [4] proposed a method to reconstruct the transverse current density $\tilde{\mathbf{J}} := \left(\tilde{J}_x, \tilde{J}_y\right)$ from measured current-induced $B^m_{z,\Omega}$ data. By discretizing the volume conductor model into N elements and assuming that current density are constant in each element, the Eq. (6.7c) can be transformed into the following matrix system:

$$\tilde{\mathbf{B}}_{N\times 1} = \mathcal{K}_{N\times 2N}\tilde{\mathbf{J}}_{2N\times 1} \quad (6.16)$$

where

$$\tilde{\mathbf{B}}_{N\times 1} = \begin{pmatrix} B^m_{z,\Omega,1} \\ B^m_{z,\Omega,2} \\ B^m_{z,\Omega,3} \\ \vdots \\ B^m_{z,\Omega,N} \end{pmatrix}, \quad \mathcal{K}_{N\times 2N} = \begin{pmatrix} K_{y,11} & -K_{x,11} & K_{y,12} & -K_{x,12} & \cdots & K_{y,1N} & -K_{x,1N} \\ K_{y,21} & -K_{x,21} & K_{y,22} & -K_{x,22} & \cdots & K_{y,2N} & -K_{x,2N} \\ K_{y,31} & -K_{x,31} & K_{y,32} & -K_{x,32} & \cdots & K_{y,3N} & -K_{x,3N} \\ \vdots & \vdots & \vdots & \vdots & \cdots & \vdots & \vdots \\ K_{y,N1} & -K_{x,N1} & K_{y,N2} & -K_{x,N2} & \cdots & K_{y,NN} & -K_{x,NN} \end{pmatrix}$$

$$\text{and, } \tilde{\mathbf{J}}_{2N\times 1} = \begin{pmatrix} \tilde{J}_{x,1} \\ \tilde{J}_{y,1} \\ \tilde{J}_{x,2} \\ \tilde{J}_{y,2} \\ \tilde{J}_{x,3} \\ \tilde{J}_{y,3} \\ \vdots \\ \tilde{J}_{x,N} \\ \tilde{J}_{y,N} \end{pmatrix}$$

The ij-th kernel elements of the matrix $K_{2N\times N}$ can be found as

$$\begin{cases} K_{x,ij} = \frac{\mu_0}{4\pi} \frac{x_i - x_j}{\left((x_i-x_j)^2+(y_i-y_j)^2+(z_i-z_j)^2\right)^{3/2}} \Delta x_j \Delta y_j \Delta z_j \\ K_{y,ij} = \frac{\mu_0}{4\pi} \frac{y_i - y_j}{\left((y_i-y_j)^2+(y_i-y_j)^2+(z_i-z_j)^2\right)^{3/2}} \Delta x_j \Delta y_j \Delta z_j \end{cases}$$

In Gao and He [4], zeroth-order Tikhonov regularization was used to solve Eq. (6.16):

$$\tilde{\mathbf{J}}(\lambda) = \left(\mathcal{K}^T\mathcal{K} + \lambda \mathbf{I}_{\mathbf{2N\times 2N}}\right)^{-1} \mathcal{K}^T \tilde{\mathbf{B}} \tag{6.17}$$

where T represents the matrix transpose, $\tilde{\mathbf{J}}(\lambda)$ is the estimated current density using a regularization parameter λ, and $\mathbf{I}$ is the identity matrix with dimension $2N \times 2N$. The regularization parameter in [4] was determined using l-curve analysis [20]. It is worth mentioning that the regularization in (6.17) has a smoothing effect. Therefore, an improper choice of λ-value may cause image blurring [20].

6.4.2 Seo's Method

Seo et al. [37] also developed a transverse current density reconstruction method using measured B_z data. Assuming that the isotropic conductivity σ is constant along the z direction, that is, $\frac{\partial\sigma}{\partial z} \approx 0$, $\tilde{\mathbf{J}}^m$ can be found as

$$\tilde{\mathbf{J}}^m(\mathbf{r}) = \nabla_{xy}^{\perp}(\phi + \alpha\psi) \tag{6.18}$$

where $\nabla_{xy}^{\perp} := \left(\frac{\partial}{\partial y}, -\frac{\partial}{\partial x}\right)$ and the terms ϕ and ψ in Eq. (6.18) are the solution of the following boundary value problem

$$\begin{cases} \nabla_{xy}^2\phi = \dfrac{1}{\mu_0}\nabla^2 B_z^m & \text{in } \Omega_l \\ \hat{\nu}\cdot\tilde{\nabla}\phi = 0 & \text{on } (\mathcal{E}^+ \bigcup \mathcal{E}^-) \bigcap \Omega_l \\ \phi = 0 & \text{on } \Gamma^+ \bigcup \Gamma^- \end{cases} \tag{6.19}$$

and

$$\begin{cases} \nabla_{xy}^2\psi = 0 & \text{in } \Omega_l \\ \nabla_{xy}\cdot\psi\hat{\nu} = 0 & \text{on } (\mathcal{E}^+ \bigcup \mathcal{E}^-) \bigcap \Omega_l \\ \psi|_{\Gamma^\pm} = \pm 1 \end{cases} \tag{6.20}$$

The scaling factor α is defined as

$$\alpha = \frac{\int_{\mathcal{E}^+\bigcap\Omega_l} \sigma\nabla u\cdot\hat{\nu}dl - \int_{\mathcal{E}^+\bigcap\Omega_l} \nabla_{xy}\phi\times\hat{\nu}dl}{\int_{\mathcal{E}^+\bigcap\Omega_l} \nabla_{xy}\psi\times\hat{\nu}dl} \tag{6.21}$$

where Ω_l is the two-dimensional slice cut by the xy plane $\{z = l\}$ (Fig. 6.1a). The integration along $\mathcal{E}^+ \bigcap \Omega_l$, Γ^+, Γ^-, and $\mathcal{E}^- \bigcap \Omega_l$ is defined in the counterclockwise direction (see Fig. 6.1b), dl is the arc length element, and $\hat{\nu}$ is the two-dimensional unit outward normal vector to $\partial\Omega_l$.

Comparing this formula to (6.17) in Sect. 6.4.4, the method is computationally complex. However note that the data used is the Laplacian of B_z $\nabla^2 B_z$. This method therefore does not require compensation for wire and electrode-related stray magnetic fields.

6.4.3 Projected Current Density Algorithm

Park et al. [22] analyzed the extent of the three-dimensional current density vector that was recoverable from only one component of measured magnetic flux density data, without any making any assumption of the conductivity distribution properties. Using the Helmholtz decomposition of the current density vector field into its curl-free and divergence-free parts, Park et al. [22] provided a reconstruction formula:

$$\mathbf{J}^P = \mathbf{J}^0 + \mathbf{J}^*, \tag{6.22}$$

where $\mathbf{J}^0$ and $\mathbf{J}^*$ are the curl-free and divergence-free contributions, respectively. The quantity $\mathbf{J}^P = \left(J_x^P, J_y^P, J_z^0\right)$ is the reconstructed three-dimensional current density vector field obtainable from one component of the measured B_z data, which is denoted the *projected current density*.

To obtain the curl-free part $\mathbf{J}^0$, a three-dimensional numerical model is constructed using knowledge of the object external boundary shape, found from MR magnitude images (please see Appendix 2 for details). A three-dimensional Laplace equation subject to the same boundary conditions as in the experiment is then solved to find $\mathbf{J}^0 = -\nabla\alpha = \left(J_x^0, J_y^0, J_z^0\right)$ by solving

$$\begin{cases} \nabla^2\alpha &= 0 \text{ in } \Omega \\ \nabla\alpha\cdot\mathbf{n} &= g \text{ on } \partial\Omega \quad \text{and,} \quad \int_{\partial\Omega}\alpha ds = 0. \end{cases} \tag{6.23}$$

Here, g are the Neumann data obtained from the experimental boundary conditions. In practice, to solve the boundary value problem in (6.23), a subject-specific three-dimensional volume conductor model with attached electrodes is built, and Eqs. (6.2)–(6.4) are solved using a homogeneous conductivity distribution $\sigma = 1$S/m and the same experimental current amplitude. The two-dimensional divergence-free current density $\mathbf{J}^* = \left(\frac{\partial\beta_l}{\partial y}, -\frac{\partial\beta_l}{\partial x}, 0\right)$ satisfies Poisson's equation [22]:

$$\begin{cases} \nabla^2_{xy}\beta_l &= \frac{1}{\mu_0}\nabla^2 B_z^m \text{ in } \Omega_l \\ \beta_l &= 0 \qquad\qquad \text{on } \partial\Omega_l. \end{cases} \tag{6.24}$$

For the homogeneous conductivity, $\sigma = \sigma_0$; the Eq. (6.1a) can be expanded as $\nabla\cdot\mathbf{J}^0 = \nabla\cdot(\sigma_0\nabla u_0) = \nabla\sigma_0\cdot\nabla u_0 + \sigma_0\nabla^2 u_0 = \sigma_0\nabla^2 u_0 = \nabla^2 u_0 = 0$ in Ω, meaning that two different homogeneous conductivity distributions, σ_1 and σ_2, subject to the same boundary condition g in Eq. (6.23), will produce the same $\mathbf{J} = -\sigma_1\nabla u_1 = -\sigma_2\nabla u_2$. Therefore, to obtain the curl-free part $\mathbf{J}^0$ in projected current density a homogeneous conductivity distribution 1 S/m (or any other constant value) can be chosen.

We may express the full three-dimensional true current density $\mathbf{J}$ by decomposing it into the form $\mathbf{J} = \mathbf{J}^0 + \mathbf{J}^* + \mathbf{J}^{\mathcal{N}}$, where $\mathbf{J}^{\mathcal{N}}$ is the component of the current which cannot be recovered from measurement of only a single component of the magnetic flux density. Park et al. [22] proved that $\langle\mathbf{J}^0, \mathbf{J}^{\mathcal{N}}\rangle = 0$ and $\langle\mathbf{J}^*, \mathbf{J}^{\mathcal{N}}\rangle = 0$, where $\langle,\rangle$ denotes the inner product (here this quantity is the same as the dot product) of two vector fields. Therefore, the $\mathbf{J}^P$ in Eq. (6.22) represents a unique projection component of $\mathbf{J}$. It has also been shown that the stability of the reconstructed projected current density within an image slice Ω_l depends on the difference between the $J_z - J_z^0$ [22] as

$$\left\|\mathbf{J} - \mathbf{J}^P\right\|_{\Omega_l} \le C\left(\left\|\frac{\partial}{\partial z}\left(J_z - J_z^0\right)\right\|_{\Omega_l} + \left\|J_z - J_z^0\right\|_{\Omega_l}\right) \tag{6.25}$$

In Eq. (6.25), J_z is the z component of the true current density and $J_z^0 = -\frac{\partial\alpha}{\partial z}$. The constant C depends on the imaging slice Ω_l. However, when compared with the two-dimensional current density, the reconstructed $\mathbf{J}^P$ provides the true current density without any error [22].

Although the $\mathbf{J}^P = \left(J_x^P, J_y^P, J_z^0\right)$ can optimally recover the three dimensional current density, for some in vivo applications problems may arise when the true current density $\mathbf{J}$ is very low in some local area inside the image slice Ω_l, because of low electrical conductivity. In other situations, the signal-to-noise (SNR) ratio in some regions may be very low due to rapid T_2/T_2^* decay. Since the noise in the B_z^m signal is inversely proportional to the SNR of the MR magnitude image, Υ, and the current injection duration T_c i.e. $sd_{B_z} \propto \frac{1}{T_c\Upsilon}$) [26, 35], noise in the measured B_z^m signal could therefore be amplified following Eq. (6.24). Examples of such regions are bone and stomach, where both have low electrical conductivity MR signal contributions. As demonstrated in Fig. 6.3, inclusion of regions that are defective for such reasons may result in large errors in reconstructed conductivity images of entire slices [28]. A regional projected current density algorithm was later developed [14, 28] to avoid noise propagation from defective areas. When this approach is used, the regional projected current density within the ROI (region of interest) $\mathcal{D}_l \subset \Omega_l$ can be defined as [14]

$$\mathbf{J}^{P,R}_{\mathcal{D}_l} = \mathbf{J}^0_{\mathcal{D}}|_{\mathcal{D}_l} + \mathbf{J}^*_{\mathcal{D}_l} = -\nabla\alpha_{\mathcal{D}}|_{\mathcal{D}_l} + \left(\frac{\partial\beta_{\mathcal{D}_l}}{\partial y}, -\frac{\partial\beta_{\mathcal{D}_l}}{\partial x}, 0\right) \tag{6.26}$$

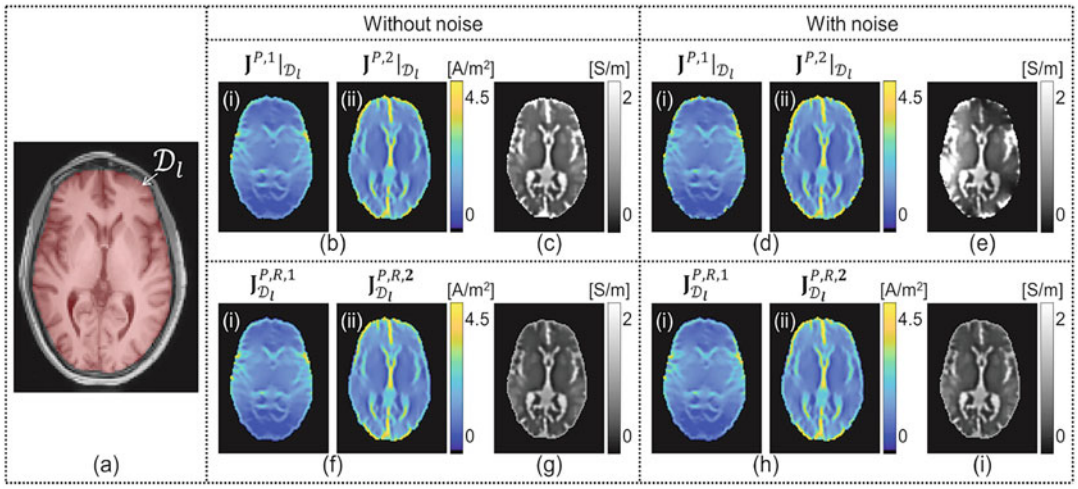

Fig. 6.3 Numerical simulation of an isotropic human head model used to demonstrate the stability of the projected and regional projected current density algorithm defined in Eqs. (6.22) and (6.31), respectively. (**a**) The segmented brain mask $\mathcal{D}_l$ is overlaid on the T1-weighted MR-magnitude image. (**b**) and (**d**) display the reconstructed $|\mathbf{J}^{P,p}|$, $p = 1, 2$ using the Eq. (6.22) for the horizontal (i) and vertical (ii) current injection at $SNR = \infty$ and added noise case, respectively. (**c**) and (**e**) display the reconstructed conductivity images using the $|\mathbf{J}^{P,p}|$, $p = 1, 2$, and the non-iterative harmonic B_z algorithm [37] demonstrates the influence of the noise propagation from the defective skull and skin region. (**f**) and (**h**) shows the reconstructed current density images using the Eq. (6.31) for the horizontal (i) and vertical (ii) current injection at $SNR = \infty$ and added noise case, respectively. The corresponding conductivities are displayed in (**g**) and (**i**), respectively

Here, the potential $\alpha_{\mathcal{D}}$ satisfies the three-dimensional Laplace equation with the *l*ocal boundary conditions:

$$\begin{cases} \nabla^2 \alpha_{\mathcal{D}} &= 0 & \text{in } \mathcal{D} \\ \nabla \alpha_{\mathcal{D}} \cdot \mathbf{n} &= \left(\mathbf{J}^0 + \frac{1}{\mu_0} \left(\frac{\partial \left(B^m_{z,\Omega} - B^0_z \right)}{\partial y}, -\frac{\partial \left(B^m_{z,\Omega} - B^0_z \right)}{\partial x}, 0 \right) \right) \cdot \mathbf{n} & \text{on } \partial\mathcal{D}. \end{cases} \tag{6.27}$$

Here, $\mathbf{J}^0 = -\nabla\alpha$ is the solution of the partial differential equation in (6.23), and B^0_z is the corresponding z component of the magnetic flux density. The term $\beta_{l,\mathcal{D}}$ is obtained from the two-dimensional Poisson equation [14]:

$$\begin{cases} \nabla^2_{xy} \beta_{\mathcal{D}_l} &= \frac{1}{\mu_0} \nabla^2 B^m_z & \text{in } \mathcal{D}_l \\ \beta_{\mathcal{D}_l} &= 0 & \text{on } \partial\mathcal{D}_l, \end{cases} \tag{6.28}$$

where $\mathcal{D} = \bigcup_{l \in (-H_{\mathcal{D}}, H_{\mathcal{D}})} \mathcal{D}_l$ and $2H_{\mathcal{D}} \subset 2H$ could be either portion or the total imaging object height. Note that the three-dimensional local ROI $\mathcal{D}$ is constructed by masking out the defective portion of each imaging slice $\mathcal{D}_l$. The MR-magnitude image may be used to segment the non-defective local region $\mathcal{D}_l$ in each imaging slice. However, in [28] a transversal J-substitution algorithm was used (see Chap. 7 for more details). Using data from a single current administration, the first update of the conductivity σ^1 can be found as

$$\sigma^1 = \sigma^0 - \frac{1}{\mu_0} \frac{\left(\frac{\partial}{\partial x} \left(B^m_{z,\Omega} - B^0_z \right), \frac{\partial}{\partial y} \left(B^m_{z,\Omega} - B^0_z \right) \right) \cdot \left(J^0_y, -J^0_x \right)}{\left(J^0_x \right)^2 + \left(J^0_y \right)^2} \tag{6.29}$$

In (6.29), σ^0= 1 S/m is the homogeneous conductivity distribution, and (J^0_x, J^0_y) is the x, y component of $\mathbf{J}^0$. This approximate reconstruction allows clear delineation of noisy regions and can be used to determine the correct local segmentation.

It has also been shown that the reconstructed regional projected current density satisfies the following stability relationship:

$$\left\|\mathbf{J}-\mathbf{J}_{\mathcal{D}}^{P,R}\right\|_{\mathcal{D}} \leq C\left(\left\|\mathbf{J}-\mathbf{J}_{\mathcal{D}}^{P}\right\|_{\mathcal{D}}\right.$$
$$\left.+\left\|\frac{1}{\mu_0}\left(-\frac{\partial B_y^{\delta}}{\partial z},\frac{\partial B_x^{\delta}}{\partial z},\frac{\partial B_y^{\delta}}{\partial x}-\frac{\partial B_x^{\delta}}{\partial y}\right)\cdot\mathbf{n}\right\|_{-\frac{1}{2}\partial\mathcal{D}}\right) \tag{6.30}$$

In this equation, $\mathbf{B}^{\delta} = \mathbf{B}_{\Omega}^{m} - \mathbf{B}^{0} = \left(B_{x,\Omega}^{m} - B_x^0, B_{y,\Omega}^{m} - B_y^0, B_{z,\Omega}^{m} - B_z^0\right)$ and $\mathbf{B}^0$ can be obtained using the Bio-Savart law (Eq. (6.6)) and current density obtained from a solution of a homogenous conductivity distribution $\mathbf{J}^0$. The additional error term in Eq. (6.30) arises from errors in the boundary approximation (see Eq. (6.27)). The reconstruction procedure for the regional projected current density algorithm is summarized in Algorithm 1.

Algorithm 1 Regional projected current density algorithm

Step 1. Construct a three-dimensional numerical model with attached electrodes from the acquired imaging slices.
Step 2. Using Eqs. (6.23) and (6.7c), obtain $\mathbf{J}^0$ and B_z^0 subject to the same experimental boundary conditions.
Step 3 Identify defective regions using approximate reconstruction of Eq. (6.29).
Step 4. Construct another three-dimensional numerical model, avoiding defective regions..
Step 5. Compute $\mathbf{J}_{\mathcal{D}}^0$ in (6.27).
Step 6. Excluding the defective region, solve Eq. (6.28) for each of the image slices to compute $\mathbf{J}_{\mathcal{D}}^*$.
Step 7. Use the results in step 3 and 4 in Eq. (6.26) to obtain the regional projected current density.

As is evident from Algorithm 1, the numerical implementation of the regional projected current density algorithm described in Eqs. (6.26)–(6.28) is computationally complex. In [28] Sajib et al. provided an alternative formula for estimating the local regional projected current density. In [28] the regional projected current density was computed as

$$\mathbf{J}_{\mathcal{D}_l}^{P,R} = \mathbf{J}^0|_{\mathcal{D}_l} + \left(\frac{\partial\Psi_{\mathcal{D}_l}}{\partial y}, -\frac{\partial\Psi_{\mathcal{D}_l}}{\partial x}, 0\right) \tag{6.31}$$

Here, $\mathbf{J}^0|_{\mathcal{D}_l}$ is the homogeneous solution of the Eq. (6.23) restricted to the local region $\mathcal{D}_l \subset \Omega_l$, and $\Psi_{\mathcal{D}_l}$ satisfies the following Poisson equation [28]:

$$\begin{cases} \nabla_{xy}^2\Psi_{\mathcal{D}_l} = \frac{1}{\mu_0}\nabla^2 B_z^m & \text{in } \mathcal{D}_l \\ \Psi_{\mathcal{D}_l} = \frac{1}{\mu_0}\left(B_{z,\Omega}^m - B_z^0\right) & \text{on } \partial\mathcal{D}_l \end{cases} \tag{6.32}$$

Compared to Algorithm 1, numerical implementation of this method is relatively simple. It is worth noting that both these regional projected current density algorithms require removal of stray magnetic fields in order to correctly specify the local regional boundary conditions (see Eqs. (6.27)–(6.32)). Two useful MATLAB (The MathWorks, Inc., Natick, Massachusetts, United States) functions, `mrci_projected_current_density1.m` implementing the Eq. (6.26) and `mrci_regional_projected_current_density.m` described in Eq. (6.31), can be found in the MR-based conductivity imaging `mrci`-toolbox [29] developed to facilitate MR-CDI research (see Fig. 6.4). This toolbox can be downloaded from the developer laboratory website www.iirc.khu.ac.kr for noncommercial use.

6.4.4 Model-Based Algorithm

The projected current density method [14, 22, 28] can optimally recover the current density information from the measured one component of the magnetic flux density data. However, the reconstruction error will be big in case of a large non-transversal component of current density (see Eqs. (6.25) and (6.30)). Note that the non-transversal current flow could be large depending on the electrode locations. It could also occur due to the presence of tissue anisotropy or when the distribution of conductivity is very variable. An example of such a case is in the brain, where the electrical conductivity of the cerebrospinal fluid is large compared to the grey matter and white matter [27]. Therefore, in order to compensate for non-transversal current flow (e.g., J_z), Jeong et al. [8] and Kwon et al. [15]

```
function Jp = mrci_projected_current_density1 (J0, Bz, reconstruction_parameters)

% J0[M×N×3]: calculated current density from a homogeneous domain
% where,
% J0x = J0(:,:,1), J0y = J0(:,:,2), and J0z = J0(:,:,3).
% Bz[M×N]: measured Bz data.
% Jp[M×N×3]: computed projected current density
% where,
% Jpx = Jp(:,:,1), Jpy = Jp(:,:,2), and Jpz = Jp(:,:,3).


function rJp = mrci_regional_projected_current_density(J0, Bz0, Bz, ROI,
reconstruction_parameters)

% J0[M×N×3]: calculated current density from a homogeneous model
% where,
% J0x = J0(:,:,1), J0y = J0(:,:,2), and J0z = J0(:,:,3).
% Bz0[M×N]: computed Bz from a homogeneous model.
% Bz[M×N]: measured Bz data.
% ROI[M×N]: region of interest (selected local region).
% rJp[M×N×3]: computed regional projected current density
% where,
% rJpx = rJp(:,:,1), rJpy = rJp(:,:,2), and rJpz = rJp(:,:,3).
```

Fig. 6.4 Example showing current density image reconstruction method implemented in mrci-toolbox [29]. For algorithm details see Sect. 6.4.3

developed another algorithm to reconstruct the three-dimensional current density, by comparing the model-predicted three-dimensional current density with that predicted from measurement of one component of magnetic flux density data. Decomposing the true current density vector, $\mathbf{J}$ into its model-predicted $\mathbf{J}^0$ and the difference current density $\mathbf{J}^\delta$ (see Fig. 6.5), we have

$$\begin{aligned}\mathbf{J} &= \mathbf{J}^0 + \mathbf{J}^\delta = \mathbf{J}^0 + \frac{1}{\mu_0}\nabla \times \mathbf{B}^\delta \\ &= \mathbf{J}^0 + \frac{1}{\mu_0}\left(\frac{\partial B_z^\delta}{\partial y} - \frac{\partial B_y^\delta}{\partial z}, -\frac{\partial B_z^\delta}{\partial x} + \frac{\partial B_x^\delta}{\partial z}, \frac{\partial B_y^\delta}{\partial x} - \frac{\partial B_x^\delta}{\partial y}\right) \\ &= \mathbf{J}^0 + \frac{1}{\mu_0}\left(\frac{\partial B_z^\delta}{\partial y}, -\frac{\partial B_z^\delta}{\partial x}\right) \\ &\quad + \frac{1}{\mu_0}\left(-\frac{\partial B_y^\delta}{\partial z}, \frac{\partial B_x^\delta}{\partial z}, \frac{\partial B_y^\delta}{\partial x} - \frac{\partial B_x^\delta}{\partial y}\right)\end{aligned} \tag{6.33}$$

where $\mathbf{B}^\delta$ is the difference between the true and model-predicted magnetic flux density, $\mathbf{B} - \mathbf{B}^0 = \left(B_{x,\Omega} - B_x^0, B_{y,\Omega} - B_y^0, B_{z,\Omega}^m - B_z^0\right)$. The current density $\mathbf{J}^1$ is updated as

$$\mathbf{J}^1 = \mathbf{J}^0 + \frac{1}{\mu_0}\left(\frac{\partial\left(B_{z,\Omega}^m - B_z^0\right)}{\partial y}, -\frac{\partial\left(B_{z,\Omega}^m - B_z^0\right)}{\partial x}, 0\right). \tag{6.34}$$

The three-dimensional model-predicted current density $\mathbf{J}^0$, subject to the same experimental boundary conditions, satisfies Equations (6.2)–(6.5). Since $\nabla \cdot \mathbf{J}^0 = 0$, the updated current density $\mathbf{J}^1$ also satisfies this continuity relation within a region Ω_t. Ω_t denotes the three-dimensional imaging region and could be a part of the entire domain Ω. The z component of the $\nabla \times \mathbf{J}^1$ in Eq. (6.34) fulfills the following condition [15]:

$$\nabla_{xy}^\perp\left(J_x^1, J_y^1\right) = \nabla_{xy}^\perp\left(J_x, J_y\right) - \frac{1}{\mu_0}\left(\frac{\partial^2 B_z^0}{\partial z^2} - \frac{\partial^2 B_{z,\Omega}^m}{\partial z^2}\right) \tag{6.35}$$

Here, $\nabla_{xy}^\perp := \left(\frac{\partial}{\partial y}, -\frac{\partial}{\partial x}\right)$. Equation (6.35) implies that the updated current density matches the measured B_z^m data with an error term depending on $B_z^m - B_z^0$.

The error between $\mathbf{J}^1$ and the true current density $\mathbf{J}$ satisfies the following stability relationship [15]:

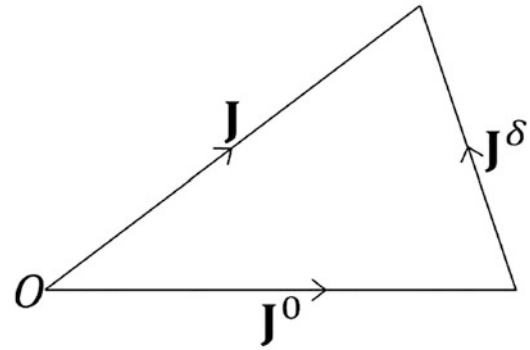

Fig. 6.5 Decomposition of the true current density vector field $\mathbf{J}$ into the model-predicted current density $\mathbf{J}^0$ and the error term $\mathbf{J}^\delta$

$$\left\|\mathbf{J}_\perp^1 - \mathbf{J}_\perp\right\|_{\Omega_t} \le C\left(\left\|\frac{\partial^2 B_z^0}{\partial z^2} - \frac{\partial^2 B_{z,\Omega}^m}{\partial z^2}\right\|_{\Omega_t} + \left\|\frac{\partial\left(J_z - J_z^0\right)}{\partial z}\right\|_{\Omega_t}\right) + C\left(\left\|\mathbf{J}_\perp^1 \cdot \mathbf{n} - \mathbf{J}_\perp \cdot \mathbf{n}\right\|_{\partial\Omega_t}\right). \tag{6.36}$$

In (6.36), $\mathbf{J}_\perp^1 = \left(J_y^1, -J_x^1\right)$ and $\mathbf{J}_\perp = \left(J_y, -J_x\right)$, and $\|\cdot\|$ denotes the L^2 norm in Ω_t. Hence, the error in the updated current density mainly depends on the differences between $B_{z,\Omega}^m - B_z^0$ and $J_z - J_z^0$. To improve approximation of the transverse component, Kwon et al. [15] suggested iteratively updating the current density using the $B_{z,\Omega}^m$ data as

$$\mathbf{J}^{n+1} = \mathbf{J}^n + \frac{1}{\mu_0}\left(\frac{\partial\left(B_{z,\Omega}^m - B_z^n\right)}{\partial y}, -\frac{\partial\left(B_{z,\Omega}^m - B_z^n\right)}{\partial x}, 0\right). \tag{6.37}$$

In [8] the model-predicted current density, $\mathbf{J}^0$ was found using a homogeneous conductivity distribution. However, for tES applications, Kwon et al. [15] used a volume conductor model derived from diffusion tensor information [40] inside the brain region and literature values of the conductivity for the skin and skull compartments to compensate for non-transverse current flow (Eq. (6.36)). Using this realistic numerical human head model, it has been demonstrated [15] that the final reconstructed current density could depend on the initial choice of volume conductor model, especially for the three-dimensional current density, $\mathbf{J}^n = \left(J_x^n, J_y^n, J_z^0\right)$. This is mainly because J_z information cannot be updated using $B_{z,\Omega}^m$ data (see Eq. (6.37)). Hence, the method may not provide the optimal current density. In fact, for $\mathbf{J}^0$ distributions derived from an initial homogeneous volume conductor model ($\sigma_0 = 1$ S/m), it has been shown [8] that there exists a *difference* current density $\mathbf{J}^D = \mathbf{J}^P - \mathbf{J}^1 = \left(J_x^P - J_x^1, J_y^P - J_y^1, 0\right) = \left(J_x^D, J_y^D, J_z^D\right)$ (see Sect. 6.4.3 and Eq. (6.35)) which depends on the difference $\frac{\partial^2\left(B_{z,\Omega}^m - B_z^0\right)}{\partial z^2}$ in the two-dimensional imaged slice Ω_l and the difference $\left(\frac{\partial\left(B_{z,\Omega}^m - B_z^0\right)}{\partial y}, -\frac{\partial\left(B_{z,\Omega}^m - B_z^0\right)}{\partial x}, 0\right)$ on the two-dimensional domain boundary $\partial\Omega_l$. However, since the boundary conditions are the same for $B_{z,\Omega}^m$ and B_z^0, the differences $\frac{\partial^2\left(B_z^m - B_z^0\right)}{\partial z^2}$ and $\left(\frac{\partial\left(B_{z,\Omega}^m - B_z^0\right)}{\partial y}, -\frac{\partial\left(B_{z,\Omega}^m - B_z^0\right)}{\partial x}, 0\right)$ could be minimized, especially in the case of an in-plane electrode configuration. Note that, in addition, prior to reconstructing the current density from the experimentally measured $B_{z,\Omega}$ data, this method also requires these data to be preprocessed to remove wire and electrode-related stray magnetic fields.

Both "projected current density" and "model-based" methods require calculation of a model-predicted current density $\mathbf{J}^0$ computed from a three-dimensional numerical model. Since in the "projected current density" method the $\mathbf{J}^0$-distribution represents the curl-free part of the current flow, it can be computed using a homogeneous conductivity distribution. This statement can be easily verified by applying the curl operator to Ohm's law (see Eq. (6.5))

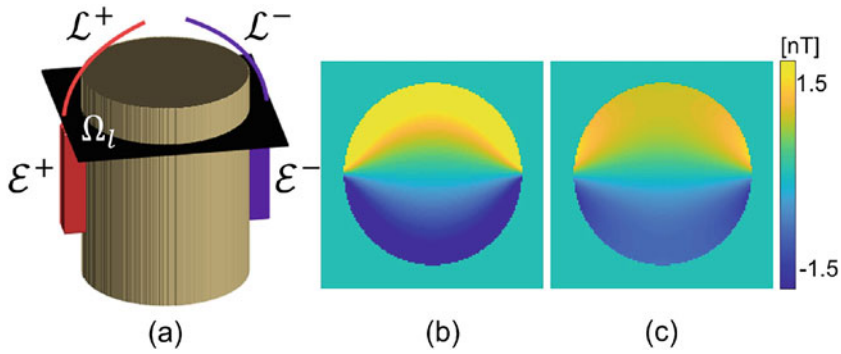

Fig. 6.6 Numerical model results demonstrating the necessity for stray magnetic field correction (**a**) Computational model domain showing the slice plane Ω_l and wire trace arrangement. (**b**) Current-induced z-component of the magnetic flux density, $B_{z,\Omega}$ in slice plane Ω_l. (**c**) Wire-created stray magnetic field $B_{z,\mathcal{L}}$ calculated using Eq. (6.39c) in same slice position

$$\nabla \times \mathbf{J}^0 = \nabla \times \left(-\sigma^0 \nabla u^0\right) = \nabla u^0 \times \nabla \sigma^0 = \mathbf{0}$$

However, in the "model-based" method, it is not necessary that $\mathbf{J}^0$ be computed from a homogeneous conductivity distribution. The model-predicted current density for this method may incorporate any inhomogeneous conductivity distribution [15]. This is particularly useful in brain imaging applications [5, 12] to compensate for any non-transversal current flow.

When compared with the projected current density $\mathbf{J}^P$, computation of $\mathbf{J}^1$ has certain advantages. The estimated $\mathbf{J}^1$ can be directly calculated by simple differentiations of the measured B_z data without solving any partial differential equations. Second, where reconstruction of $\mathbf{J}^P$ requires numerical solution of the Poisson equation in the entire slice Ω_l using the Laplacian of B_z as a source term, calculation of $\mathbf{J}^1$ recovers current in the chosen ROI (local region), $\mathbb{R}_l \subset \Omega_l$, without being affected by possible noise propagation from defective regions. The MATLAB function mrci_projected_current_density2.m implementing this method also can be in found in the `mrci`-toolbox [29].

6.5 Correction of Stray Magnetic Field

It is important to correct the measured MR phase data to estimate the correct internal current flow $\mathbf{J}$, even though one can take advantage of the fact that $\nabla^2 (\mathbf{B}_\mathcal{E} + \mathbf{B}_\mathcal{L}) = 0$ [22] offered by some reconstruction algorithms such as the projected current density method (see Sect. 6.4.4). However, as demonstrated in Fig. 6.3, in the presence of local defective regions, the reliability of the reconstructed $\mathbf{J}^P$ can deteriorate due to noise propagation. Therefore, removing stray magnetic fields is crucial, especially in in-vivo neuro-imaging contexts where wires cannot easily be constrained along the measurement direction [6, 31]. In this section we briefly explain the process to remove the stray magnetic field from measured $\mathbf{B}_q^m$, $q = x, y, z$ data, using a three-dimensional numerical model built from MR experimental data and a forward modellng approach (Fig. 6.6).

6.5.1 $\mathbf{B}_\mathcal{L}$-Field Correction

Correction of wire-created stray magnetic field can be performed by creating a three-dimensional numerical model of the wire paths and computing and compensating for the contribution of $\mathbf{B}_\mathcal{L}$ fields in image slices. Several methods for detecting wire trajectories [6,31] appear in the literature. For example, in [31] wire paths were determined using high-resolution T_1-weighted images. Since most wires cannot be detected in conventional MR pulse sequences, wires can be encapsulated in silicon tubing to increase the MR signal they produce [31]. Once the three-

dimensional wire trajectory is reconstructed from the centroid of the segmented tube mask, the Bio-Savart law can be used to estimate the $\mathbf{B}_{\mathcal{L}}$ field as

$$\mathbf{B}_{\mathcal{L}^{\pm}} = \frac{I\mu_0}{4\pi}\int_{\mathcal{L}} \hat{\mathbf{a}}(\mathbf{r}^{'}) \times \frac{\mathbf{r}-\mathbf{r}^{'}}{|\mathbf{r}-\mathbf{r}^{'}|^3} dl^{'} \tag{6.38}$$

where I is the known amplitude of current used in the CDI experiment and $\hat{\mathbf{a}}$ is the unit vector in the direction of the current flow at $\mathbf{r}^{'} \in \mathcal{L}^{\pm}$. Assuming that the wire trajectory $\mathcal{L}^{\pm}$ is represented by a set of M discrete points in three-dimensional space $k = \{1, 2, \cdots, M\}$, the line integral in (6.38) can be converted to

$$B_{x,\mathcal{L}^{\pm}}(x, y, z = l) = \frac{I\mu_0}{4\pi}\sum_{k=1}^{M-1} \frac{(y^{'}_{k+1}-y^{'}_k)(z-z^{'}_k) - (z^{'}_{k+1}-z^{'}_k)(y-y^{'}_k)}{\left\{(x-x^{'}_k)^2 + (y-y^{'}_k)^2 + (z-z^{'}_k)^2\right\}^{3/2}} \tag{6.39a}$$

$$B_{y,\mathcal{L}^{\pm}}(x, y, z = l) = \frac{I\mu_0}{4\pi}\sum_{k=1}^{M-1} \frac{(z^{'}_{k+1}-z^{'}_k)(x-x^{'}_k) - (x^{'}_{k+1}-x^{'}_k)(z-z^{'}_k)}{\left\{(x-x^{'}_k)^2 + (y-y^{'}_k)^2 + (z-z^{'}_k)^2\right\}^{3/2}} \tag{6.39b}$$

$$B_{z,\mathcal{L}^{\pm}}(x, y, z = l) = \frac{I\mu_0}{4\pi}\sum_{k=1}^{M-1} \frac{(x^{'}_{k+1}-x^{'}_k)(y-y^{'}_k) - (y^{'}_{k+1}-y^{'}_k)(x-x^{'}_k)}{\left\{(x-x^{'}_k)^2 + (y-y^{'}_k)^2 + (z-z^{'}_k)^2\right\}^{3/2}} \tag{6.39c}$$

Since the MR-imaging parameters are known, Eqs. (6.39a)–(6.39c) can be used to determine the $\mathbf{B}_{\mathcal{L}}$ field within the imaging slice located at the position (x, y, z).

6.5.2 $\mathbf{B}_{\mathcal{E}}$-Field Correction

In most MR-CDI experiments, carbon or copper electrodes are used to deliver imaging currents. These have relatively high conductivities compared to the body. As a result, the electrode-related stray magnetic field is mainly due to current flow on the electrode surface. Assuming that the thickness of the electrodes are negligible i.e., $t \to 0$, the surface current density $\mathbf{J}_{\mathcal{S}}$ satisfies the following Poisson equation [16]:

$$\begin{cases} -\nabla \cdot \mathbf{J}_{\mathcal{S}} = \pm I\,\delta(\mathbf{r}-\mathbf{r}_0) & \text{in } \mathcal{E} = \mathcal{E}^{+} \bigcup \mathcal{E}^{-} \\ -\mathbf{J}_{\mathcal{S}} \cdot \hat{l} = 0 & \text{on } \partial\mathcal{E}. \end{cases} \tag{6.40}$$

Here, δ is the Dirac delta function, and $\hat{l}$ is the outward normal vector on the surface boundary. Since the lead wire is represented by a line $\mathcal{L}$ (see Sect. 6.5.1), the source or sink current at the point where the wire meets the electrodes $\mathcal{E}^{\pm}$ can be modeled as a point source in Eq. (6.40). The finite element method can be used to solve (6.40) [16] (see Chap. 2 for details). Assuming that the electrode surface $\mathcal{E}$ is represented by a set of $NE_{\mathcal{S}}$ discrete elements e and current is constant within the each element, the Bio-Savart law can be used to obtain $B_{\mathcal{E}}$ in any electrode $\mathcal{E}$ using

$$B_{\mathcal{E},x}(x, y, z = l) = \frac{\mu_0}{4\pi}\sum_{e=1}^{NE_{\mathcal{S}}} \frac{(z-z^{'}_e)J_y^{(e)}(x^{'}_e, y^{'}_e, z^{'}_e) - (y-y^{'}_e)J_z^{(e)}(x^{'}_e, y^{'}_e, z^{'}_e)}{\left\{(x-x^{'}_e)^2 + (y-y^{'}_e)^2 + (z-z^{'}_e)^2\right\}^{3/2}} \Delta s^{'}_e \tag{6.41a}$$

$$B_{\mathcal{E},y}(x, y, z = l) = \frac{\mu_0}{4\pi}\sum_{e=1}^{NE_{\mathcal{S}}} \frac{(x-x^{'}_e)J_z^{(e)}(x^{'}_e, y^{'}_e, z^{'}_e) - (z-z^{'}_e)J_x^{(e)}(x^{'}_e, y^{'}_e, z^{'}_e)}{\left\{(x-x^{'}_e)^2 + (y-y^{'}_e)^2 + (z-z^{'}_e)^2\right\}^{3/2}} \Delta s^{'}_e \tag{6.41b}$$

$$B_{\mathcal{E},z}(x, y, z = l) = \frac{\mu_0}{4\pi}\sum_{e=1}^{NE_{\mathcal{S}}} \frac{(y-y^{'}_e)J_x^{(e)}(x^{'}_e, y^{'}_e, z^{'}_e) - (x-x^{'}_e)J_y^{(e)}(x^{'}_e, y^{'}_e, z^{'}_e)}{\left\{(x-x^{'}_e)^2 + (y-y^{'}_e)^2 + (z-z^{'}_e)^2\right\}^{3/2}} \Delta s^{'}_e \tag{6.41c}$$

where, $\mathbf{J}_{\mathcal{S}}^{(e)} = \left(J_x^{(e)}, J_y^{(e)}, J_z^{(e)}\right)$ is the current density at the element's center $(x^{'}_e, y^{'}_e, z^{'}_e)$, $\Delta s^{'}_e$ is the element area and $NE_{\mathcal{S}}$ represents the total number of elements in the electrode.

6.6 Conclusion

To assess current flow patterns inside biological tissue, magnetic resonance current density imaging (MR-CDI) utilizes the MR measurement technique and can find numerous clinical applications including as internal or transcranial brain stimulation [5, 9, 12, 30]. However, the utility of MR-CDI is limited by constraints of MR measurement techniques. The methods discussed in this chapter use measured single-component data and additional information generated by numerical models to reconstruct current density. While not considered here, recent developments in deep-learning models could be useful in future MR-CDI image reconstruction techniques [32]. We hope that this chapter will provide a useful guide to new researchers working in this area.

Appendix 1

Directional Derivative Operator

Finite difference methods can generally be used to estimate the directional derivative of an image. The x-directional derivative of a two-dimensional image $I(x, y)$ near about the point $x = x + \Delta$ is defined as,

$$\frac{\partial I(x,y)}{\partial x} = \lim_{\Delta \to 0} \frac{I(x+\Delta, y) - I(x,y)}{\Delta} \tag{6.42a}$$

$$= \lim_{\Delta \to 0} \frac{0 \times I(x-\Delta, y) + (-1) \times I(x,y) + (1) \times I(x+\Delta, y)}{\Delta} \tag{6.42b}$$

Here, Δ denotes the x-directional step size. Discretization of Eq. (6.42a) is known as a forward-difference method. Likewise, the backward-difference formula can be written at a point $x = x - \Delta$,

$$\frac{\partial I(x,y)}{\partial x} = \lim_{\Delta \to 0} \frac{I(x,y) - I(x-\Delta, y)}{\Delta} \tag{6.43a}$$

$$= \lim_{\Delta \to 0} \frac{(-1) \times I(x-\Delta, y) + (1) \times I(x,y) + (0) \times I(x+\Delta, y)}{\Delta} \tag{6.43b}$$

Numerically the forward or backward-difference formula can be realized as,

$$\frac{\partial I(x,y)}{\partial x} \approx \frac{1}{\Delta}[0 \quad -1 \quad 1] * I(x,y) \tag{6.44a}$$

$$\approx \frac{1}{\Delta}[-1 \quad 1 \quad 0] * I(x,y) \tag{6.44b}$$

Here, $*$ denotes the convolution operator. Likewise, the y-directional gradient can be obtained from

$$\frac{\partial I(x,y)}{\partial y} \approx \frac{1}{\Delta} \begin{bmatrix} 1 \\ -1 \\ 0 \end{bmatrix} * I(x,y) \tag{6.45a}$$

$$\approx \frac{1}{\Delta} \begin{bmatrix} 0 \\ 1 \\ -1 \end{bmatrix} * I(x,y) \tag{6.45b}$$

While this simple operator can be used to find the image gradient, this method suffers from the truncation error in the order of $O(\Delta)$. Using the Taylor series expansion, this can be easily verified

$$I(x+\Delta, y) = I(x, y) + \left(\frac{\Delta}{1!}\right)\frac{\partial I}{\partial x} + \left(\frac{\Delta^2}{2!}\right)\frac{\partial^2 I}{\partial x^2} + \left(\frac{\Delta^3}{3!}\right)\frac{\partial^3 I}{\partial x^3}\cdots \quad (6.46a)$$

$$I(x-\Delta, y) = I(x, y) - \left(\frac{\Delta}{1!}\right)\frac{\partial I}{\partial x} + \left(\frac{\Delta^2}{2!}\right)\frac{\partial^2 I}{\partial x^2} - \left(\frac{\Delta^3}{3!}\right)\frac{\partial^3 I}{\partial x^3}\cdots \quad (6.46b)$$

Therefore, to reduce the truncation error in the order of $O\left(\Delta^2\right)$, the central-difference method is widely used. From Eqs. (6.46a) and (6.46b),

$$\frac{I(x+\Delta, y) - I(x-\Delta, y)}{2\Delta} = \frac{\partial I}{\partial x} + \left(\frac{\Delta^2}{3!}\right)\frac{\partial^3 I}{\partial x^3} = \cdots \quad (6.47a)$$

$$= \frac{\partial I}{\partial x} + O\left(\Delta^2\right) \quad (6.47b)$$

The directional derivative using the central-difference method can be computed as

$$\frac{\partial I(x, y)}{\partial x} \approx \frac{1}{2\Delta}[-1 \quad 0 \quad 1] * I(x, y) \quad (6.48a)$$

$$\frac{\partial I(x, y)}{\partial y} \approx \frac{1}{2\Delta}\begin{bmatrix} -1 \\ 0 \\ 1 \end{bmatrix} * I(x, y) \quad (6.48b)$$

Directional Derivative for Noisy Data

Due to measurement noise, estimation of the image gradient, $\nabla_{xy} I(x, y) = \left[\frac{\partial I}{\partial x}, \frac{\partial I}{\partial y}\right]^T$ using the simple finite difference operator (see Eqs. (6.48a) and (6.48b)) often fails to produce the desired output. A lower order local-polynomial fitting method (known as a Savitzky-Golay filter [33]) is one possible approach to estimate the directional-derivative of a noisy image. A detailed explanation of the Savitzky-Golay method is beyond the scope of this chapter. The interested reader may find more information in [33] and [34].

The other possible choice is to reduce the noise-level before calculating the image gradient. For a two-dimensional noisy image $I(x, y)$ the filtered image $I_f(x, y)$ can be expressed as

$$I_f(x, y) = I(x, y) * G(x, y) \quad (6.49)$$

Here, $G(x, y)$ is the two-dimensional filter function. Taking the two-dimensional Fourier transform operator, $\mathcal{F}$ directional directional derivative of Eq. (6.49) yields

$$\mathcal{F}\left[\frac{\partial I_f(x, y)}{\partial \tilde{q}}\right] = -ik_{\tilde{q}} I_f^{\mathcal{F}}(k_x, k_y) \quad (6.50a)$$

$$= \left[-ik_{\tilde{q}} I^{\mathcal{F}}(k_x, k_y)\right] G^{\mathcal{F}}(k_x, k_y) \quad (6.50b)$$

$$= I^{\mathcal{F}}(k_x, k_y)\left[-ik_{\tilde{q}} G^{\mathcal{F}}(k_x, k_y)\right] \quad (6.50c)$$

Where $\tilde{q} = x$ or, y, and $G^{\mathcal{F}}(k_x, k_y)$, $I_f^{\mathcal{F}}(k_x, k_y)$ represents the Fourier transom of the function $G(x, y)$ and $I_f(x, y)$ respectively. k_x, and k_y denotes the spatial frequency in x, and y-directions, respectively. Now taking the inverse Fourier operator $\mathcal{F}^{-1}$ on both sides of the Eqs. (6.50b) and (6.50c)

$$\frac{\partial I_f(x, y)}{\partial \tilde{q}} = \frac{\partial I(x, y)}{\partial \tilde{q}} * G(x, y) \quad (6.51a)$$

$$= I(x, y) * \frac{\partial G(x, y)}{\partial \tilde{q}}. \quad (6.51b)$$

In practice, a Gaussian-function $G(x, y)$ is generally chosen. Use of a Gaussian-function is advantageous because of the separability property of this function. A two-dimensional Gaussian-filter function with variance σ_G^2 can be written as

$$G(x, y) = \frac{1}{2\pi\sigma_G^2}\exp\left\{-\frac{x^2 + y^2}{2\sigma_G^2}\right\} \quad (6.52)$$

Note that the two-dimensional Gaussian function $G(x, y)$ is separable, meaning that $G(x, y)$ can be expressed as a product of two one-dimensional Gaussian functions $G_x(x)$ and $G_y(y)$,

$$G(x, y) = \frac{1}{\sqrt{2\pi\sigma_G^2}} \exp\left\{-\frac{y^2}{2\sigma_G^2}\right\} \left[\frac{1}{\sqrt{2\pi\sigma_G^2}} \exp\left\{-\frac{x^2}{2\sigma_G^2}\right\}\right]^T = G_y G_x^T \quad (6.53)$$

Here, the one-dimensional Gaussian functions $G_x(x)$ and $G_y(y)$ are expressed as column vectors and T denotes the transpose operation. The x- and y-directional derivatives can be written as

$$\frac{\partial G(x, y)}{\partial x} = G_y \left[\frac{\partial G_x}{\partial x}\right]^T \quad (6.54a)$$

$$\frac{\partial G(x, y)}{\partial y} = \left[\frac{\partial G_y}{\partial y}\right] G_x^T \quad (6.54b)$$

One-dimensional directional-derivatives of a Gaussian function can be written as

$$\frac{\partial G_{\tilde{q}}}{\partial \tilde{q}} = -\frac{1}{\sqrt{2\pi\sigma_G^2}} \frac{\tilde{q}}{\sigma_G^2} \exp\left\{-\frac{\tilde{q}^2}{2\sigma_G^2}\right\} = -\frac{\tilde{q}}{\sigma_G^2} G_{\tilde{q}}$$

From Eqs. (6.51b), (6.54a) and (6.54b)

$$\frac{\partial I_f(x, y)}{\partial x} = I(x, y) * \left\{G_y \left[\frac{\partial G_x}{\partial x}\right]^T\right\} \quad (6.55a)$$

$$\frac{\partial I_f(x, y)}{\partial y} = I(x, y) * \left\{\left[\frac{\partial G_y}{\partial y}\right]^T G_x\right\} \quad (6.55b)$$

From the definition of the convolution it is easy to show that a separable kernel function leads to a separable convolution in the sense that we may first convolve along the rows with a one dimensional kernel function followed by a convolution along the columns of the image as [2],

$$\frac{\partial I_f(x, y)}{\partial x} = I(x, y) * \left[\frac{\partial G_x}{\partial x}\right]^T * G_y \quad (6.56a)$$

$$\frac{\partial I_f(x, y)}{\partial y} = I(x, y) * G_x^T * \left[\frac{\partial G_y}{\partial y}\right] \quad (6.56b)$$

Equation (6.56a) or (6.56b) can be interpreted as a smoothing of the image along the perpendicular direction followed by derivative operation along this direction. By defining x, and y-directional derivative kernels as D_x, and D_y,

$$D_x = \left[\frac{\partial G_x}{\partial x}\right]^T * G_y \quad (6.57a)$$

$$D_y = G_x^T * \left[\frac{\partial G_y}{\partial y}\right] \quad (6.57b)$$

Note that though the two-dimensional differentiating kernel can be expressed as matrix product (see Eqs. (6.55a) and (6.55b)), expressing the equation in convolution form is advantageous (see Eqs. (6.57a), and (6.57b)) because this form of equation can easily be expanded into higher dimensions. Expansion of the derivative kernel into higher dimensions (dimension = 3) is left as an exercise for the reader.

Numerical Implementation of the Directional Derivative

Methods such as direct discretization of the Gaussian functions with known variance can be used to discretize the Eqs. (6.57a) and (6.57b) [2]. However, in practice the Gaussian function is discretized using a binomial coefficients. A binomial coefficient of window size w can be found using Pascal sequence. The Pascal sequence generation can be written as [21],

$$\begin{aligned} \mathrm{Pa}[n, w] &= \frac{w!}{(w-n)!\, n!}, \quad 0 \le n \le w \\ &= 0, \qquad \text{otherwise} \end{aligned} \quad (6.58)$$

The discretized Gaussian function, $\widetilde{G}_w[n]$ and its derivative $\widetilde{\mathrm{D}G}_w[n]$ therefore, can be expressed as [21],

$$\widetilde{G}_w[n] = \mathrm{Pa}[n, w-1] \quad (6.59a)$$

$$\widetilde{\mathrm{D}G}_w[n] = \mathrm{Pa}[n, w-2] - \mathrm{Pa}[n-1, w-2] \quad (6.59b)$$

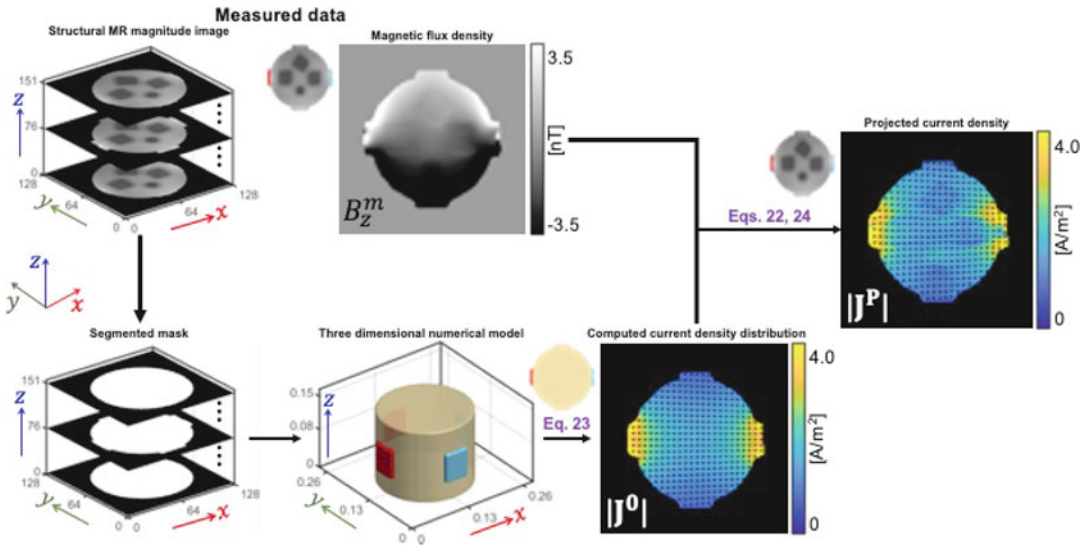

Fig. 6.7 Flow diagram for projected current density reconstruction method described in section. To compute the model-predicted current density $|\mathbf{J}|^0$ using Eqs. (6.23), a three-dimensional numerical model is constructed from boundary shape of the acquired MR magnitude image. Equations (6.22) and (6.24) are then applied to compute the projected current density from the measured B_z^m and the computed $|\mathbf{J}|^0$ data

The coefficients obtained from Eqs. (6.59a) and (6.59b) must be normalized. In [2] Eqs. (6.59a) and (6.59b) are normalized as

$$\left[\widetilde{G}_w\right]_{\mathrm{N}} = \sum_{n=0}^{w-1} \widetilde{G}_w[n] \tag{6.60a}$$

$$\left[\widetilde{\mathrm{D}G}_w\right]_{\mathrm{N}} = \left| \sum_{n=0}^{w-1} n\widetilde{\mathrm{D}G}_w[n] \right| \tag{6.60b}$$

It is worth mentioning that the pixel dimension Δ must also be multiplied with Eq. (6.60b) to obtain the appropriate dimension of the discrete derivative kernel.

Example For a window size $w = 3$, Eqs. (6.59a) and (6.59b) will provide $\widetilde{G}_w[n] = [1 \;\; 2 \;\; 1]^T$, and $\widetilde{\mathrm{D}G}_w[n] = [-1 \;\; 0 \;\; 1]^T$, respectively. The corresponding normalization factor can be found from Eqs. (6.60a) and (6.60b), $\left[\widetilde{G}_w\right]_{\mathrm{N}} = 4$, and $\left[\widetilde{\mathrm{D}G}_w\right]_{\mathrm{N}} = 2$. Now using equation, (6.57a), and (6.57b), the x, and y-directional discrete derivative kernel can be found as,

$$\widetilde{D}_x = \frac{1}{2\Delta}(-1 \quad 0 \quad 1) * \frac{1}{4}\begin{pmatrix}1\\2\\1\end{pmatrix} = \frac{1}{8\Delta}\begin{pmatrix}-1 & 0 & 1\\-2 & 0 & 2\\-1 & 0 & 1\end{pmatrix}$$

$$\widetilde{D}_y = \frac{1}{4}(1 \quad 2 \quad 1) * \frac{1}{2\Delta}\begin{pmatrix}1\\0\\-1\end{pmatrix} = \frac{1}{8\Delta}\begin{pmatrix}1 & 2 & 1\\0 & 0 & 0\\-1 & -2 & -1\end{pmatrix}$$

Appendix 2

Figure 6.7 shows an example flowchart of current density analysis using the projected current density method of Park et al. [22]. Three slices are reconstructed by solving a numerical model of the object and using (6.22) to compute $\mathbf{J}^0$ and then the gradient of β data obtained from Eq. (6.24). The results are combined (6.22) to obtain the projected current density distribution $\mathbf{J}^P$ within each slice.

References

1. K. Beravs, D. White, I. Serša, F. Demsar, Electric current density imaging of bone by MRI. Magn. Reson. Imag. **15**, 909–15 (1997)
2. S. Birchfield, *Image Processing and Analysis*, 1st edn. (Cengage Learning, Boston, 2016)
3. H.R. Gamba, D.T. Delpy, Measurement of electrical current density distribution within the tissues of the head by magnetic resonance imaging. Med. Biol. Eng. Comput. **36**, 165–70 (1998)
4. N. Gao, B. He, Noninvasive imaging of bioimpedance distribution by means of current reconstruction magnetic resonance electrical impedance tomography. IEEE Trans. Biomed. Eng. **55**, 1530–38 (2008)
5. C. Göksu, L.G. Hanson, H.R. Siebner, P. Ehses, K. Scheffler, A. Thielscher, Human in-vivo brain magnetic resonance current density imaging (MR-CDI). Neuroimage **171**, 26–39 (2018)
6. C. Göksu, K. Scheffler, H.R. Siebner, A. Thielscher, L.G. Hanson, The stray magnetic fields in magnetic resonance current density imaging (MRCDI). Phys. Med. **59**, 142–50 (2019)
7. Y.Z. Ider, O. Birgul, O.F. Oran, O. Arikan, M.J. Hamamura, L.T. Muftuler, Fourier transform magnetic resonance current density imaging (FT-MRCDI) from one component of magnetic flux density. Phys. Med. Biol. **55**, 3177–99 (2010)
8. W.C. Jeong, S.Z.K. Sajib, H.J. Kim, O.I. Kwon, Focused current density imaging using internal electrode in magnetic resonance electrical impedance tomography (MREIT). IEEE Trans. Biomed. Eng. **61**, 1938–46 (2014)
9. M.V. Jog, R.X. Smith, K. Jann, W. Dunn, B. Lafon, D. Truong, A. Wu, L. Parra, M. Bikson, D.J.J. Wang, In-vivo imaging of magnetic fields induced by transcranial direct current stimulation (tDCS) in human brain using MRI. Sci. Rep. **6**, 34385 (2016)
10. M.L.G. Joy, G.C. Scott, R.M. Henkelman, In vivo detection of applied electric currents by magnetic resonance imaging. Magn. Reson. Imag. **7**, 89–94 (1989)
11. M.L.G. Joy, V.P. Lebedev, J.S. Gati, Imaging of current density and current pathways in rabbit brain during transcranial electrostimulation. IEEE Trans. Biomed. Eng. **46**, 1139–49 (1999)
12. A.K. Kasinadhuni, A. Indahlastari, M. Chauhan, M. Schär, T.H. Mareci, R.J. Sadleir, Imaging of current flow in the human head during transcranial electrical therapy. Brain Stimul. **10**, 764–72 (2017)
13. H.S. Khang, B.I. Lee, S.H. Oh, E.J. Woo, S.Y. Lee, M.H. Cho, O.I. Kwon, J.R. Yoon, J.K. Seo, *J*-substitution algorithm in magnetic resonance electrical impedance tomography (MREIT): phantom experiments for static resistivity images. IEEE Trans. Med. Imag. **21**, 695–702 (2002)
14. H.J. Kim, S.Z.K. Sajib, W.C. Jeong, M.N. Kim, O.I. Kwon, E.J. Woo, Analysis of local projected current density from one component of magnetic flux density in MREIT. Inverse Probl. **29**, 075001 (2013)
15. O.I. Kwon, S.Z.K. Sajib, I. Serša, T.I. Oh, W.C. Jeong, H.J. Kim, E.J. Woo, Current density imaging during transcranial direct current stimulation using DT-MRI and MREIT: algorithm development and numerical simulations. IEEE Trans. Biomed. Eng. **63**, 168–75 (2016)
16. B.I. Lee, S.H. Oh, E.J. Woo, S.Y. Lee, M.H. Cho, O.I. Kwon, J.K. Seo, J.Y. Lee, W.S. Baek, Three-dimensional forward solver and its performance analysis for magnetic resonance electrical impedance tomography (MREIT) using recessed electrodes. Phys. Med. Biol. **48**, 1971–86 (2003)
17. C.C. McIntyre, N.V. Thakor, Uncovering the mechanisms of deep brain stimulation for parkinson's disease through functional imaging, neural recording, and neural modeling. Crit. Rev. Biomed. Eng. **30**, 249–81 (2002)
18. C.C. McIntyre, S. Mori, D.L. Sherman, N.V. Thakor, J.L. Vitek, Electric field and stimulating influence generated by deep brain stimulation of the subthalamic nucleus. Clin. Neurophysiol. **115**, 589–95 (2004)
19. D. Miklavčič (ed.), *Handbook of Electroporation* (Springer, Berlin, 2017)
20. J.L. Mueller, S. Siltanen, *Linear and Nonlinear Inverse Problems with Practical Applications*. (Society for Industrial and Applied Mathematics, Philadelphia, 2012)
21. M.S. Nixon, A.S. Aguado, *Feature Extraction & Image Processing for Computer Vision*, 3rd edn. (Academic, New York, 2012)
22. C. Park, B.I. Lee, O.I. Kwon, Analysis of recoverable current from one component of magnetic flux density in MREIT. Phys. Med. Biol. **52**, 3001–13 (2007)
23. P. Pešikan, M.L.G. Joy, G.C. Scott, R.M. Henkelman, Two-dimensional current density imaging. IEEE Trans. Instrum. Meas. **39**, 1048–53 (1990)
24. H.C. Pyo, O.I. Kwon, J.K. Seo, E.J. Woo, Identification of current density distribution in electrically conducting subject with anisotropic conductivity distribution. Phys. Med. Biol. **50**, 3183–96 (2005)
25. B.J. Roth, N.G. Sepulveda, J.P. Wikswo, Using a magnetometer to image a two dimensional current distribution. J. Appl. Phys. **65**, 361 (1989)
26. R.J. Sadleir, S.C. Grant, S.U. Zhang, B.I. Lee, H.C. Pyo, S.H. Oh, C. Park, E.J. Woo, S.Y. Lee, O. Kwon, J.K. Seo, Noise analysis in magnetic resonance electrical impedance tomography at 3 and 11 T field strengths. Physiol. Meas. **26**, 875–884 (2005)
27. R.J. Sadleir, T.D. Vannorsdall, D.J. Schretlen, B. Gordon, Transcranial direct current stimulation (tDCS) in a realistic head model. NeuroImage **51**, 1310–18 (2010)
28. S.Z.K. Sajib, H.J. Kim, O.I. Kwon, E.J. Woo, Regional absolute conductivity reconstruction using projected current density in MREIT. Phys. Med. Biol. **57**, 5841–59 (2012)
29. S.Z.K. Sajib, N. Katoch, H.J. Kim, O.I. Kwon, E.J. Woo, Software toolbox for low-frequency conductivity and current density imaging using MRI. IEEE Trans. Biomed. Eng. **64**, 2505–14 (2017)

30. S.Z.K. Sajib, T.I. Oh, H.J. Kim, O.I. Kwon, E.J. Woo, In vivo mapping of current density distribution in brain tissues during deep brain stimulation (DBS). AIP Adv. **7**, 015004 (2017)
31. S.Z.K. Sajib, M. Chauhan, G. Banan, S. Sahu, L. Wang, T.H. Mareci, R.J. Sadleir, Compensation of lead-wire magnetic field contributions in MREIT experiment using image segmentation: a phantom study, in *Proceedings of the 27th Annual Meeting of the ISMRM* ISMRM (2019), p. 5049
32. S.Z.K. Sajib, M. Chauhan, O.I. Kwon, R.J. Sadleir, Magnetic-resonance-based measurment of electromagnetic fields and conductivity in vivo using single current administration - a machine learning approach. PLoS ONE **16**, 28 (2021)
33. A. Savitzky, M.J.E. Golay. Smoothing and differentiation of data by simplified least squares procedures. Analy. Chem. **36**, 1627–39 (1964)
34. A. Savitzky, M.J.E. Golay, What is a Savitzky-Golay filter? IEEE Signal Process. Mag. **28**, 111–17 (2011)
35. G.C. Scott, M.L.G. Joy, R.L. Armstrong, R.M. Henkelman, Measurement of nonuniform current density by magnetic resonance. IEEE Trans. Med. Imag. **10**, 362–74 (1991)
36. G.C. Scott, M.L.G. Joy, R.L. Armstrong, R.M. Henkelman, Sensitivity of magnetic-resonance current-density imaging. J. Magn. Reson. **97**, 235–254 (1992)
37. J.K. Seo, J. Kiwan, C. Lee, E.J. Woo, Non-iterative harmonic B_z algorithm in MREIT. Inverse Probl. **27**, 085003 (2011)
38. J.K. Seo, E.J. Woo, *Nonlinear Inverse Problems in Imaging* (Wiley, Hoboken, 2012)
39. I. Serša, M. Kranjc, D. Miklavčič, Current density imaging sequence for monitoring current distribution during delivery of electric pulses in irreversible electroporation. BioMed. Eng. OnLine **14**, S6 (2015)
40. D.S. Tuch, V.J. Wedeen, A.M. Dale, J.S. George, J.W. Belliveau, Conductivity tensor mapping of the human brain using diffusion tensor MRI. Proc. Natl. Acad. Sci. **98**, 111697–701 (2001)
41. R.S. Yoon, T.P. DeMonte, K.F. Hasanov, D.B. Jorgenson, M.L.G. Joy, Measurement of thoracic current flow in pigs for the study of defibrillation and cardioversion. IEEE Trans. Biomed. Eng. **50**, 1167–73 (2003)

Magnetic Resonance Electrical Impedance Tomography

7

Saurav Z. K. Sajib and Rosalind Sadleir

Abstract

Magnetic Resonance Electrical Impedance Tomography (MREIT) is a high-resolution bioimpedance imaging technique that has developed over a period beginning in the early 1990s to measure low-frequency (<1 kHz) tissue electrical properties. Low-frequency electrical properties are particularly important because they provide valuable information on cell structures and ionic composition of tissues, which may be very useful for diagnostic purposes. MREIT uses one component of the magnetic flux density data induced due to an exogenous-current administration, measured using an MRI machine, to reconstruct isotropic or anisotropic electrical property distributions. The MREIT technique typically requires two linearly independent current administrations to reconstruct conductivity uniquely. Since its invention, researchers have explored its potential for measuring electrical conductivity in regions such as the brain and muscle tissue. It has also been investigated in disease models, for example, cerebral ischemia and early tumor detection. In this chapter, we aim to provide a solid foundation of the different MREIT image reconstruction algorithms, including both isotropic and anisotropic conductivity reconstruction approaches. We will also explore the newly developed diffusion tensor magnetic resonance electrical impedance tomography (DT-MREIT) method, a practical method for anisotropic tissue property imaging, at the end of the chapter.

7.1 Introduction

MREIT is a method for imaging low-frequency electrical tissue properties at low frequencies. The data used in MREIT reconstructions are obtained using MRI. MREIT can be used to produce high-resolution cross-sectional low-frequency conductivity and current density distributions inside the human body [4, 64, 73, 75]. When low-frequency current is injected into an electrically conducting object through a pair of surface electrodes, it creates internal voltage u, current density, $\mathbf{J} = (J_x, J_y, J_z)$ and magnetic flux density $\mathbf{B} = (B_x, B_y, B_z)$ distributions [33, 40]. Using an MRI scanner with its main magnetic field aligned along the z-direction, we can only measure the one component of the magnetic flux density data [18, 61, 62]. Early MREIT

S. Z. K. Sajib · R. Sadleir (✉)
School of Biological Health System Engineering, Arizona State University, Tempe, AZ, USA
e-mail: ssajib1@asu.edu; rsadleir@asu.edu

R. Sadleir, A. S. Minhas (eds.), *Electrical Properties of Tissues*, Advances in Experimental Medicine and Biology 1380, https://doi.org/10.1007/978-3-031-03873-0_7

approaches assumed measurement of the full magnetic flux density vector $\mathbf{B} = (B_x, B_y, B_z)$ as the core data used in finding current density or conductivity distributions [19]. As we noted in Chap. 6, this requires rotations of the object inside the MRI scanner [18, 61, 62]. When all three components of **B** are known it is possible to directly calculate the current density distribution using the Amperes law, $\mathbf{J} = \frac{1}{\mu_0}\nabla \times \mathbf{B}$ [18,61,62]. However, object rotation is often impractical and may cause registration or conformation errors [19].

In general, MREIT requires at least two independent current injections [4, 64, 73] to reconstruct conductivity, even if the all components of magnetic flux density distributions are measured. Reconstruction algorithms such as the J-substitution algorithm [29] and CCVSR algorithm [4] have been developed using full measurement of **B** and data from two independent current injections. However, these methods also suffer from problems caused by the need for object rotation [19]. For convenient clinical implementation of the MREIT method, those using only one component of the measured magnetic flux density data are preferred. In this chapter, we consider methods using one component only and discuss the conductivity distributions that can be found using them.

As discussed in Chap. 1, at low frequencies the electrical conductivity of the biological tissue exhibits directional or *anisotropic* properties, meaning that the conductivity measured using fields applied along different principal directions varies. For example, in tissues such as white matter and muscle, conductivities measured using current applied longitudinally along the fiber or tract directions are much higher than when transverse current is applied. In general, electrical conductivity at a point within tissue may be expressed as a 3×3 symmetric positive definite tensor that has six unique components: $C_{xx}, C_{xy}, C_{xz}, C_{yy}, C_{yz}$ and C_{zz}, that is

$$\mathbb{C} = \begin{pmatrix} C_{xx} & C_{xy} & C_{xz} \\ C_{yx} & C_{yy} & C_{yz} \\ C_{zx} & C_{zy} & C_{zz} \end{pmatrix} = \begin{pmatrix} C_{xx} & C_{xy} & C_{xz} \\ C_{xy} & C_{yy} & C_{yz} \\ C_{xz} & C_{yz} & C_{zz} \end{pmatrix}. \tag{7.1}$$

If the conductivity does not depend on direction, it is *isotropic*, and the conductivity may be expressed as a scalar. We could represent this type of property in the form of Eq. (7.1) as an identity matrix multiplied by this scalar value, i.e.,

$$\mathbb{C} = \sigma \begin{pmatrix} 1 & 0 & 0 \\ 0 & 1 & 0 \\ 0 & 0 & 1 \end{pmatrix} \tag{7.2}$$

The Harmonic B_z algorithm [72] was the first method to use a single component of **B** to reconstruct isotropic conductivity. As in [29] and [4], data from two independent current injections were also required [46, 65, 72]. Results from this algorithm showed the possibilities of obtaining high-resolution conductivity images using one-component data. More recently, methods such as the transversal J-substitution algorithm [44] and the non-iterative [68] or absolute conductivity imaging methods [45] have also been developed. The feasibility of MREIT in clinical applications has been further substantiated by results obtained with nonbiological [32, 47] and biological phantom studies [35, 48] and postmortem [21] and in vivo animal [22] and human studies [23].

Reconstruction of anisotropic conductivity distributions requires recovery of the six independent entries in the conductivity tensor, which requires more data. Collection of single-component data from more than six independent current injections may, in principle, be used to reconstruct anisotropic distributions. Seo et al. [66] first proposed an algorithm to reconstruct anisotropic conductivity distributions. In order to determine all six components in (7.1), the method requires data from at least seven independent current injections. Though this method is theoretically capable of reconstructing the anisotropic conductivity distribution, this method is so sensitive to noise that no experimental result has yet been reported. Subsequently, other methods [7–9, 43, 55] have been proposed, but none of these methods have proved capable of recovering the full conductivity tensor. The need to measure a large number of data sets and attaching a large number of electrodes is also a limitation for this approach. For this reason,

most MREIT algorithms have concentrated on reconstruction of isotropic or equivalent isotropic conductivity distributions.

However, other ways of obtaining anisotropic conductivity properties can be considered. Since water molecules and the ions responsible for conductive properties coexist in the same biological environment, Tuch et al. [70,71] proposed that the eigenvectors of conductivity and diffusion tensors should be identical and therefore suggested an alternative model for determining the anisotropic conductivity as

$$\lambda_{C,k} = \frac{\sigma_e}{d_e}\left[\lambda_{D,k}\left(\frac{d_i}{3d_e}+1\right) + \lambda_{D,k}^2\frac{d_i}{3d_e^2}+\frac{2}{3}d_i\right]+O(d_i^2),\ k=1,2,3 \tag{7.3}$$

where $\lambda_{C,k}$ and $\lambda_{D,k}$ $k=1,2,3$ are the eigenvalues of the conductivity and the diffusion tensors, respectively; σ_e is the extracellular conductivity; d_i and d_e are the intra- and extracellular diffusion coefficients, respectively; and $O(d_i^2)$ is bounded as d_i^2 tends to infinity. Using experimentally obtained diffusion tensor data of the brain, Tuch et al. [70,71] determined an empirical scaling factor which converted the measured diffusion tensor data to its equivalent electrical conductivity. However, since this factor did not depend on ionic concentration [30,58], the estimated conductivity may not have been accurate [30,52].

Following the work of Tuch et al. [70,71], and using current density information obtained using MR-CDI, Ma et al. [39] and Kwon et al. [30] independently proposed algorithms to reconstruct the scaling factor. The methods combine magnetic flux density images with those of the water diffusion tensor that can be obtained using diffusion-weighted imaging [1]. The technique was named diffusion tensor magnetic resonance electrical impedance tomography, or DT-MREIT. In addition to the development of DT-MTREIT techniques, significant improvements in MREIT data acquisition provided by the multi-echo ICNE pulse sequence [41] and SPMGRE-ICNE pulse sequences [49] combined with use of multiple receiver coils [16] enabled high quality B_z and current density data to be obtained within a clinical setting. DT-MREIT techniques have now resulted in measurements of anisotropic conductivity in the brain in vivo [5,17].

7.2 Preliminaries

7.2.1 Fundamental Equations for MREIT

As in Sect. 6.2, we first describe the partial differential equations and boundary conditions applicable to MREIT experiments and used in constructing computational models used in reconstructions. The divergence free condition of current density ($\nabla\cdot\mathbf{J}=0$) induced inside the domain $\Omega\in\mathbb{R}^3$ due to the externally injected current I through the attached pair of surface electrodes $\mathcal{E}^{\pm}$ satisfies the partial differential equation [63]

$$\nabla\cdot\mathbf{J}=\nabla\cdot(-\sigma\nabla u)=0 \quad \text{in} \quad \Omega \tag{7.4a}$$

$$I=\pm\int_{\mathcal{E}^{\pm}}\sigma\frac{\partial u}{\partial\mathbf{n}}\cdot d\mathbf{s},\ \nabla u\times\mathbf{n}=0 \text{ on } \mathcal{E}^{+}\bigcup\mathcal{E}^{-} \tag{7.4b}$$

$$-\sigma\frac{\partial u}{\partial\mathbf{n}}=0 \quad \text{on} \quad \partial\Omega\backslash\left(\mathcal{E}^{+}\bigcup\mathcal{E}^{-}\right) \tag{7.4c}$$

As noted in Sect. 6.2, the condition, $-\sigma\frac{\partial u}{\partial\mathbf{n}}=0$ on the object boundary in Eq. (7.4c) ensures that the current density outside the imaging object is zero. Moreover, $\nabla u\times\mathbf{n}=0$ on the electrodes $\mathcal{E}^{\pm}$ guarantees a constant potential on the electrodes. The condition $I=\pm\int_{\mathcal{E}^{\pm}}\sigma\frac{\partial u}{\partial\mathbf{n}}\cdot d\mathbf{s}$ is the total current injected into the object. Alternatively, it has been shown that Eqs. (7.4a)–(7.4c) can be converted to [63]

$$\begin{cases}\nabla\cdot(-\sigma\nabla\tilde{u})=0 & \text{in} \quad \Omega\\ \tilde{u}|_{\mathcal{E}^{+}}=1 \quad \tilde{u}|_{\mathcal{E}^{-}}=0 & \\ -\sigma\frac{\partial\tilde{u}}{\partial\mathbf{n}}=0 & \text{on} \quad \partial\Omega\backslash\left(\mathcal{E}^{+}\bigcup\mathcal{E}^{-}\right)\end{cases} \tag{7.5}$$

In this form we specify the (constant) voltage applied at each electrode. This Dirichlet form of the PDE boundary conditions is preferred to (7.4a)–(7.4c) because it is difficult to specify the Neumann boundary condition on each point of

the electrodes. We denote the solution from this form of the equations $\tilde{u}$. Once $\tilde{u}$ is obtained from Eq. (7.5), the actual voltage distribution u that solves the boundary value problem (7.4a)–(7.4c) is

$$u = \beta \tilde{u} \tag{7.6}$$

where the scale factor β is the ratio of the experimentally injected current I and the total current $\int_{\mathcal{E}^+} \sigma \frac{\partial \tilde{u}}{\partial \mathbf{n}} \cdot d\mathbf{s}$ injected in the model

$$\beta = \frac{I}{\int_{\mathcal{E}^+} \sigma \frac{\partial \tilde{u}}{\partial \mathbf{n}} \cdot d\mathbf{s}}. \tag{7.7}$$

The current density distribution $\mathbf{J}$ may then be calculated via Ohm's law:

$$\mathbf{J} = -\sigma \nabla u. \tag{7.8}$$

If required, the magnetic flux density $\mathbf{B} = \left(B_x, B_y, B_z\right)$ can be obtained from $\mathbf{J}$ the Biot-Savart law:

$$\mathbf{B}(\mathbf{r}) = \frac{\mu_0}{4\pi} \int_\Omega \mathbf{J}(\mathbf{r}') \times \frac{\mathbf{r} - \mathbf{r}'}{|\mathbf{r} - \mathbf{r}'|^3} d\mathbf{r}' \tag{7.9}$$

where $\mu_0 = 4\pi \times 10^{-7}$ H/m is the permeability of free space.

The current density $\mathbf{J}$ and the induced magnetic flux density $\mathbf{B}$ are also related via Ampere's law:

$$\mathbf{J} = \frac{1}{\mu_0} \nabla \times \mathbf{B}. \tag{7.10}$$

7.2.2 Characteristics of B_z Distributions

In MREIT, the inverse problem involves reconstructing an unknown conductivity distribution σ from knowledge of the measured z-component of the magnetic flux density B_z data, the boundary geometry of the object, the location of current injection electrodes, and the injected current amplitude.

From (7.9), the z-component of the magnetic flux density; B_z can be expressed explicitly as

$$B_z(\mathbf{r}) = \frac{\mu_0}{4\pi} \int_\Omega \frac{\left(y - y'\right) J_x(\mathbf{r}') - \left(x - x'\right) J_y(\mathbf{r}')}{|\mathbf{r} - \mathbf{r}'|^3} d\mathbf{r}'. \tag{7.11}$$

Here, J_x and J_y are the x and y components of the current density $\mathbf{J}$, respectively.

Using measured B_z and its corresponding current density information to reconstruct conductivity has some limitations. These are listed below.

- First, there is a scaling uncertainty of σ associated with Eq. (7.11). Consider the case that a known current is applied to electrodes on an object with conductivity distribution σ. If the conductivity is multiplied by any positive constant $c > 0$ such that the conductivity becomes $\tilde{\sigma} = c\sigma$, the current density throughout the object and, therefore, B_z are identical. That is, it can be shown [20, 63] that $\tilde{B}_z = B_z$. This problem can be solved by measuring or assuming the voltage between the two fixed boundary points (e.g., by using voltage measurement electrodes placed on the surface) or by assuming the conductivity in some part of the imaged object is known. In this case MREIT can be used to reconstruct absolute conductivity distributions [20, 63].
- The second problem arises from the fact that the tangential component of the associated current density $\mathbf{J}$ contains distinguishable boundary information at the tissue interface, as shown in Fig. 7.1. To explain this, consider a three-dimensional conductive domain $\Omega \in \mathbb{R}^3$ consisting of one anomaly region $\mathcal{D}$ and a background region $\Omega \backslash \mathcal{D}$. The conductivity of the background is defined as σ_0, and the anomaly conductivity is defined as $\sigma = \sigma_0 + \delta\sigma$. From fundamental electromagnetic principles [69], any point on the anomaly subdomain boundary, $\zeta \in \partial\mathcal{D}$ satisfies the relations

$$\begin{cases} -\sigma_0 \nabla u^+(\zeta) \cdot \boldsymbol{\nu} = -(\sigma_0 + \delta\sigma) \nabla u^-(\zeta) \cdot \boldsymbol{\nu} \\ \nabla u^+(\zeta) \cdot \boldsymbol{\tau} = \nabla u^-(\zeta) \cdot \boldsymbol{\tau} \end{cases} \tag{7.12}$$

where $\boldsymbol{\nu}$ and $\boldsymbol{\tau}$ are normal and tangential unit vectors on $\partial\mathcal{D}$, respectively, and the voltage distributions u^+ and u^- are defined as

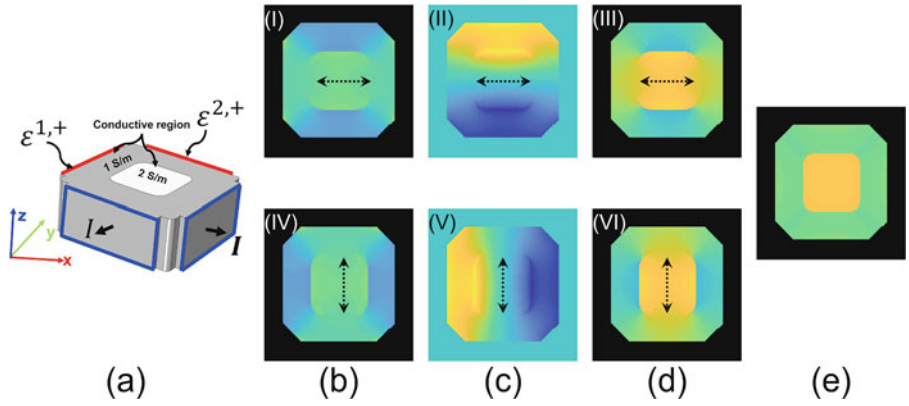

Fig. 7.1 Three-dimensional numerical model results illustrating the influence of Eq. (7.14). (**a**) To demonstrate the relation in (7.14) a rectangular-shaped conductive object with dimension $250\times250\times200\,\text{mm}^3$ and conductivity 2 S/m is placed in the center of the rectangular container (dimension $500\times500\times200\,\text{mm}^3$). The conductivity of the outside region was set to 1 S/m. The problem was solved subject to transverse current flow between electrodes $\mathcal{E}^{1,+}$ and $\mathcal{E}^{1,-}$ (I, II, and III) and $\mathcal{E}^{2,+}$ and $\mathcal{E}^{2,-}$ (IV, V, and VI). Parts (**b**), (**c**), and (**d**) show magnitudes of the current density, z-component of the magnetic flux density and reconstructed conductivity for the two projections. Arrows indicate the absence of boundary information. (**e**) demonstrates the conductivity reconstructed using data from both current projections

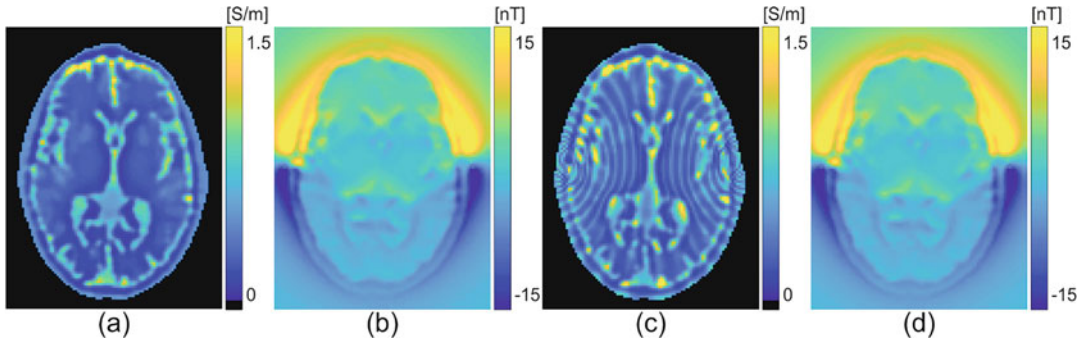

Fig. 7.2 Two different isotropic conductivity distributions (**a**) $J/|\nabla u|$ and (**c**) $J/|\nabla w|$ where u and $w = \phi(u)$ are two different voltage solutions of the boundary value problem in (7.4a)–(7.4c) that produce the same $\mathbf{J} = -\sigma\nabla u = -\frac{\sigma}{\phi(u(\mathbf{r}))}\nabla w$ and B_z (shown in (**b**) and (**d**)) [20, 63]. The strictly increasing continuously differentiable function ϕ was chosen so that $\phi\,(u(\mathbf{r})) = 1 + (3/7)\cos\,(50\,\pi\,u(\mathbf{r}))$. The voltage distribution u was solved for current flow between electrodes placed on right and left temporal locations

$$u^+ = u|_{\Omega\setminus\mathcal{D}} \quad \text{and,} \quad u^- = u|_{\mathcal{D}} \tag{7.13}$$

Decomposing the current density vector $\mathbf{J}$ into normal and tangential parts at the subdomain interface, $\mathbf{J}(\zeta) = (\mathbf{J}\cdot\boldsymbol{\nu})\boldsymbol{\nu}(\zeta)+(\mathbf{J}\cdot\boldsymbol{\tau})\boldsymbol{\tau}(\zeta)$. Finally, using Eq. (7.12) we have

$$\mathbf{J}^+(\zeta) - \mathbf{J}^-(\zeta) = \left(\delta\sigma\nabla u^-(\zeta)\cdot\boldsymbol{\tau}\right)\boldsymbol{\tau} \tag{7.14}$$

where the current density vectors $\mathbf{J}^+$ and $\mathbf{J}^-$ are defined in the background and anomaly regions, respectively, in a similar manner to u^+ and u^-.

This result implies ambiguity. Any conductivity gradient $\nabla\sigma$ perpendicular to equipotential surfaces caused by a specific current flow is not reflected in the current density within $\mathcal{D}$ and therefore is invisible to the corresponding B_z distribution. This phenomenon is demonstrated in Fig. 7.2, where two distinct conductivity distributions satisfy the same boundary value problem

Algorithm 2 General procedure of the MREIT reconstruction algorithm

Step 1. Obtain $\Gamma^{m,p}$ function for Eq. (7.16a) from measured data.
Step 2. Construct a numerical model, including electrodes, from acquired MR magnitude images.
Step 3. Solve Eq. (7.15) using some initial guess $\sigma = \sigma^0$ for each of the NP current injections; compute the functions Γ^p in (7.16a).
Step 4. Solve Eq. (7.16a) to obtain $\hat{\sigma}$.

(7.4a)–(7.4c) [14, 20, 63] and produce the same B_z. For this reason, conductivity reconstruction using a single-current injection is generally ill-posed without prior knowledge of surface conductivity [50] or measuring boundary voltage information [28].

Two-current MREIT reconstructions can be used to address these issues [13, 72]. For single-current MREIT, the method of Kwon et al. [28] uses knowledge of the boundary potential to uniquely determine internal distribution of the conductivity. However, experimental realization of this method is difficult because measurement of additional boundary voltages is difficult [28]. For two-dimensional cases, unique determination of the internal distribution of σ is also possible if surface conductivity is known [50].

7.3 Approaches to the MREIT Inverse Problem

Consider measurement of NP sets of B_z data using multiple current injections $p = 1, 2, \cdots, NP$, the MREIT forward problem for each case can be written:

$$\begin{cases} \nabla \cdot (-\sigma \nabla \tilde{u}^p) = 0 & \text{in} \quad \Omega \\ \tilde{u}^p|_{\mathcal{E}^{p,+}} = 1 \quad \tilde{u}^p|_{\mathcal{E}^{p,-}} = 0 & \\ -\sigma \frac{\partial \tilde{u}^p}{\partial \mathbf{n}} = 0 & \text{on} \quad \partial\Omega \backslash (\mathcal{E}^{p,+} \cup \mathcal{E}^{p,-}) \\ u^p = \beta^p \tilde{u}^p \qquad \text{where,} \quad \beta^p = \frac{I}{\int_{\mathcal{E}^{p,+}} \sigma \frac{\partial \tilde{u}^p}{\partial \mathbf{n}} \cdot d\mathbf{s}} & \\ \mathbf{J}^p = -\sigma \nabla u^p & \\ B_z^p(\mathbf{r}) = \frac{\mu_0}{4\pi} \int_\Omega \frac{(y-y') J_x^p(\mathbf{r}') - (x-x') J_y^p(\mathbf{r}')}{|\mathbf{r}-\mathbf{r}'|^3} d\mathbf{r}' & \end{cases} \tag{7.15}$$

As mentioned in Chap. 6, in MREIT B_z images are acquired from a portion of three-dimensional domain as a stack of axial slices arranged perpendicularly to the z-axis (see Fig. 6.1 of Chap. 6).

The MREIT inverse problem, that is, the determination of the electrical conductivity distribution from measured B_z data can be expressed as a minimization problem that compares model-predicted data Γ^p calculated using Eq. (7.15) to measured data $\Gamma^{m,p}$

$$\hat{\sigma}(\mathbf{r}) = \min \left(\sum_{p=1}^{NP} \left\| \Gamma^{m,p} - \Gamma^p \right\| \right) \quad \text{in } \Omega_t \tag{7.16a}$$

$$\hat{\sigma}(\mathbf{r}) = \sigma_0 \quad \text{on } \partial\Omega_t. \tag{7.16b}$$

In Eq. (7.16b) we assume that the conductivity value on the two-dimensional domain boundary $\partial\Omega_t$ is known a priori, to deal with the uniqueness issue described in Sect. 7.2.2. In Eq. (7.16a) the measured data $\Gamma^{m,p}$ can be B_z^m, its Laplacian, or the current density calculated from the B_z^m data (Fig. 7.3).

The finite element method [6] can be used to solve the problem in (7.15) and generate Γ^p data. Lee et al. [33] developed a custom finite element framework to solve MREIT forward problems. Minhas et al. [40] also developed a method to solve the forward problem using commercial software (COMSOL Multiphysics (COMSOL, Burlingham MA, USA)).

Simulated magnetic flux density can be estimated from (7.9) and a model-computed $\mathbf{J}$. Several numerical methods have been developed to compute the B_z [40]. For example, direct-discretization of the Biot-Savart law in a regular grid was described by Lee et al. [33], and Minhas et al. proposed [40] a hybrid approach based on solution of the Poisson equation (7.21) inside the domain Ω for a known $\mathbf{B}$ value at the domain boundary $\partial\Omega$. However, for fast computation of B_z, Eq. (7.11) may be converted to [51, 74]

$$B_z(\mathbf{r}) = \mu_0 \left(K_y * J_x - K_x * J_y \right)(\mathbf{r}). \tag{7.17}$$

Here, $*$ represents the convolution operator and the convolution kernels K_x and K_y are defined as

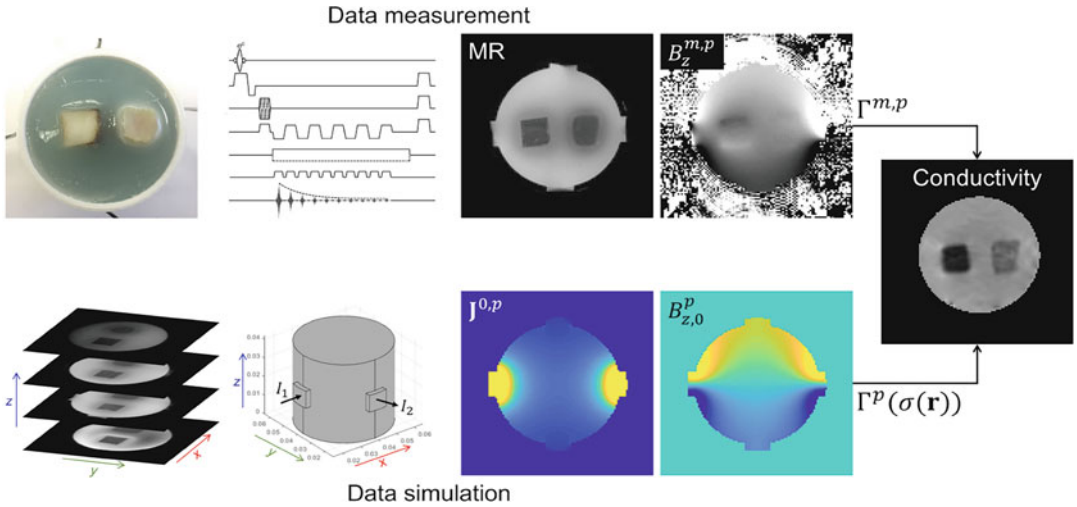

Fig. 7.3 Illustration of the conductivity reconstruction process in MREIT. Conductivity is reconstructed by comparing the measured data $\Gamma^{m,p}$ (upper row) with the computer-simulated model data Γ^{p} (bottom row). A three-dimensional finite element model is built from acquired MR magnitude information. The experimental boundary conditions are used to solve Eq. (7.15) and obtain Γ^{p}, $p = 1, 2$

$$K_x = \frac{1}{4\pi}\frac{x}{|\mathbf{r}|^3} \quad \text{and} \quad K_y = \frac{1}{4\pi}\frac{y}{|\mathbf{r}|^3} \tag{7.18}$$

respectively. A similar approach can be formulated for the other components of $\mathbf{B}$. Equation (7.17) can be implemented using fast Fourier transform (FFT) as [51, 74]

$$B_z(\mathbf{r}) = 4\pi\mathcal{F}^{-1}\left\{\mathcal{F}(K_y)\cdot\mathcal{F}(J_x) - \mathcal{F}(K_x)\cdot\mathcal{F}(J_y)\right\}(\mathbf{r}) \tag{7.19}$$

where $\mathcal{F}$ represents the FFT operator.

```
function Bz = mrci_Bzconv (J, VoxelSize)

% This MatLab routine calculates Bz from
equation (7.19).
% J[N1×N2×N3×2]: x, and y-components of the
current density vector field
% where, Jx = J(:,:,:,1), Jy = J(:,:,:,2).
% VoxelSize[1 × 3]: voxel size in
millimeter.
% Bz [N1 × N2 × N3]: calculated Bz data.

[N1, N2, N3, ~] = size(J)
VoxelSize = VoxelSize*1E-3;
paddSize =[N1, N2, N3];
[X1, X2, X3] = mesh-
grid(−N1 : N1 − 1, −N2 : N2 − 1, −N3 : N3 − 1);
X1 = X1*VoxelSize(1); X2 = X2*VoxelSize(2);
X3 = X3*VoxelSize(3);
R = (X1.^2+X2.^2+X3.^2).^(3/2);
K1 = X1./R; K1(isnan(K1)|isnan(K1)) = 0; K1 =
fftn(K1);
K2 = X2./R; K2(isnan(K2)|isnan(K2)) = 0; K2 =
fftn(K2);
```

```
FJ1 = fftn(padarray(flipud(squeeze
(J(:,:,:,1))),paddSize,0,'post'))
FJ2 = fftn(padarray(flipud(squeeze
(J(:,:,:,2))),paddSize,0,'post'))
Bz = 1E-7*ifftshift(real(ifftn(FJ1.*K2-
FJ2.*K1)))*prod(VoxelSize);
Bz = flipud(Bz(1 : N1, 1 : N2, 1 : N3));
```

As noted in Chap. 6, the acquired B_z^m signal measured by the MRI system may be corrupted with wire-induced magnetic flux density, $B_{z,\mathbb{L}}$, and electrode-induced magnetic flux density signals $B_{z,\mathcal{E}}$, where $\mathbb{L} = \mathcal{L}^+ \bigcup \mathcal{L}^-$ and $\mathcal{E} = \mathcal{E}^+ \bigcup \mathcal{E}^-$ [33]. The electrode-induced magnetic flux density is mainly due to currents flowing through the electrode surface [33]. In order to compensate for wire-induced magnetic flux density, one may constrain wires to run along the z-direction. However, in many situations, for example, in transcranial direct current stimulation experiments [11, 59], it is difficult to constrain the wire path in this way. For projections $p = 1, 2, \cdots, NP$, the acquired measured magnetic flux density at any point $\mathbf{r}$ within an object can therefore be described by [33]

$$B_z^{m,p}(\mathbf{r}) = \frac{\mu_0}{4\pi}\int_\Omega \frac{(y-y')\,J_x^p(\mathbf{r}') - (x-x')\,J_y^p(\mathbf{r}')}{|\mathbf{r}-\mathbf{r}'|^3}\, d\mathbf{r}' + B_{z,\mathbb{L}^p} + B_{z,\mathcal{E}^p}. \tag{7.20}$$

In Chap. 6, we saw that in many cases it was necessary to model B_z contributions from wires and electrodes in order to correctly estimate and compensate for them in CDI. We now consider how this may affect conductivity reconstruction algorithms.

In many reconstruction methods, compensation is not necessary. Applying the curl operator to both sides of Ampere's law (7.10) and using the divergence free condition of the magnetic flux density ($\nabla \cdot \mathbf{B} = 0$), we obtain

$$\frac{1}{\mu_0}\nabla^2\mathbf{B}(\mathbf{r}) = -\nabla \times \mathbf{J}(\mathbf{r}). \tag{7.21}$$

Note that Eq. (7.21) applies within any domain $\mathbf{r} \in \Omega$ or, $\mathbb{L}$ or, $\mathcal{E}$. However, at any outside point, that is, $\mathbf{r} \in \Omega \backslash \left(\mathbb{L} \bigcup \mathcal{E}\right)$, the Laplacian of B_z is zero and $\nabla^2 B_{z,\mathbb{L}}(\mathbf{r}) = \nabla^2 B_{z,\mathcal{E}}(\mathbf{r}) = 0$. Therefore, reconstruction algorithms that use the Laplacian of measured $B_z^{m,p}$ data can ignore the possible contributions from lead wires and electrodes to B_z. Examples of such algorithms are the harmonic B_z [46,65] and the non-iterative harmonic B_z algorithms [45,68]. However, these algorithms are prone to problems with low SNR data because computation of the Laplacian will tend to amplify noise.

The transverse J-substitution algorithm uses the first derivative of the measured $B_z^{m,p}$ $p \in 1, 2$ data [44], and thus any wire- or electrode-created stray magnetic field signal must be removed before conductivity reconstruction. After compensation, this algorithm works well for cases with low SNR data. Fortunately for these reconstructions, if wire trajectories can be recovered, effects of stray fields can be minimized using computational modeling [59].

7.4 Isotropic Image Reconstruction Algorithms in MREIT

Isotropic MREIT image reconstruction methods minimize the difference between the measured and model-predicted data (see Eq. (7.16a)–(7.16b)) assuming that the electrical conductivity is expressed by Eq. (7.2), using B_z data measured from multiple projections (see Sect. 7.3). Isotropic MREIT algorithms are simple relative to retrieval of the components in Eq. (7.1), because only one value, σ, per pixel is reconstructed. A number of algorithms, such as the sensitivity matrix method [2, 3, 73], algebraic reconstruction algorithm [13], the J-substitution algorithm [29], and harmonic B_z method [65] have been developed to reconstruct isotropic electrical conductivity distributions. As mentioned earlier, these algorithms can be considered as minimizing the differences between measured and model data. Another example of an isotropic MREIT reconstruction algorithm was developed by Gao et al. [10], where MREIT was proposed as a means of finding the electrical conductivity of the skin, skull, and brain tissue. This B_z-based parametric reconstruction algorithm [10] used the simplex method, to minimize differences between measured data with model data generated using (7.15) and estimated conductivity values. While this method may yet prove useful for finding brain tissue conductivity, no experimental results have been yet been reported. To alleviate the uniqueness problem (see Sect. 7.2.2 and Fig. 7.2), Kwon et al. [28] also proposed an algorithm based on equipotential lines reconstructed using measured B_z data. This method also requires voltage data measured from the object boundary to reconstruct the equipotential lines. However, in practice this method is sensitive to noise propagating along the equipotential lines. Later, Kwon et al. [29] developed the J-substitution algorithm, which has since been used to determine isotropic electrical conductivity distributions during electroporation processes [26, 27]. Another algorithm, the harmonic B_z method [46], was developed shortly after and has been used to perform in vivo human and animal imaging studies [22, 23]. In this section we briefly detail features of a few isotropic MREIT reconstruction algorithms.

7.4.1 Sensitivity-Based Algorithm

The sensitivity matrix-based method is based on a linearized relationship between measured B_z data and the conductivity distribution σ [2,3]:

$$\Delta B_z = \mathcal{S}\Delta\sigma \tag{7.22}$$

where ΔB_z is the difference between B_z measured in an object having homogenous and perturbed conductivity distributions σ^0 and $\sigma^0+\Delta\sigma$, respectively. The solution for the conductivity perturbation $\Delta\sigma$ is found by inverting the system in Eq. (7.22), where $\mathcal{S}$ can be found by discretizing the Biot-Savart law (Eq. (7.11)) for multiple projection data $p = 1, 2, 3, \cdots, NP$.

This method has been used to obtain electrical conductivity distributions in a phantom experiment [42] and in an in vivo experiment in rats to determine tumor conductivity [42]. Note that because B_z data are used directly, this algorithm requires removal of any stray magnetic fields caused by wires or electrodes from measured data.

7.4.2 J-Substitution Algorithm

Early versions of the J-substitution algorithm assume that the full current density vector $\mathbf{J}^m = \left(J_x^m, J_y^m, J_z^m\right)$ has already been measured from an MRCDI experiment. Using the measured magnitude of the current density data, $J^m = \sqrt{\left(J_x^m\right)^2 + \left(J_y^m\right)^2 + \left(J_z^m\right)^2}$, Kwon et al. [29] developed an isotropic image reconstruction method by minimizing the integrated difference $\Psi(\sigma)$ between J^m and the model-predicted current density $\sigma(\mathbf{r})E_\sigma(\mathbf{r})$:

$$\Psi(\sigma) = \int_\Omega |J^m(\mathbf{r}) - \sigma(\mathbf{r})E_\sigma(\mathbf{r})|^2 d\mathbf{r}. \tag{7.23}$$

Here, $E_\sigma(\mathbf{r}) = |\nabla u_\sigma|$ is the magnitude of the electric field obtained using a numerical model after solving Eq. (7.5)–(7.7) for a given conductivity distribution σ.

Vectorizing the imaging slice into $\Omega_t = \bigcup_{n=0}^{N-1}\Omega_{t,n}$ (see Fig. 7.4), Eq. (7.23) can be written as

$$\widetilde{\Psi}(\sigma_0, \sigma_1, \sigma_2, \cdots, \sigma_{N-1}) = \sum_{n=0}^{N-1}\int_{\Omega_{t,n}} \left|J^m(\mathbf{r}) - \sigma_n(\mathbf{r})E_\sigma(\mathbf{r})\right|^2 d\mathbf{r} \tag{7.24}$$

where the conductivity σ_n is assumed to be constant in each element $\Omega_{t,n}$ and the electric field $E_\sigma(\mathbf{r})$ can be expressed as a function of the discrete conductivity distribution $[\sigma_0, \sigma_1, \sigma_2, \cdots, \sigma_{N-1}]^T$ [29].

Differentiating Eq. (7.24) with respect to σ_q ($q \in 0 \ldots N-1$), we obtain

$$\begin{aligned}\tfrac{1}{2}\tfrac{\partial\widetilde{\Psi}}{\partial\sigma_q} &= \int_{\Omega_{t,q}} E_\sigma(\mathbf{r})\left[\sigma_q E_\sigma(\mathbf{r}) - J^m(\mathbf{r})\right] d\mathbf{r} \\ &\quad + \sum_{n=0}^{N-1}\int_{\Omega_n}\sigma_n\tfrac{\partial E_\sigma(\mathbf{r})}{\partial\sigma_n}\left[\sigma_n E_\sigma(\mathbf{r}) - J^m(\mathbf{r})\right] d\mathbf{r}\end{aligned} \tag{7.25}$$

By setting $\frac{1}{2}\frac{\partial\widetilde{\Psi}}{\partial\sigma_q} = 0$, the representative conductivity σ_q for the region $\Omega_{t,q}$ can be found as [29]

$$\sigma_q = \frac{J^m(\mathbf{r}_q)}{E_\sigma(\mathbf{r}_q)} \quad \text{for } q = 0, 1, 2, \cdots N-1 \tag{7.26}$$

where $\mathbf{r}_q$ is the center point of the element $\Omega_{t,q}$. Using two independent current administrations $J^{m,p}$, $p \in 1, 2$, the $(k+1)$th update of the conductivity is written as

$$\sigma_q^{k+1} = \frac{\sum_{p=1}^{2} J^{m,p}(\mathbf{r}_q)E_\sigma^{k,p}(\mathbf{r}_q)}{\sum_{p=1}^{2}\left[E_\sigma^{k,p}(\mathbf{r}_q)\right]^2} \tag{7.27}$$

The J-substitution algorithm can also be used when only B_z is measured. Park et al. [50] developed a projected-current-density-based algorithm see Chap. 6. Using reconstructed projected current density data $\mathbf{J}^{P,p}$, $p \in 1, 2$, instead of the full measured $\mathbf{J}^m$, the J-substitution algorithm yields [57]

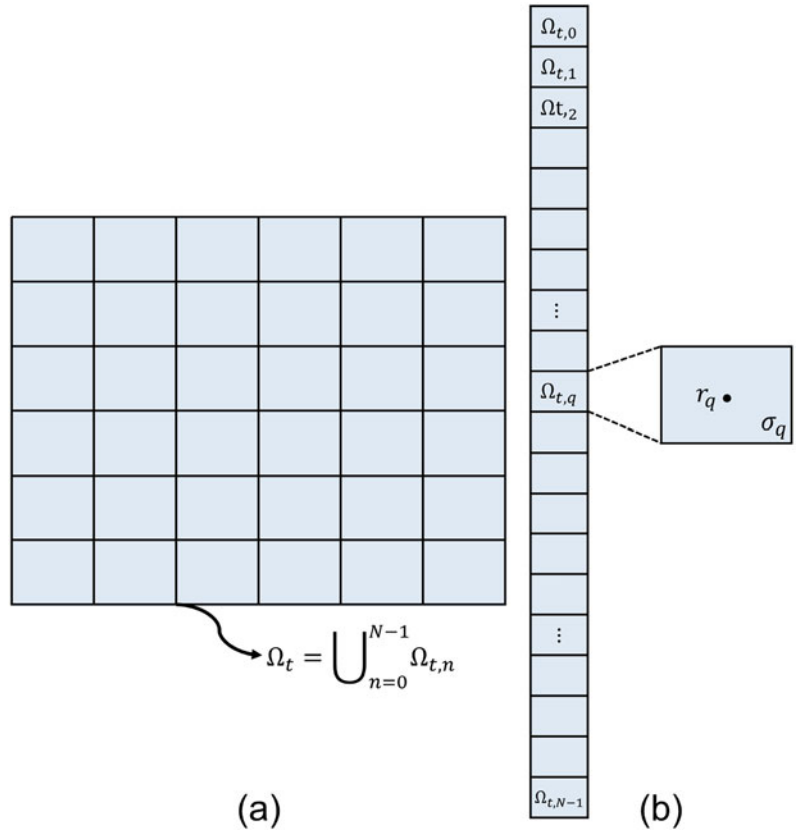

Fig. 7.4 Discrete representation of the imaging plane Ω_t used in J-substitution algorithm. (**a**) Original image plane. (**b**) The image pixels can also be arranged as a column vector. The representative conductivity σ_q which is assumed to be constant for the discrete domain $\Omega_{t,q}$ for, $q = 0, 1, 2, \cdots, N-1$ is shown at right

$$\sigma_q^{k+1} = \frac{\sum_{p=1}^{2} \left\langle \mathbf{J}^{P,p}(\mathbf{r}_q), \mathbf{E}_\sigma^{k,p}(\mathbf{r}_q) \right\rangle}{\sum_{p=1}^{2} \left\langle \mathbf{E}_\sigma^{k,p}(\mathbf{r}_q), \mathbf{E}_\sigma^{k,p}(\mathbf{r}_q) \right\rangle} \tag{7.28}$$

where $\langle , \rangle$ represents the inner product of the two vectors and $\mathbf{E}_\sigma = [E_{\sigma_x}, E_{\sigma_y}, E_{\sigma_z}]^T$ denotes the components of the model-predicted electric field vector. In order to uniquely determine the internal conductivity distribution, the condition $|\mathbf{J}^1 \times \mathbf{J}^2| \neq 0$ must be satisfied [29, 63].

7.4.3 Harmonic B_z Algorithm

At low frequencies, the relationship between the conductivity σ, voltage distribution u, and the z-component of the magnetic flux density B_z satisfies the relation

$$\frac{\partial u}{\partial y}\frac{\partial \sigma}{\partial x} - \frac{\partial u}{\partial x}\frac{\partial \sigma}{\partial y} = \frac{1}{\mu_0}\nabla^2 B_z. \tag{7.29}$$

This is the z-component of (7.21).

Since the voltage distribution u is a nonlinear function of the conductivity distribution σ, the harmonic B_z algorithm uses this equation to update the conductivity gradients using the measured B_z and model-predicted voltage data u. Because two gradient components must be found, B_z data from at least two current injections must be measured. For two current injections, the expression used to calculate the updated gradient $\widetilde{\nabla}\sigma$, where $\widetilde{\nabla} := (\frac{\partial}{\partial x}, \frac{\partial}{\partial y})$ takes the following matrix form [46, 58, 65]:

$$\begin{pmatrix} \frac{\partial u_1^k}{\partial y} & -\frac{\partial u_1^k}{\partial x} \\ \frac{\partial u_2^k}{\partial y} & -\frac{\partial u_2^k}{\partial x} \end{pmatrix} \begin{pmatrix} \frac{\partial \sigma^{k+1}}{\partial x} \\ \frac{\partial \sigma^{k+1}}{\partial y} \end{pmatrix} = \frac{1}{\mu_0} \begin{pmatrix} \nabla^2 B_z^{m,1} \\ \nabla^2 B_z^{m,2} \end{pmatrix} \text{ or} \tag{7.30}$$

$$U^k s^{k+1} = b \tag{7.31}$$

From Eq. (7.31), it is clear that the unique reconstruction of the conductivity is only possible when $|\widetilde{\nabla}u^1 \times \widetilde{\nabla}u^2| \neq 0$ is satisfied, that is, when the matrix U^k is non-singular. If electrode pairs are placed approximately orthogonal to each other, this condition is generally satisfied, and the gradients are also orthogonal to each other. However, this orthogonality condition is not satisfied for currents flowing near the object boundary, or near internal structures with very low conductivities. In practical conditions where there is measurement noise, $\widetilde{\nabla}\sigma^{k+1}$ is calculated from a regularized least-squares solution:

$$s^{k+1} = \left(U^{k^T} U^k + \frac{\kappa}{|U^{k^T} U^k|} \mathbf{I} \right) U^{k^T} b \quad (7.32)$$

Here, U^{k^T} is the transpose of the stiff matrix in Eq. (7.31), κ is a regularization constant, and $\mathbf{I}$ is the 2×2 identity matrix. Once the solution for $\widetilde{\nabla}\sigma^{k+1}$ is obtained for the slice Ω_t, the conductivity can be estimated using Poisson's equation [57]:

$$\begin{cases} \widetilde{\nabla}^2 \sigma^{k+1} = \widetilde{\nabla} \cdot s^{k+1} & \text{in } \Omega_t \\ \sigma^{k+1} = \sigma_0 & \text{on } \partial\Omega_t \end{cases} \quad (7.33)$$

where σ_0 is the known or assumed boundary conductivity value, as discussed in Sect. 7.3. It is important to note that the harmonic B_z algorithm requires computing the second derivative of B_z data, which tends to amplify noise in the data. PDE-based [34] or ramp-preserving [37] denoising strategies may be employed to mitigate these effects.

7.4.4 Transversal J-Substitution Algorithm

The transversal J-substitution algorithm was proposed as another alternative to the J-substitution algorithm when full current density vector data is not available. Instead of measuring the full magnetic flux density data, the transversal J-substitution algorithm iteratively updates the transverse (x,y) components of the current density, that is, the those components in the plane perpendicular to the measured $\mathbf{B}$ component, as [44]

$$\begin{aligned} \tilde{J}_x^{k+1,p} &= \frac{1}{\mu_0}\left(\frac{\partial B_z^{m,p}}{\partial y} - \frac{\partial B_z^{k,p}}{\partial y} \right) - \sigma^k \frac{\partial u^{k,p}}{\partial x} \\ \tilde{J}_y^{k+1,p} &= \frac{1}{\mu_0}\left(\frac{\partial B_z^{m,p}}{\partial x} - \frac{\partial B_z^{k,p}}{\partial x} \right) - \sigma^k \frac{\partial u^{k,p}}{\partial y} \end{aligned} \quad (7.34)$$

where $\tilde{J}_x^{k+1,p}$ and $\tilde{J}_y^{k+1,p}$ are the x and y components of the $(k+1)$th update of the intermediate current density and $p \in 1, 2$. $B_z^{k,p}$ and $u^{k,p}$ represent the kth update of the B_z and the voltage distribution obtained using the σ information from the MREIT forward solution for (Eq. (7.15)) at the previous step, respectively. The least-squares solution for the $(k+1)$th conductivity update takes the form

$$\sigma^{k+1} = \sigma^k - \frac{1}{\mu_0} \frac{\sum_{p=1}^{2} \langle \widetilde{\nabla}^{\perp} \left(B_z^{m,p} - B_z^{k,p} \right), \nabla u^{k,p} \rangle}{\sum_{p=1}^{2} \langle \nabla u^{k,p}, \nabla u^{k,p} \rangle} \quad (7.35)$$

The formula in Eq. (7.35) has advantages for low SNR signals. Recall that the SNR in measured B_z is proportional to the injected current amplitude and current injection duration. In clinical MREIT applications, it is desirable to collect data with the lowest practical scan duration and current amplitudes. It can be shown that the accumulated noise contributed by measured B_z in the 1st update of the conductivity is [44]

$$sd(\sigma^1)(\mathbf{r}) = \frac{sd_{B_z}(\mathbf{r})}{\mu_0 \Delta} \frac{\sqrt{3}}{4} \frac{1}{\sqrt{\sum_{p=1}^{NP} \langle \widetilde{\nabla} u_i^0, \widetilde{\nabla} u_i^0 \rangle}} \quad (7.36)$$

In Eq. (7.36) it is assumed that the noise standard deviation in B_z, sd_{B_z}, is the same for the all current injections and the derivatives $\frac{\partial}{\partial x}$ and $\frac{\partial}{\partial y}$ are computed using the kernels:

$$\frac{\partial}{\partial x} = \frac{1}{8\Delta} \begin{pmatrix} -1 & 0 & 1 \\ -2 & 0 & 2 \\ -1 & 0 & 1 \end{pmatrix}$$

$$\text{and} \quad \frac{\partial}{\partial y} = \frac{1}{8\Delta} \begin{pmatrix} 1 & 2 & 1 \\ 0 & 0 & 0 \\ -1 & -2 & -1 \end{pmatrix}$$

For further details please see Appendix 1 of Chap. 6. While this method provides an updated conductivity at low SNR, recall that additional data processing steps are needed to remove wire- and electrode-created stray magnetic fields.

7.4.5 Non-iterative Harmonic B_z Algorithm

The noise level in measured magnetic flux density data, sd_{B_z}, depends on the current injection duration T_c and signal-to-noise ratio (SNR) of the MR magnitude image, Υ [53,61] via

$$sd_{B_z} \propto \frac{1}{\gamma T_c \Upsilon}. \tag{7.37}$$

Here, $\gamma = 42.576 \times 10^6$ Hz/T is the gyromagnetic ratio of the proton. From Eq. (7.37), for a particular MR-pulse sequence and a fixed injection current I, noise standard deviation depends inversely on T_c. It may hence be difficult to obtain sufficient SNR in measured data in clinical settings. Even though iterative PDE-based [34] or ramp-preserving [37] denoising techniques may improve B_z data quality, important information about conductivity structure boundaries may be lost as the iterative processes smooth these transitions. Therefore, it is difficult to use an iterative MREIT algorithm to obtain absolute conductivity values, even if boundary voltages or conductivities are known a priori, mainly because the iterative process accumulates noise with each step.

The characteristics of the iterative harmonic B_z algorithm were investigated by Sajib et al. [54]. A simple two-dimensional circular phantom model with an internal anomaly was used to find an analytic expression for the k-th update of the anomaly conductivity as

$$\delta\sigma^k = \frac{\delta\sigma}{2+\xi}\left[2+\xi\left\{1-\left(\frac{\xi}{2+\xi}\right)^{k-1}\right\}\right], \tag{7.38}$$

where

$$\xi := \delta\sigma\left(1+\left(\frac{r_0}{R}\right)^2\right).$$

From Eq. (7.38), the first update of the conductivity is

$$\sigma^1 = 1+\delta\sigma^1 = 1+\frac{2\delta\sigma}{2+\delta\sigma\left(1+\left(\frac{r_0}{R}\right)^2\right)} \tag{7.39}$$

where r_0 and R are the anomaly and disk radii, respectively, shown in Fig. 7.5a and η^* is the anomaly conductivity perturbation.

Equation (7.38) shows some key characteristics of the iterative harmonic B_z algorithm. Specifically, if the conductivity distribution is similar to the background conductivity, the first update σ^1 almost recovers the correct absolute value. The difference between σ^1 and the true conductivity σ depends on the size of r_0 and the anomaly conductivity value. Figure 7.5b shows the relative error $E\left(\sigma^1\right) := \frac{|\sigma-\sigma^1|}{\sigma}$ dependence on the conductivity value for a fixed anomaly size, and Fig. 7.5c shows error dependence on anomaly size for a fixed conductivity value. For a fixed anomaly size, relative error increases as the conductivity value increases. Therefore, the first conductivity update may not produce an anomaly conductivity very close to the actual value. Therefore, to minimize the difference between the true and reconstructed one, it is necessary to iteratively update the conductivity. Depending on the anomaly size and the actual conductivity value, the number of iterations required may of course vary (Fig. 7.5d), and this process is vulnerable to additional errors caused by measurement noise.

The *non-iterative* harmonic B_z [68] or absolute conductivity [45] algorithm proceeds from a variation of (7.21)

$$J_y\frac{\partial \ln\sigma}{\partial x} - J_x\frac{\partial \ln\sigma}{\partial y} = -\nabla^2 B_z/\mu_0 \tag{7.40}$$

where J_x and J_y are the x and y components of the current density vector field $\mathbf{J}$.

The non-iterative harmonic B_z [68] or absolute conductivity [45] algorithm uses Eq. (7.40), to solve the unknown $\widetilde{\nabla}\sigma$ at each pixel position using two independent current injections $p = 1, 2$ using

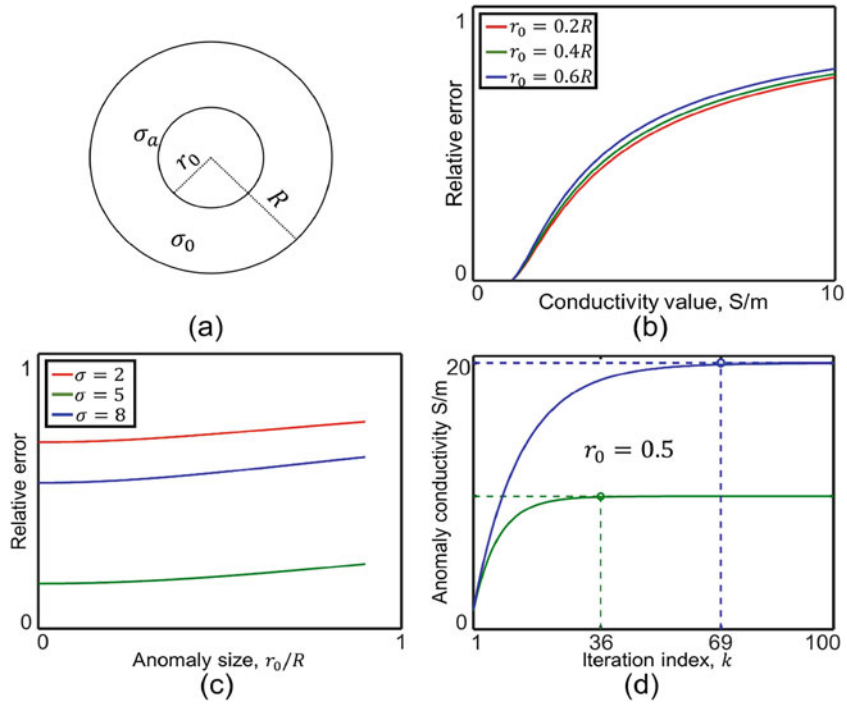

Fig. 7.5 Demonstration of convergence characteristics of harmonic B_z algorithm [54]. (**a**) Two-dimensional circular domain with radius R containing an anomaly with radius r_0. The conductivity of the background domain was set to $\sigma_0 = 1$ S/m, and anomaly conductivity was set to $\sigma_a = \sigma_0 + \delta\sigma$. Current was delivered through two opposing pairs of point electrodes attached to the domain boundary $\partial\Omega$. (**b**) Relative error $E(\sigma^1) := \frac{|\sigma - \sigma^1|}{\sigma}$ dependence on anomaly conductivity for three anomaly sizes r_0, (**c**) dependence of relative error on anomaly size for three conductivities (values in S/m), and (**d**) convergence characteristics of harmonic B_z algorithm for anomalies with $r_0 = 0.5$ and conductivities of 10 and 20 S/m, respectively

$$\widetilde{\nabla} \ln \sigma = -\frac{1}{\mu_0} \begin{pmatrix} J_y^1 & -J_x^1 \\ J_y^2 & -J_x^2 \end{pmatrix}^{-1} \begin{pmatrix} \nabla^2 B_z^{m,1} \\ \nabla^2 B_z^{m,2} \end{pmatrix} \tag{7.41}$$

As in the harmonic B_z algorithm described above, once $\widetilde{\nabla} \ln \sigma$ is obtained from Eq. (7.41), the Poisson equation can be solved with a known boundary conductivity to recover the absolute conductivity, in a similar manner to (7.33). Current density image reconstruction methods described in Chap. 6 can be used to find the x and y components of current density required by (7.41). For example, in [50] the projected current density $\mathbf{J}^P$ was used to reconstruct conductivity using this method. The projected current density is the best approximation of the true current density that can be computed using single-component magnetic flux density data [50, 57]. It was shown in [50] that the L^2 error in the conductivity reconstructed using the non-iterative harmonic B_z method depends on the proportion of the current density flowing in the z-direction J_z. It has also been demonstrated that the conductivity reconstructed by the original harmonic B_z algorithm may be severely affected by noise propagation from defective regions [24, 54]. Such defective regions include those with low conductivity or short T_2 values such as may be found in skull or bone. Therefore, a newer version of this reconstruction algorithm was proposed by Sajib et al. [54] based on *regional* projected current density data.

7.4.6 Dual-Loop Algorithm

In applications such as electroporation or transcranial direct current stimulation, it is desirable to find the electric field distribution caused by

these therapeutic currents [26, 27, 31]. Although current density information can be obtained from magnetic flux density experiments, the conductivity distribution must also be known to determine the electric field via Ohm's law. As mentioned in Sect. 7.2.2, it is possible to uniquely determine the conductivity distribution if the boundary voltage or conductivity is known a priori. Therefore, to reconstruct the electric field for a specific electrode configuration, two currents must still be administered to reconstruct MREIT images, with a known boundary conductivity assumed, to see the internal structures via the current density $\mathbf{J}$ (see Fig. 7.1 in Sect. 7.2.2 for further detail).

Using single-current magnetic flux density data, Lee et al. [36] proposed reconstruction of the conductivity distribution σ from the estimated projected current density data [50] by using Kirchhoff's voltage law (KVL) applied to a mimetic discretized rectangular grid, $\Omega_t = \bigcup_{m=1,n=1}^{N_x,N_y} \Omega_{t,mn}$ (Fig. 7.6). They showed that by applying the KVL over both primary $\Omega_{t,mn}$ and secondary loops $\Omega'_{t,mn}$ (Fig. 7.6), the conductivity σ within common regions can be found as in [36], using

$$\frac{J_x^P(p_{ij,1})}{\sigma(x_i, y_{j-1})} + \frac{J_y^P(p_{ij,2})}{\sigma(x_i, y_j)} - \frac{J_x^P(p_{ij,3})}{\sigma(x_i, y_j)} - \frac{J_y^P(p_{ij,4})}{\sigma(x_{i-1}, y_j)} = 0 \tag{7.42}$$

and

$$\frac{J_x^P(p'_{ij,1})}{\sigma(x_i, y_j)} + \frac{J_y^P(p'_{ij,2})}{\sigma(x_{i+1}, y_j)} - \frac{J_x^P(p'_{ij,3})}{\sigma(x_i, y_{j+1})} - \frac{J_y^P(p'_{ij,4})}{\sigma(x_i, y_j)} = 0, \tag{7.43}$$

where $p_{ij,1}$, $p_{ij,2}$, $p_{ij,3}$, and $p_{ij,4}$ in Eq. (7.42) are the center points located at coordinates (x_{i-1}, y_{j-1}), (x_i, y_{j-1}), (x_i, y_j), and (x_{i-1}, y_j), respectively, and $J_{x,y}^P$ are components of the projected current density $\mathbf{J}^P$. For $\Omega'_{t,mn}$ the loop vertices are given by, $p'_{ij,1}=\left(x_i, \frac{y_{j-1}+y_j}{2}\right)$, $p'_{ij,2}=\left(\frac{x_i+x_{i+1}}{2}, y_j\right)$, $p'_{ij,3}=\left(x_i, \frac{y_j+y_{j+1}}{2}\right)$, and $p'_{ij,4}=\left(\frac{x_{i-1}+x_i}{2}, y_j\right)$ (Fig. 7.6).

Note that this *dual-loop* network is designed in such a way that x, y-components of projected current $\mathbf{J}^P$ vectors at the points $\left(p'_{ij,1}, p_{ij,2}\right)$ and $\left(p_{ij,3}, p'_{ij,4}\right)$ (Fig. 7.6) are used simultaneously to determine σ values at that position [36].

Using linear interpolation of $\mathbf{J}^P$ vectors at the center of the nodes shown in Fig. 7.6, and with the assumption that σ values are known on the boundary, the dual-loop network defines an overdetermined system containing a total of $2(N_x-2)(N_y-2)$ equations and $(N_x-2)(N_y-2)$ internal nodes for the slice Ω_t, where N_x and N_y are respectively the number of pixels along the x and y direction in the slice. The regularized least-squares solution of the dual-loop matrix system can be found by solving

$$\Xi = \left(\mathcal{A}^T\mathcal{A} + \kappa\mathbf{I}\right)^{-1}\mathcal{A}^T\mathbf{b} \tag{7.44}$$

where $\mathcal{A} = (\mathcal{A}_\mathbf{p}, \mathcal{A}_\mathbf{s})^T$ and $\mathbf{b} = (\mathbf{b}_\mathbf{p}, \mathbf{b}_\mathbf{s})^T$, κ represents a regularization parameter, $\mathbf{I}$ is the identity matrix, and the superscript T denotes matrix transpose. The solution vector Ξ contains inverse conductivity values, $\frac{1}{\sigma}$ for each node. The elements of the stiff matrices $\mathcal{A}_\mathbf{p}$ (primary) and $\mathcal{A}_\mathbf{s}$ (secondary) in Eq. (7.44) contain the numerator terms from Eqs. (7.42) and (7.43), respectively.

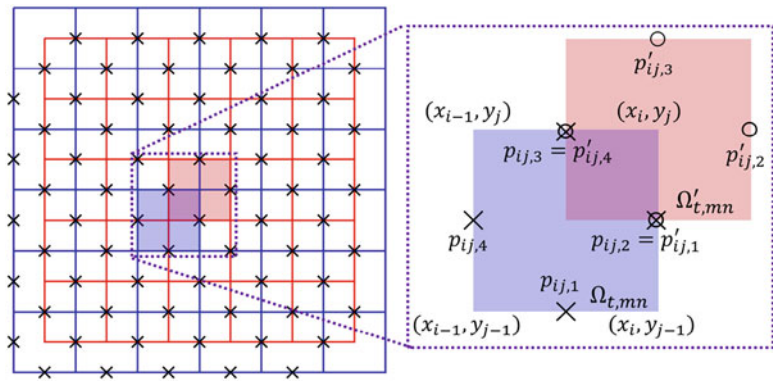

Fig. 7.6 Schematic of the dual-loop network. The primary loop is shaded in blue and the secondary (primed) loop is shaded in red

The corresponding load vector $\mathbf{b_p}$ or $\mathbf{b_s}$ contains known boundary voltage differences, estimated from known boundary Ξ and $\mathbf{J}^P$ values around the loop perimeter.

Lee et al. [36] also demonstrated that properties of single-loop conductivity reconstructions based on the KVL were strongly influenced by local changes in current flow, noise, and reconstruction pathway. Since both x and y components of the current density vector are considered simultaneously at intersection points of dual-loops (Fig. 7.6), the dual-loop method is less sensitive to reconstruction path. However, the performance of the method is still limited due to the due to artifacts along equipotential lines, that is, perpendicular to the current flow [36], and therefore may not be appropriate for clinical applications.

7.5 Anisotropic Image Reconstruction Algorithms in MREIT

Biological tissues such as brain white matter and skeletal muscle exhibit anisotropic properties at low frequencies [12]. As noted in (7.1), the anisotropic conductivity can be expressed as a 3×3 symmetric and positive definite tensor. In the presence of tissue anisotropy, Ohm's law takes the form

$$\begin{aligned} J_x &= -C_{xx}\frac{\partial u}{\partial x} - C_{xy}\frac{\partial u}{\partial y} - C_{xz}\frac{\partial u}{\partial z} \\ J_y &= -C_{xy}\frac{\partial u}{\partial x} - C_{yy}\frac{\partial u}{\partial y} - C_{yz}\frac{\partial u}{\partial z} \\ J_z &= -C_{xz}\frac{\partial u}{\partial x} - C_{yz}\frac{\partial u}{\partial y} - C_{zz}\frac{\partial u}{\partial z} \end{aligned} \tag{7.45}$$

If the tissue properties are isotropic (see Eq. (7.8)), the current density and electric field vectors are parallel. However, this is not true if tissue properties are anisotropic (see (7.45)). In general, to reconstruct anisotropic tissue property in MREIT, six unknown variables per voxel must be found. In the following sections, we describe a few MREIT algorithms which have been developed for anisotropic tissue imaging.

7.5.1 Seo's Algorithm

Seo et al. [66] proposed the first algorithm to reconstruct anisotropic conductivity distribution in MREIT. This iterative method requires at least seven linearly independent current injections. The proposed algorithm is based on the following identity:

$$\begin{aligned} \frac{1}{\mu_0}\nabla^2 B_z = &\left(-\frac{\partial C_{xx}}{\partial y} + \frac{\partial C_{xy}}{\partial x}\right)u_x + \left(-\frac{\partial C_{xy}}{\partial y} + \frac{\partial C_{yy}}{\partial x}\right)u_y \\ &+ \left(-\frac{\partial C_{xz}}{\partial y} + \frac{\partial C_{yz}}{\partial x}\right)u_z + C_{xy}\left(u_{xx} - u_{yy}\right) \\ &+ \left(C_{xx} + C_{yy}\right)u_{xy} + C_{yz}u_{xz} - C_{xz}u_{yz} \end{aligned} \tag{7.46}$$

The C_{ij}, $i, j \in x, y, z$ are the tensor entries of (7.1). For $p = 1, 2, \cdots NP$ independent current patterns, the identity (7.46) can be written as a $NP \times 7$ matrix system:

$$\begin{pmatrix} u_x^1 & u_y^1 & u_z^1 & u_{xx}^1 - u_{yy}^1 & u_{xy}^1 & u_{xz}^1 & -u_{yz}^1 \\ \vdots & & & \ddots & & & \vdots \\ u_x^{NP} & u_y^{NP} & u_z^{NP} & u_{xx}^{NP} - u_{yy}^{NP} & u_{xy}^{NP} & u_{xz}^{NP} & -u_{yz}^{NP} \end{pmatrix} \begin{pmatrix} s_1 \\ s_2 \\ s_3 \\ s_4 \\ s_5 \\ s_6 \\ s_7 \end{pmatrix} \frac{1}{\mu_0} \begin{pmatrix} \nabla^2 B_z^1 \\ \vdots \\ \nabla^2 B_z^{NP} \end{pmatrix} \tag{7.47}$$

where

$$\mathbf{s} = \begin{pmatrix} -\frac{\partial C_{xx}}{\partial y} + \frac{\partial C_{xy}}{\partial x} \\ -\frac{\partial C_{xy}}{\partial y} + \frac{\partial C_{yy}}{\partial x} \\ -\frac{\partial C_{xz}}{\partial y} + \frac{\partial C_{yz}}{\partial x} \\ C_{xy} \\ -C_{xx} + C_{yy} \\ C_{yz} \\ C_{xz} \end{pmatrix}$$

Here, u^p is the voltage distribution corresponding to the pth current injection, and $u_x^p = \frac{\partial u^p}{\partial x}$. The off-diagonal elements of the conductivity tensor can be obtained directly from Eq. (7.47) as

$$\begin{cases} C_{xy} = s_4 \\ C_{xz} = s_7 \\ C_{yz} = s_6 \end{cases} \tag{7.48}$$

In order to determine the first diagonal element C_{xx} of the symmetric positive definite system matrix in (7.1), one can solve the two-dimensional Poisson equation:

$$\begin{cases} \widetilde{\nabla}^2 C_{xx} = \frac{\partial s_2}{\partial x} - \frac{\partial s_1}{\partial y} - \frac{\partial^2 s_5}{\partial x^2} + \frac{\partial^2 s_4}{\partial x \partial y} + \frac{\partial^2 s_4}{\partial y^2} & \text{in } \Omega_t \\ C_{xx} = C_{xx,0} & \text{on } \partial\Omega_t \end{cases} \tag{7.49}$$

Similarly, the next diagonal element C_{yy} can be obtained from the known boundary conductivity $C_{yy,0}$

$$\begin{cases} \widetilde{\nabla}^2 C_{yy} = \frac{\partial s_2}{\partial x} - \frac{\partial s_1}{\partial y} + \frac{\partial^2 s_5}{\partial y^2} + 2\frac{\partial^2 s_4}{\partial x \partial y} & \text{in } \Omega_t \\ C_{yy} = C_{xx,0} + s_5 & \text{on } \partial\Omega_t \end{cases} \tag{7.50}$$

Finally, using the divergence free condition of the current density ($\nabla \cdot \mathbf{J} = 0$), the tensor entry C_{zz} component can be found using

$$\begin{pmatrix} u_z^1 & u_{zz}^1 \\ \vdots & \vdots \\ u_z^{NP} & u_{zz}^{NP} \end{pmatrix} \begin{pmatrix} \frac{\partial C_{zz}}{\partial z} \\ C_{zz} \end{pmatrix} = \begin{pmatrix} \psi^1 \\ \vdots \\ \psi^{NP} \end{pmatrix} \tag{7.51}$$

where

$$\psi^p = \frac{\partial J_x^p}{\partial x} + \frac{\partial J_y^p}{\partial y} - \frac{\partial}{\partial z}\left(C_{xz} u_x^p + C_{yz} u_y^p\right).$$

The x and y components of the current density J_x and J_y for the pth projection can be recovered using

$$\begin{cases} -J_x^p = C_{xx} u_x^p + C_{xy} u_y^p + C_{xz} u_z^p \\ -J_y^p = C_{xy} u_x^p + C_{yy} u_y^p + C_{yz} u_z^p \end{cases}$$

The value of C_{zz} depends on the previously computed C_{xx}, C_{xy}, C_{xz}, C_{yy}, and C_{yz} values and can therefore be obtained from Eq. (7.51).

In order to initiate the proposed anisotropic algorithm outlined in Eq. (7.47), Seo et al. suggested finding the voltage distribution u using an equivalent isotropic conductivity distribution, reconstructed using the harmonic B_z algorithm. This is a potential source of error in this algorithm. Although this method is in theory capable of reconstructing anisotropic conductivity distributions, it is so sensitive to noise that no experimental results have been reported. It nonetheless provides a useful platform for the discussion of subsequent algorithms.

7.5.2 Axial Anisotropic Conductivity Reconstruction Algorithm

Nam and Kwon [43] proposed an axial (transverse) anisotropic conductivity reconstruction algorithm, where the axial conductivity tensor is defined as $\mathbb{C}_a = \begin{bmatrix} C_{xx} & C_{xy} \\ C_{xy} & C_{yy} \end{bmatrix}$. The method is based on projected current density [50] data recovered from one component of the magnetic flux density. It requires data from two independent current injections.

From Ohm's law, we have (Eq. (7.45)):

$$\begin{aligned} -J_x &= C_{xx} u_x + C_{xy} u_y \approx -J_x^P \\ -J_y &= C_{xy} u_x + C_{yy} u_y \approx -J_y^P . \end{aligned} \tag{7.52}$$

For the $p = 1, 2$ independent current patterns, Eq. (7.52) can be written in matrix form as

$$\mathbf{U}\hat{\mathbb{C}} = \tilde{\mathbf{J}} \tag{7.53}$$

where

$$\mathbf{U} = \begin{pmatrix} u_x^1 & u_y^1 & 0 \\ 0 & u_x^1 & u_y^1 \\ u_x^2 & u_y^2 & 0 \\ 0 & u_x^2 & u_y^2 \end{pmatrix}, \qquad \hat{\mathbb{C}} = \begin{pmatrix} C_{xx} \\ C_{xy} \\ C_{yy} \end{pmatrix}$$

and, $$\tilde{\mathbf{J}} = -\begin{pmatrix} J_x^{P,1} \\ J_y^{P,1} \\ J_x^{P,2} \\ J_y^{P,2} \end{pmatrix}.$$

The regularized least-squares solution of Eq. (7.53) is

$$\hat{\mathbb{C}} = \left(\mathbf{U}^T \mathbf{U} + \kappa \mathbf{I}\right) \mathbf{U}^T \tilde{\mathbf{J}} \tag{7.54}$$

where κ is a regularization parameter, $\mathbf{U}^T$ is the transpose matrix of $\mathbf{U}$ and $\mathbf{I}$ denotes the 3×3

identity matrix. An inhomogeneous initial guess $\hat{\mathbb{C}}^0 = \sigma \mathbf{I}$, where σ is the equivalent isotropic conductivity estimated from the harmonic B_z algorithm [65], is used to initiate the reconstruction algorithm. It has been validated using a numerical phantom and a postmortem canine brain experiment with 40 mA current injection data [43].

7.5.3 Other Anisotropic Image Reconstruction Algorithms

Several other algorithms, originally proposed to find isotropic conductivity images, have been extended to include anisotropic imaging. For example, Değirmenci and Eyüboğlu [7] proposed an equipotential projection algorithm for reconstructing the axial anisotropic conductivity. Unlike the equipotential reconstruction method for isotropic conductivity reconstruction [28], this "equipotential projection" algorithm requires knowledge of both boundary conductivity and voltage data, since the current density vector field is not parallel to equipotential lines for anisotropic conductivity distribution cases (see Eq. (7.52)).

Sajib et al. [55] extended the dual-loop method [36] (see Sect. 7.4.6) to obtain an apparent orthotropic tensor $\mathbb{C}_o = \begin{bmatrix} C_{xx} & 0 \\ 0 & C_{yy} \end{bmatrix}$, using data from two linearly independent projected current densities $\mathbf{J}^{P,p}$, $p \in 1, 2$. Since the dual-loop method is sensitive to noise propagating along equipotential lines, an effective denoising method based on minimizing the total variation of the current density data was used as a preprocessing step. In [8, 9], Değirmenci and Eyüboğlu also extended the sensitivity-based matrix method (see Sect. 7.4) and harmonic B_z algorithms to find the orthotropic conductivity tensor distributions. For their anisotropic harmonic B_z algorithm, the identity in (7.55) was discretized using a forward difference approach:

$$\mu_0 \nabla^2 B_z = -\frac{\partial C_{xx}}{\partial y} u_x + \frac{\partial C_{yy}}{\partial x} u_y - (C_{xx} - C_{yy}) u_{xy}. \tag{7.55}$$

The conductivity at internal nodes was then reconstructed using model-predicted u data and the known boundary conductivities.

7.6 Diffusion Tensor Magnetic Resonance Electrical Impedance Tomography: DT-MREIT

The performance of all anisotropic MREIT conductivity reconstruction methods described in Sect. 7.5 is limited by the number of measurements and the fact that J_z cannot be measured, as well as the presence of measurement noise (see Sect. 7.3). Diffusion tensor magnetic resonance electrical impedance tomography (DT-MREIT) is an alternative that uses prior information collected by another MRI technique, diffusion tensor imaging, to aid recovery of the components of the anisotropic conductivity tensor (7.1). By neglecting the intracellular diffusion coefficient d_i in Eq. (7.3) and assuming that conductivity and diffusion tensor share the same eigenvectors, the conductivity tensor reconstructed in DT-MREIT is expressed as [71]

$$\mathbb{C} \approx \eta \mathbb{D} \tag{7.56}$$

where $\mathbb{D}$ is the water diffusion tensor measured using diffusion-weighted imaging methods [1] and given by the 3×3 symmetric positive definite matrix:

$$\mathbb{D} = \begin{pmatrix} D_{xx} & D_{xy} & D_{xz} \\ D_{xy} & D_{yy} & D_{yz} \\ D_{xz} & D_{yz} & D_{zz} \end{pmatrix} \tag{7.57}$$

The variable $\eta := \frac{\sigma_e}{d_e}$ determined at each location is called the effective conductivity to diffusivity ratio (ECDR) or simply the "scale factor." The extracellular conductivity may be affected by several factors, including ionic composition, medium viscosity, and extracellular volume fraction. The goal of the DT-MREIT technique is to reconstruct the position-dependent scale fac-

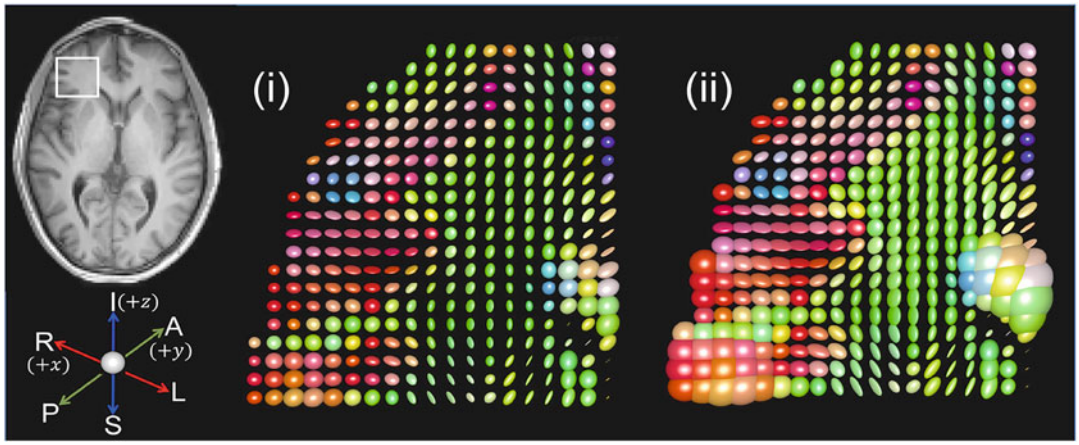

Fig. 7.7 In vivo human brain DT-MREIT experimental results [5]. The image at left displays the location of a brain ROI overlaid with a T_1-weighted MR magnitude image. Reconstructed conductivity tensor images within the ROI outlined are shown using (i) position-dependent [30, 39] and (ii) global scaling factors [71]. The tensors representing each voxel are shown as ellipsoids with semi-axial radii of each ellipsoid proportional to conductivity eigenvalues. Ellipsoidal axes are oriented along eigenvector directions, and colors indicate orientation of the principal eigenvector

tor distribution from measured diffusion tensors combined with magnetic flux density data.

To reconstruct scale factor distributions, methods such as the direct-inversion (also known as non-iterative DT-MREIT) algorithm and diffusion-weighted J-substitution algorithm have been developed. We briefly explain these methods below (Fig. 7.7).

7.6.1 Non-iterative DT-MREIT Algorithm

Ohm's law expressed for the case of an anisotropic medium, $\mathbf{J} = -\mathbb{C}\nabla u = -\eta\mathbb{D}\nabla u$, gives rise to the following relation [30]:

$$\nabla\times(\mathbb{D}^{-1}\mathbf{J}) = -\frac{\nabla\eta}{\eta}\times(\eta\nabla u) = \nabla\log\eta\times(\mathbb{D}^{-1}\mathbf{J}). \tag{7.58}$$

For $NP = 2$ independent current injections, the non-iterative DT-MREIT algorithm reconstructs an image of the scale factor distribution η by solving the following linear system of equations:

$$\begin{pmatrix} \left(\mathbb{D}^{-1}\mathbf{J}^1\right)_y & -\left(\mathbb{D}^{-1}\mathbf{J}^1\right)_x \\ \left(\mathbb{D}^{-1}\mathbf{J}^2\right)_y & -\left(\mathbb{D}^{-1}\mathbf{J}^2\right)_x \end{pmatrix} \begin{pmatrix} \frac{\partial\log\eta}{\partial x} \\ \frac{\partial\log\eta}{\partial y} \end{pmatrix} = \begin{pmatrix} \frac{\partial\left(\mathbb{D}^{-1}\mathbf{J}^1\right)_y}{\partial x} - \frac{\partial\left(\mathbb{D}^{-1}\mathbf{J}^1\right)_x}{\partial y} \\ \frac{\partial\left(\mathbb{D}^{-1}\mathbf{J}^2\right)_y}{\partial x} - \frac{\partial\left(\mathbb{D}^{-1}\mathbf{J}^2\right)_x}{\partial y} \end{pmatrix} \tag{7.59}$$

In [30] full current density data $\mathbf{J}^p$ for $p = 1, 2$ are replaced by the projected current density $\mathbf{J}^{P,p}$ computed using the measured $B_z^{m,p}$. In [30] the regularized least-squares solution is obtained via regularization as

$$\widetilde{\nabla}\ln\eta = \left(\mathbf{A}^T\mathbf{A} + \frac{\kappa}{|\mathbf{A}^T\mathbf{A}|}\mathbf{I}\right)\mathbf{A}^T\mathbf{b} \tag{7.60}$$

where κ is a regularization constant and $\mathbf{I}$ is the 2×2 identity matrix. From (7.60), the stiff matrix $\mathbf{A}$ and corresponding load vector $\mathbf{b}$ are defined as

$$\mathbf{A} = \begin{pmatrix} \left(\mathbb{D}^{-1}\mathbf{J}^{P,1}\right)_y & -\left(\mathbb{D}^{-1}\mathbf{J}^{P,1}\right)_x \\ \left(\mathbb{D}^{-1}\mathbf{J}^{P,2}\right)_y & -\left(\mathbb{D}^{-1}\mathbf{J}^{P,2}\right)_x \end{pmatrix}$$

and,

$$\mathbf{b} = \begin{pmatrix} \frac{\partial\left(\mathbb{D}^{-1}\mathbf{J}^{P,1}\right)_y}{\partial x} - \frac{\partial\left(\mathbb{D}^{-1}\mathbf{J}^{P,1}\right)_x}{\partial y} \\ \frac{\partial\left(\mathbb{D}^{-1}\mathbf{J}^{P,2}\right)_y}{\partial x} - \frac{\partial\left(\mathbb{D}^{-1}\mathbf{J}^{P,2}\right)_x}{\partial y} \end{pmatrix}$$

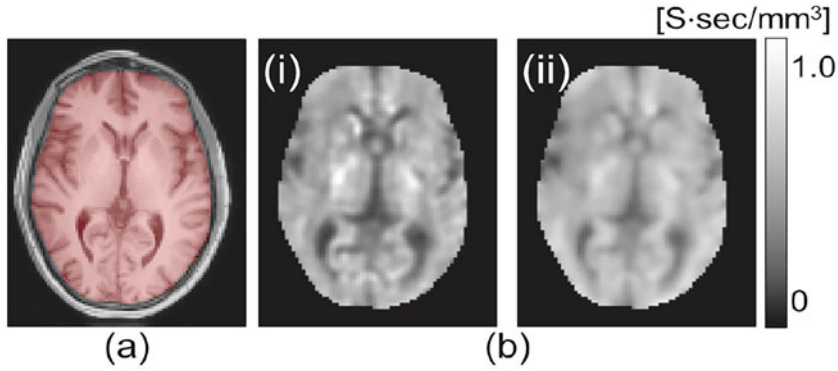

Fig. 7.8 Example of reconstructed scale factor images from an in vivo human brain experiment [5]. (**a**) T1-weighted MR magnitude image overlaid with brain mask. (**b**) (i) and (ii) Reconstructed scale factor from (7.60) found by optimizing the GCV function in (7.63). The GCV function was minimized using 3×3 neighbourhood information

Ma et al. [39] also proposed an algorithm to reconstruct $\widetilde{\nabla} \ln \eta$ using two independent current data $I^p,\ p \in 1, 2$, via

$$\widetilde{\nabla} \ln \eta = a_1 \left(\mathbb{D}^{-1}\mathbf{J}^1\right) + a_2 \left(\mathbb{D}^{-1}\mathbf{J}^2\right) + a_3 \left(\mathbb{D}^{-1}\mathbf{J}^1 \times \mathbb{D}^{-1}\mathbf{J}^2\right) \tag{7.61}$$

For independent current injections, the coefficients in (7.61) take the form

$$\begin{cases} a_1 = \frac{(\nabla \times \mathbb{D}^{-1}\mathbf{J}^2)\cdot(\mathbb{D}^{-1}\mathbf{J}^1 \times \mathbb{D}^{-1}\mathbf{J}^2)}{|\mathbb{D}^{-1}\mathbf{J}^1 \times \mathbb{D}^{-1}\mathbf{J}^2|^2} \\ a_2 = \frac{(\nabla \times \mathbb{D}^{-1}\mathbf{J}^1)\cdot(\mathbb{D}^{-1}\mathbf{J}^2 \times \mathbb{D}^{-1}\mathbf{J}^1)}{|\mathbb{D}^{-1}\mathbf{J}^1 \times \mathbb{D}^{-1}\mathbf{J}^2|^2} \\ a_3 = \frac{(\nabla \times \mathbb{D}^{-1}\mathbf{J}^2)\cdot(\mathbb{D}^{-1}\mathbf{J}^2)}{|\mathbb{D}^{-1}\mathbf{J}^1 \times \mathbb{D}^{-1}\mathbf{J}^2|^2} \end{cases} \tag{7.62}$$

Ma et al. [39] conducted an experiment using a pineapple phantom to experimentally demonstrate the method. Instead of reconstructing projected current density from $B_z^{m,p},\ p \in 1, 2$, they measured full current density vectors by rotating the pineapple. The η were then reconstructed from the estimated $\widetilde{\nabla} \ln \eta$ and known boundary scale factor values at the boundary by solving Poisson's equation (7.33) (modified to solve for logged quantities).

The regularization constant κ in (7.60) at each pixel position may be determined by minimizing the generalized cross-validation (GCV) function (Fig. 7.8) [58],

$$GCV(\kappa) = \frac{\sum_{i=1}^{2} \left(\frac{\hat{b}_i}{s_i^2 + \kappa}\right)^2}{\left(\sum_{i=1}^{2} \frac{1}{s_i^2 + \kappa}\right)^2}. \tag{7.63}$$

Here, $s_i,\ i \in 1, 2$ are the two singular values ($U \Sigma V^T$) of the $2N \times 2$ stiff matrix $\tilde{\mathbf{A}}$ defined at the neighbourhood $\mathcal{N}_{(x,y)} = \{(x_i, y_i) \in 1, 2 \cdots N\}$ around the pixel position (x, y) as

$$\tilde{\mathbf{A}} = \begin{pmatrix} w_1 \mathbf{J}^1_{\mathbb{D}y}(x_1, y_1) & -w_1 \mathbf{J}^1_{\mathbb{D}x}(x_1, y_1) \\ w_1 \mathbf{J}^2_{\mathbb{D}y}(x_1, y_1) & -w_1 \mathbf{J}^2_{\mathbb{D}x}(x_1, y_1) \\ \vdots & \vdots \\ w_N \mathbf{J}^1_{\mathbb{D}y}(x_N, y_N) & -w_N \mathbf{J}^1_{\mathbb{D}x}(x_N, y_N) \\ w_N \mathbf{J}^2_{\mathbb{D}y}(x_N, y_N) & -w_N \mathbf{J}^2_{\mathbb{D}x}(x_N, y_N) \end{pmatrix} \tag{7.64}$$

The *pseudocurrent*.[1] $\mathbf{J}^p_{\mathbb{D}} = \mathbb{D}^{-1}\mathbf{J}^{P,p},\ p \in 1, 2$ and the $\hat{b} = U^T \tilde{\mathbf{b}}$. The load vector $\tilde{\mathbf{b}}$ can be found as

[1] The term *pseudocurrent* was first introduced by Ma et al. [39].

$$\tilde{\mathbf{b}} = \begin{pmatrix} w_1 \left(\frac{\partial \mathbf{J}^1_{\mathbb{D}_y}(x_1,y_1)}{\partial x} - \frac{\partial \mathbf{J}^1_{\mathbb{D}_x}(x_1,y_1)}{\partial y} \right) \\ w_1 \left(\frac{\partial \mathbf{J}^2_{\mathbb{D}_y}(x_1,y_1)}{\partial x} - \frac{\partial \mathbf{J}^2_{\mathbb{D}_x}(x_1,y_1)}{\partial y} \right) \\ \vdots \\ w_N \left(\frac{\partial \mathbf{J}^1_{\mathbb{D}_y}(x_N,y_N)}{\partial x} - \frac{\partial \mathbf{J}^1_{\mathbb{D}_x}(x_N,y_N)}{\partial y} \right) \\ w_N \left(\frac{\partial \mathbf{J}^2_{\mathbb{D}_y}(x_N,y_N)}{\partial x} - \frac{\partial \mathbf{J}^2_{\mathbb{D}_x}(x_N,y_N)}{\partial y} \right) \end{pmatrix}. \tag{7.65}$$

The weight w_i is related to the MR magnitude ρ and the noise level h associated with the measured B_z^m via

$$w_i = \frac{e^{-h||\rho(x_i,y_i)-\rho(x,y)||}}{\sum_{J=1}^{N} e^{-h||\rho(x_j,y_j)-\rho(x,y)||}}. \tag{7.66}$$

The denominator in Eq. (7.66) guarantees that $w_i \leq 1$. The reconstruction process flow diagram shown in Appendix 1 uses the method in Kwon et al. [30].

7.6.2 Diffusion-Weighted *J*-Substitution Algorithm

The conductivity tensor image reconstruction in DT-MREIT can also be performed by adopting a J-substitution approach [17]. For NP independent current injections I_p for $p = 1, \cdots, NP$, the diffusion-weighted J-substitution algorithm iteratively updates the conductivity tensor as

$$\mathbb{C}^{k+1} = -\left(\frac{\sum_{p=1}^{NP} \langle \mathbf{J}^{P,p}, \mathbb{D}\nabla u^{k,p} \rangle}{\sum_{p=1}^{NP} \langle \mathbb{D}\nabla u^{k,p}, \mathbb{D}\nabla u^{k,p} \rangle} \right) \mathbb{D} \tag{7.67}$$

where $u^{k,p}$ is a solution of (7.15) with the tensor estimate at the kth iteration $\mathbb{C}^k$ substituted for σ and $\mathbf{J}^{P,p}$ is the computed projected current density using the measured $B_z^{m,p}$, $p \in 1, 2$ data. Using this algorithm, Jeong et al. [17] determined in vivo brain conductivity tensor distributions for two canine subjects. A homogeneous initial guess $\eta^0 = 0.7735$ S·s/mm^3 was used [70] to initiate the canine brain reconstruction. However, as noted in [57], the choice of initial guess only affects the number of iterations required to ensure convergence. Recently, Lee et al. [38] demonstrated that this method could reconstruct electrical conductivity tensor images using single-current administration data. The kth update of the scale factor η^{k+1} using "single-current-diffusion-weighted J-substitution" can be found as [38]

$$\eta^{k+1}(\mathbf{r}) = -\frac{\left(\sum_{\mathbf{r}_i \in \mathcal{N}_{(x,y)}} w_i \mathbf{J}^p(\mathbf{r}_i) \right) \cdot \left(\sum_{\mathbf{r}_i \in \mathcal{N}_{(x,y)}} w_i \nabla u^k(\mathbf{r}_i) \right)}{\left(\sum_{\mathbf{r}_i \in \mathcal{N}_{(x,y)}} w_i \mathbb{D}(\mathbf{r}_i) \nabla u^k(\mathbf{r}_i) \right) \cdot \left(\sum_{\mathbf{r}_i \in \mathcal{N}_{(x,y)}} w_i \nabla u^k(\mathbf{r}_i) \right)} \tag{7.68}$$

The weighting function w_i is defined within pixels in the neighbourhood of each point $\mathbf{r}_i$, $\mathcal{N}_{(x,y)} = \{\mathbf{r}_i = (x_i, y_i) \in 1, 2, \cdots N\}$ and depends on the noise level in measured data (see Eq. (7.66)). The two-current administration version of the conductivity tensor reconstruction process using the diffusion-weighted J-substitution algorithm is described in Appendix 2.

7.7 Image Reconstruction Toolbox

The Impedance Imaging Research Center (IIRC), Korea (`http://iirc.khu.ac.kr`), developed a software toolbox for isotropic and equivalent isotropic conductivity reconstruction called CoReHA (conductivity reconstructor using harmonic algorithm) [15]. The methods implemented in CoReHA are based on the harmonic B_z algorithm [46, 65]. This software includes three major components:

- *Preprocessing*: Experimentally obtained magnetic flux density data often contain noise due to numerous factors. The toolbox provides preprocessing steps that can be used to denoise the $B_z^{m,p}$, $p = 1, 2$ data using techniques such as ramp-preserving denoising [37].
- *Model construction*: As described in Sect. 7.3, model construction is an essential step in conductivity reconstruction. CoReHA uses MR magnitude images to make models of the ob-

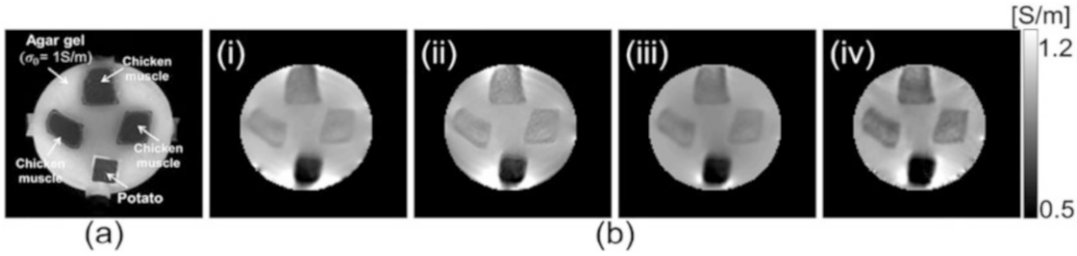

Fig. 7.9 Example of reconstructed equivalent isotropic conductivity in a biological tissue phantom. (**a**) MR magnitude images show distribution of biological tissue. The phantom was filled with an agar-gel background material that had isotropic conductivity $\sigma_0 = 1$ S/m. A detailed description of the phantom can be found in Chap. 4. (**b**) Reconstructed conductivity images using (i) J-substitution (see Sect. 7.4.2), (ii) J^T-substitution (see Sect. 7.4.4), (iii) harmonic B_z (see Sect. 7.4.3), and (iv) non-iterative harmonic B_z (see Sect. 7.4.5) algorithms. The MATLAB-based `mrci`-toolbox functions [57], `mrci_J_substitution.m`, `mrci_JT_substitution.m`, `mrci_harmonic_Bz.m`, and `mrci_noniterative_harmonic_Bz.m` were used to reconstruct images

ject geometry and electrodes. Users can use a level-set-based semiautomated segmentation tool to extract the boundary geometry and electrode locations. This software also allows the user to define source and sink electrodes and current amplitudes depending on the experimental conditions. An additional manual segmentation tool is also provided in this software so that the user can define a region of interest (ROI) for local conductivity estimation. The software then uses the experimental boundary conditions to solve the two-dimensional Laplace equation in (7.15) using the finite element method.

- *Conductivity image reconstruction*: In CoReHA, conductivity images are reconstructed using the harmonic B_z algorithm. To apply this algorithm, it is essential to calculate the $\nabla^2 B_z^{m,p}$, $p \in 1, 2$. To calculate the three-dimensional Laplacian $\nabla^2 : \left(\frac{\partial^2}{\partial x^2}, \frac{\partial^2}{\partial y^2}, \frac{\partial^2}{\partial z^2}\right)$, the software requires data from three consecutive slices. In many experimental situations, only one slice of data may be collected. Because of this, CoReHA allows both two- and three-dimensional Laplacian calculations to be made. CoReHA users can also reconstruct the conductivity within a chosen ROI using the local harmonic B_z algorithm [67].

The major limitation of CoReHA software is that users can only implement the harmonic B_z algorithm and the software is not extensible. To facilitate adoption of other algorithms, newer software called the MR-based conductivity imaging (MRCI) toolbox was developed [57] by the IIRC. This MATLAB-based toolbox was originally released with 11 functions. Among these, three functions implement current density image reconstructions. For isotropic imaging, the software implements the projected-current-density-based J-substitution, non-iterative harmonic B_z algorithms, and transversal J-substitution algorithms as well as the harmonic B_z algorithm (Fig. 7.9). Two functions, the non-iterative DT-MREIT method and the diffusion-weighted J-substitution algorithm, are also included in this software toolbox to enable reconstruction of anisotropic conductivity images. Note that instead of diffusion-weighted MRI data, the user must provide reconstructed diffusion tensor data, because there are many algorithms available to compute $\mathbb{D}$. For many algorithms it is necessary to solve the two-dimensional Poisson equation (7.33). A function using the central finite-difference method named "`mrci_poisson_solver2D.m`" was also included in the toolbox to reconstruct conductivity or scale factor images. However,

this software does not include any forward solver to solve the Poisson equation (7.15). For that purpose the user may use any commercially available finite element software integrated with MATLAB such as COMSOL Multiphysics (MLI, COMSOL Inc, Burlington, MA, USA) or custom finite element implementations. Both CoReHA and the MRCI toolbox are free for non commercial use and are available at http://iirc.khu.ac.kr.

```
   function sigma =
mrci_harmonic_Bz(gradU, Bz,
reconstruction_parameters)

% gradU[M×N×2×E]: calculated two-
dimensional gradient of voltage
% where,
% ux = gradU(:,:,1,:), uy =
gradU(:,:,2,:).
% Bz[M×N×E]: measured Bz data.
% sigma[M×N]: reconstructed conductivity
image.

function C = mrci_dtmreit_noniterative(J,
D, reconstruction_parameters)

 % J[M×N×3×E]: estimated current
density image.
 % where,
 % Jx = J(:,:,1,:), Jy = J(:,:,2,:), and
Jz = J(:,:,3,:).
 % D[M×N×6]: water diffusion tensor
image.
 % where,
 % Dxx = D(:,:,1), Dxy = D(:,:,2),
Dxz = D(:,:,3), Dyy = D(:,:,4), Dyz =
D(:,:,5),and Dzz = D(:,:,6).
 % C[M×N×6]: reconstructed conductivity
tensor image.
```

7.8 Conclusion

The importance and promise of low-frequency electrical conductivity imaging is enormous. Since low-frequency electrical conductivity is affected by ion concentration mobility [56], it could potentially provide a new window for diagnostic techniques. Recently, Kim et al. [25] have demonstrated that MREIT methods could be useful for early detection of liver diseases. This technique is also useful for monitoring the electromagnetic field distribution for electrical brain stimulation [60]. The MREIT electrical conductivity reconstruction problem is generally a complex mathematical procedure. In this chapter, we therefore presented several reconstruction algorithms, to illustrate the range of approaches that can be adopted and to identify those that have proven practical. The algorithms described in this chapter have mostly already been validated using phantom and in vivo animal and human imaging data. We hope that this chapter will provide an essential guide to the researcher working in this field and those developing novel algorithms.

Appendix 1

See Fig. 7.10.

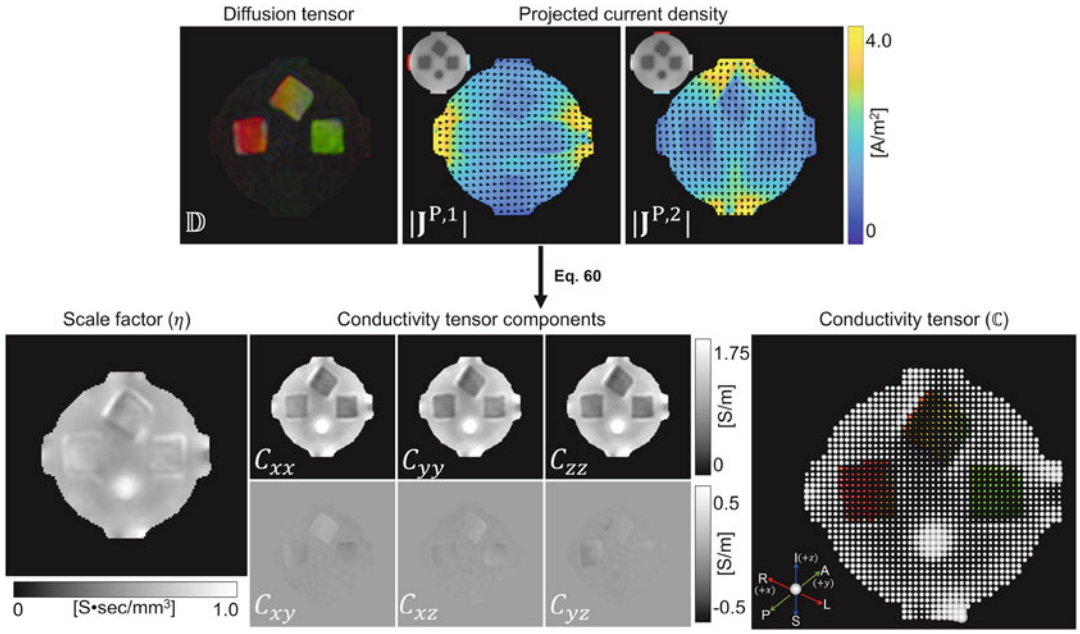

Fig. 7.10 Flow diagram for conductivity tensor reconstruction process using the non-iterative DT-MREIT algorithm [30]. The top row displays the measured diffusion tensor and reconstructed projected current density induced due to noncollinear current flow inside the imaging object which are used as an input to the algorithm. The bottom-left figure shows the reconstructed scale factor image obtained after solving the equation (7.60) described in Sect. 7.6.1. The reconstructed conductivity tensor components obtained from the scale factor and measured diffusion tensor are displayed in the middle column of the bottom row. The conductivity tensor is displayed at the bottom-right panel. Conductivity tensor of each voxel is represented by tri-axial ellipsoids. The radii of each ellipsoid are proportional to the eigenvalues, and their axes are oriented along the directions of the eigenvectors. The colors of the ellipsoid shown in the top-middle panel indicate the orientation of the principle eigenvector.

Appendix 2

See Fig. 7.11.

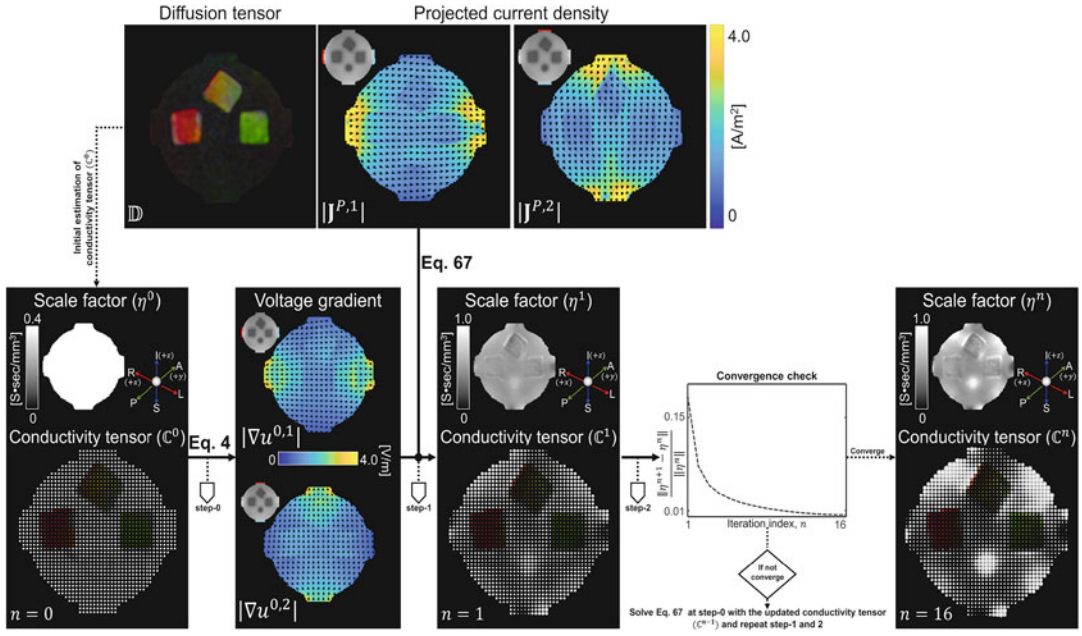

Fig. 7.11 Flow diagram for conductivity tensor reconstruction process using iterative DT-MREIT algorithm described in Jeong et al. [17]. The top row displays the measured diffusion tensor and reconstructed projected current density induced due to noncollinear current flow inside the imaging object. These images were used as an input to the algorithm. A global scale factor of $\eta^0 = 0.4\,\mathrm{S}\cdot\mathrm{s/mm}^3$ was used to obtain the initial $\mathbb{C}^0$ distribution. The Laplace Eq. (7.4a) subject to the same boundary conditions was also solved to calculate the ∇u distribution. The $\mathbf{J}^P$, $\mathbb{D}$ and ∇u information was used to update the scale factor and the corresponding conductivity tensor (7.67). The process was repeated until the solution converged. The bottom-right image displays the reconstructed scale factor and conductivity tensor at iteration number (n) 16.

References

1. P.J. Basser, J. Mattiello, D. LeBihan, MR diffusion tensor spectroscopy and imaging. Biophys. J. **66**, 256–67 (1994)
2. O. Brigul, Y.Z. Ider, Use of the magnetic field generated by the internal distribution of injected currents for electrical impedance tomography, in *Proceedings of the 9th International Conference on Electrical Bio-Impedance* (1995), pp. 418–419
3. O. Brigul, Y.Z. Ider, Electrical impedance tomography using the magnetic field generated by injected currents, in *Proceedings of the 18th Annual International Conference on IEEE Engineering in Medicine and Biology Society* (IEEE EMBC, 1996), pp. 784–785
4. O. Birgul, B.M. Eyüboğlu, Y.Z. Ider, Current constrained voltage scaled reconstruction (CCVSR) algorithm for MR-EIT and its performance with different probing current patterns. Phys. Med. Biol. **6**, 215–225 (1998)
5. M. Chauhan, A. Indahlastari, A.K. Kasinadhuni, M. Schär, T.H. Mareci, R.J. Sadleir, Low-frequency conductivity tensor imaging of the human head *in vivo* using DT-MREIT: first study. IEEE Trans. Med. Imaging **37**, 966–976 (2018)
6. A.J. Davis, *The Finite Element Method: A First Approach* (Oxford University Press, 1980)
7. E. Değirmenci, B.M. Eyüboğlu, Anisotropic conductivity imaging with MREIT using equipotential projection algorithm. Phys. Med. Biol. **52**, 7229–7242 (2007)
8. E. Değirmenci, B.M. Eyüboğlu, Image reconstruction in magnetic resonance conductivity tensor imaging (MRCTI). IEEE Trans. Med. Imaging **31**, 525–532 (2012)
9. E. Değirmenci, B.M. Eyüboğlu, Practical realization of magnetic resonance conductivity tensor imaging (MRCTI). IEEE Trans. Med. Imaging **32**, 601–608 (2013)
10. N.S. Gao, A. Zhu, B. He, A new magnetic resonance electrical impedance tomography (MREIT) algorithm: the RSM-MREIT algorithm with applications to estimation of human head conductivity. Phys. Med. Biol. **51**, 3067–3083 (2006)
11. C. Göksu, K. Scheffler, H.R. Siebner, A. Thielscher, L.G. Hanson, The stray magnetic fields in magnetic resonance current density imaging (MRCDI). Phys. Med. **59**, 142–50 (2019)
12. S. Grimnes, O.G. Martinsen, *Bioimpedance and Bioelectricity Basics* (Academic Press, Waltham, 2015)
13. Y.Z. Ider, S. Onart, Algebric reconstruction for 3D magnetic resonance electrical impedance tomography (MREIT) using one component of magnetic flux density. Physiol. Meas. **25**, 281–294 (2004)
14. Y.Z. Ider, S. Onart, W.R.B. Lionheart, Uniqueness and reconstruction in magnetic resonance electrical impedance tomography (MREIT). Physiol. Meas. **24**, 591–604 (2003)
15. K. Jeon, C.O. Lee, Coreha 2.0: a software package for *in vivo* MREIT experiments. Comput. Math. Methods Med. **2013**, 941745 (8 pages) (2013)
16. W.C. Jeong, M. Chauhan, S.Z.K. Sajib, H.J. Kim, I. Serša, O.I. Kwon, E.J. Woo, Optimization of magnetic flux density measurement using multiple RF receiver coils and multi-echo in MREIT. Phys. Med. Biol. **59**, 4827–4844 (2014)
17. W.C. Jeong, S.Z.K. Sajib, K. Nitish, H.J. Kim, O.I. Kwon, E.J. Woo, Anisotropic conductivity tensor imaging of *in vivo* canine brain using DT-MREIT. IEEE Trans. Med. Imaging **36**, 124–131 (2017)
18. M.L.G. Joy, G.C. Scott, R.M. Henkelman, *In vivo* detection of applied electric currents by magnetic resonance imaging. Magnetic Resonance Imaging **7**, 89–94 (1989)
19. H.S. Khang, B.I. Lee, S.H. Oh, E.J. Woo, S.Y. Lee, M.H. Cho, O.I. Kwon, J.R. Yoon, J.K. Seo, *J*-substitution algorithm in magnetic resonance electrical impedance tomography (MREIT): Phantom experiments for static resistivity images. IEEE Trans. Med. Imaging **21**, 695–702 (2002)
20. Y.J. Kim, O.I. Kwon, J.K. Seo, E.J. Woo, Uniqueness and convergence of conductivity image reconstruction in magnetic resonance electrical impedance tomography. Inverse Prob. **19**, 1213–1225 (2003)
21. H.J. Kim, B.I. Lee, Y. Cho, Y.T. Kim, B.T. Kang, H.M. Park, S.Y. Lee, J.K. Seo, E.J. Woo, Conductivity imaging of canine brain using a 3 T MREIT system: postmortem experiments. Physiol. Meas. **28**, 1341–1353 (2007)
22. H.J. Kim, T.I. Oh, Y.T. Kim, B.I. Lee, E.J. Woo, J.K. Seo, S.Y. Lee, O.I. Kwon, C. Park, B.T. Kang, *In vivo* electrical conductivity imaging of a canine brain using a 3 T MREIT system. Physiol. Meas. **29**, 1145–1155 (2008)
23. H.J. Kim, Y.T. Kim, A.S. Minhas, W.C. Jeong, E.J. Woo, J.K. Seo, O.I. Kwon, *In vivo* high resolution conductivity imaging of the human leg using MREIT: the first human experiment. IEEE Trans. Med. Imaging **28**, 1681–1687 (2009)
24. H.J. Kim, Saurav Z. K. S., W. C. Jeong, M. N. Kim, O. Kwon, and E. J. Woo. Analysis of local projected current density from one component of magnetic flux density in MREIT. Inverse Prob. **29**, 075001 (2013)
25. J.W. Kim, H.B. Kim, Y.J. Hue, N. Choi, B.K. Katoch, J.A. Park, H.J. Kim, E.J. Woo, MR-based electrical conductivity imaging of liver fibrosis in an experimental rat model. J. Magn. Resonance Imaging **53**, 554–63 (2021)
26. M. Kranjc, F. Bajd, I. Serša, D. Miklavčič, Magnetic resonance electrical impedance tomography for monitoring electric field distribution during tissue electroporation. IEEE Trans. Med. Imaging **30**, 1771–1778 (2011)
27. M. Kranjc, B. Markelc, F. Bajd, M. Čemažar, I. Serša, T. Blagus, D. Miklavčič, *In situ* monitoring of electric field distribution in mouse tumor during electroporation. Radiology **274**, 115–123 (2015)

28. O.I. Kwon, J.Y. Lee, J.R. Yoon, Equipotential line method for magnetic resonance electrical impedance tomography. Inverse Prob. **18**, 1089–1100 (2002)
29. O.I. Kwon, E.J. Woo, J.R. Yoon, J.K. Seo, Magnetic resonance electrical impedance tomography (MREIT): simulation study of *J*-substitution algorithm. IEEE Trans. Biomed. Eng. **49**, 160–167 (2002)
30. O.I. Kwon, W.C. Jeong, S.Z.K. Sajib, H.J. Kim, E.J. Woo, Anisotropic conductivity tensor imaging in MREIT using directional diffusion rate of water molecules. Phys. Med. Biol. **59**, 2955–2974 (2014)
31. O. Kwon, S.Z.K. Sajib, I. Serša, Y.I. Oh, W.C. Jeong, H.J. Kim, E.J. Woo, Current density imaging during transcranial direct current stimulation (tDCS) using DT-MRI and MREIT: algorithm development and numerical simulations. IEEE Trans. Biomed. Eng. **63**, 168–175 (2016)
32. B.I. Lee, S.H. Oh, E.J. Woo, S.Y. Lee, M.H. Cho, O. Kwon, J.K. Seo, W.S. Baek, Static resistivity image of a cubic saline phantom in magnetic resonance electrical impedance tomography (MREIT). Physiol. Meas. **24**, 579–589 (2003)
33. B.I. Lee, S.H. Oh, E.J. Woo, S.Y. Lee, M.H. Cho, O. Kwon, J.K. Seo, J.Y. Lee, W.S. Baek, Three-dimensional forward solver and its performance analysis in magnetic resonance electrical impedance tomography (MREIT) using recessed electrodes. Phys. Med. Biol. **48**, 1971–1986 (2003)
34. B.I. Lee, S.H. Lee, T.S. Kim, O.I. Kwon, E.J. Woo, J.K. Seo, Harmonic decomposition in PDE-based denoising technique for magnetic resonance electrical impedance tomography. IEEE Trans. Biomed. Eng. **52**, 1912–1920 (2005)
35. B.I. Lee, S.H. Oh, T.S. Kim, E.J. Woo, S.Y. Lee, O. Kwon, J.K. Seo, Basic setup for breast conductivity imaging using magnetic resonance electrical impedance tomography. Phys. Med. Biol. **51**, 443–455 (2006)
36. T.H. Lee, H.S. Nam, M.G. Lee, Y.J. Kim, E.J. Woo, O.I. Kwon, Reconstruction of conductivity using the dual-loop method with one injection current in MREIT. Phys. Med. Biol. **55**, 7523–7539 (2010)
37. C.O. Lee, K. Jeon, S. Ahn, H.J. Kim, E.J. Woo, Ramp-preserving denoising for conductivity image reconstruction in magnetic resonance electrical impedance tomography. IEEE Trans. Biomed. Eng. **58**, 2038–50 (2011)
38. M.B. Lee, H.J. Kim, E.J. Woo, O.I. Kwon, Anisotropic conductivity tensor imaging for transcranial direct current stimulation (tDCS) using magnetic resonance diffusion tensor imaging (MR-DTI). PLoS One **13**, e0197063 (2018)
39. W. Ma, T.P. DeMonte, A.I. Nachman, N.M.H. Elsaid, M.L.G. Joy, Experimental implementation of a new method of imaging anisotropic electric conductivities (2013), pp. 6437–6440
40. A.S. Minhas, H.H. Kim, Z.J. Meng, Y.T. Kim, H.J. Kim, E.J. Woo, Three-dimensional MREIT simulator of static bioelectromagnetism and MRI. Biomed. Eng. Lett. **1**, 129–136 (2011)
41. A.S. Minhas, Y.T. Kim, P.J. Yoo, T.I. Oh, E.J. Woo, Experimental performance evaluation of multi-echo ICNE pulse sequence in magnetic resonance electrical impedance tomography. Magn. Resonance Med. **66**, 957–965 (2011)
42. L.T. Muftuler, M. Hamamura, O. Birgul, O. Nalcioglu, Resolution and contrast in magnetic resonance electrical impedance tomography (MREIT) and its application to cancer imaging. Technol. Cancer Res. Treatment **3**, 599–609 (2004)
43. H.S. Nam, O.I. Kwon, Axial anisotropic conductivity imaging based on projected current density in MREIT. IEEE Trans. Med. Imaging **29**, 781–789 (2010)
44. H.S. Nam, B.I. Lee, J. Choi, C. Park, O.I. Kwon, Conductivity imaging with low level current injection using transversal *J*-substitution algorithm in MREIT. Phys. Med. Biol. **52**, 6717–6730 (2007)
45. H.S. Nam, C. Park, O.I. Kwon, Non-iterative conductivity reconstruction algorithm using projected current density in MREIT. Phys. Med. Biol. **53**, 6947–6961 (2008)
46. S.H. Oh, B.I. Lee, E.J. Woo, S.Y. Lee, M.H. Cho, O. Kwon, J.K. Seo, Conductivity and current density image reconstruction using harmonic B_z algorithm in magnetic resonance electrical impedance tomography. Phys. Med. Biol. **48**, 3101–3116 (2003)
47. S.H. Oh, B.I. Lee, T.S. Park, S.Y. Lee, E.J. Woo, M.H. Cho, J.K. Seo, O.I. Kwon, Magnetic resonance electrical impedance tomography at 3 Tesla field strength. Magn. Resonance Med. **51**, 1292–1296 (2004)
48. S.H. Oh, B.I. Lee, E.J. Woo, S.Y. Lee, T.S. Kim, O. Kwon, J.K. Seo, Electrical conductivity images of biological tissue phantoms in MREIT. Physiol. Meas. **26**, S279–S288 (2005)
49. T.I. Oh, W.C. Jeong, J.E. Kim, S.Z.K. Sajib, H.J. Kim, O.I. Kwon, E.J. Woo, Noise analysis in fast magnetic resonance electrical impedance tomography (MREIT) based on spoiled multi gradient echo (spmge) pulse sequence. Phys. Med. Biol. **59**, 4723–4738 (2014)
50. C. Park, B.I. Lee, O. Kwon, Analysis of recoverable current from one component of magnetic flux density in MREIT. Phys. Med. Biol. **52**, 3001–3013 (2007)
51. B.J. Roth, N.G. Sepulveda, J.P. Wikswo, Using a magnetometer to image a two dimensional current distribution. J. Appl. Phys. **65**, 361 (1989)
52. M. Rullmann, A. Anwander, M. Dannhauer, S.K. Waefield, F.H. Fuffy, C.H. Wolters, EEG source analysis of epileptiform activity using a 1 mm anisotropic hexahedra finite element head model. NeuroImage **44**, 390–410 (2009)
53. R.J. Sadleir, S.U. Grant, Z. Sung et al., Noise analysis in magnetic resonance electrical impedance tomography at 3 and 11 T field strengths. Physiol. Meas. **26**, 875–884 (2005)
54. S.Z.K. Sajib, H.J. Kim, O.I. Kwon, E.J. Woo, Regional absolute conductivity reconstruction using projected current density in MREIT. Phys. Med. Biol. **57**, 5841–5859 (2012)

55. S.Z.K. Sajib, J.E. Kim, W.C. Jeong, H.J. Kim, O.I. Kwon, E.J. Woo, Reconstruction of apparent orthotropic conductivity tensor image using magnetic resonance electrical impedance tomography. J. Appl. Phys. **117**, 104701 (2015)
56. S.Z.K. Sajib, O.I. Kwon, H.J. Kim, E.J. Woo, Electrodeless conductivity tensor imaging (CTI) using mri: basic theory and animal experiments. Biomed. Eng. Lett. **8**, 273–82 (2018)
57. S.Z.K. Sajib, K. Nitish, H.J. Kim, O.I. Kwon, E.J. Woo, Software toolbox for low-frequency conductivity and current density imaging using MRI. IEEE Trans. Biomed. Eng. **64**, 2505–2514 (2017)
58. S.Z.K. Sajib, M.B. Lee, H.J. Kim, E.J. Woo, O.I. Kwon, Extracellular total electrolyte concentration imaging for electrical brain stimulation (EBS). Sci. Rep. **8**, 209 (2018)
59. S.Z.K. Sajib, M. Chauhan, G. Banan, S. Sahu, L. Wang, T.H. Mareci, R.J. Sadleir, Compensation of lead-wire magnetic field contributions in MREIT experiment using image segmentation: a phantom study, in *Proceedings of the 27th Annual Meeting of the ISMRM*. ISMRM (2019), p. 5049
60. S.Z.K. Sajib, M. Chauhan, O.I. Kwon, R.J. Sadleir, Magnetic-resonance-based measurement of electromagnetic fields and conductivity *in vivo* using single current administration – a machine learning approach. PLoS One **16**, e0254690 (2021)
61. G.C. Scott, M.L.G. Joy, R.L. Armstrong, R.M. Henkelman, Measurement of nonuniform current density by magnetic resonance. IEEE Trans. Med. Eng. **10**, 362–374 (1991)
62. G.C. Scott, M.L.G. Joy, R.L. Armstrong, R.M. Henkelman, Sensitivity of magnetic-resonance current-density imaging. J. Magn. Resonance **97**, 235–254 (1992)
63. J.K. Seo, E.J. Woo, *Nonlinear Inverse Problems in Imaging* (John Wiley & Sons, 2012)
64. J.K. Seo, E.J. Woo, Electrical tissue property imaging at low frequency using MREIT. IEEE Trans. Biomed. Eng. **61**, 1390–1399 (2014)
65. J.K. Seo, J.R. Yoon, E.J. Woo, O. Kwon, Reconstruction of conductivity and current densityimages using only one component of magnetic field measurements. IEEE Trans. Biomed. Eng. **50**, 1121–1124 (2003)
66. J.K. Seo, H.C. Pyo, C.J. Park, O.I. Kwon, E.J. Woo, Image reconstruction of anisotropic conductivity tensor distribution in MREIT: computer simulation study. Phys. Med. Biol. **49**, 4371–4382 (2004)
67. J.K. Seo, S.W. Kim, S. Kim, J.J. Liu, E.J. Woo, K. Jeon, C. Lee, Local harmonic b_z algorithm with domain decomposition in MREIT: computer simulation study. IEEE Trans. Med. Imaging **27**, 1754–1761 (2008)
68. J.K. Seo, J. Kiwan, C. Lee, E.J. Woo, Non-iterative harmonic b_z algorithm in MREIT. Inverse Prob. **27**, 085003 (2011)
69. J.S. Startton, *Electromagnetic Theory* (McGraw-Hill, 1941)
70. D.S. Tuch, V.J. Wedeen, A.M. Dale, J.S. George, J.W. Belliveau, Conductivity tensor mapping of biological tissue using diffusion MRI. Ann. N. Y. Acad. Sci. **888**, 314–316 (1999)
71. D.S. Tuch, V.J. Wedeen, A.M. Dale, J.S. George, J.W. Belliveau, Conductivity tensor mapping of the human brain using diffusion tensor MRI. Proc. Natl. Acad. Sci. **98**, 11697–11701 (2001)
72. E.J. Woo, J.K. Seo, Magnetic resonance electrical impedance tomography (MREIT) for high-resolution conductivity imaging. Physiol. Meas. **29**, R1–R26 (2008)
73. E.J. Woo, S.Y. Lee, C.W. Mun, Impedance tomography using internal current density distribution measured by nuclear magnetic resonance, in *Proceedings of International Symposium on Optics, Imaging, and Instrumentation*. SPIE, vol. 2299 (1994), pp. 377–385
74. H. Yazdanian, G.B. Saturnino, A. Thielscher, K. Knudsen, Fast evaluation of the biot-savart integral using FFT for electrical conductivity imaging. J. Comput. Phys. **411**, 109408 (2020)
75. N. Zhang, Electrical impedance tomography based on current density imaging. MS Thesis, Univeristy of Toronto, Canada, 1992

Magnetic Resonance Electrical Properties Tomography (MREPT)

8

Ulrich Katscher, Atul Singh Minhas, and Nitish Katoch

Abstract

This chapter explains the magnetic resonance electrical impedance tomography (MREPT) technique used to image electrical properties at high frequencies. The chapter describes the MREPT data acquisition methods, current state-of-the-art image reconstruction algorithms, and experiments with phantoms, animals, and humans.

8.1 Introduction

Magnetic resonance electrical properties tomography (MREPT) is a technique to measure the electrical properties (EPs) of body tissues, such as electrical conductivity and permittivity, at the Larmor frequency of MRI. For example, MREPT performed at 3T and 9.4T provides EPs at 128 and 400 MHz, respectively.

8.2 MREPT Data Acquisition

Unlike MREIT or DT-MREIT, MREPT does not require any external current to map EPs. Instead, the reconstruction of EPs relies on the knowledge of the complex RF transmit (TX) field $B_1 = |B_1|e^{i\phi}$, given by its amplitude $|B_1|$ (corresponding to local flip angle α) and phase ϕ. Although these two quantities belong to the same physical field, usually two different MR sequences are applied to measure $|B_1|$ and ϕ, i.e., there is a (large) family of sequences measuring $|B_1|$ (so-called B_1-mapping methods) and another (somewhat smaller) family of sequences measuring ϕ. These two families of pulse sequences are summarized in the Sects. 8.3 and 8.3.2.

The image reconstruction algorithms in EPT involve a second derivative in all three spatial directions (see Sect. 8.4.2), which is the reason why a volumetric data set has to be acquired for EPT. Thus, a single 2D image is not sufficient, but instead a "true" 3D dataset or multiple 2D datasets are required. Multiple 2D datasets are more robust in case of patient motion, however, might suffer from inconsistent sequence calibration between slices, hampering differentiation in

U. Katscher
Philips Research, Hamburg, Germany
e-mail: ulrich.katscher@philips.com

A. S. Minhas (✉)
School of Engineering, Macquarie University, Wallumattagal Campus, Macquarie Park, NSW, Australia
e-mail: atul.minhas@mq.edu.au

N. Katoch
Department of Biomedical Engineering, Kyung Hee University, Seoul, South Korea
e-mail: nitish@khu.ac.kr

R. Sadleir, A. S. Minhas (eds.), *Electrical Properties of Tissues*, Advances in Experimental Medicine and Biology 1380, https://doi.org/10.1007/978-3-031-03873-0_8

through-plane direction. This problem is eliminated by acquiring true 3D datasets.

8.3 Pulse Sequences and Data Processing for B_1 *Magnitude* Measurement

Mapping $|B_1|$ has been investigated since the early days of MR, and over the decades, a large number of these B_1-mapping methods has been developed, independent of EPT. In general, the higher the accuracy of the B_1-mapping method, the better it is for EPT. The accuracy of B_1-mapping methods has been investigated both in general studies without EPT [33] and in EPT [6]. The most popular B_1-mapping methods nowadays appear to be actual flip angle imaging (AFI) [45], Bloch-Siegert shift method (BSS, [35]), and dual refocusing echo acquisition mode method (DREAM, [31]). These methods are briefly described in the following subsections.

AFI

The AFI method [45] uses a steady-state sequence which applies two identical RF pulses followed by two different repetition times TR_1 and TR_2. After each RF pulse, a gradient echo signal is acquired. If TR_1 and TR_2 are sufficiently short and if the transverse magnetization is completely spoiled, the ratio $u(\mathbf{r}) = S_2(\mathbf{r})/S_1(\mathbf{r}))$ of the two measured signal intensity distributions $S_1(\mathbf{r})$ and $S_2(\mathbf{r})$ corresponding to TR_1 and TR_2 depends on flip angle $\alpha(\mathbf{r})$ via $v = TR_2/TR_1$:

$$u(\mathbf{r}) = \frac{1 + v\cos\alpha(\mathbf{r})}{v + \cos\alpha(\mathbf{r})} \tag{8.1}$$

and, thus, the spatial distribution of $\alpha(\mathbf{r})$ can be calculated as

$$\alpha(\mathbf{r}) = \arccos\left(\frac{vu(\mathbf{r}) - 1}{v - u(\mathbf{r})}\right). \tag{8.2}$$

BSS

The Bloch-Siegert shift (BSS) is caused by irradiating with an off-resonance RF pulse following conventional spin excitation. When applying the off-resonance RF in the kilohertz range, spin nutation can be neglected, and the primarily observed effect is a spin precession frequency shift. This shift is proportional to the square of the magnitude of B_1. Placing gradient imaging after the off-resonance pulse yields spatially resolved B_1 maps [35]. The phase difference of two acquisitions, with the RF pulse applied at two frequencies symmetrically around the water resonance, is used to eliminate undesired off-resonance effects due to B_0 inhomogeneities and chemical shift. Care has to be taken that occurring SAR (upped by the off-resonance pulses) does not exceed physiologically and legally recommended limits.

DREAM

The dual refocusing echo acquisition mode (DREAM) technique applies a stimulated echo acquisition mode (STEAM) preparation sequence followed by a tailored single-shot low-angle gradient echo train. In contrast to conventional STEAM imaging, both, the stimulated echo and the free induction decay (FID), are refocused quasi-simultaneously as gradient-recalled echoes [31]. In a post-processing step, the actual flip angle of the STEAM preparation RF pulse is derived from the ratio of the two measured signals. Due to this quasi-simultaneous acquisition of the two images (practically all B_1-mapping methods rely in one or the other way on the acquisition of two separate images), DREAM seems to be one of the fastest B_1-mapping methods of all B_1-mapping methods discussed today.

All these B_1-mapping methods would allow to measure absolute values of B_1, which are typically in the range of 5–15 μT. However, the knowledge of absolute values of B_1 is not required for the reconstruction of electrical properties (not even for reconstructing electrical properties quantitatively). It should be noted that it is also irrelevant for EPT to optimize the flip angle or make a careful consideration for calculation of the magnetic field H (unit A/m) and the magnetic flux density B (unit T).

8.3.1 Examples of B_1 *Magnitude* Measurements

The B_1 magnitude obtained using the AFI method is illustrated in Fig. 8.1 for an example phantom and in vivo measurements in the human brain. For each of these experiments, AFI method has been used with a voxel size of $4 \times 4 \times 8$ mm^3, sagittal imaging plane, foldover in anterior/posterior direction, a field of view (FoV) of 224×224 mm^2 in-plane, and 160 mm through-plane. For in vivo experiments, a slight in-plane rotation has been applied such that backfolding from eye motion is placed below the brain. AFI was performed with flip angle = 60^o, TR1 = 30 ms, TR2 = 160 ms, TE = 2.5 ms, and NEX = 1, yielding a total acquisition time of 3:33 min. Afterward, spatial resolution of the B_1 magnitude maps was increased linearly to $1 \times 1 \times 1$ mm^3 to match the spatial resolution of the B_1 phase maps shown in the next Sect. 8.3.2.

8.3.2 Pulse Sequences and Data Processing for B_1 *Phase* Measurement

Mapping of B_1 magnitude, as discussed in the previous section, has been undertaken for decades without having EPT in mind. This is not the case for mapping of B_1 phase ϕ, which became popular only during the last few years specifically with respect to EPT. The main challenge in mapping ϕ is the suppression of phase contributions unrelated to RF penetration [9], particularly phase contributions arising from (a) B_0 inhomogeneities (also called off-resonance effects), (b) patient motion, and (c) eddy currents induced by gradient switching. A direct measurement of ϕ as phase of TX RF field is not possible with a standard MR system. Instead, we have to rely on its superposition with its counterpart, the receive RF field (RX), yielding the so-called transceive (TRX) phase. From this point, ϕ should be interpreted as the TRX phase. This section describes the measurement of the B_1 TRX phase, and its background theory is described in the subsequent section. Three types of sequences are discussed for measuring TRX phase: spin echo (SE)-based sequences, steady-state free precession (SSFP) sequences, and sequences with ultrashort/zero echo time (UTE/ZTE).

We would like to emphasize it as a warning that phase is a very sensitive quantity. While it is a big advantage for EPT to be able to detect even small changes of conductivity, unfortunately it makes phase susceptible to all sorts of artifacts. Even in phantoms, it is very difficult to obtain an artifact-free conductivity map with EPT. This feature has to be kept in mind if acceleration methods like parallel imaging or compressed sensing are applied, which in theory do not change phase and should thus be compatible with EPT phase measurements but in practice may introduce additional artifacts. Note that even small artifacts introduced by these techniques could spoil the reconstruction results.

SE

The easiest way to exclude the unwanted B_0-related phase is to apply spin echo-based sequences, where the refocusing RF pulse eliminates this phase contribution automatically. Since standard SE sequences tend to have excessive acquisition times, particularly for the required volumetric dataset, all kinds of accelerated ("turbo") sequence versions have been applied. Effects of eddy currents from gradient switching can be eliminated by repeating the measurement with inverted gradient polariza-

(continued)

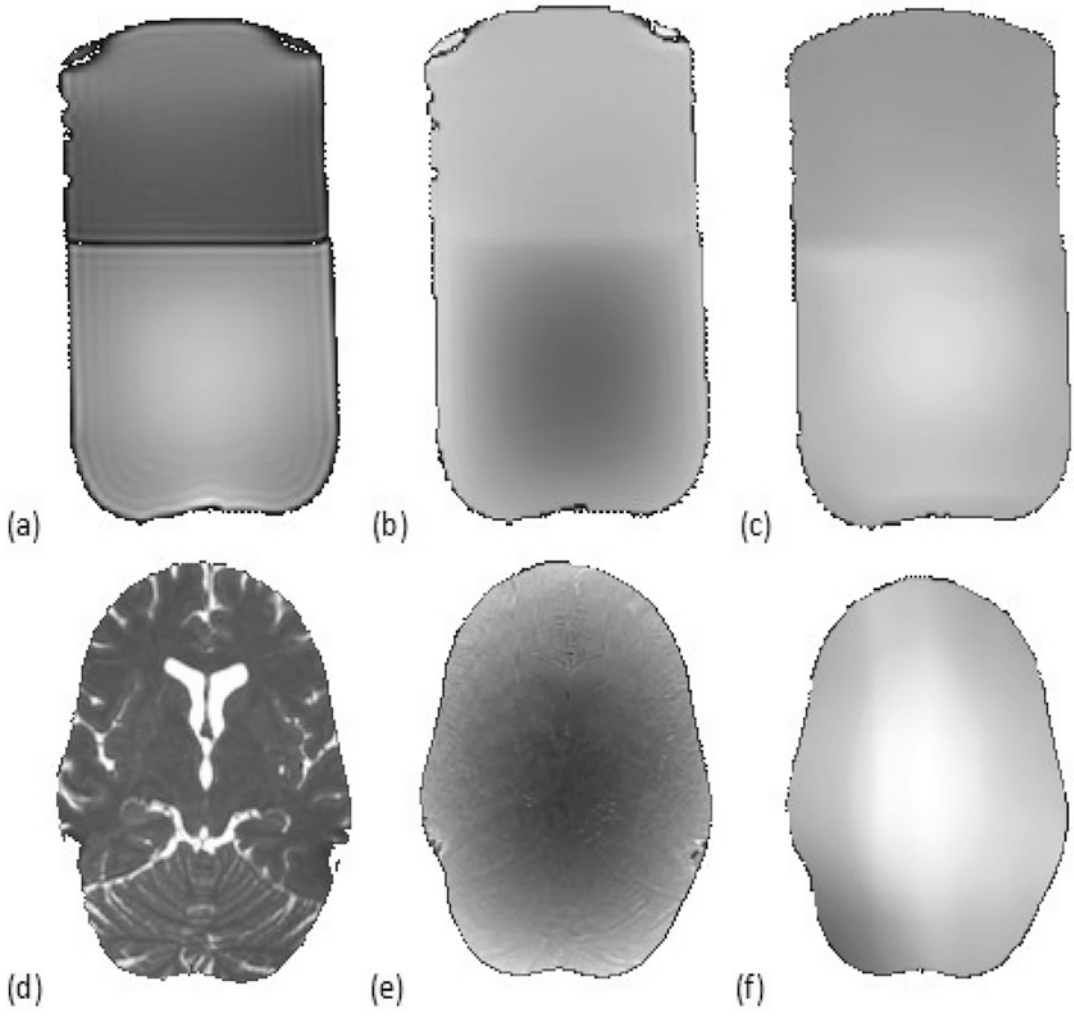

Fig. 8.1 Measurements of phantom and in vivo (axial reformats). Magnitude of SSFP image (**a, d**), transceive phase of SSFP image (**b, e**) taken as B_1 phase, and B_1 magnitude (**c, f**) measured with AFI

tion and averaging the two results (before or after EPT reconstruction) [41]. Effects of patient motion can be suppressed by, e.g., using a double spin echo sequences [4]. For enhanced SNR, multi-spin multi-echo (MSME) can be applied [24], and echoes can be combined by using a method described in [24].

SSFP

Gradient echo sequences contain unwanted B_0-related phase contributions, unless the gradients are balanced over time. Gradients balanced in each of the spatial direction leads to the so-called "steady-state free precession (bSSFP)" sequence. This sequence is very SNR-efficient, robust with respect to motion, shows negligible effect of eddy currents, and thus seems to be the method

(continued)

of choice for determination of ϕ in EPT [39]. The bSSFP sequence is used in the experimental results described in Fig. 8.1 for B_1 phase mapping. However, a major issue is the appearance of banding artifacts, exhibiting signal voids and phase jumps where B_0 inhomogeneities are large for a given TR. Therefore, we must check in each experiment if bSSFP is applicable for the given region of interest and for the given MR system with its individual capability to minimize TR as well as B_0 inhomogeneities. Methods have been reported to eliminate bSSFP banding artifacts (see, e.g., [6]); however, this comes at a cost of (significantly) extended scan duration.

UTE/ZTE

The unwanted phase contribution from B_0 inhomogeneities increases roughly linearly with echo time. Thus, the shorter the echo time, the smaller this unwanted phase contribution. This is the reason why ultrashort or zero echo time (UTE/ZTE) sequences are able to provide a phase which can be used for EPT [21, 37]. Since the SNR of particular tissue types with short relaxation times benefit greatly from ultrashort/zero TE, this idea might become valuable for investigating corresponding tissues like the cartilage or lung [15].

8.3.3 Examples of B_1 *Phase* Measurement

For illustration of B_1 phase mapping with both phantom and in vivo human experiments, a bSSFP sequence has been applied with the geometric setup coinciding with the B_1 magnitude mapping sequence described in Sect. 8.3.1 above. For example, the same location of FOV, sagittal planes, and foldover in anterior/posterior direction was used as that of the AFI method in Sect. 8.3.1 above. However, in vivo FOV was slightly rotated due to backfolding from eye motion, which for B_1 phase mapping typically causes even bigger artifacts than for B_1 magnitude mapping. Sequence parameters were voxel size$= 2 \times 2 \times 2\,\text{mm}^3$, flip angle = 30°, TR = 2.5 ms, TE = 1.2 ms, NEX = 12 for phantom and voxel size$= 1 \times 1 \times 1\,\text{mm}^3$, flip angle = 30°, TR = 3.5 ms, TE = 1.7 ms, and NEX = 2 for in vivo, yielding a total acquisition time of 4:30 min for phantom and 4:10 min for in vivo. SSFP sequences are usually accompanied by very sharp and nasty acoustic noise; thus ear plugs for the volunteer are absolutely necessary.

A commercial 3T scanner (Philips Ingenia, Best, the Netherlands) has been applied for the example scans using a two-channel RF body coil in quadrature mode for RF TX and an eight-channel RF head coil for RF RX (for the described experiments, a single TX channel RF body coil would do as well). The built-in option CLEAR ("constant level of appearance") was used to combine the eight RF RX channels based on RX sensitivities measured in a pre-scan, yielding a TRX phase as if the body coil would have been used both for TX and RX. If no such option is available at the scanner applied, RF RX channels can be combined in a post-processing step, e.g., as it is done for parallel imaging [34] with reduction factor R = 1, using separately measured RX sensitivities. A detailed description of RF coil combination for EPT is given by [22, 24]. B_1 phase maps of example slices for both, phantom and in vivo, are shown in Fig. 8.1b, e. The phase jump of 180° occurring in the oil compartment has been compensated offline to better visualize spatial phase distribution.

8.4 MREPT Image Reconstruction

8.4.1 Physical Background

This section outlines the physical and mathematical background of EPT. More details are given in corresponding reviews [16, 27]. For beginners

it is recommended to start EPT with its most simplified version, which is

$$\sigma = \frac{\nabla^2 \phi}{\omega \mu_0} \tag{8.3}$$

The essential message of this equation is that conductivity σ is proportional to the curvature of the B_1-phase ϕ. The measurement of ϕ is described in Sect. 8.3.2, and the calculation of curvature numerically is described in a post-processing step in Sect. 8.4.2 below. The curvature is obtained by the second derivative in all three spatial dimensions, given by ∇^2 in (8.3). The Larmor frequency ω and the vacuum permeability μ_0 (assumed to be constant) act as scaling factors to convert the phase curvature to quantitative conductivity values with the SI unit (S/m). Thus, in this simplest form, no iteration, matrix inversion, or other "advanced" numerical method is required for EPT, and conductivity can be calculated (semi-) locally in a straightforward manner.

As next step, to calculate not only conductivity but also permittivity, a complex version of (8.3) is needed (sometimes called "truncated" Helmholtz equation)"

$$\boldsymbol{\kappa} = \omega\varepsilon - i\sigma = -\frac{\nabla^2 B_1^+}{\omega \mu_0 B_1^+} \tag{8.4}$$

The real part of (8.4) comprises permittivity; the imaginary part comprises conductivity. Equation (8.4) is accurate assuming that electrical properties κ are locally constant, i.e., $\nabla\boldsymbol{\kappa} = 0$ (the so-called local homogeneity assumption, LHA). If the LHA is not fulfilled, the equation gets more complicated, yielding "full" Helmholtz equation:

$$\kappa \mathbf{B_1} = -\frac{\nabla^2 \mathbf{B_1}}{\omega \mu_0} - \frac{(\nabla \kappa/\kappa) \times (\nabla \times \mathbf{B_1})}{\omega \mu_0} \tag{8.5}$$

Comparing Eqs. (8.4) and (8.5), we can notice that the Eq. (8.5) requires not only the introduction of an additional term on the right hand side, to handle the local inhomogeneity of κ, but also the transition to a vector equation. Note that the vector $\mathbf{B_1} = \left[B_{1x}, B_{1y}, B_{1z}\right]$ describes the RF coil's full magnetic field instead of the previously used scalar B_1^+ (the positive circularly polarized component of $\mathbf{B_1}$; see below). Equation (8.5), which involves only $\mathbf{B_1}$, can be derived by taking the curl of both sides of the Ampere's law with Maxwell's correction ($\nabla \times \mathbf{B_1} = i\mu_0\kappa\mathbf{E}$) and then combining it with Faraday's law from Maxwell's equations ($\nabla \times \mathbf{E} = -i\omega\mathbf{B_1}$) assuming time-harmonic fields. Gurler et al. [7] have shown that for $\sigma^2 \gg (\omega\varepsilon)^2$, Eq. (8.5) can be transformed into the transceive phase-based EPT equation as

$$(\nabla\sigma/\sigma) \cdot \nabla\phi^{tr} - \nabla^2\phi^{tr} + 2\omega\mu_0\sigma = 0 \tag{8.6}$$

As mentioned above, a standard MR system allows only the measurement of the so-called transceive (TRX) phase, which is the superposition of RF TX phase and RF RX phase. The TX phase required for the Eq. (8.6) above can be estimated by scaling the measured TRX phase ϕ_{tr} by a factor 1/2 assuming that TX and RX phase are equal (so-called "TRX Phase Assumption," TPA). Before doing so, care has to be taken that the measured phase is correctly unwrapped. Fortunately, phase unwrapping does not need to be 3D (a rather nontrivial task) but could be 1D (a rather trivial task) performed separately for each spatial direction—in connection with the numerical differentiation, which can also be performed in each spatial direction separately (see below). Doing this scaling of $\phi = \phi_{tr}/2$ will provide us the following equation:

$$\sigma = \frac{\nabla^2\phi}{\omega\mu_0} - \frac{(\nabla\sigma/\sigma) \cdot \nabla\phi}{\omega\mu_0} \tag{8.7}$$

Equation (8.7) is in the form of a convection-reaction equation and thus dubbed cr-EPT. For a locally constant σ, $\nabla\sigma = 0$, and therefore Eq. (8.7) reduces to Eq. (8.3).

Complex Components of $\mathbf{B_1}$

MR measurements of $\mathbf{B_1}$, B_1^+, or even ϕ are challenging. The longitudinal component B_{1z} is generally not measurable, but for the usually applied RF quadrature volume

(continued)

coils, this is much smaller than B_{1x} and B_{1y} and is thus frequently neglected. The transverse components B_{1x} and B_{1y} could be derived from the positive $(B_{1x}+iB_{1y})/2$ and negative $(B_{1x}-iB_{1y})/2$ circularly polarized components, related to the TX and RX field of an RF coil, respectively. However, MRI allows only the magnitude of the TX field B_1^+ to be measured exactly, e.g., by methods presented in the Sect. 8.3 above, thus asking for further model assumptions to solve Eq. (8.5) [7, 25] and bring it in the form of Eq. (8.7). Note that $|B_1^+|$ is referred to as B_1 in Sect. 8.2.

8.4.2 Numerics

Most EPT reconstruction techniques, particularly the standard EPT reconstruction technique for beginners, are based on numerical differentiation, first and foremost by applying Eq. (8.3) for post-processing of measured TRX phase maps. However, numerical differentiation has a strong noise-amplifying effect, and that is why EPT reconstructions typically consist of two steps, differentiation and denoising. Thus, denoising filters for EPT should not be considered as cosmetic operations to improve some awkward reconstruction results but as an inherently required reconstruction step. Of course there are countless techniques published for both numerical differentiation and denoising. This chapter focusses on the description of techniques which are (a) easy to implement and (b) already applied in the framework of EPT.

Numerical Differentiation

It is impossible to perform numerical differentiation on a single voxel. Instead, to obtain the derivative of a certain voxel (the "target voxel"), a number of voxels around the target voxel are required (the "kernel"). The derivative is obtained by summing up all voxels of the kernel using suitable weighting coefficients D_n. The optimum choice of D_n leads to an intricate discussion but always starts with the simplest choice, which is determined starting with

$$\frac{\partial\phi}{\partial r} \approx \frac{\Delta\phi}{\Delta r} = \frac{\phi_{n+1}-\phi_n}{\Delta r} \tag{8.8}$$

as first derivative of ϕ with respect to r (r representing an arbitrary spatial direction). This equation replaces the infinitesimal differentiation operation ∂ by finite differences Δ, and these finite differences correspond to differences of neighbor voxels $n+1$ and n. The neighbor voxels have a distance Δr, which is the same as the voxel size in this direction. Continuing this way to the second derivative as required by Eq. (8.3) yields

$$\frac{\partial^2\phi}{\partial r^2} \approx \frac{\frac{\phi_{n+1}-\phi_n}{\Delta r}-\frac{\phi_n-\phi_{n-1}}{\Delta r}}{\Delta r} = \frac{\phi_{n+1}-2\phi_n+\phi_{n-1}}{(\Delta r)^2} \tag{8.9}$$

i.e., the same technique as before applied to two neighbor voxels of the first derivative. Voxel n is the target voxel, and the kernel consists of three voxels n, $n-1$, and $n+1$. The weighting coefficients for these three voxels are $D_n = \{+1,-2,+1\}$ as taken from the numerator of the right hand side of (8.9), yielding the simplest choice of weighting coefficients. It can be easily checked for the example phase of $\phi_n = n^2$ that (8.9) yields the desired curvature of $(1\cdot 1^2 - 2\cdot 0^2 + 1\cdot 1^2)/1^2 = 2$ (at $n=0$) or, as equivalent example, $(1\cdot(-3)^2 - 2\cdot(-2)^2 + 1\cdot(-1)^2)/1^2 = 2$ (at $n=-2$). The transition from the 1D case given in (8.9) to the 3D case as required by (8.3) is a trivial step, since (8.9) can be applied just thrice, once for each spatial direction x, y, and z, and the results added.

For a noiseless situation, as usually delivered by electromagnetic field simulation

(continued)

software, (8.9) yields rather perfect results (at least with sufficiently small voxel size and within areas of homogeneous electric properties). The situation gets complicated with the onset of noise in the measured ϕ (or artificial noise added to the simulation result), which is strongly amplified by (8.9). Although denoising is typically performed in a separate step (see below "Local Denoising"), noise can additionally be treated by increasing the numerical differentiation kernel, with weights optimized for denoising. The drawback of this concept is a loss of spatial resolution, i.e., increasing kernel size lowers noise and spatial resolution of the resulting conductivity map, just as would happen by choosing larger voxels for measurement. Thus, a suitable trade-off for the kernel size has to be found, which depends on the SNR of the measured image. The complexity of this discussion is demonstrated in [20]. A typical trade-off might be a kernel size of 11 voxels per direction, with weighting coefficients designed to fit a parabola to the voxels, as is given by Savitzky and Golay [36] and is thus usually called Savitzky-Golay coefficients:

$$D_n = \{+15, +6, -1, -6, -9, -10, -9, -6, -1, +6, +15\}/429. \tag{8.10}$$

Interestingly, these coefficients itself have the shape of a parabola. Savitzky-Golay coefficients for other kernel size are described in [36]. The minimum Savitzky-Golay kernel has a size of three coefficients and coincides with (8.9).

Numerical Denoising

Numerical denoising is typically performed after the differentiation step. Attempts of denoising before the differentiation step [30] might be hampered by the intrinsic feature of the B_1 magnitude and phase of being nonconstant, whereas electrical properties tend to be approximately constant over each tissue type, and constant quantities are easier to denoise than nonconstant quantities. Again, numerical denoising is a very large field, and this subsection sketches only two filter types most simple and applied in EPT community: the Gaussian filter and the median filter. As for numerical differentiation, denoising is always based on an ensemble of voxels around the target voxel, thus now leading to the "filter kernel." The geometric size and shape of the filter kernel might coincide with the differentiation kernel, but not necessarily. The Gaussian filter obtains its weighting coefficients F_n from a Gauss function

$$F_n = \exp(-a(n - n_0)^2) \tag{8.11}$$

with its maximum located at the target voxel n_0. The width of the Gauss function is determined by the parameter a, which can be chosen freely and distinguishes strong filtering (small a, i.e., broad exponential function) from weak filtering (large a, i.e., narrow/peaked exponential function). For large a, it does not make sense to use a very large kernel size as most of the weighting coefficients might be close to zero anyway. For small a, the kernel size has a big impact on the strength of the filter. The Gaussian filter is a "classical" filter which not only denoises but also blurs the image and is again to some extent equivalent with using larger voxels during acquisition. The median filter is slightly less simple than the Gaussian filter but typically yields more "realistic" results than the Gaussian filter, tending to preserve edges instead of blurring them. In a first step, the median filter creates a histogram of the kernel's values. In contrast to a standard histogram,

(continued)

it is advantageous to choose the bins of the histogram so small that all bins contain only one or zero voxels. In a second step, the filter identifies the histogram's median value as 50% of the voxels above and 50% below this value. This median value is then assigned to the corresponding target voxel of the denoised image. The median filter does not include free parameters in contrast to the Gauss filter (having freely adjustable parameter a).

Local Adaptation of Kernel Shape

As outlined above, Eqs. (8.3) and (8.4) are based on the local homogeneity assumption, LHA. This LHA is most often violated at boundaries separating tissues with differing electrical properties, and due to the finite size of differentiation and filter kernel, it is also violated if these tissue boundaries are somewhere inside the kernel. This is the reason why both, differentiation and filter kernel, should be shaped such that they never cross tissue boundaries. In other words, for each target voxel, the kernel should contain only voxels which belong to the same tissue type as the target voxel. This is relatively straightforward to implement and supersedes the much more sophisticated implementation of (8.3) and (8.4) having the same goal: to overcome the EPT boundary problem.

To shape the differentiation and filter kernel locally to the individual tissue boundaries, the magnitude image can be taken into account, which is acquired together with the transceive phase (i.e., typically a SE-based or SSFP image, see Sect. 8.3.2 above). The easiest way to take this magnitude image into account is to compare the signal of the target voxel with the signal of the (potential) kernel voxel. Thus, a maximum kernel size is defined, and within this maximum kernel, all voxels n are skipped which signals' $S(n)$ differ from the target voxel's signal $S(n_0)$ by more than a predefined threshold R_{thresh} [17]:

$$|S(n)/S(n_0) - 1| > R_{thresh} \qquad (8.12)$$

A related strategy is to apply an edge detection filter to the magnitude image and to iteratively increase the kernel from the target voxel up to the surrounding edges [13].

It should be noted that boundary artifacts have two origins, a physical and a numerical [28]. The physical artifact is caused by the missing term in (8.4) and can be removed by using (8.5), which includes the missing term. The numerical artifact is caused by the discontinuity in the phase or in its first derivative, which is *not* removed using (8.4) but using (8.5). However, both types of boundary artifacts are removed by the described local shaping of differentiation and filter kernel.

8.4.3 Advanced EPT Reconstruction Techniques

MREPT clinical studies have recently started appearing in some research works such as the breast cancer study reported by Shin et al. [38] and the brain tumor study reported by Tha et al. [40]. Notably, the EPs reconstructed in these studies are based on Eq. (8.3) using numerical differentiation, which indicates that even the simplest possible version of EPT is able to yield meaningful clinical results. Nevertheless, researchers are attempting to improve EPT by developing more advanced reconstruction techniques. A big step toward more advanced EPT reconstruction techniques is to replace Eqs. (8.3) and (8.4) by Eqs. (8.5) and (8.7) for better handling of the EPT boundary problem. As mentioned earlier, this strategy has been chosen

for "gradient EPT" [25] or "convection-reaction EPT" [7,8,10]. These techniques however are still based on numerical differentiation. Methods have also been developed to overcome the need for numerical differentiation. Some of these methods are summarized in this section. These methods belong to the family of forward reconstructions and machine learning reconstructions.

Forward Reconstruction

Standard EPT can be considered as a "backward" solution: a measured B_1 (or its phase ϕ) is taken and post-processed to get back to the underlying electrical properties. In contrast, "forward" solutions start with an assumed distribution of electrical properties (assumed patient tissue structure), then simulates the resulting B_1, and compares the simulated and measured B_1. Typically, this yields an iterative process, which optimizes the assumed input electrical properties until difference between the simulated, and the measured B_1 is minimized (method pioneered by Balidemaj et al. [3] as "contrast source inversion" EPT (CSI-EPT). No differentiation or denoising is required for such forward solutions, which can be regarded as advantage of this method. Instead, two reconstruction steps are applied: the forward simulation of the B_1 field (e.g., including the question of how far the knowledge of the applied RF coil and its shield is required for this goal [2]) and the iteration of the input electrical properties (e.g., including the question of optimal initial iteration [23]). However, since there is requirement of iterative steps for reconstruction, this can easily exceed the complexity and the CPU time required for reconstruction with "forward" EPT compared to the "backward" EPT.

Machine Learning Reconstruction

First steps have been undertaken to test the ability of EPT for machine learning, which is another way to circumvent differentiation and denoising required by Eqs. (8.3), (8.4), (8.5), and (8.7). The main challenge in this context is to provide sufficient ground truth, i.e., a multitude of examples connecting B_1 field and electrical properties. In a first attempt, ground truth was provided by a dictionary containing small patches of B_1 fields together with underlying electrical properties, taken from electromagnetic simulations of homogeneous spheres [11]. More advanced, neural networks have been applied to learn the connection between B_1 fields and electrical properties, as provided by 2D brain simulations and applied to measured B_1 fields [29]. As is always the case, a lengthy learning process is required for the network, allowing for very fast reconstruction of the individually measured patient. Again, as is always the case, generalization might be an issue, i.e., how much a measured B_1 field is allowed to differ from the training data and still having a chance to be reconstructed reliably. Generalization of course improves with the variety of ground truth data, but one has to keep in mind that simulating B_1 fields from assumed tissue structures is a rather time-consuming procedure (see above "Forward Reconstruction").

8.4.4 Permittivity Reconstruction

Continuing to more advanced reconstruction methods, it might become possible to obtain not only satisfying conductivity results but also satisfying permittivity results. Permittivity is much less considered in EPT studies than conductivity. This is not only due to the less known meaning of this parameter (particularly among clinicians) but also because it is discriminated by underlying physics to be less sensitive for B_1 measurements and, thus, even more prone to low SNR than conductivity. Studies suggest that with standard EPT, satisfying in vivo

permittivity results cannot be expected below a main field strength of 7T [42]; however, this might change for advanced versions of EPT.

8.5 MREPT Experiments

8.5.1 Phantom Experiment

It is very simple to build a phantom which fulfils basic requirements to start with EPT. In short, roughly half of a bottle is filled with saline in a first step, and in a second step, oil is added to the saline until the bottle is filled, yielding a phantom with two compartments. The oil will always swim on the saline; thus a sharp boundary between the compartments is guaranteed (without any unwanted vessel wall, foil, or the like separating the two compartments). Furthermore, a conductivity contrast is guaranteed, since oil has typically a very low conductivity (close to zero), and saline has a conductivity significantly different from zero. All required substances are harmless, cheap, and stable. Some more details are given in the following sections.

The Bottle In principle, any bottle or vessel can be used, as long as it does not contain any metallic material (i.e., preferably made from plastic or glass), can be closed tightly (watch out for leaking oil/saline), and fits into the receive RF (head) coil used for MRI data acquisition. In fact, it should be as large as possible to permit high SNR by enabling a large voxel size.

The Saline For simple initial experiments, just tap water can be used with standard table salt (sodium chloride, NaCl) added. A conductivity σ should be adjusted which is somewhat high but yet reasonably within the physiologic range, for instance $\sigma \approx 1$ S/m. This value corresponds to roughly 6.5 g NaCl per liter H_2O (about a "teaspoon of salt"). For more precise quantities of NaCl and its relation with conductivity, see Chap. 2 (MREIT Phantoms).

The Oil For simple initial experiments, some standard oil for cooking from the supermarket is sufficient (e.g., rape oil, sunflower oil, olive oil). All these types of oil have the two necessary features, i.e., swimming on water and conductivity of approximately zero; thus the cheapest (and/or scentless) oil available might be taken. Pouring the oil onto the water might lead to small bubbles at the oil/water interface, which typically dissolve within a few hours without further interaction.

MRI of the Phantom
In principle, contrast agent might be used for this phantom, but is not mandatory. Both saline and oil might show suboptimal signal, but sufficient SNR could be achieved by reasonable voxel size and number of averages. The use of contrast agent might be tricky since (a) it usually changes conductivity, and (b) it might be soluble only in water (saline) but not in oil, thus leading to a nasty huge signal difference between the compartments. A picture of such a phantom is shown in Fig. 8.2, and corresponding MR images are shown in Fig. 8.1a–c.

8.5.2 In Vivo Human Experiment

It is straightforward to perform initial in vivo EPT experiments. First, a healthy subject willing to volunteer is required, and approval of the corresponding local Institutional Review Board (IRB) (or Ethics Committee) has to be obtained. It is strongly recommended to start with imaging the brain of the volunteer, which is the part of the body with the lowest motion, sufficiently high structural contrast, and no problems with water/-fat chemical shift. Using the sequence discussed below, SNR in the brain is large enough to perform the EPT experiment within a few minutes, which is a duration for which all healthy subjects are easily able to keep still. MR images of such an in vivo experiment are shown in Fig. 8.1d–f.

The literature electrical properties of brain tissue [5] at 128 MHz (i.e., Larmor frequency at B_0 = 3T) are given in Table 8.1 below. Conductivity of grey and white matter are within the typical range of around 0.5 S/m of all tissue types which

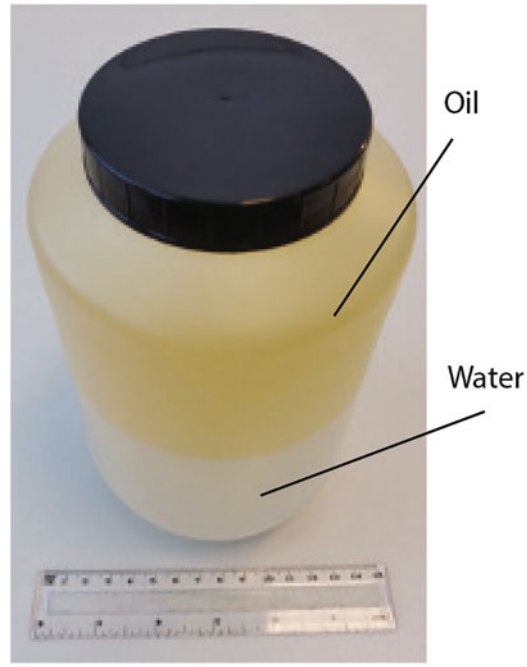

Fig. 8.2 Photo of phantom with two compartments. Upper compartment, rape oil; lower compartment, saline. The bottle has a diameter of roughly 12 cm and a height of roughly 15 cm

Table 8.1 Electrical properties of brain tissue types at 128 MHz according to [5]

	Grey matter (GM)	White matter (WM)	Cerebrospinal fluid (CSF)
Conductivity (S/m)	0.59	0.34	2.14
Permittivity ($/\varepsilon_0$)	73.5	52.5	84.0

are not fluids (high conductivity) or fat or bone (both low conductivity). In fact, CSF has the highest tissue conductivity reported, even higher than all other body fluids typically in the range 1.0–1.5 S/m. Similarly, permittivity of CSF is the highest one reported, close to the maximum permittivity of water. Grey and white matter are in an intermediate range, and fat and bone are at the lower end of the tissue permittivity range [5].

The only issue connected with EPT brain imaging is cardiac pulsation transferred to cerebrospinal fluid (CSF) [18]. Without pulsation, the conductivity of CSF is quite high compared to surrounding gray/white matter (GM/WM), thus yielding a clearly visible conductivity contrast as outlined above. However, with pulsation, roughly 50% of scans show a corrupted CSF conductivity, depending on the incidental distribution of k-space acquisition in relation to cardiac cycle. Cardiac triggering does not help in this situation, since optimal point in time in cardiac cycle for EPT acquisition is different for different parts of the brain (due to traveling of pulsation wave throughout brain over cardiac cycle). Corrupted CSF conductivity is hardly a problem since clinicians are usually not interested in CSF conductivity. However, if a "nice" conductivity map free of CSF pulsation artifacts is desired, the easiest way is to repeat the measurement a couple of times and check for conductivity map with lowest amount of pulsation artifacts.

8.5.3 Examples of Phantom/In Vivo Reconstructions

Phantom Reconstructions

Different reconstruction examples of phantom conductivity are shown in Fig. 8.3. Us-

(continued)

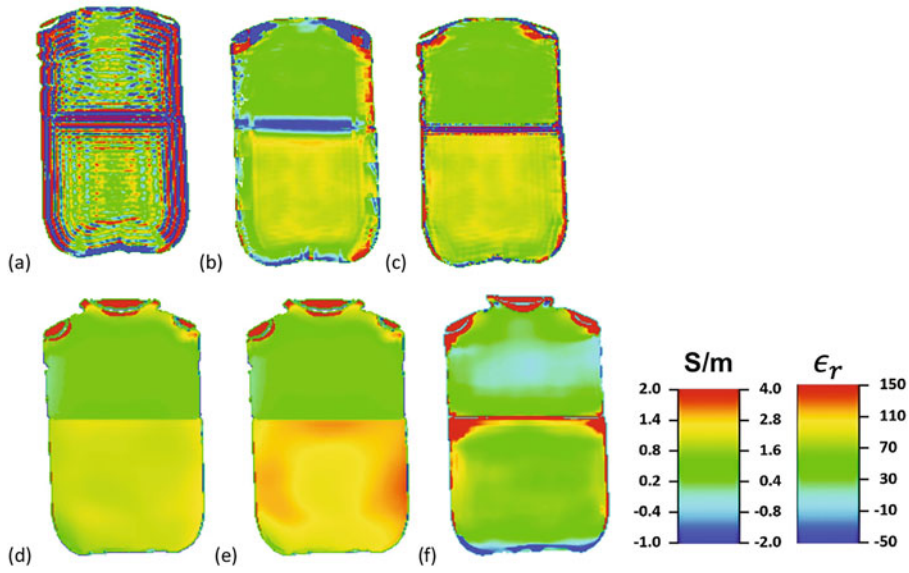

Fig. 8.3 Different reconstruction examples of phantom conductivity. Numbers on the right hand side of the conductivity color scale apply to (**a**) and numbers on the left-hand side to (**b**)–(**e**). (**a**) Reconstruction using a small differentiation kernel, conductivity appears noisy and with strong ripples. (**b**) Reconstruction with a larger kernel removes noise and ripples but yields a strong artifact along the compartment boundary. (**c**) Reconstruction taking compartment boundaries into account reduces the boundary artifact. (**d**) Reconstruction including a median filter removes most of the remaining noise and ripples in part (**c**). (**e**) Reconstruction assuming a constant B_1 magnitude, i.e., a purely phase-based reconstruction using (8.3). (**f**) Relative permittivity, corresponding to reconstruction of (**d**)

ing a small differentiation kernel of three voxels, reconstructed conductivity appears noisy and with strong ripples as is visible in Fig. 8.3a. Please note that color scale of Fig. 8.3a is twice the color scale of the remaining subplots to better visualize the effects. The larger kernel of 11 voxels from Eq. (8.10) removes noise and ripples but yields a strong artifact (over/undershoot) along the compartment boundary, as is visible from Fig. 8.3b. Taking compartment boundaries into account during differentiation via Eq. (8.12) greatly reduces this artifact (Fig. 8.3c). The median filter, again using (8.12), removes most of the remaining noise and ripples (Fig. 8.3d). If B_1 magnitude is ignored by assuming a constant B_1 magnitude (i.e., using Eq. (8.3) instead of (8.7)), saline compartment shows a ring-shaped increase of conductivity (Fig. 8.3e). This increase corresponds to areas with strong gradients of the B_1 magnitude, as visible on Fig. 8.1c. Since in the oil compartment, B_1 magnitude is rather flat anyway, no significant difference is observed in this compartment between Fig. 8.1d, e. Reconstructed permittivity suffers from more artefacts than conductivity, but the permittivity difference between oil and saline is clearly visible in Fig. 8.3f.

In Vivo Reconstructions in the Human Brain

In analogy to the phantom results shown in Fig. 8.3, different reconstruction examples of in vivo brain conductivity are shown in Fig. 8.4. Using again the small differentiation kernel of three voxels, reconstructed

(continued)

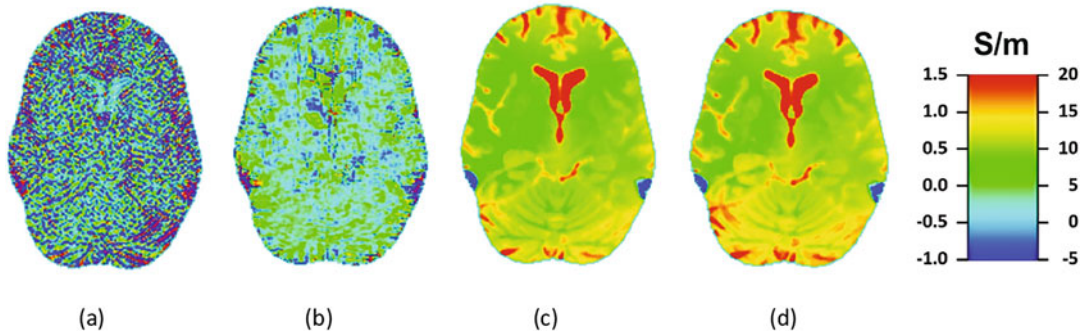

Fig. 8.4 Different reconstruction examples of brain conductivity. Numbers on the right hand side of the color scale apply to (**a**)–(**b**) and numbers on the left-hand side to (**c**)–(**d**). (**a**) Reconstruction using a small differentiation kernel, conductivity appears noisy and with strong ripples. (**b**) Reconstruction with a larger kernel reduces noise and ripples. (**c**) Reconstruction taking compartment boundaries and a median filter into account essentially removes noise and ripples. (**d**) Reconstruction assuming a constant B_1 magnitude, i.e., a purely phase-based reconstruction using (8.3)

conductivity appears noisy and with strong ripples (Fig. 8.4a). Please note that again different color scales have been applied for the different subplots to better visualize the effects. The larger kernel of 11 voxels reduces noise and ripples (Fig. 8.4b). Taking into account a median filter and compartment boundaries, via Eq. (8.12), greatly reduces noise and ripples (Fig. 8.4c). If the effect of B_1 magnitude is ignored by assuming a constant B_1 magnitude (i.e., using (8.3) instead of (8.7)), a slight increase of conductivity appears toward the rim of the brain (visible by increased appearance of orange and red areas). As for the phantom, this increase corresponds to gradients of the B_1 magnitude, as visible on Fig. 8.1f. Small banding artifacts are visible in the lower left and right, arising from air cavities in the ears, leading to nonphysical ("blue") negative conductivity in these areas.

Inference from Phantom and In Vivo Experiments

The results allow the conclusion that although conductivity is encoded in the B_1 phase, it is usually not obvious by visual inspection of the phase, particularly in vivo. The specific setup of the phantom enables our eyes to distinguish a flat phase in the oil compartment from the curved phase in the saline compartment. This is no longer the case for in vivo: here, a global phase curvature across the brain is visible, but different local curvature according to anatomic details cannot be distinguished by our sight.

8.5.4 Preclinical Experiments

Various preclinical EPT studies have been performed in the recent years, predominantly on rodent models. According to the human studies conducted, the preclinical studies investigated mainly tumors models [12, 24, 26, 32, 43] but also stroke models [1, 14, 19]. An exemplary result for a rat tumor model [24] is shown in Fig. 8.5, reporting conductivity values increasing linearly with tumor growth, while diffusion values do not change with tumor growth. This study has been performed at 9.4T, representative for the trend toward high field strength for preclinical studies (up to 21.1T applied in [1]), but standard clinical field strength does not prohibit preclinical EPT studies (e.g., [14, 32]). While brain mapping appears to

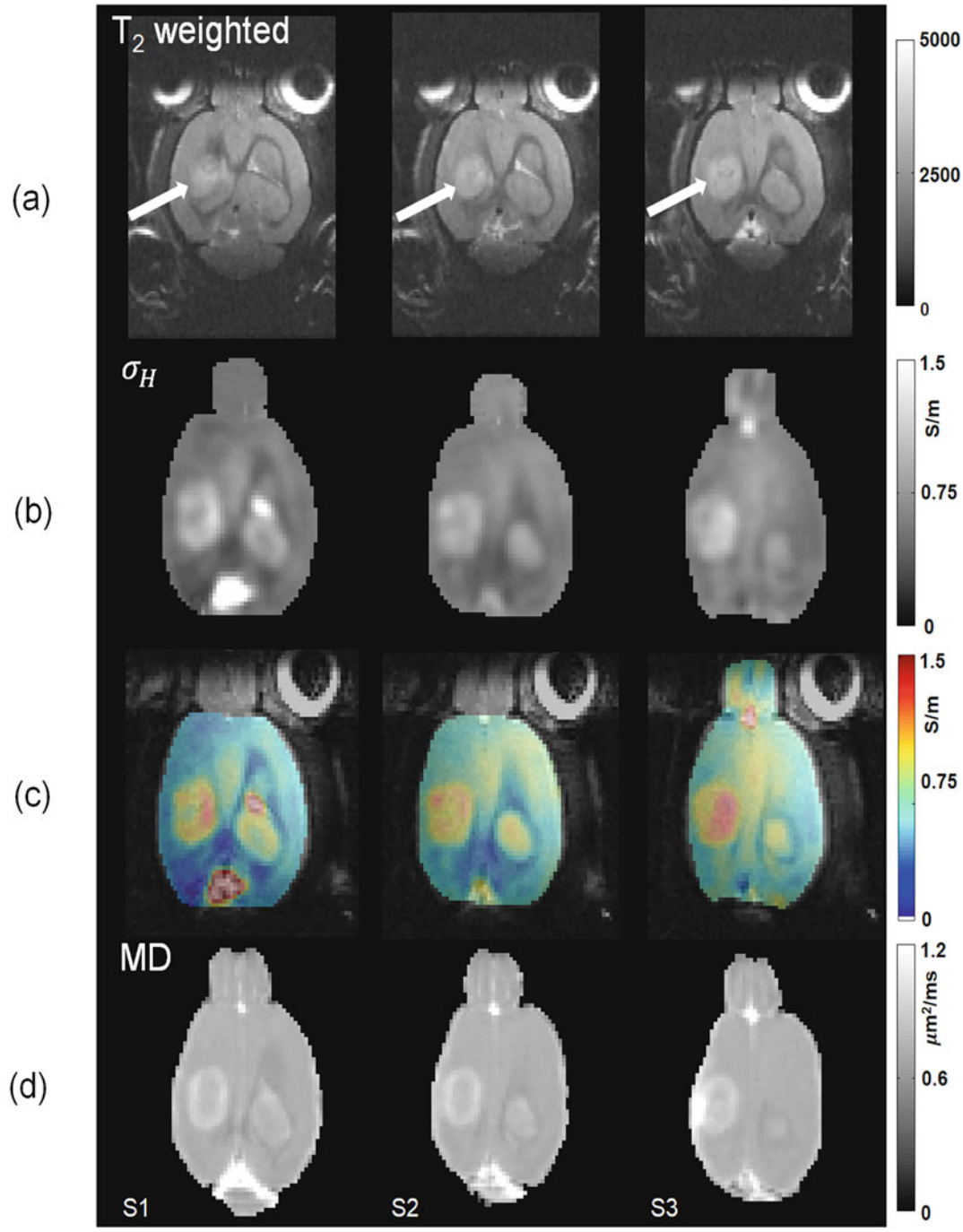

Fig. 8.5 Example of preclinical experiment [24]. F98 rat brain tumor images for three slices S1, S2, S3 showing the widest spread of the tumor growth in the brain of this rat. (**a**) T2-weighted images, (**b**) high-frequency conductivity images at 400 MHz, (**c**) conductivity images in (**c**) overlayed over the images in (**a**), and (**d**) mean diffusivity (MD) images

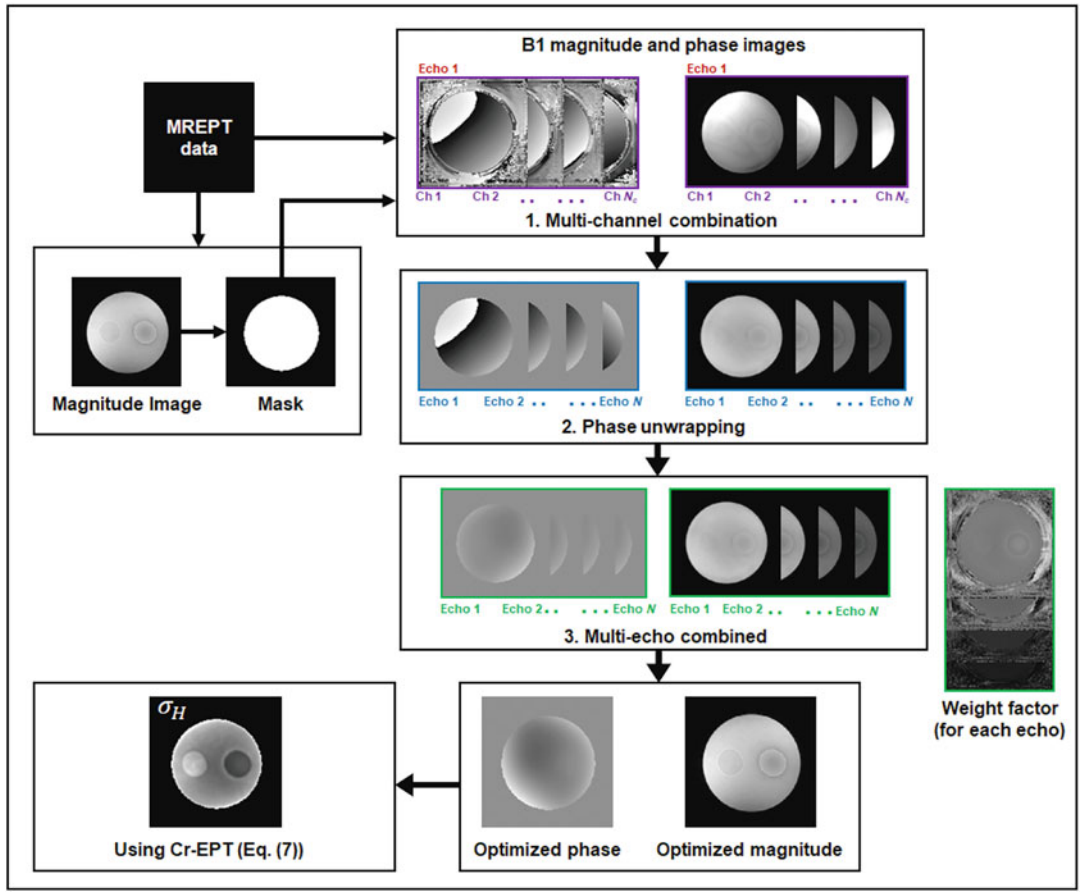

Fig. 8.6 Example of EPT workflow in case that multiple echoes have been acquired with multiple RF RX coils. Starting from the upper left, the pre-processing steps required to combine the multichannel and multi-echo data acquired with multi-echo spin/gradient echo pulse sequences are depicted, eventually leading to the final reconstruction result (lower left)

be the most promising application of EPT, cardiac EPT is obviously one of the most challenging applications, and only a single cardiac animal study has been published yet (reporting a decreased conductivity in the infarcted area [44]).

Appendix

When single echo pulse sequences are used in phase-based EPT, the $\mathbf{B_1}$ phase calculation is straightforward. However, when multi-echo pulse sequences are used with multichannel receive RF coils, the phase calculation becomes complicated. While various methods are developed for combination of channels and echoes to create one phase image per slice, they all have some generic steps. These steps are demonstrated using a cylindrical shaped phantom with two cylindrical anomalies in Fig. 8.6. Note that the background voxels of conductivity images are generally removed by segmenting the masks from magnitude images. This is illustrated in Fig. 8.6 and the effect of using mask is evident in Fig. 8.5b and (c) images.

References

1. G. Amouzandeh, F. Mentink-Vigier, S. Helsper, F.A. Bagdasarian, J.T. Rosenberg, S. Grant, Magnetic resonance electrical property mapping at 21.1 T: a study

of conductivity and permittivity in phantoms, ex vivo tissue and in vivo ischemia. Phys. Med. Biol. **65**, 055007 (2019)
2. A. Arduino, L. Zilberti, M. Chiampi, O. Bottauscio, CSI-EPT in presence of RF-shield for MR-coils. IEEE Trans. Med. Imag. **36**, 1396–1404 (2017)
3. E. Balidemaj, C.A. van den Berg, J. Trinks, A.L. van Lier, A.J. Nederveen, L.J. Stalpers, H. Crezee, R.F. Remis, CSI-EPT: a contrast source inversion approach for improved MRI-based electric properties tomography. IEEE Trans. Med. Imag. **34**, 1788–96 (2015)
4. N. Choi, M. Ghim, S. Yang, S.Y. Zho, D.H. Kim, In vivo conductivity mapping using double spin echo for flow effect removal, in *Proceedings of the 19th Annual Meeting of the ISMRM* (ISMRM, Concord, 2011), p. 4466
5. C. Gabriel, S. Gabriel, E. Corthout, The dielectric properties of biological tissues: I. Literature survey. Phys. Med. Biol. **41**, 2231–2249 (1996)
6. S. Gavazzi, C.A.T. van den Berg, A. Sbrizzi, H.P. Kok, L.J.A. Stalpers, J.J.W. Lagendijk, H. Crezee, A.L.H. van Lier, Accuracy and precision of electrical permittivity mapping at 3T: the impact of three B1 mapping techniques. Magn. Reson. Med. **81**, 3628–3642 (2019)
7. N. Gurler, Y.Z. Ider, Gradient-based electrical conductivity imaging using mr phase. Magn. Reson. Med. **77**(1), 137–150 (2017)
8. N. Gurler, O.M. Oran, H.D. Keklikoglu, Y.Z. Ider, Application of generalized phase based electrical conductivity imaging in the subacute stage of hemorrhagic and ischemic strokes, in *Proceedings of the 24th Annual Meeting of the ISMRM*, p. 2994 (ISMRM, Concord, 2016)
9. E.M. Haacke, L.S. Pepropoulos, E.W. Nilges, D.H. Wu, Extraction of conductivity and permittivity using magnetic resonance imaging. Phys. Med. Biol. **36**, 723–734 (1991)
10. F.S. Hafalir, O.F. Oran, N. Gurler, Y.Z. Ider, Convection-reaction equation based magnetic resonance electrical properties tomography (cr-mrept). IEEE Trans. Med. Imag. **33**(3), 777–793 (2014)
11. N. Hampe, M. Herrmann, T. Amthor, C. Findeklee, M. Doneva, U. Katscher, Dictionary-based electric properties tomography. Magn. Reson. Med. **81**, 342–349 (2019)
12. I. Hancu, J.C. Roberts, S. Bulumulla, S.K. Lee, On conductivity, permittivity, apparent diffusion coefficient, and their usefulness as cancer markers at MRI frequencies. Magn. Reson. Med. **73**, 2025–2029 (2015)
13. L. Huang, F. Schweser, K.H. Herrmann, M. Krämer, A. Deistung, J.R. Reichenbach, A Monte Carlo method for overcoming the edge artifacts in MRI-based electrical conductivity mapping, in *Proceedings of the 22nd Annual Meeting of the ISMRM* (ISMRM, 2014), p. 3190
14. U. Jensen-Kondering, L. Shu, R. Böhm, O. Jansen, In-vivo pilot study at 3 tesla: feasibility of electric properties tomography in a rat model of stroke. Phys. Med. **9**, 100024 (2020)
15. U. Katscher, P. Börnert, Imaging of lung conductivity using ultrashort echo-time imaging, in *Proceedings of the 24th Annual Meeting of the ISMRM* (ISMRM, 2016), p. 2923
16. U. Katscher, C.A.T. van den Berg, Electric properties tomography: biochemical, physical and technical background, evaluation and clinical applications. NMR Biomed. **30**, 3729 (2017)
17. U. Katscher, K. Djamshidi, T. Voigt, M. Ivancevic, H. Abe, G. Newstead, J. Keupp, Estimation of breast tumor conductivity using parabolic phase fitting, in *Proceedings of the 20th Annual Meeting of the ISMRM* (ISMRM, 2012), p. 3482
18. U. Katscher, C.H. Stehning, K.K. Tha, The impact of CSF pulsation on reconstructed brain conductivity, in *Proceedings of the 26th Annual Meeting of the ISMRM* (ISMRM, 2018), p. 546
19. D.H. Kim, M. Chauhan, M.O. Kim, W.C. Jeong, H.J. Kim, I. Sersa, O.I. Kwon, E.J. Woo, Frequency-dependent conductivity contrast for tissue characterization using a dual-frequency range conductivity mapping MR method. IEEE Trans. Med. Imag. **34**, 507–513 (2015)
20. S.K. Lee, S. Bulumulla, I. Hancu, Theoretical investigation of random noise-limited signal-to-noise ratio in MR-based electrical properties tomography. IEEE Trans. Med. Imag. **34**, 2220–2232 (2015)
21. S.K. Lee, S. Bulumulla, F. Wiesinger, L. Sacolick, W. Sun, I. Hancu, Tissue electrical property mapping from zero echo-time magnetic resonance imaging. IEEE Trans. Med. Imag. **34**, 541–550 (2015)
22. J.S. Lee, J.W. Shin, D.H. Kim, MR-based conductivity imaging using multiple receiver coils. Magn. Reson. Med. **76**, 530–539 (2016)
23. R. Leijsen, C.A.T. van den Berg, R. Remis, A. Webb, S. Mandija, Improving tissue electrical properties reconstructions by exploiting the benefits of combining deep learning-EPT and 3d contrast source inversion-EPT, in *Proceedings of the 27th Annual Meeting of the ISMRM* (ISMRM, 2019), p. 5050
24. C. Lesbats, N. Katoch, A.S. Minhas, A. Taylor, H.J. Kim, E.J. Woo, H. Poptani, High-frequency electrical properties tomography at 9.4t as a novel contrast mechanism for brain tumors. Magn. Reson. Med. **86**(1), 382–392 (2021)
25. J. Liu, X. Zhang, S. Schmitter, P.F. van de Moortele, B. He, Gradient-based electrical properties tomography (gEPT): a robust method for mapping electrical properties of biological tissues in vivo using magnetic resonance imaging. Magn. Reson. Med. **74**, 634–646 (2015)
26. J. Liu, Q. Shao, Y. Wang, G. Adriany, J. Bischof, P.F. van de Moortele, B. He, In vivo imaging of electrical properties of an animal tumor model with an 8-channel transceiver array at 7 T using electri-

cal properties tomography. Magn. Reson. Med. **78**, 2157–2169 (2017)
27. J. Liu, Y. Wang, U. Katscher, B. He, Electrical properties tomography based on B1 maps in MRI: principles, applications, and challenges. IEEE Trans. Biomed. Eng. **64**, 2515–2530 (2017)
28. S. Mandija, A. Sbrizzi, U. Katscher, P.R. Luijten, C.A.T. van den Berg, Error analysis of helmholtz-based MR-electrical properties tomography. Magn. Reson. Med. **80**, 90–100 (2018)
29. E.F. Mandija, S. Meliadò, N.R.F. Huttinga, P.R. Luijten, C.A.T. van den Berg, Opening a new window on MR-based electrical properties tomography with deep learning. Sci. Rep. **9**, 8895 (2019)
30. E. Michel, D. Hernandez, M.H. Cho, S.Y. Lee, Denoising of B1 field maps for noise-robust image reconstruction in electrical properties tomography. Med. Phys. **41**, 1–9 (2014)
31. K. Nehrke, P. Börnert, DREAM-A novel approach for robust, ultrafast, multislice b1 mapping. Magn. Reson. Med. **68**, 1517–1526 (2012)
32. J.A. Park, K.J. Kang, I.O. Ko, K.C. Lee, B.K. Choi, N. Katoch, J.W. Kim, H.J. Kim, O.I. Kwon, E.J. Woo, In vivo measurement of brain tissue response after irradiation: comparison of T2 relaxation, apparent diffusion coefficient, and electrical conductivity. IEEE Tran. Med. Imag. **38**, 2779–2784 (2019)
33. R. Pohmann, K. Scheffler, A theoretical and experimental comparison of different techniques for b_1 mapping at very high fields. NMR Biomed. **26**, 265–275 (2013)
34. K.P. Pruessmann, M. Weiger, M.B. Scheidegger, P. Boesiger, SENSE: sensitivity encoding for fast MRI. Magn. Reson. Med. **42**, 952–962 (1999)
35. L.I. Sacolick, F. Wiesinger, I. Hancu, M.W. Vogel, B1 mapping by Bloch-Siegert shift. Magn. Reson. Med. **63**, 1315–1322 (2010)
36. A. Savitzky, M.J.E. Golay, Smoothing and differentiation of data by simplified least squares procedures. Anal. Chem. **36**, 1627–1639 (1964)
37. F. Schweser, L. Huang, K.H. Herrmann, M. Krämer, A. Deistung, J.R. Reichenbach, Conductivity mappingusing ultrashort echo time (UTE) imaging, in *Proceedings of the 27th Annual Meeting of the ISMRM* (ISMRM, 2013), p. 4190
38. J.W. Shin, M.J. Kim, J.S. Lee, Initial study on in vivo conductivity mapping of breast cancer using MRI. Magn. Reson. Med. **42**, 371–378 (2015)
39. C. Stehning, T.R. Voigt, U. Katscher, Real-time conductivity mapping using balanced SSFP and phase-based reconstruction, in *Proceedings of the 19th Annual Meeting of the ISMRM* (ISMRM, 2011), p. 128
40. K.K. Tha, U. Katscher, S. Yamaguchi, C. Stehning, S. Terasaka, N. Fujima, K. Kudo, K. Kazumata, T. Yamamoto, M. Van Cauteren, H. Shirato, Noninvasive electrical conductivity measurement by MRI: a test of its validity and the electrical conductivity characteristics of glioma. Eur. Radiol. **28**, 348–355 (2018)
41. A.L.H. van Lier, D.O. Brunner, K.P Pruessmann et al., B1 phase mapping at 7T and its application for in vivo electrical conductivity mapping. Magn. Reson. Med. **67**, 552–561 (2012)
42. A.L.H. van Lier, A. Raaijmakers, T. Voigt, J.J. Lagendijk, U. Katscher, C.A.T. van den Berg, Electric properties tomography in the human brain at 1.5, 3, and 7 T: a comparison study. Magn. Reson. Med. **71**, 354–363 (2014)
43. P.P. Vasudevan, R. Aminzadeh, N. de Geeter, B. Descamps, L. Dupré, W. Joseph, R. van Holen, In vivo electrical conductivity imaging of animal tumor model at 7T using EPT, in *Proceedings of the 1st World Conference on Biomedical Applications of Electromagnetic Fields* (European Cooperation in Science and Technology, Brussels, 2018), pp. 1–2
44. T. Voigt, A. Schuster, M. Ishida, C. Stehning, A. Chiribiri, E. Nagel, T. Schaeffter, Conductivity imaging of an ischemic pig heart model using electric properties tomography, in *Proceedings of the 20th Annual Meeting of the ISMRM* (ISMRM, 2012), p. 3483
45. V.L. Yarnykh, Actual flip-angle imaging in the pulsed steady state: a method for rapid three-dimensional mapping of the transmitted radiofrequency field. Magn. Reson. Med. **57**, 192–200 (2007)

Index

R. Sadleir, A. S. Minhas (eds.), *Electrical Properties of Tissues*, Advances in Experimental Medicine and Biology 1380, https://doi.org/10.1007/978-3-031-03873-0